University of Patras

Department of Mechanical Engineering & Aeronautics

Applied Mechanics & Vibrations Laboratory

Structural Analysis & Active Materials Group

Development and Application of a Novel Semi-Active Piezoelectric Tuned Mass Damper for Robust Vibration Control of Flexible Structures with Focus on Airframe Structures

Grigorios M. Chatziathanasiou

Mechanical and Aeronautics Engineer

A dissertation submitted in partial fulfilment of the requirements for the degree of Doctor of Philosophy.

Patras, 2024

University of Patras, Department of Mechanical Engineering and Aeronautics

Grigorios M. Chatziathanasiou

© 2024 – All rights reserved

Dedicated to my parents,

Michalis and Panagiota

and my brothers,

Dimitris and Nikos

ΠΟΛΥΤΕΧΝΙΚΗ ΣΧΟΛΗ
Τμήμα Μηχανολόγων & Αεροναυπηγών Μηχανικών
Τομέας Εφηρμ. Μηχανικής, Υλικών & Εμβιομηχανικής

Πάτρα, GR 26504
e-mail:
saravanos@mech.upatras.gr
http://saam.mech.upatras.gr/
τηλ: +30-2610-969437

17 Ιουνίου 2024

Προς: Τμήμα Μηχανολόγων Μηχανικών & Αεροναυπηγών,
Πολυτεχνική Σχολή, Πανεπιστήμιο Πατρών
Θέμα: Έγκριση Διδακτορικής Διατριβής του Υποψήφιου Διδάκτορα **κ. Γρηγορίου Χατζηαθανασίου**

Η επταμελής εξεταστική επιτροπή, η οποία συγκροτήθηκε σύμφωνα με την απόφαση 33903/17/05/2024 της Συνέλευσης του Τμήματος, αποτελούμενη από τους κκ. Δημήτριο Σαραβάνο, (Επιβλέποντα της διδακτορικής διατριβής), Σπήλιο Φασόη και Δημοσθένη Πολύζο, Καθηγητές του Τμήματος Μηχανολόγων και Αεροναυπηγών Μηχανικών του Πανεπιστημίου Πατρών, τον κ. Ιωάννη Αντωνιάδη, Καθηγητή της Σχολής Μηχανολόγων Μηχανικών του Εθνικού Μετσόβιου Πολυτεχνείου, τον κ. Ιωάννη Σακελλαρίου, Αναπληρωτή Καθηγητή του Τμήματος Μηχανολόγων και Αεροναυπηγών Μηχανικών του Πανεπιστημίου Πατρών, και τους κκ. Νικόλαο Χρυσοχοΐδη και Άγγελο Φιλιππάτο, Επίκουρους Καθηγητές του Τμήματος Μηχανολόγων και Αεροναυπηγών Μηχανικών του Πανεπιστημίου Πατρών, συνεδρίασε σήμερα (Δευτέρα, 17 Ιουνίου 2024) για την κρίση της διδακτορικής διατριβής του υποψήφιου διδάκτορα **κ. Γρηγορίου Χατζηαθανασίου**, με θέμα:

«Ανάπτυξη και Εφαρμογή ενός Καινοτόμου Ημιενεργού Πιεζοηλεκτρικού Συντονισμένου Αποσβεστήρα για τον Εύρωστο Έλεγχο Ταλαντώσεων σε Εύκαμπτες Κατασκευές με Έμφαση σε Αεροπορικές Δομές»»

Ο υποψήφιος διδάκτορας παρουσίασε το ερευνητικό έργο το οποίο συντελέστηκε κατά την εκπόνηση της διδακτορικής του διατριβής και το υποστήριξε ενώπιον της εξεταστικής επιτροπής. Η επιτροπή ψήφισε ΟΜΟΦΩΝΑ ότι το περιεχόμενο της διατριβής είναι πρωτότυπο και αποτελεί ουσιαστική συμβολή στην επιστήμη του Μηχανολόγου και Αεροναυπηγού Μηχανικού, και βαθμολόγησε την διατριβή με τον βαθμό ΑΡΙΣΤΑ. Επιπλέον, η επιτροπή διεπίστωσε ότι ο υποψήφιος έχει αποκτήσει αξιόλογη επιστημονική και ερευνητική ωριμότητα και τον προτείνει για την απόκτηση Διδακτορικού Διπλώματος από το Τμήμα.

Η Επιτροπή:

κ. Δημήτρης Σαραβάνος, Καθηγητής	DIMITRIOS SARAVANOS 18/06/2024 18:48
κ. Σπήλιος Φασόης, Καθηγητής	SPILIOS FASOIS 17/06/2024 17:48
κ. Ιωάννης Αντωνιάδης, Καθηγητής	Ioannis Antoniadis Ioannis Antoniadis 17.06.2024 18:23
κ. Δήμο Πολύζος, Καθηγητής	
κ. Ιωάννης Σακελλαρίου, Αναπληρωτής Καθηγητής	IOANNIS SAKELLARIOU 18/06/2024 15:08
κ. Νικόλαος Χρυσοχοΐδης, Επίκουρος Καθηγητής	NIKOLAOS CHRYSOCHOIDIS 18/06/2024 15:25
κ. Άγγελος Φιλιππάτος, Επίκουρος Καθηγητής	ANGELOS FILIPPATOS 18/06/2024 16:29

Ψηφιακή Βεβαίωση Εγγράφου

Μπορείτε να ελέγξετε την ισχύ του εγγράφου σκανάροντας το QR code ή εισάγοντας τον κωδικό στο docs.gov.gr/validate

Κωδικός εγγράφου: zTjKJSc87cP0buLBXyYr9g

Υπογραφή:
ΔΗΜΟΣΘΕΝΗΣ ΠΟΛΥΖΟΣ
Πατρώνυμο: ΚΩΝΣΤΑΝΤΙΝΟΣ
ΑΦΜ: 025512808
Ημ. Υπογραφής: 17/06/2024 18:54:13

Acknowledgements

Here, I would like to express my gratitude to all the people who contributed to the successful completion of this dissertation.

My supervisor Professor Dimitris Saravanos, who proposed me this very interesting topic and offered me the chance to broaden my knowledge and perception on structural dynamics and vibration control. Professor Saravanos had a constant supervision of my work and progress, beneficially assisting my research and guiding me towards the most appropriate academic paths. Our close and frequent collaboration is a major factor for the development of the present thesis, and I am truly thankful for this. I will always look up to him for his sharpness, passion for research, and broad knowledge of the engineering science.

I would like to acknowledge and sincerely thank the Assistant Professor Nikolaos Chrysochoidis, for his valuable help throughout all the years of my PhD life, and especially for his immense contribution to the experimental campaigns of this thesis. I am truly in debt for his support and advice not only in academic issues, but in all aspects of everyday life. I would also like to express my sincere appreciation to Professor S.D. Fassois, member of my advisory committee, for our fruitful collaboration and his very insightful comments and guidance, which had great impact on this thesis and especially on Chapter 8. Furthermore, I want to thank the rest of the members of the examining committee: Professor Ioannis Antoniadis (member of the three-party committee), Professor Demosthenes Polyzos, Associate Professor Ioannis Sakellariou, and Assistant Professor Angelos Filippatos, for their valuable comments and remarks on the presented research and their interesting questions during the defence of the dissertation.

I want to deeply thank my parents Michalis and Panagiota, and my brothers Dimitris and Nikos, for the inspiration they gave me, their unconditional support, and valuable suggestions. Providing me with the opportunity to make my own choices, and knowing their presence in any necessity, allowed me to look forward and focus on my thesis.

At this point, I would like to express my gratitude to all the people who did not only encourage me to keep on going all the years of my thesis, but also contributed to making this an enjoyable journey. My fellow lab mates Grigoris-Christos Kardarakos and Dimitris Dimitriou, for our laughs, our stimulating discussions, and the solutions we found to many of our common problems. My dearest friends from the pre-graduate years, who continued their PhD journey at the Department of Mechanical Engineering and Aeronautics in the University of Patras, Giorgos Vlachospyros and Giorgos Galanopoulos, for all the discussions and the fun we had. PhD Candidates Thomas Zaragkas, Iakovos Delasoudas, Giorgos Kotsinis, Loukas Adamos, Kyriakos Kritikakos and Drs Nikos Athanasopoulos, Theodoros Machairas, Dimitris Siorikis, and Lykourgos Kontaxis, for the good times we had together and their unconditional

assistance. My friends from my school years and undergraduate studies, for tolerating my forgetfulness, and preserving beautiful and truthful relationships, despite the miles between us. Last but not least, I would like to express my deepest appreciation to Anastasia Maria Kiapoka, for her endless support, positive energy, and constant faith in me. Our long discussions and her well-aimed advice became a valuable companion and pushed me to continue and complete this dissertation.

“We are the sultans of swing”

Dire Straits

Abstract

Mechanical systems and structures may experience conditions or dynamic excitations that result in oscillatory motion and vibrations. *Flexible structures*, such lightweight means of transportations (aircrafts, rotorcrafts, yachts, etc.) are more susceptible to *high amplitude vibrations* due to their low-frequency and lightly damped structural modes. Vibrations in such structures are attributed to a variety of stimuli, such as motors, rotors, and aerodynamic loads, creating potentially frequency-varying broadband and / or tonal excitations. Contemporary trends towards higher efficiency transport engines and lower weight of the structures (for less fuel consumption and CO_2 emissions) using composite materials, lead to higher structural oscillations with lower damping capacity. Excessive vibrations in such structures are undesirable, as they affect the safety and comfort of the passengers, reduce the material fatigue life, and may even lead to structural failure. Therefore, vibration control is extremely crucial in these structures, aiming at the reduction of the amplitude of the vibrations, in order to ensure the reliability of their function. An appropriate ***antivibration mechanism*** should exhibit *multi-modal* and *multi-tonal* vibration control capabilities, *adaptability* to potentially frequency-varying applied loads, and minimal requirements for added weight and power supply.

Towards the vibration control of flexible structures that satisfy these demanding requirements, this dissertation addresses the development and application of a novel semi-active electromechanical antivibration device, comprising an *auxiliary mass*, mounted on a specialty *piezoelectric device*, whose terminals are connected to a *shunt resistive-inductive (RL) circuit*. The piezoelectric device provides the stiffness for the resonant mass oscillator and introduces high electromechanical energy conversion and coupling. This concept is very promising in terms of high and versatile vibration attenuation potential, due to its various mechanisms for absorbing and dissipating the host structure kinetic energy. The transformed, by the piezoelectric device, electrical energy can be *dissipated into heat*, due to the shunt circuit tunable resistance, while the resonant mass and the inductance-tunable shunt circuit eigenfrequency can absorb very high vibrational energy (*energy sinks*). The proposed device combines the high vibration control capabilities of the tuned mass damper (TMD) and the great tuning and controlled damping characteristics of the shunt piezoelectric device. Therefore, this device is defined in this dissertation as a piezoelectric semi-active tuned mass damper (***SATMD***).

Initially, a specialty *piezoelectric transducer* is carefully selected to exhibit low effective stiffness and high piezoelectric coefficient. The rest components of the SATMD antivibration device are designed and assembled on the selected piezoelectric transducer. The sole SATMD is *modeled and experimentally characterized*, revealing two pairs of electromechanically coupled poles. The experimentally demonstrated effects of the shunt circuit impedance are compared to computational results, showing great agreement.

Next, the performance of the piezoelectric SATMD is evaluated experimentally and numerically on a simplified lumped mass structure. The dynamic equations of motion of the SATMD – host structure

system are formulated. The transfer functions show that the introduced antiresonances on the host structure coincide with the sole SATMD eigenfrequencies. *Resistance* increases the *damping* capabilities of the coupled electromechanical system, while *inductance* introduces a new, highly tunable, *oscillator* in the system, which enhances the coupling and conversion of kinetic to electrical energy. The SATMD can compensate for the purely mechanical TMD disadvantages, providing broadband vibration suppression, and offering great retuning capabilities. The experimental measurements validate the developed models.

The performance of the antivibration device capabilities is subsequently presented on large and flexible structures. For the computational model, a reduced-ordered modal space structural dynamics model is formulated, coupled with the SATMD device, and the RL shunt electric circuit. The SATMD is attached to a scaled-down airframe prototype, which is used as the laboratory testing structure. The SATMD demonstrates great *multi-modal and multi-tonal vibration attenuation* capabilities. Furthermore, it is shown that the two introduced antiresonances are independent of the host structure dynamic characteristics, and as a result the appropriate SATMD auxiliary mass and inductance can be decided based only on the structure frequency response. This special and versatile feature is used for the antivibration performance of the SATMD on a BO105 S helicopter, accomplishing beneficial reduction to two excessive vibration frequencies during real-flight conditions.

Furthermore, the SATMD *design strategy* is studied, aiming at multi-modal vibration reduction of the scaled down-airframe model, under broadband excitation. The optimal parameters are compared to an ad-hoc design strategy. Including the auxiliary mass in the optimization scheme, simultaneous 90% acceleration reduction is achieved in all studied structural modes, and it is proved that the auxiliary mass is not necessarily optimally tuned to a host structure mode.

Finally, an *adaptive control* concept and algorithm is developed based on the effects that each of the tunable parameters (resistance and inductance) introduces to the host structure behavior. Estimates of the frequency response of the structure are based on the measured acceleration, yielding the highest frequency peak (critical frequency) at each control time period. The inductance to suppress each critical frequency is independent of the host structure dynamics, whereas the resistance is calculated based on the acceleration response of the structure. The developed adaptive algorithm is tested on the scaled-down airframe model, which is assumed to undergo both gradual and abrupt mass alterations. The adaptive SATMD achieves great continuous vibration control, proving the effectiveness of the developed algorithm.

Περίληψη

Μηχανικά συστήματα και κατασκευές ενδέχεται να αντιμετωπίσουν συνθήκες ή δυναμικές διεγέρσεις που οδηγούν σε ταλαντωτικές κινήσεις και κραδασμούς. Οι *εύκαμπτες κατασκευές*, όπως ελαφρά μέσα μεταφοράς (αεροσκάφη, ελικοφόρα, σκάφη αναψυχής, κ.λπ.) είναι πιο επιρρεπείς σε *ταλαντώσεις υψηλού πλάτους*, λόγω των χαμηλόσυχνων και ελαφρά αποσβεννυμένων ιδιομορφών τους. Οι κραδασμοί σε τέτοιες δομές αποδίδονται σε μία ποικιλία διεγέρσεων, όπως κινητήρες, ρότορες, και αεροδυναμικά φορτία, δημιουργώντας δυνητικά συχνοτικά-μεταβαλλόμενες διεγέρσεις ευρέως φάσματος και / ή τονικές διεγέρσεις. Οι σύγχρονες τάσεις για κινητήρες υψηλότερης απόδοσης και κατασκευές με χαμηλότερο βάρος (για χαμηλότερη κατανάλωση καυσίμων και εκπομπές CO_2), με χρήση σύνθετων υλικών, οδηγούν σε υψηλότερες ταλαντώσεις με χαμηλότερη ικανότητα απόσβεσης. Οι έντονοι κραδασμοί σε αυτές τις κατασκευές είναι ανεπιθύμητοι, καθώς επηρεάζουν την ασφάλεια και την άνεση των επιβατών, μειώνουν την κοπωτική διάρκεια ζωής των υλικών, και μπορεί να οδηγήσουν ακόμα και σε αστοχία. Επομένως, ο έλεγχος των κραδασμών είναι εξαιρετικά κρίσιμος, στοχεύοντας στη μείωση του πλάτους των κραδασμών, ώστε να διασφαλίζεται η αξιοπιστία στη λειτουργία τους. Ένας κατάλληλος ***αντικραδασμικός μηχανισμός*** θα πρέπει να παρουσιάζει δυνατότητες *πολυμορφικού* και *πολυτονικού* ελέγχου των κραδασμών, *προσαρμοστικότητα* σε δυνητικά μεταβαλλόμενα συχνοτικά φορτία, και ελάχιστες απαιτήσεις για αύξηση βάρους και τροφοδοσία ρεύματος.

Για τον έλεγχο των κραδασμών σε εύκαμπτες κατασκευές που ικανοποιεί αυτές τις απαιτητικές προδιαγραφές, η παρούσα διατριβή πραγματεύεται την ανάπτυξη και εφαρμογή μίας καινοτόμου ημιενεργής ηλεκτρομηχανικής αντικραδασμικής συσκευής, αποτελούμενη από μία *βοηθητική μάζα*, τοποθετημένη σε μία ειδική *πιεζοηλεκτρική συσκευή*, οι ακροδέκτες της οποίας είναι συνδεδεμένοι με ένα ηλεκτρικό *κύκλωμα παροχέτευσης αντίστασης – αυτεπαγωγής (RL)*. Η πιεζοηλεκτρική συσκευή παρέχει τη δυσκαμψία για τον συντονισμένο ταλαντωτή μάζας και προσφέρει υψηλή ηλεκτρομηχανική μετατροπή ενέργειας και σύζευξη. Μία τέτοια αντικραδασμική συσκευή είναι πολλά υποσχόμενη όσον αφορά την υψηλή και ευέλικτη μείωση των κραδασμών, λόγων των διάφορων μηχανισμών της για απορρόφηση και διάχυση της κινητικής ενέργειας της κατασκευής ενδιαφέροντος. Η ηλεκτρική ενέργεια που εμφανίζεται, λόγω της πιεζοηλεκτρικής συσκευής, μπορεί να *διαχυθεί σε θερμότητα*, λόγω της ρυθμιζόμενης αντίστασης στο κύκλωμα, ενώ η συντονισμένη μάζα και η επαγωγικά ρυθμιζόμενη ηλεκτρική ιδιοσυχνότητα στο κύκλωμα μπορούν να απορροφήσουν πολύ υψηλά ποσοστά της ταλαντωτικής ενέργειας (*ενεργειακοί αποταμιευτήρες*). Η προτεινόμενη συσκευή συνδυάζει τις υψηλές δυνατότητες ελέγχου κραδασμών του συντονισμένου αποσβεστήρα μάζας (tuned mass damper: TMD) και τα εξαιρετικά χαρακτηριστικά συντονισμού και ελεγχόμενης απόσβεσης της πιεζοηλεκτρικής συσκευής με ηλεκτρικό κύκλωμα παροχέτευσης. Επομένως, αυτή η συσκευή ορίζεται σε αυτή τη διατριβή ως ένας πιεζοηλεκτρικός ημιενεργός συντονισμένος αποσβεστήρας μάζας (semi-active TMD: ***SATMD***).

Αρχικά, μία εξειδικευμένη *πιεζοηλεκτρική συσκευή* επιλέγεται προσεκτικά, έτσι ώστε να έχει χαμηλή δυσκαμψία και υψηλό πιεζοηλεκτρικό συντελεστή. Τα υπόλοιπα εξαρτήματα της αντικραδασμικής συσκευής SATMD σχεδιάζονται και συναρμολογούνται με βάση την επιλεγμένη πιεζοηλεκτρική συσκευή. Ο SATMD *μοντελοποιείται και χαρακτηρίζεται πειραματικά*, αποκαλύπτοντας δύο ζεύγη ηλεκτρομηχανικά συζευγμένων πόλων. Τα πειραματικά αποδεδειγμένα φαινόμενα της σύνθετης εμπέδησης του κυκλώματος διακλάδωσης συγκρίνονται με τα υπολογιστικά αποτελέσματα, παρουσιάζοντας μεγάλη συμφωνία.

Στη συνέχεια, η απόδοση του πιεζοηλεκτρικού SATMD αξιολογείται πειραματικά και αριθμητικά σε μια απλοποιημένη κατασκευή ενδιαφέροντος συγκεντρωμένης μάζας. Σχηματίζονται οι δυναμικές εξισώσεις ισορροπίας του συστήματος SATMD – κατασκευής ενδιαφέροντος. Οι συναρτήσεις μεταφοράς δείχνουν ότι οι εισαγόμενοι αντισυντονισμοί στην κατασκευή ενδιαφέροντος συμπίπτουν με τις ιδιοσυχνότητες SATMD. Η *αντίσταση* αυξάνει τις δυνατότητες απόσβεσης του συζευγμένου ηλεκτρομηχανικού συστήματος, ενώ η *αυτεπαγωγή* εισάγει έναν νέο, εύκολα ρυθμιζόμενο, *ταλαντωτή* στο σύστημα, ο οποίος ενισχύει τη σύζευξη και τη μετατροπή της κινητικής σε ηλεκτρική ενέργεια. Ο SATMD μπορεί να αντισταθμίσει τα μειονεκτήματα του αμιγώς μηχανικού TMD, παρέχοντας ευρυζωνική καταστολή κραδασμών και προσφέροντας δυνατότητες επανασυντονισμού. Οι πειραματικές μετρήσεις επικυρώνουν τα αναπτυγμένα μοντέλα.

Η επίδοση των δυνατοτήτων της αντικραδασμικής συσκευής παρουσιάζεται στη συνέχεια σε μεγάλες και εύκαμπτες κατασκευές. Για το υπολογιστικό μοντέλο, αναπτύσσεται ένα μοντέλο δυναμικής μειωμένης τάξης στο μορφικό χώρο, σε συνδυασμό με τη συσκευή SATMD και το ηλεκτρικό κύκλωμα RL. Ο SATMD προσαρτάται σε ένα μειωμένο πρωτότυπο πλαίσιο αεροσκάφους, το οποίο χρησιμοποιείται ως δομή εργαστηριακών δοκιμών. Ο SATMD επιδεικνύει εξαιρετικές δυνατότητες *πολυμορφικής και πολυτονικής μείωσης των κραδασμών*. Επιπλέον, αποδεικνύεται ότι οι δύο εισαγόμενοι αντισυντονισμοί είναι ανεξάρτητοι από τα δυναμικά χαρακτηριστικά της κατασκευής ενδιαφέροντος, και ως αποτέλεσμα η κατάλληλη βοηθητική μάζα και η αυτεπαγωγή του SATMD μπορούν να ρυθμιστούν με βάση μόνο την απόκριση συχνότητας της κατασκευής. Αυτό το ειδικό και ευέλικτο χαρακτηριστικό χρησιμοποιείται για την αντικραδασμική απόδοση του SATMD σε ένα ελικόπτερο BO105 S, επιτυγχάνοντας ευεργετική μείωση σε δύο συχνότητες έντονων δονήσεων κατά τη διάρκεια πραγματικών συνθηκών πτήσης.

Επιπλέον, μελετάται η *στρατηγική σχεδιασμού* του SATMD, με στόχο την πολυμορφική μείωση κραδασμών του μειωμένου μοντέλου πλαισίου αεροσκάφους, υπό ευρυζωνική διέγερση. Οι βέλτιστες παράμετροι συγκρίνονται με μια ad-hoc στρατηγική σχεδιασμού. Συμπεριλαμβάνοντας τη βοηθητική μάζα στο σχήμα βελτιστοποίησης, επιτυγχάνεται ταυτόχρονη μείωση του πλάτους των επιταχύνσεων όλων των μελετώμενων ιδιομορφών κατά 90%, και αποδεικνύεται ότι η βοηθητική μάζα δεν είναι απαραίτητα βέλτιστα συντονισμένη σε μια ιδιομορφή της κατασκευής ενδιαφέροντος.

Τέλος, αναπτύσσεται ένας αλγόριθμος *προσαρμοστικού ελέγχου*, με βάση τις επιδράσεις που έχει κάθε μία από τις ρυθμιζόμενες παραμέτρους (αντίσταση και επαγωγή) στη συμπεριφορά της κατασκευής

ενδιαφέροντος. Οι εκτιμήσεις της απόκρισης συχνότητας της κατασκευής βασίζονται στη μετρούμενη επιτάχυνση, βρίσκοντας την υψηλότερη συχνοτική κορυφή (κρίσιμη συχνότητα) σε κάθε χρονική περίοδο ελέγχου. Η αυτεπαγωγή για την καταστολή κάθε κρίσιμης συχνότητας είναι ανεξάρτητη από τη δυναμική της κατασκευής ενδιαφέροντος, ενώ η αντίσταση υπολογίζεται με βάση την απόκριση επιτάχυνσης της δομής. Ο ανεπτυγμένος προσαρμοστικός αλγόριθμος δοκιμάζεται στο μειωμένο μοντέλο πλαισίου αεροσκάφους, το οποίο υφίσταται τόσο σταδιακές, όσο και απότομες αλλαγές μάζας. Ο προσαρμοστικός SATMD επιτυγχάνει εξαιρετικό συνεχή έλεγχο κραδασμών, αποδεικνύοντας την αποτελεσματικότητα του αναπτυγμένου αλγορίθμου.

Contents

Acknowledgements I

Abstract VI

Περίληψη VIII

Contents XI

List of Tables XVI

List of Figures XVII

List of Symbols XXII

Chapter 1: Introduction 1

1.1 Problem Statement and Motivation 1

1.2 Control Strategies on Flexible Structures 2

1.2.1 Passive Control Systems 3

1.2.2 Active Control Systems 4

1.2.3 Semi-Active Control Systems 4

1.3 Dissertation Scope and Objectives 5

1.4 Research Contributions and Novelty 6

1.5 Dissertation Outline 7

Chapter 2: Literature Review on the Vibration Control of Structures using Tuned Mass Dampers and Shunt Circuit Piezoelectric Devices 9

2.1 Tuned Mass Dampers 9

2.1.1 Overview and Operating Principles 9

2.1.2 Applications on Flexible Structures 10

2.1.3 Optimization Studies 11

2.1.4 Semi-active Control Studies 11

2.2 Shunt Circuit Piezoelectric Devices 12

2.2.1 Overview and Operating Principles 12

2.2.2 Applications on Flexible Structures 14

2.2.3 Optimization Studies 14

2.2.4 Semi-active Control Studies 15

2.3 Combinations of TMDs with Shunt Circuit Piezoelectric Devices 15
2.3.1 Piezoelectric Patches Attached to Thin Antivibration Structures 15
2.3.2 Shunt Piezoelectric Devices Providing the Stiffness for the Auxiliary Mass Oscillation 17
2.4 Open Questions and Challenges 21
Chapter 3: Experimental Apparatus for Vibration Testing 22
Chapter 4: Modeling, Specification and Characterization of the Piezoelectric SATMD 25
4.1 Sole SATMD Computational Model 25
4.1.1 Constitutive Equations in Piezoelectric Layers 25
4.1.2 Multilayer Piezoelectric Devices Equivalent Properties 27
4.1.3 Sole Conventional TMD 31
4.1.4 Sole Piezoelectric SATMD 31
4.1.4.1 Open Circuit 32
4.1.4.2 Shunt Circuit 33
4.1.4.2.1 Equations of Motion 33
4.1.4.2.2 Transfer Functions 33
4.2 Piezoelectric Device Desirable Features and Selection 34
4.2.1 Desirable Features and Characteristics for the Piezoelectric Transducer 34
4.2.2 Piezoelectric Device Configurations and Selection 35
4.3 SATMD Host Structure Integration and Components 37
4.3.1 Host Structure Integration and Uniaxial Movement 37
4.3.2 Auxiliary Mass and SATMD Assembly 38
4.3.3 Shunt circuit 39
4.4 Experimental Setup for SATMD Characterization 40
4.5 Shunt Circuit Impedance Effects 42
4.5.1 Resistance Effect 42
4.5.2 Inductance Effect 43
4.5.3 Combined Impedance Effect 45
4.6 Concluding Remarks 46
Chapter 5: Modeling and Performance of SATMD on a Lumped Mass Host Structure 48

5.1 SATMD – Lumped Mass Structure System Model 48
5.1.1 Conventional TMD 48
5.1.2 Piezoelectric SATMD 49
5.1.2.1 Equations of motion 49
5.1.2.2 Transfer Functions 52
5.2 Experimental Setup of Lumped Mass Host Structure 53
5.3 Baseline Performance with Passive TMD 54
5.4 Resistance Effect 55
5.5 Inductance Effect 57
5.6 Combined Impedance Effect 62
5.7 Concluding Remarks 65
Chapter 6: Modeling and Performance of SATMD on Large and Flexible Structures 66
6.1 SATMD – Large and Flexible Structure System Model 66
6.1.1 Detailed Finite Element Model 66
6.1.2 Reduced Order Modal Space Model 67
6.2 Scaled-Down Airframe Prototype Structure 69
6.2.1 Experimental Setup 69
6.2.2 Host Structure Finite Element and ROM Model 71
6.2.3 Broadband Multi-Modal Excitation 72
6.2.3.1 Baseline Performance with Passive TMD 72
6.2.3.2 Resistance Effect 73
6.2.3.3 Inductance Effect 75
6.2.3.4 Combined Impedance Effect 79
6.2.4 Multi-Tonal Excitation 82
6.2.4.1 Baseline Performance with Passive TMD 82
6.2.4.2 Inductance Effect 84
6.2.4.3 Simultaneous Suppression of Tonal Excitations 86
6.2.4.3.1 Tonal excitations at 70Hz and 158Hz 86
6.2.4.3.2 Tonal excitations at 47Hz and 80Hz 87

6.2.4.4 Single Tonal Excitation and High Amplitude Harmonic 88
6.3 Field Application on a BO-105 S Helicopter Structure 89
6.4 Concluding Remarks 92
Chapter 7: SATMD Design Strategy 93
7.1 SATMD Position Selection 93
7.2 SATMD Electromechanical Properties 96
7.2.1 SATMD Properties from Ad-Hoc Design 96
7.2.1.1 Auxiliary Mass and Inductance 96
7.2.1.2 Resistance 98
7.2.2 SATMD Properties from Optimal Design 99
7.2.2.1 Auxiliary Mass as Selected in the Ad-Hoc Design 100
7.2.2.1.1 R-L Shunt Impedance 100
7.2.2.1.2 R-L-C Shunt Impedance 100
7.2.2.1.3 Custom Piezoelectric Transducer with R-L-C Shunt Impedance 102
7.2.2.2 Auxiliary mass as an Optimization Parameter 103
7.3 Concluding Remarks 106
Chapter 8: Development and Testing of Adaptive Control Concept for the SATMD 107
8.1 Adaptive Control Concept 107
8.1.1 System Identification 109
8.1.2 Parameters Tuning 109
8.1.2.1 Inductance 109
8.1.2.2 Resistance 109
8.1.3 Adaptive Control Algorithm 110
8.2 Case Studies in Scaled-Down Airframe Prototype Structure 110
8.2.1 Case Studies' Details 111
8.2.1.1 Time Increment and Control Period 111
8.2.1.2 Welch Method 111
8.2.1.3 Recursive AR Model 112
8.2.1.4 Resistance Gain 114

8.2.2 Gradual mass change 114
8.2.3 Abrupt mass change 118
8.3 Concluding Remarks 121
Chapter 9: Conclusions and Suggestions 122
9.1 General Conclusions 122
9.2 Suggestions for Future Research 124
Appendix A: APA1500L Technical Data Sheet 125
Appendix B: Newmark Implicit Numerical Time Integration Method 127
References 128
Thesis Publications 141

List of Tables

Table 4.1. SATMD model parameters. 42

Table 5.1. Model parameters and characteristics. 54

Table 5.2. Ultimate experimentally obtained reductions in modal peaks. 65

Table 6.1. Dimensions, materials and properties of the prototype and numerical simulation. 70

Table 6.2. Modal characteristics of studied modal frequencies. 71

Table 6.3. Amplitude of mode shapes at fuselage tip and tail. 73

Table 6.4. Piezoelectric device characteristics. 73

Table 6.5: Experimental accelerance reduction at various airframe locations compared to baseline in the vicinity of each Mode. 81

Table 6.6. Modal Characteristics of the studied modal frequencies. 83

Table 6.7. SATMD Specifications. 84

Table 7.1. Amplitude of mode shapes at fuselage tip and tail. 94

Table 7.2. Auxiliary masses to tune different structural Modes. 97

Table 7.3. Ad-hoc and optimal SATMD parameters, with selected auxiliary mass. 100

Table 7.4. Reductions achieved in each structural Mode with various SATMD parameters, with selected auxiliary mass. 102

Table 7.5. Optimal SATMD parameters, including the auxiliary mass. 104

Table 7.6. Reductions achieved in each structural Mode with various SATMD parameters. 105

Table 8.1. RMS acceleration values in the gradual mass change case study. 117

Table 8.2. RMS acceleration values in the abrupt mass change case study. 120

List of Figures

Figure 1.1. Examples of lightweight means of transportation. (a) 2.1 PIPISTREL VIRUS SW 121 Aircraft; (b) BO 105 S Helicopter; (c) Yacht. 2

Figure 2.1. Conventional TMD on a lumped mass structure. 9

Figure 2.2. Shunt piezoelectric patch on a flexible host structure. 13

Figure 2.3. Antivibration device combining an antivibration beam and an attached shunt piezoelectric patch. 16

Figure 2.4. Antivibration device with a shunted piezoelectric configuration that provides the stiffness for an auxiliary resonant mass. 18

Figure 2.5. Proposed structure for the piezoelectric device in [89]. (a) Radial (d_{31}) expansion of the ceramic causes an axial motion of the device; (b) Blocked force test of the developed device.[89] 19

Figure 3.1. Experimental Setup. 22

Figure 3.2. Shakers used for the laboratory tests. (a) LDS V406; (b) LDS V201. 23

Figure 3.3. Complete experimental setup for a down-scaled airframe model. 23

Figure 3.4. Constructed FRF example based on experimental measurements. 24

Figure 4.1. Piezoelectric layer. 27

Figure 4.2. Multilayer piezoelectric material and equivalent stack model. 28

Figure 4.3. Piezoelectric device equilibrium. (a) Mechanical components; (b) Electrical components. 29

Figure 4.4. Conventional sole TMD structure. 31

Figure 4.5. Sole SATMD structure. (a) Schematic illustration; (b) Shunt circuit. 32

Figure 4.6. Examples of prestressed piezoelectric devices, produced by CEDRAT TECHNOLOGIES. 36

Figure 4.7. Examples of amplified piezoelectric devices, produced by CEDRAT TECHNOLOGIES. (c) is the one that is used for studied SATMD. 37

Figure 4.8. Aluminum base with vertical guides. 37

Figure 4.9. Auxiliary mass used for the SATMD. (a) Main auxiliary mass component with two linear bearings; (b) Additional auxiliary mass components. 38

Figure 4.10. Assembly of the SATMD. 39

Figure 4.11. Shunt circuit elements. (a) Potentiometer; (b) Coils. 40

Figure 4.12. Sole SATMD characterization setup. (a) Experimental Setup; (b) Schematic illustration. 41

Figure 4.13. Frequency response (acceleration) of mass in the sole SATMD configuration in short (black color) and open circuit (blue color). Analytical results are presented with continuous curves and experimental measurements with full circles. 42

Figure 4.14. Resistance effect in the frequency response (acceleration) of mass of the sole SATMD under various resistive impedances. (a) Experimental results; (b) Simulation results. 43

Figure 4.15. Inductance effect in the frequency response of the sole SATMD. (a) Acceleration of mass; (b) Charge in the shunt circuit. 45

Figure 4.16. Combined resistance-inductance effect in the frequency response (acceleration) of mass of the sole SATMD under various impedances. (a) Experimental results; (b) Simulation results. 46

Figure 5.1. Conventional TMD on lumped mass structure. 48

Figure 5.2. SATMD on lumped mass structure. (a) Schematic illustration; (b) Shunt circuit. 49

Figure 5.3. Experimental setup for the SATMD on a simplified host structure. 53

Figure 5.4. Frequency response of the host structure (main mass) without (Baseline) and with the passive TMD. (a) Experimental results; (b) Simulation results. 54

Figure 5.5. Resistance effect on host structure: (a) Experimental results; (b) Simulation results. 55

Figure 5.6. Root Loci for increasing resistance. Symbols "+" and "*" indicate the pole locations of maximum modal damping for structural mode I and II, respectively. 57

Figure 5.7. Inductance effect on frequency response functions. (a) Main mass acceleration; (b) Auxiliary mass acceleration; (c) Shunt circuit charge; (d) Shunt circuit charge cases: short circuit, 35mH and 50mH. 59

Figure 5.8. Inductance effect on frequency response of the main structure (colored results) and the sole SATMD eigenfrequencies with the same auxiliary mass (black dashed curves). 60

Figure 5.9. The two bifurcation points (symbols "*" and "+") with inductance increase and R=1 Ohm. (a) Electrical components of the eigenvectors; (b) Root Loci. 61

Figure 5.10.. The two bifurcation points (symbols "*" and "+") with inductance increase and R=20 Ohm. (a) Electrical components of the eigenvectors; (b) Root Loci. 62

Figure 5.11. Combined resistance-inductance effect on structure: (a) Experimental results; (b) Simulation results 64

Figure 6.1. Shunted piezoelectric SATMD attached to a multi-DOF host structure. (a) FEM discretized host structure; (b) Shunt circuit. 67

Figure 6.2. Experimental Setup. (a) Down-scaled airframe model; (b) Piezoelectric device attached under fuselage tip in vertical direction. 70

Figure 6.3. Airframe tip vertical frequency response. 70

Figure 6.4. Undamped mode shapes of structural eigenfrequencies. (a) 36Hz; (b) 47Hz; (c) 64Hz; (d)Normalized amplitude of mode shapes. 71

Figure 6.5. Experimental frequency response compared to mode superposition analysis. (a) Fuselage tip;(b) Fuselage center; (c) Wing tip. 72

Figure 6.6. Frequency response (acceleration) of the fuselage tip without (Baseline) and with the passive TMD. (a) Experimental results; (b) Simulation results. 73

Figure 6.7: Resistance effect on fuselage tip. (a) Experimental results; (b) Simulation Results. 74

Figure 6.8: Predicted and measured accelerance at various location of the airframe structure. (a)-(b) Fuselage tip; (c)-(d) Fuselage center; (e)-(f) Wing tip. 75

Figure 6.9: Inductance effect on the frequency response functions of key state variables. (a) Shunt circuit charge; (b) Auxiliary mass acceleration; (c) Fuselage tip acceleration. 76

Figure 6.10: Inductance effect on frequency response functions for 150mH, 275mH, 400mH, 525mH. (a) Shunt circuit charge; (b) Auxiliary mass acceleration; (c) Fuselage tip acceleration. 78

Figure 6.11: Inductance effect on fuselage tip. (a) Experimental results; (b) Simulation Results. 79

Figure 6.12: Inductance effect on the accelerance; left column experimental, right column simulation results. (a)-(b) Fuselage center; (c)-(d) Wing tip. 81

Figure 6.13: Acceleration response of the fuselage tip to Dirac Excitation. (a) Baseline system, (b) Short Circuit system; (c) SATMD system. 82

Figure 6.14. Frequency response (acceleration) of the fuselage tip without (Baseline) and with the passive TMD. (a) Experimental results; (b) Simulation results. 83

Figure 6.15. Inductance effect on frequency response of the fuselage tip (colored results) and the sole SATMD eigenfrequencies with the same auxiliary mass (black dashed curves). 84

Figure 6.16. Experimental inductance effect on the frequency response functions of the fuselage tip acceleration, with the Passive TMD tuned to 73Hz; (a) 30 mH - 6 Ohm; (b) 330mH - 15 Ohm. 85

Figure 6.17. Predicted and measured tip acceleration under tonal excitations at 70Hz and 158Hz without and with the SATMD; (a), (b) Time- and frequency-domain measurements; (c), (d) Time- and frequency-domain simulation results. 87

Figure 6.18. Predicted and measured tip acceleration under tonal excitations at 70Hz and 158Hz without and with the SATMD; (a), (b) Time- and frequency-domain measurements; (c), (d) Time- and frequency-domain simulation results. 88

Figure 6.19. Experimental inductance effect on the frequency response functions of the fuselage tip acceleration, with the Passive TMD tuned to 84Hz; 30 mH - 6 Ohm..... 89

Figure 6.20. Measured tip acceleration under tonal excitations at 79Hz and 158Hz without and with the SATMD; (a), (b) Time domain measurements; (b) Frequency domain results. 89

Figure 6.21. BO 105 S Helicopter used for the experimental campaign; (a) Front view; (b) Rear view and SATMD position. 90

Figure 6.22. FFT vertical acceleration of BO 105 S during cruise speed conditions without the SATMD. 91

Figure 6.23. FFT vertical acceleration of BO 105 S during cruise speed condition. (a) Passive TMD with 0.7kg auxiliary mass; (b) SATMD with 0.7kg auxiliary mass and 150 mH inductance. 91

Figure 7.1. Scaled-down airframe model with the excitation and measurement coinciding at the middle of the airframe tail, and the SATMD attached to different positions. (a) SATMD at tail; (b) SATMD at tip. 95

Figure 7.2. Numerical results of the airframe model, with the auxiliary mass selected to tune Mode II, and the SATMD positions presented in Fgr. (a) Passive TMD performance; (b) SATMD performance, selecting inductance to tune Mode III. 95

Figure 7.3. Inductance effect on the fuselage tip, selecting different auxiliary masses for the SATMD. (a) Auxiliary mass for Mode I; (b) Auxiliary mass for Mode II; (c) Auxiliary mass for Mode III. 97

Figure 7.4. Inductance effect on the electric current when the auxiliary mass tunes the SATMD to Mode II. 98

Figure 7.5. Resistance effect on the fuselage tip for auxiliary mass that tune the SATMD to Mode II, and inductance that tunes the Mode III. 98

Figure 7.6. Frequency response (acceleration) of fuselage tip without the SATMD and with various designed shunt circuit configurations of the SATMD, selecting auxiliary mass to tune Mode II (the passive TMD, the L-SATMD, and RL-SATMD). 99

Figure 7.7. Frequency response (acceleration) of fuselage tip without the SATMD and with various shunt circuit configurations of the SATMD, selecting auxiliary mass to tune Mode II (the passive TMD, the designed RL-SATMD, and the optimal SATMDs with progressively ascending number of optimization parameters). 101

Figure 7.8. Inductance effect on the frequency responses of the SATMD with auxiliary mass that tunes Mode II and optimal C and ē. (a) Acceleration of tip; (b) Shunt circuit current. 103

Figure 7.9. Frequency response (acceleration) of fuselage tip without the SATMD and with optimal shunt circuit configurations of the SATMD, including the auxiliary mass in the optimization (the optimal SATMDs with progressively ascending number of optimization parameters). 104

Figure 7.10. Inductance effect on the frequency responses of the SATMD with optimal auxiliary mass, C and ē. (a) Acceleration of tip; (b) Shunt circuit current. 105

Figure 8.1. Adaptive algorithm for the SATMD. 110

Figure 8.2. Numerical acceleration results of the fuselage tip of the airframe model, under white noise excitation, with the SATMD at the fuselage tip, operating with the auxiliary mass that passively tunes the structural Mode II, and the optimal R-L values found for this auxiliary mass. 113

Figure 8.3. Results on the RAR order based on model selection criteria. (a) RSS/SSS; (b) BIC. 114

Figure 8.4. Frequency response estimations with gradual mass change. (a) Mass change in time; (b) Critical frequencies found with Welch and RAR model; (c) Welch and RAR frequency response estimation at 9.2s; (d) Welch and RAR frequency response estimation at 9.2s. 115

Figure 8.5. Results of the adaptive control algorithm gradual mass change case study. (a) Resistance; (b) Inductance; (c) RMS values; (d) values after 20 s. 117

Figure 8.6. Acceleration results of the gradual mass change case study in time. 118

Figure 8.7. Frequency response estimations with abrupt mass change. (a) Mass change in time; (b) Critical frequencies found with Welch and RAR model. 119

Figure 8.8. Results of the adaptive control algorithm in the abrupt mass change case study. (a) Resistance; (b) Inductance; (c) RMS values; (d) values after 20 s. 120

Figure 8.9. Acceleration results of the abrupt mass change case study in time. 120

List of Symbols

R	Resistance
L	Inductance
m_d	Auxiliary mass
m_l	Lumped host structure mass
s_{ij}	Elastic compliance tensor
d_{ik}	Tensor of the piezoelectric strain coefficients
ε_{lk}	Electric permittivity tensor of the material
S_i	Engineering strain
σ_j	Mechanical stress
D_l	Electric displacement
E_k	Electric field
C_{ij}^E	Elastic stiffness tensor
e_{ik}	Tensor of the piezoelectric stress coefficients
A_{layer}	Piezoelectric layer area
q_{layer}	Single piezoelectric layer charge
Δu_{layer}	Single piezoelectric layer displacement
h_{layer}	Thickness of the piezoelectric layer
$\Delta\varphi$	Potential difference
f_p	Piezoelectric internal device force
q_{out}	Charge free to flow in an electric circuit
q_{in}	Charge stored in the piezoelectric material
q_p	Total charge of the piezoelectric material
h_{stack}	Multilayer piezoelectric device thickness or stack length
Δu_d	Multilayer piezoelectric displacement in direction 3
C_p^S	Equivalent capacitance of the piezoelectric device, under constant strain conditions
$\overline{e}$	Equivalent piezoelectric stress coefficient of the multilayer piezoelectric material
k_p^E	Equivalent mechanical stiffness of the multilayer piezoelectric material under zero electric field
$\varepsilon_{33,tot}^S$	Total electric permittivity of the piezoelectric multilayer
N_{layers}	Number of layers in a multilayer piezoelectric material
C_p	Electrical capacitance
k_d	Mechanical stiffness of the damping device

k_l	Stiffness of the lumped mass structure
c_d	Equivalent damping of the damping device
c_l	Damping of the lumped mass structure
u_d	Displacement of the damping device
$\dot{u}_d$	Velocity of the damping device
$\ddot{u}_d$	Acceleration of the damping device
u_l	Displacement of the lumped mass host structure
$\dot{u}_l$	Velocity of the lumped mass host structure
$\ddot{u}_l$	Acceleration of the lumped mass host structure
$\dot{q}_{out}$	Current flowing in the shunt circuit
F	External force
ω	Angular velocity
z_i	State space variables
A	State space system matrix
B	State space force matrix
p_i	System poles
Φ_{li}	Undamped eigenvectors of the host structure
M_{kl}	Mass of a structure with multiple degrees of freedom
C_{kl}	Damping of a structure with multiple degrees of freedom
K_{kl}	Stiffness of a structure with multiple degrees of freedom
s	Host structure node of antivibration device attachment
u_n	Nodal displacement of the structure in the direction parallel to the antivibration device operating direction
δ_{kn}	The Kronecker delta
Φ_n	Line-vector, where each element is the amplitude of the mode shape of the host structure at the degree of freedom, where the antivibration device is attached
Q_i^H	Vector of modal participation factors without the presence of the SATMD
Q_i	Vector of the modal participation factors of the host structure with the attached SATMD
P	the modal force
$\overline{M}$	Modal mass matrix
$\overline{K}$	Modal stiffness diagonal matrix
$\bar{C}$	Modal damping matrix
N_b	Number of blades in a rotorcraft
f_{crit}	Critical frequency detected in the control algorithm
a_{RMS}^k	Acceleration RMS value at time period k

G_R	Resistance gain in the control algorithm
a_t	Host structure acceleration measured at the position which coincides with the SATMD placement
Δt	Time increment for Newmark integration
ΔT	Control period of the control algorithm
$\hat{\theta}[t]$	Estimated AR parameter vector at the current time instant t

Chapter 1: Introduction

1.1 Problem Statement and Motivation

Mechanical systems and structures are frequently exposed to dynamic conditions that result in vibrations. Flexible structures are more susceptible to high amplitude vibrations due to their low-frequency and lightly damped structural modes, leading to long decay time of vibrations and fatigue problems. The term “flexible structures” generally imply flimsy lightweight structures that are used both in everyday life and in special or high-tech applications. Typical flexible structure examples include civil engineer large constructions, such as wind turbines, tall buildings and large bridges, lightweight means of transportation, such as aircrafts, yachts and automobiles, lightweight metal structures, such as factory floors, TV/radio towers and architect designs in buildings and stadiums, space applications, such as spacecrafts and large antennas, etc. Excessive vibrations in flexible applications are undesirable, as they affect the safety and comfort of the nearby human presence, reduce the material fatigue life, and may even lead to structural failure. Therefore, vibration control is extremely crucial in these structures, aiming at the reduction of the amplitude of the vibrations, in order to ensure the reliability of their function [1], [2]. This subject has gathered a great deal of scientific and industrial interest. Sophisticated vibration control techniques are usually required to mitigate the structural oscillations of flexible structures, due to their special attributes and lightweight configurations.

This dissertation primarily focuses on the vibration control of lightweight means of transportation, such as airframe structures of airplanes (Figure 1.1a) and rotorcrafts (Figure 1.1b). Vibrations in such structures are attributed to a variety of stimuli, such as motors, rotors, aerodynamic loads, wheel, or rail interfaces, etc. The applied loads may have limited frequency content, due to the harmonic motion of the engine in a single frequency, leading to tonal or multi-tonal excitations, or broad spectrum frequency content, such as the aerodynamic loads and the flowing boundary level, exciting multiple structural modes. It is also a very frequent phenomenon that the frequency content of the exciting loads changes during operation. Notable examples are varying tonal excitations due to changes in engine/rotor RPMs, varying broadband low-frequency excitation due to unsteady aerodynamic forces on aircrafts, and variation of the dynamic characteristics of the structure, due to changes in structural parameters (e.g., mass diminution due to fuel consumption). Furthermore, the contemporary trend towards increasing the efficiency and power of modern transport engines leads to an increase in the levels of emitted vibrations and noise. At the same time, the tendency to reduce the weight of the structures in order to reduce the fuel consumption and the CO_2 emissions, coupled with the increasing use of composite materials, leads to higher structural oscillations with lower damping capacity. Unless sufficient vibration mitigation is achieved, the material fatigue life of the structure is reduced, and the structural oscillations are

transmitted to the passengers, highly deteriorating the passenger comfort. Therefore, high vibration attenuation levels are highly crucial.



(a) *(b)*

Figure 1.1. Examples of lightweight means of transportation. (a) 2.1 PIPISTREL VIRUS SW 121 Aircraft; (b) BO 105 S Helicopter.

The applied antivibration mechanism used in such structures should cope with multiple demanding requirements. It should be able to provide multi-modal vibration control in low frequency range (therefore, exhibit high damping capacity) and / or multi-tonal vibration suppression (therefore, entail multiple resonant oscillators, known as energy sinks). Furthermore, it is highly important that the applied vibration control technique is able to recognize and adapt to potentially frequency-varying applied loads during operation. In addition, the antivibration mechanism should feature low weight to limit the fuel consumption and CO_2 emissions, require low or even zero power consumption not to burden the system electronics, and exhibit minimal structural interference, such that host structure dynamics remain unchanged.

1.2 Control Strategies on Flexible Structures

The vibration control of flexible structures has been vigorously studied over the past few decades, because of its high importance for human safety and comfort, and its beneficial impact on multiple industries. The control strategies are usually classified, based on their energy demands, to passive, active, and semi-active. The passive control techniques function passively, without the need for any external power supply, whereas the active control techniques require a high power supply (usually with a power amplifying system), in order to create vibration-cancelling forces. The semi-active control

strategies require minimal power supply or external manual modulation to alter their tunable parameters and adapt to potentially frequency-varying applied loads.

1.2.1 Passive Control Systems

Passive vibration control methods are intrinsically stable and rely on absorbing and / or dissipating significant parts of the host structure vibrational energy. Typical examples include viscoelastic dampers [3] and viscous fluid dampers [4]. These techniques usually attenuate and dampen higher frequency modes, whose vibrations are less perceptible by humans. Other examples of passive vibration control entail a secondary system, where an introduced resonant oscillator absorbs high amount of vibrational energy from the host structure.

One of the most known passive vibration control systems is the tuned mass damper (TMD) [5]. In its conventional form, a TMD device consists of a spring-damper element and a small auxiliary mass [6], which are tuned to a resonant frequency or dominating excitation frequency, resulting in significant vibration suppression of the main structure via the introduction of a tuned anti-resonance and modest dissipation. When accurately tuned, the auxiliary mass performs an opposite vibration from the host structure (out-of-phase motion), highly reducing the host structure oscillation. Further literature review and information on this method is discussed in Chapter 2. The tuned liquid dampers (TLDs) are also known for their passive vibration control capabilities [7], absorbing structural energy by means of viscous action of fluid, wave breaking, and liquid sloshing.

Alternative vibration reduction can be achieved, if the kinetic or strain energy of the structure is transformed into electrical energy and then dissipated by electric means. This energy conversion can be realized by integrating an electromechanically coupled transducer (piezoelectric [8] or electromagnetic [9]) into the vibrating structure, shunted to an external circuit with a given Resistive-Inductive-Capacitive (RLC) impedance. In the electric circuit, the resistive, inductive, and capacitive components are the electrical analogs of damping, mass, and reciprocal of stiffness of a purely mechanical system, respectively. Piezoelectric transducers directly convert strain energy to electrical through the direct piezoelectric effect. This technique is extensively covered in Chapter 2. Electromagnetic transducers on the other hand, are limited to metallic or magnetic applications and demand the presence of an external coil in order to achieve the desirable electromechanical energy conversion.

Passive control systems usually lead to the non-negligible increase in the total weight of the structure, which is not desired in most flexible applications. Moreover, these strategies are not particularly beneficial for applications which experience loads of varying frequency content during their operation, because they are unable to adapt to the changes.

1.2.2 Active Control Systems

In active control configurations, an actuator driven by an external power source applies a vibration-cancelling force to the structure to suppress the vibration. They are very attractive due to their ability to adapt to different loading conditions and to control different vibration modes of the host structure. Active control systems require sensor inputs to identify the external excitation (feedforward control [10]) or the host structure status (feedback control [11]), before calculating the appropriate force in the control algorithm, and driving it to structure with the control devices (actuators). Active tuned mass dampers (ATMDs) [12], [13], and active piezoelectric devices (patches [14]–[18] or stacked devices [19]) are typical examples of active control systems.

However, active control systems suffer from various disadvantages, such as contingent instability, excessive need for power supply, large added mass, especially when power amplifiers are needed, requirement for complex systems and frequent maintenance which increase the cost, and sophisticated algorithms, such as the delayed resonator [20], H_2 and H_∞ techniques [21], [22], FxLMS [23], [24], and LQR [25]. These demanding challenges make the active control solutions appear relatively seldom in real-life applications and only for very high vibration control in delicate applications.

1.2.3 Semi-Active Control Systems

Semi-active vibration control methods enjoy the stability of a passive system and the adaptive control properties of an active system, making them a great candidate for many vibration control applications. These devices passively absorb and dissipate a significant part of the host structure vibrational energy in tuned frequency ranges. If the loading conditions change and detune the device, sensory equipment is used to identify the alteration, followed by changes in the device tunable parameters to retune the system. The required power input for the adjustment of the tunable parameters is much smaller than the energy supply needed for active control systems. For their great versatility and low power requirements, the semi-active control systems have attracted an enormous amount of scientific attention in the last decades.

The semi-active control techniques emerge from passive control systems with tunable parameters, which interact with the host structure dynamics. Typical examples of such systems are the controllable liquid dampers (CLDs) [26], the tunable TMDs [27] and the tunable shunt circuits of the piezoelectric devices [28]. The electrorheological (ER) [29] and magnetorheological (MR) [30] fluids, which emerge from the TLDs, work with electric and magnetic fields, respectively, to control the antivibration device stiffness and damping. These controllable fluids have a unique ability to reversibly change from free-flowing, linear viscous fluids to semi-solids with a controllable yield strength in only a few milliseconds. The MR fluid dampers have gathered greater scientific interest due to their higher maximum yield stress, temperature independence, and low power-driven performance [31], [32].

The tunable TMDs exhibit tunable stiffness, damping, and mass properties, therefore adjusting the device frequency to cope with the applied loads frequency variation [33]. Furthermore, changes in the resistance, inductance, and capacitance of the shunt circuit of the piezoelectric devices attached to the host structure can alter the shunt circuit resonance and damping, addressing potential changes in the host structure loading conditions [34]. A great deal of scientific work has been conducted for these two semi-active vibration control techniques, which are extensively covered in Chapter 2. Their combined antivibration performance could offer great adaptive and very high attenuation levels to flexible structures, yet has been lightly addressed in the literature, highly motivating the current work and dissertation.

1.3 Dissertation Scope and Objectives

In the context of the previous sections, the scope of this work is to introduce, develop and evaluate a semi-active antivibration device, which provides high vibration control capabilities to flexible structures in a broad and potentially altering low-frequency spectrum, focusing on the vibrations that mainly affect the human comfort. The studied mechanism consists of a specialty piezoelectric device connected to an external Resistive-Inductive (RL) electric circuit, and an auxiliary mass. The piezoelectric device provides the stiffness and damping for the resonant mass oscillation and introduces high electromechanical energy conversion and coupling. As a result, the vibrational energy of the host structure can be absorbed both in the kinetic energy of the resonating mass, and in the electric energy of the shunt circuit. Further structural energy can be dissipated in the mechanical damping of the piezoelectric device and in the resistive impedance of the shunt circuit. Therefore, this device combines the high vibration control capabilities of the TMD and the great tuning and controlled damping characteristics of the shunt piezoelectric device. For this reason, this device is defined in this dissertation as a piezoelectric semi-active tuned mass damper (SATMD).

The studied antivibration device could cope with all the demanding vibration control requirements of the lightweight means of transportation. It provides two resonant oscillators for the suppression of harmonic excitations, and a tunable resistive impedance for broadband damping capacity. The potential frequency-varying applied loads could be compensated by controlling the shunt circuit impedance, therefore retuning the device to optimal vibration attenuation conditions, without strenuous alterations in the device mechanical components. Furthermore, the required low added weight could be ensured by appropriate selection of the piezoelectric device. In addition, the low power supply demands could be satisfied, since only a switching circuit is needed for the shunt impedance alterations. Finally, for the SATMD integration to the host structure, its firm attachment to a position that experiences high amplitude vibrations should be sufficient, exhibiting minimal structural interference.

In order to successfully develop and evaluate the performance of the proposed antivibration device, the conducted work is divided into successive milestones, each of which constitutes one of the dissertation objectives, enlisted below:

- SATMD design, including the selection of the appropriate piezoelectric device and assembly of the rest components, modeling, and experimental characterization.
- Modeling, analytical, and experimental evaluation of the SATMD performance on a lumped mass host structure, to comprehend the various mechanisms for absorbing and dissipating the host structure kinetic energy.
- Modeling, experimental, and computational evaluation of the SATMD vibration control performance on various large and flexible structures, to examine its capabilities for multi-modal and multi-tonal vibration control.
- Investigation of the SATMD characteristics, in terms of the position of its structural integration on the flexible structure, and its electromechanical properties, aiming at multi-modal vibration mitigation of a flexible host structure.
- Development and testing of an adaptive control concept for the SATMD on a flexible host structure, which exhibits changing dynamic characteristics.

For better organization and flow of the dissertation, these objectives are separately addressed in Chapters 4 – 8.

1.4 Research Contributions and Novelty

The main contributions and innovative aspects of this thesis are summarized below.

- The design, development, experimental characterization, and lumped-parameters modeling of a TMD-shunted piezoelectric stack device. The selection of the piezoelectric device is extremely crucial, as it provides very high electromechanical coupling, and allows the employment of a very small auxiliary mass and the development of a petite antivibration device, able to be integrated in complex flexible structures, such as airframe structures. Since this device combines the high vibration control capabilities of the TMD and the great semi-active characteristics of the shunt piezoelectric device, it is defined in this dissertation as a piezoelectric semi-active tuned mass damper (SATMD).
- The modeling and experimental evaluation of the SATMD – lumped mass host structure system, to clearly comprehend the SATMD – host structure interaction, along with the mechanisms of the enhancement of electromechanical coupling, energy conversion and vibration mitigation, provided by resistance and inductance.

- The modeling and experimental evaluation of the SATMD – multiple DOF host structure, to evaluate the performance of the developed device under various applied loads, and on multiple host structures. Also, the appropriate auxiliary mass selection and the antivibration device performance for multi-modal and multi-tonal vibration control.
- The development and testing of an adaptive control concept for the SATMD on a flexible host structure with changing dynamic characteristics, which achieves real-time adaptation and control.

1.5 Dissertation Outline

This PhD thesis consists of 9 chapters, which progressively introduce, develop, and evaluate the antivibration performance of the proposed SATMD device.

Chapter 1: The problem of excessive vibrations in flexible structures is discussed, focusing on airframe structures, which motivates the current work. The various types of controls in flexible structure applications are briefly presented, highlighting the benefits of the semi-active control strategies. Subsequently, the main scope and objectives of the dissertation are introduced, before giving the outline of the thesis.

Chapter 2: A literature review of the most important research works on the vibration control of flexible structures, using TMDs, shunt piezoelectric devices, and their combinations, is presented.

Chapter 3: The experimental apparatus and setup used for the multiple experimental campaigns is presented, including all excitation, sensory and signal processing equipment.

Chapter 4: The model, concept, and development of the proposed electromechanical antivibration device is addressed. The equivalent properties of multilayer piezoelectric devices are calculated based on the constitutive piezoelectric equations and used for the prediction of sole device behavior. The selection of the piezoelectric transducer and the SATMD device assembly is addressed. An experimental campaign is designed and executed for the characterization of the device equivalent properties. Finally, the effects of the shunt circuit resistance and inductance to the auxiliary mass are presented and discussed.

Chapter 5: The SATMD vibration reduction performance is evaluated on a simplified structure, such that the in-depth investigation of the complex electromechanical system effects and tuning mechanisms is allowed. The equations of equilibrium for the SATMD – lumped mass structure system are formulated, and the computational results are compared to the experimental measurements of the SATMD on a designed lumped mass structure experimental setup.

Chapter 6: The performance of the proposed piezoelectric SATMD is evaluated on large and flexible structures. A reduced-ordered modal space structural dynamics model is formulated, coupled with the SATMD device, and the RL shunt electric circuit. The SATMD performance is demonstrated

experimentally and numerically on a scaled-down airframe prototype structure under broadband white noise excitation, as well as multi-tonal harmonic excitation. Finally, the SATMD is evaluated on a field application on a BO-105 S helicopter during real-flight conditions.

Chapter 7: The design variables of the piezoelectric SATMD, namely (1) the location of its structural integration and (2) its electromechanical characteristics, are investigated and optimized. As a case study, the selected host structure is a down-scaled airframe prototype, which functions under broadband excitation.

Chapter 8: An adaptive control concept for the SATMD is developed and tested, such that the antivibration device can be self-tuned and retuned, to achieve continuous high vibration control efficiency. The developed adaptive algorithm is put into test in two case studies of changes in the dynamic characteristics on the scaled-down airframe protype.

Chapter 9: The presented work and main contributions are summarized, while topics for future research are identified and discussed.

Chapter 2: Literature Review on the Vibration Control of Structures using Tuned Mass Dampers and Shunt Circuit Piezoelectric Devices

This Chapter presents a literature review of the most important research works on the vibration control of flexible structures, using TMDs, shunt piezoelectric devices, and their combinations. Subsequently, the literature open questions and challenges of this topic are identified, and the research contributions of this thesis are introduced to fill many of the literature gaps.

2.1 Tuned Mass Dampers

A bibliography research is presented for the TMD, introducing its operating principles and focusing on applications on flexible structures. Subsequently, optimal TMDs are investigated in terms of parameters and placement, and contributions on semi-active TMDs are presented.

2.1.1 Overview and Operating Principles

Tuned Mass Dampers (TMDs), first proposed by Frahm in 1911 [35], have been used as means of vibration reduction for over a century. When functioning under tonal vibrations, such devices are frequently named as tuned vibration absorbers (TVAs) or vibration neutralizers (VNs) [27], whereas when functioning under broadband excitations, they are known as (TMDs) [5]. The developed antivibration device in this dissertation aims both at damping the broadband excitations and at suppressing tonal vibrations. To distinguish itself from other absorber or neutralizers which do not employ an auxiliary mass, the TMD term will be used in this study.

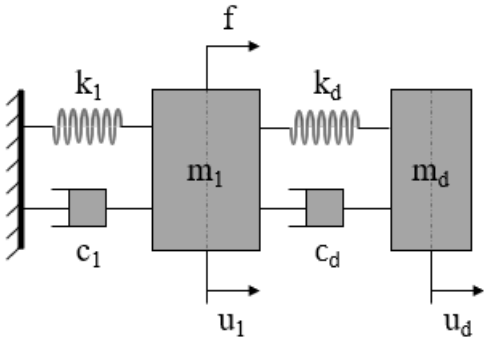


Figure 2.1. Conventional TMD on a lumped mass structure.

Traditionally, these devices are attached to the main structure and consist of a spring-damper element and an auxiliary mass (Figure 2.1), which is able to oscillate independently and as a consequence absorb part of the kinetic energy of the system [36]. The dynamic characteristics of this absorber are chosen, such that the TMD is tuned to a resonant frequency or dominating excitation frequency, resulting in significant vibration suppression of the main structure via the introduction of a tuned anti-resonance and modest dissipation. When accurately tuned, the auxiliary mass performs an opposite vibration from the host structure (out-of-phase motion), highly reducing the host structure oscillation. Although the integration of a TMD in a structure typically introduces an anti-resonance on a single frequency of interest, it also generates two new frequency peaks, one slightly lower and another slightly higher than the initial resonance, which can be of similarly high amplitude, especially when the TMD is lightly damped. Already by 1957, Den Hartog [6] deeply analyzed and explored the tuning rules of the TMD, developing and establishing the fixed-point theory. A great deal of studies have been dedicated to further analyze the tuning rules and anti-resonance of the TMD [37]–[39]. An important drawback of this device is that it not easy to retune, in the event of an alternation in the dynamic characteristics of the hosting system (e.g. mass diminution or stiffness degradation). A change in the auxiliary mass or redesign and new integration of the TMD would be necessary, which could result to a costly venture and / or a considerable downtime for the host structure.

2.1.2 Applications on Flexible Structures

Numerous practical applications of TMDs in large and flexible structures have been reported. In civil engineer applications, TMDs have been extensively investigated and applied to mitigate the vibrations of tall buildings that are induced by wind and seismic loads [5], [40], [41]. Applications of TMDs in bridge structures have also been thoroughly studied, to reduce the oscillations induced by either wind loading [42] or by high-speed trains [43], [44]. Furthermore, TMD systems have been investigated to control offshore wind turbine vibrations due to aerodynamic, sea wave or seismic loads [45], [46]. In marine transportation applications, TMDs have been studied to ensure a high comfort level in yachts, which is mainly affected by engine induced vibrations [47], [48]. In aeronautical structures, the TMD effectiveness for vibration and noise control of a fuselage has been theoretically studied [49], and subsequently optimized in terms of placement and spring stiffness [50]. Furthermore, TMD systems have been investigated for the vibration suppression in helicopters, where the preliminary design of a semi-active electromagnetic TMD has been studied [51], and a combined passive and active TMD has been investigated and tested [52]. Yet, besides their widespread applications, TMDs suffer from limited effectiveness over a narrow frequency range and can only suppress vibrations around a single fixed resonant or tonal frequency. In order to control vibrations from multiple resonant or tonal excitation frequencies in large and flexible structures, multiple Tuned Mass Damper (MTMD) systems have been exploited in many research works applications [53]–[55]. However, the implementation of multiple

TMDs requires abundant space for the devices' structural integration and may add substantial weight, which could be hindrance in transportation applications, and especially in airframe structures.

2.1.3 Optimization Studies

Optimization studies for TMD applications usually imply appropriate tuning of the TMD properties or selection of the placement of the TMD integration on a large and flexible structure for optimal vibration control. Most research works consider the analytical optimization of TMD properties, without focusing on specific flexible structure applications. An efficient numerical approach based on the descent-subgradient method is proposed in [55] to maximize the minimal damping of modes in a prescribed frequency range, comparing the performance of minimax, H_2, and H_∞ optimal TMDs. A hybrid analytical H_∞-H_2 optimization approach is proposed in [56], combining the advantages of H_∞ and H_2 solutions. In order to compensate for the uncertainty of system variables and the fact that maximum vibration reduction is achieved only when the TMD is lightly damped, a robust optimum design criterion for the case of random vibrations was proposed in [57]. The tuning of a TMD is considered in [58], such that either the kinetic energy of the host structure is minimised or the power dissipation within the absorber device is maximised, which showed that the two optimization criteria are simultaneously satisfied, if the host structure is approximated as a damped single degree of freedom. Considering the TMD optimization for bridge applications, a set of five tuned-mass dampers (TMD) is designed and optimized in [59], considering not only the displacement limitations of bridges but also the limitations of stroke length of the dampers. Most of the scientific interest for TMD optimization on flexible structures has been dedicated to tall buildings, also considering the placement of MTMDs. A multi-objective optimization problem formulation is presented in [60] for the design of a TMD for either a base excitation or an external load of a building, seeking to simultaneously minimize structural responses, the TMD mass and the TMD stroke. Considering the TMD placement, in a single mode vibration suppression investigation, a TMD should be placed at the location where maximum normalized amplitude of the corresponding mode shape of the flexible structure occurs. However, selecting the placement of MTMDs for improved vibration control results on multiple modes in multi-storey building can be a quite challenging procedure. The effectiveness of the multi-mode control of a seismically excited building with distributed multiple tuned mass is investigated in [40]. Finally, the optimal placement and properties of multiple TMDs are studied in [61], using genetic algorithms (GAs).

2.1.4 Semi-active Control Studies

The semi-active structural vibration control consists of two basic components: the system identification and the semi-active tuning of the antivibration mechanism. The modal parameters of the host structure, namely the structure eigenfrequencies, modal damping, and mode shapes of the structure, are usually

sufficient for the system identification, when TMDs are used as the antivibration mechanism [62]–[64]. More advanced methods for system identification can be also used, such as the Kalman filter [65]–[67]. More focus in the existing literature is given on the semi-active concepts that the TMDs utilize to achieve adaptive control. Remembering the conventional TMD, it consists of a stiffness element, a viscous damper, and an auxiliary mass. Therefore, the semi-active TMD properties emerge from using concepts for variable stiffness, damping and mass. Most research works have been dedicated to variable stiffness studies [67]–[69], while another concept has been patented [70]. Pendulum TMDs (PTMDs) have also been evaluated for their semi-active capabilities, since an alteration in the pendulum length changes the device apparent stiffness, thus can accurately retune the antivibration device [66], [71], [72]. Another prototype semi-active TMD with variable stiffness has also been introduced and characterized, featuring a pre-stressable leaf-spring as the support for the oscillating mass [73], however the studies remained solely to the device itself. Moreover, changes in the damping characteristics of the TMD have been earlier studied in [33], [74]. The variable mass is more difficult to implement without manual intervention, however a water tank-water pump concept has been numerically and experimentally tested [75]. Smart materials have also been examined for changing the TMD characteristics and provide semi-active control, such MR fluids [32], [76], and shape memory alloys (SMAs) [77], [78]. Finally, combinations of piezoelectric materials and TMDs have gathered a lot of scientific attention for the multiple benefits they provide in semi-active vibration attenuation systems and are covered in detail later in this Chapter.

2.2 Shunt Circuit Piezoelectric Devices

Regarding the shunt piezoelectric vibration control concept, a short introduction to the piezoelectric materials and phenomena is first discussed, before analyzing the vibration control principles. Then, some enhancements of shunt circuit are presented, which improve the energy exchange and coupling with the existing structure. Applications on flexible structures follow, including optimization approaches and adaptive techniques.

2.2.1 Overview and Operating Principles

Piezoelectric material applications are based on interaction between the electrical and the mechanical field, making them very popular both as sensors and as actuators. The most known piezoelectric materials are piezoceramics (PZT), which exhibit high piezoelectric coefficients and brittleness, and the piezopolymers (PVDF), which exhibit lower piezoelectric coefficients and are more ductile. The characteristics of the piezoelectric materials that make them very attractive for sensory and actuator applications are the direct and converse piezoelectric phenomenon, respectively. In the direct phenomenon, a mechanical load creates a non-negligible charge, which is manifested as a potential

difference in the piezoelectric material edges, whereas in the converse effect, the application of an electric field creates a strain in the piezoelectric material, which can lead to the development of stresses and forces in constrained conditions. The mathematical representation of these effects for a thin piezoelectric ply are presented in the constitutive equations of Chapter 4.

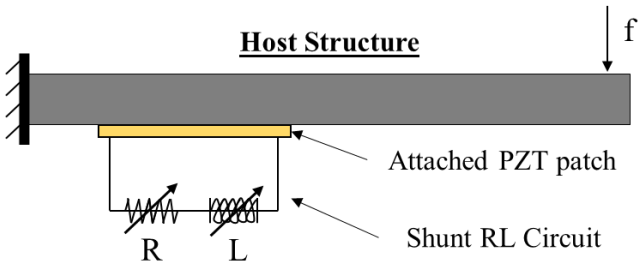


Figure 2.2. Shunt piezoelectric patch on a flexible host structure.

High vibration attenuation can be achieved, if the kinetic or strain energy of the structure is transformed into electrical energy and then dissipated by electric means. This energy conversion can be realized by attaching an electromechanically coupled transducer, such as a piezoelectric patch, on a vibrating structure (Figure 2.2), shunted to an external circuit with a given Resistive-Inductive-Capacitive (RLC) impedance. In the electric circuit, the resistive, inductive, and capacitive components are the electrical analogs of damping, mass, and reciprocal of stiffness of a purely mechanical system, respectively. Piezoelectric patches directly convert strain energy to electrical through the direct piezoelectric effect. Shunted piezoelectric patches and films attached to the surface of a vibrating structure, have gathered extreme scientific attention since the original pioneering works of Forward [79] and Hagood and Von Flotow [80]. This is because shunt dampers offer great tuning and retuning potential, by simply changing the levels of impedance of the external circuit. For the prediction of resistively shunted piezoceramic damping, a modal strain approach was proposed [81], whereas the mechanics for the analysis of damping in composite plates with multiple resistively shunted piezoelectric layers were developed [82] and further extended to also encompass the damping contribution of viscoelastic composite plies [83]. For the in-plane conditions, a theoretical framework was developed for predicting the nonlinear damping and damped vibration of laminated composite strips under in-plane loading [84]. An interesting tuning technique based on equal mode damping was investigated in [85]. However, when multiple shunted piezoelectric transducers are attached to a flexible structure, their individual interactions alongside the spill-over from residual modes affect the calibration accuracy. For this reason, explicit correction terms that represent these effects are presented in [86] for multiple shunted piezoelectric transducers targeting a single vibration mode.

2.2.2 Applications on Flexible Structures

By default, attached piezoelectric patches for vibrations control are destined for flexible structures, which produce great deformations and strains [87], [88], since higher strains in the structure lead to higher electromechanical energy conversion and coupling. In the scientific community, piezoelectric materials originally belonged to the "smart materials" family, and the flexible structures they were attached to belonged to the "smart structures" family [17], [89]. Lately, the nomenclature frequently used for these materials and structures is "meta-materials" and "meta-structures" [90]–[93], respectively. In order to achieve multiple mode vibration suppression in flexible structures, using only one piezoelectric transducer, and a combination of shunt circuits, various methods have been developed and tested [94]–[96]. For the improvement of the vibration control performance in flexible structures, various shunt circuit enhancements have been suggested and studied. Synthetic impedance circuits were proposed [97]–[99], to overcome implementation limitations that arise when a low frequency mode must be suppressed, a task that requires high inductance levels and thus bulky inductors. Conversely, tuning the shunt damper to a higher vibration mode through capacitance, requires cancelation of the transducer capacitive impedance; for this reason, multiple negative synthetic capacitance circuits were reported and implemented [100]–[106]. The effect of negative capacitance, inductance and resistance in the shunt circuit was also investigated to actively control flexural wave band gaps in beam-type acoustic metamaterials, using the piezoelectric shunted technique [90]. Furthermore, synchronized switching techniques were employed to the shunt circuit for improved multi-modal damping capabilities [107]–[110]. Finally, a great deal of scientific work has been focused on simultaneous energy harvesting and vibration control, using attached piezoelectric patches. This concept is based on transforming the strain energy of the host structure into useful power, to supply the device itself for autonomous semi-active performance, or other devices in the same circuitry. Some very recent examples can be found in [92], [111]. For a more exhaustive review on the shunted piezoelectric damping, the interested researcher can refer to [34], [112].

2.2.3 Optimization Studies

One of the first works for optimal RL circuits found that optimal resistance and inductance creates a plateau in the peak of a displacement versus frequency curve of a structural mode, while inductance deviations may shift the targeted frequency to a new value [113]. In another study [98], a systematic method was presented, for determining the resistance values by minimizing the H_2 norm of the damped system. The flexural vibration control effects produced on a distributed two-dimensional thin structure by a shunted piezoelectric patch tuned vibration absorber was studied in [114]. This work also showed that the classical 2-DOF approach of the host structure and the piezoelectric device is not sufficient to identify the optimal tuning parameters of the shunt. In the works [115]–[117], the authors derived a frequency domain formulation for the optimal resistance and inductance of the shunt circuit in such a

way as to maximise the energy dissipated in the resistance. Lately, the optimal tuning for vibration control has been derived based on the maximisation of the shunt electric power absorption, called extremum seeking algorithm, both for broadband [118], and for tonal [119] excitations.

2.2.4 Semi-active Control Studies

Shunt piezoelectric patches aiming at vibration attenuation can provide great tuning capabilities, due the rather simple changes in the shunt circuit, which can be manifested as frequency and damping alterations on the host structure. However, relatively few research works are found in the literature. A self-tuning piezoelectric absorber for a single structural mode was first introduced in [120], by adaptively tuning the electrical resonance, namely the shunt inductance and resistance, selecting the RMS voltage across the shunt circuit as the minimization criterion. In a similar manner, the effect of broadband disturbances on structures with multiple high profile modes was considered in [28], where the adaptive control was performed by synthetic impedance. A new technique for adaptive shunt circuit control was implemented by minimizing the relative phase difference between a vibration reference signal and the shunt current [121]. Experiments on a cantilever beam validated the proposed technique and demonstrated the simplicity of implementation. In [122], [123], the resistive and inductive components of the shunt are tuned online with an extremum seeking gradient search algorithm to maximise the time-averaged electric power absorbed by the shunt, thus implementing the control without the need of additional sensors to monitor the vibration of the structure. Lately, a semi-passive resonant shunt with tunable inductance for harmonically excited structures was developed, where the tunable inductor was realized using ferrite cores [124].

2.3 Combinations of TMDs with Shunt Circuit Piezoelectric Devices

A deep dive in the existing literature with combinations of TMDs and shunt piezoelectric systems for vibration control of flexible structures is attempted, to study the developed approaches and detect potential literature gaps. The found works can be divided into two categories. The first one includes studies where piezoelectric patches are attached to beams, which are further integrated into the host structure, while the second category entails concepts where the piezoelectric devices provide the stiffness for the auxiliary mass oscillation.

2.3.1 Piezoelectric Patches Attached to Thin Antivibration Structures

As seen in the previous subsection regarding the passive or semi-active vibration attenuation systems that entail solely piezoelectric materials, the most common practice is to firmly attach piezoelectric patches to smooth flexible structure surfaces, such as beams and strips, and transform the structure

strain energy to electrical, to further manipulate it in the shunt circuit. Some researchers advanced this idea and studied the beam plus attached piezoelectric patch combination as a novel hybrid antivibration device (Figure 2.3). Integrating such antivibration devices to vibrating flexible host structures, the attached beam can transform part of the host structure kinetic energy to beam kinetic energy (TMD effect), while the strain energy of the beam can be further transformed to electrical energy by the piezoelectric patch. Selecting the antivibration beam materials and geometry, or even attaching an auxiliary mass at the edge of the antivibration beam, can target specific frequency ranges of interest for the host structure. Some studies investigating this concept are presented below.

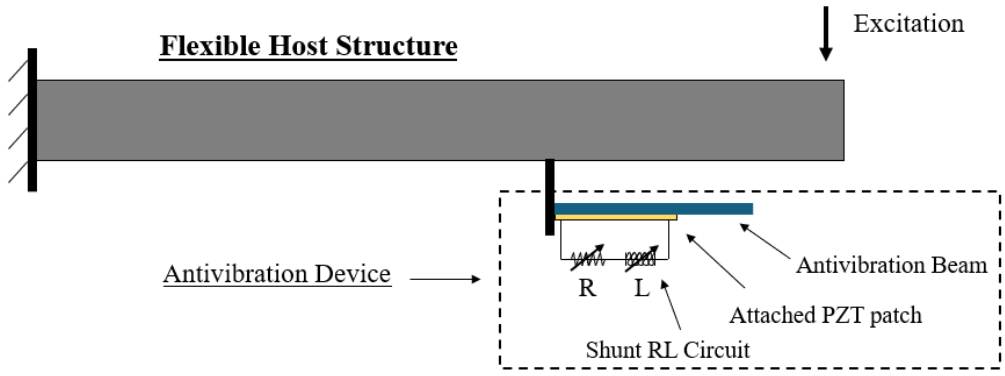


Figure 2.3. Antivibration device combining an antivibration beam and an attached shunt piezoelectric patch.

Lallart et al. [125] utilized this concept and demonstrated an electromechanical TMD, as seen in Figure 2.3, also featuring nonlinear Synchronized Switch Damping on Inductor (SSDI) in the shunt circuit. A steel cantilever beam with the proposed electromechanical semi-passive nonlinear TMD attached to the free end demonstrated the principles of operation. A lumped 2-DOF model and a respective FEM model evaluated the control performance of the proposed antivibration device, while experiments were carried out to validate the simulation. The proposed electromechanical TMD significantly outperforms purely mechanical TMDs and electromechanical passive TMDs with same dynamical parameters.

Heuss et al. [126] presented another work of this combined approach and showed that simulations and experimental analyses are very effective in predicting the behavior of these electromechanical systems. Applying a purely resistive or resonant resistant shunt altered the damping characteristics of the absorber, whereas its tuning frequency can be adapted to the excitation frequency, using a negative capacitance shunt circuit.

A very comprehensive analytical study was on the same subjected was performed by Yamada and Asami [127], where a lumped 1-DOF vibration system and a continuous body were used as the host structure, and the governing equations were theoretically derived to accurately estimate the mass ratio of the beam-type dynamic vibration absorber and the equivalent stiffness ratio of the piezoelectric elements.

The optimum values of the proposed piezoelectric vibration absorber were obtained. Furthermore, the effectiveness of the proposed methods and theoretical analysis were verified through experiments.

Manzoni et al. [128] recently dived into the possibility to strongly improve the adaptation capability of the combined beam-attached piezoelectric patch antivibration device, by applying negative capacitances and therefore independently shifting a number of eigenfrequencies equal to the number of the attached piezoelectric elements. Mathematical formulations were provided for linking the values of the capacitances and the resulting shifts of the eigenfrequencies, and vice versa. Furthermore, the stability of the electro-mechanical system is investigated, since the negative capacitances are based on active elements (operational amplifiers), giving rules about the tuning of these negative capacitances. All the theoretical outcomes were validated through an experimental campaign with a 0.21m cantilever beam equipped with two piezoelectric patches.

Lately, Rezai et al. [129] investigated the simultaneous energy harvesting and vibration suppression capabilities of the beam-piezoelectric layer antivibration device, incorporating the exciter dynamics. The continuous electromechanical equations governing the coupled system of the main beam-piezoelectric TMD-shaker were first developed. The study showed that the exciter (electromechanical shaker) force drops at the system resonance frequencies, meaning that a constant force sine sweep is difficult in practice, and does not allow model validation and empirical assessment of the TMD. The force drop off phenomenon was examined, and a constant shaker input voltage sweep was proposed instead of a constant force sweep. The results showed that the constant voltage sweep worked well to investigate the performance of the TMD and captured the shaker force drop off phenomenon. The system parameters showed significant effects on the dynamical response of the harvested power, the vibration response, and the applied force. Overall, the TMD demonstrated efficient performance in reducing vibration and harvesting energy.

2.3.2 Shunt Piezoelectric Devices Providing the Stiffness for the Auxiliary Mass Oscillation

An example where the piezoelectric device ca provide the stiffness for the auxiliary mass is illustrated in Figure 2.4. All of the examples studied above comprise single piezoelectric layers, which transform mechanical energy to electrical (direct piezoelectric effect), working in the d_{31} direction, meaning that they develop potential difference in their “3” direction (poling direction), when strains are applied in the “1” direction (host structure or antivibration beam direction). Single piezoelectric layers cannot provide the stiffness for the auxiliary mass oscillation unless structural enhancements are made.

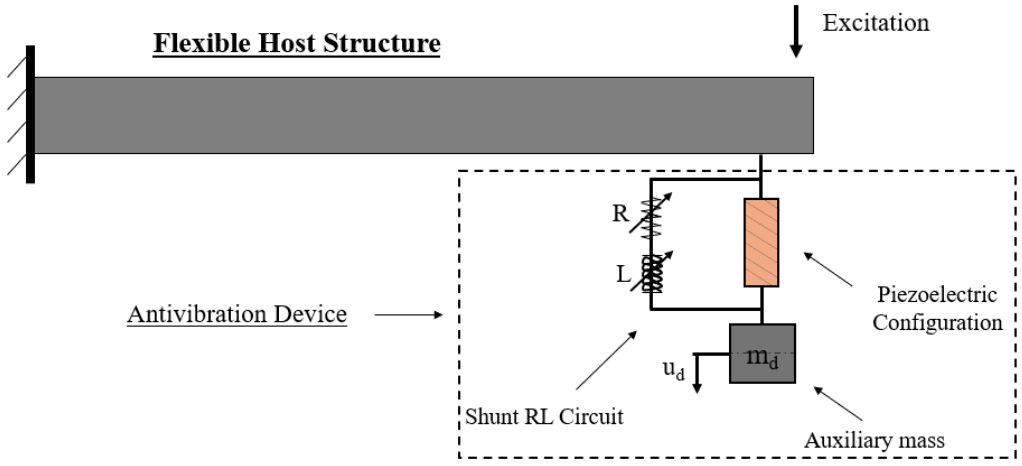
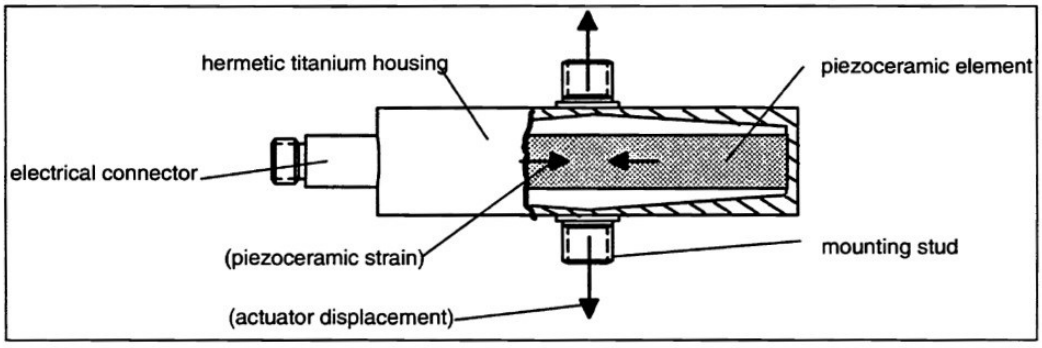
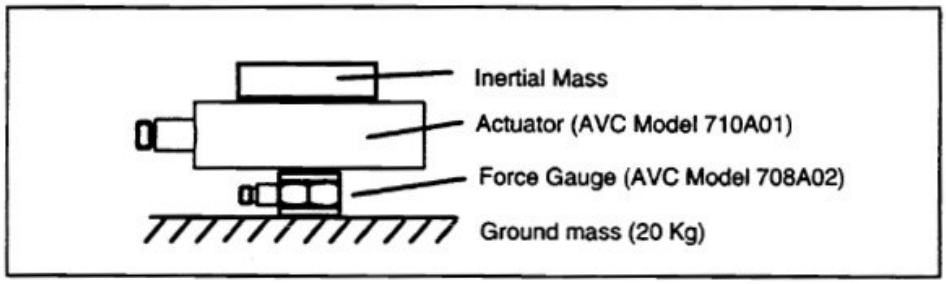


Figure 2.4. Antivibration device with a shunted piezoelectric configuration that provides the stiffness for an auxiliary resonant mass.

The first ever combination of shunt piezoelectric damping combined with an auxiliary mass, aiming at passive or semi-active vibration control, featured a structural housing (Figure 2.5a) and was presented by Dosch et al. [89]. The device shown is in Figure 2.5a utilizes the d_{31} piezoelectric constant, such that radial expansion of the piezoceramic, acting through the curvature of the actuator end caps, results in an amplified axial displacement. One side of the actuator is attached to the structure and the opposite end is fixed to an inertial mass. By appropriate sizing of the inertial mass, the resonant frequency of the actuator can be tuned to optimize performance. The displacement amplification design also achieves lower resonant frequency of the sole device, needing a smaller mass for low-frequency tuning. A lumped parameter model is developed for this device, and the analytical results were compared to experimental measurements, regarding the blocked force of the device (Figure 2.5b), and its effect on a flexible structure. A structural anti-resonance was depicted at the frequency response of the flexible structure, and specifically at the resonant frequency of the actuator, similarly to the passive TMD effect. The study showed that the inertial mass should be chosen such that the resonant frequency of the actuator is equal to the dominant disturbance frequency.



(a)



(b)

Figure 2.5. Proposed structure for the piezoelectric device in [89]. (a) Radial (d_{31}) expansion of the ceramic causes an axial motion of the device; (b) Blocked force test of the developed device.[89]

Evolving this concept, the authors in [130] investigated the electromechanical properties of a piezoceramic in conjunction with an external passive electrical shunt circuit, aiming at altering the natural frequency and damping of the device. An analytical model of the device was created to predict changes in natural frequency and damping due to passive electrical shunting. Capacitive shunting was found to only alter the natural frequency of the device, while resistive shunting alters both the natural frequency and damping. Experiments using both passive capacitive and passive resistive shunt circuits verified the ability to predictably shift the natural frequencies of the piezoceramic inertial actuator by more than 5%.

The studies on this device were subsequently advanced in [131], where Davis and Lesieutre presented their work on the development of an actively tuned antivibration device and its successful application on a flexible structure, operating under variable tonal excitations. As shown in their previous work, capacitive loads can alter the resonance of the device, and the tuning range was bounded by its short- and open-circuit resonance frequencies. No resistive shunting was used in this work, since maximum response reductions are achieved only when the absorber is lightly damped and accurately tuned to the frequency of concern. Another very remarkable contribution of this article, was the concept and implementation of an active tuning method, for creating the appropriate capacitive impedance under different excitations frequencies. A control scheme was developed to estimate the desired tuning frequency from the sensor signals, to determine the appropriate shunt capacitance, and then to provide it. For the implementation, the shunt circuit exhibited 10 discrete steps over the tuning range, using a relay-driven parallel capacitor ladder circuit. Experimental results showed great tuning capabilities, proving the developed device superior performance in variable tonal excitations, compared to the passive TMD.

Another concept where the piezoelectric device could provide the stiffness for the auxiliary mass oscillation, is the use of a piezoelectric stack configurations. These multilayer configurations entail a large number of stacked thin piezoelectric layers, separated by electrodes, and working in the d_{33} direction, meaning that the beneficial strain is generated in the poling direction “3”, therefore

perpendicular to the layer surface. These devices exhibit high piezoelectric coefficient, however, usually entail very high stiffness, demanding big and bulky mass in order to achieve tuning to low frequency ranges. For these reasons, the up-to-date literature that utilizes piezoelectric stacks and an auxiliary mass are limited only to analytical reports or flexible structures where the large added mass is not a hindrance, such as civil engineering applications.

Ali and Adhikari [132] presented an analytical investigation of the prospect using a resistively-shunted piezoelectric stack-TMD device for possible energy harvesting. The authors assumed that the original structure was sensitive to vibrations, however the absorber element was confined. They used an approximate fixed-point theory to find a closed form expression for optimal frequency ratio of the vibration absorber, having as primary goal the vibration control of the host structure, and as secondary goal the energy harvesting. The changes in the optimal parameters of the vibration absorber due to the addition of the energy harvesting electrical circuit were derived, showing that broadband energy harvesting can be obtained, combined with vibration reduction in the primary structure, with a proper choice of harvester parameters.

In a more recent analytical study, Høgsberg [133] reported a theoretical investigation of the root loci of a 3-DOF system, consisting of a structural mass, the absorber mass and an RL shunted ideal piezoelectric element, and used the principal of equal damping [37], [85] to determine the optimal parameters of the system.

In another analytical study with a shunted piezo stack and an auxiliary mass aiming at robust vibration control frequencies, Zhao et al. [134] used pure capacitive or inductive circuits to create a piezo-based tuned vibration neutraliser, and resistive-capacitive or resistive-inductive circuits to dampen broadband frequency excitation. For the capacitive and inductive circuits, tuning strategies were derived to adjust the shunt impedance, whereas in the case of resistive-capacitive and resistive-inductive shunt circuits, an H_2 optimization criterion was used for tuning the piezoelectric tuned mass damper.

Lai et al [135] proposed a low-cost and efficient piezoelectric tuned mass damper (Piezo-TMD) for structural vibration reduction and energy harvesting, numerically tested on a footbridge, under pedestrian loading. The proposed antivibration device consisted of a proof mass, multiple piezoelectric stacks connected to a shunting circuit. A spring is considered to be connected mechanically in series to the multi-stack piezoelectric device, to lower its effective stiffness. After deriving the equations of motion, an optimal design procedure for the Piezo-TMD was proposed to achieve simultaneous maximum vibration reduction and energy harvesting. The simulation results show that the Piezo-TMD performs better than the optimal conventional TMD in terms of vibration reduction, while efficiently converting the absorbed mechanical energy to electricity. Including inductance in the optimization algorithm led to significant reduction of the PZT stack number, thereby significantly reducing the cost of the antivibration device.

Very recently, Sheng and Xiang [136] investigated the performance of a TMD-piezoelectric stacks configuration system, aiming at simultaneous energy harvesting and vibration control. The antivibration

device configuration consisted of 4 piezoelectric devices, mechanically connected in parallel and to the auxiliary mass. Only resistive load was considered in the shunt circuit. A railway bridge was selected as the research object to investigate the performance of the selected device. The electromechanical coupling equations between the bridge and the piezoelectric TMD were calculated and verified by a scaled model experiment. The optimized parameters results show that when the damper is completely replaced by the piezoelectric transducers, the two optimization functions of energy harvesting and vibration control can be simultaneously optimized. It is noted that this study was published later than the publication of the author's scientific works in international journal and conferences.

2.4 Open Questions and Challenges

Big potential for broadband, adaptive, and high vibration attenuation capabilities, manifests itself using antivibration devices which combine shunted stack piezoelectric configurations and TMDs, since TMDs can absorb high amounts of kinetic energy of the host structure, while stacked piezoelectric devices can transform much kinetic energy to electrical, due to their high piezoelectric coefficients. The main hindrance for applications in flexible structures is the large mass needed for tuning to low frequencies, due to the high stiffness of the piezoelectric stack. For this reason, all scientific works on this topic until now are purely analytical and numerical, except for one very recent publication [136]. For this reason, a great deal of open questions and challenges remain to be answered, some of which are listed below.

- The development, characterization, and dynamic behavior of a novel configuration, where a relatively small mass is attached to a shunted stacked piezoelectric device.
- The analytical and experimental testing of a TMD-piezoelectric stack device on flexible structures, and the effects of its shunt impedance to the host structure.
- The development of the governing equations of a multiple DOF host structure and the TMD-piezoelectric stack device.
- The testing of such a device to broadband and multi-tonal excitation, in order to evaluate its performance under such conditions. Also, the investigation of mechanical tuning of the auxiliary mass for enhanced performance in such conditions.
- The development of an adaptive algorithm for TMD-piezoelectric stack devices, to achieve semi-active frequency and damping tuning.

Recognizing the existing literature challenges and gaps, this work presents significant novelties in the field, as demonstrated in the next Chapters, and as covered in Section 1.4.

Chapter 3: Experimental Apparatus for Vibration Testing

Multiple experimental campaigns were conducted for enhancing the study and augmenting the content of this thesis, varying from lab-scale simplified setups to full-scale on field applications. Experimental demonstrations of the proposed SATMD capabilities are essential, both for showcasing the introduced antivibration behavior, and for validating the developed numerical models. This Chapter addresses and describes the experimental apparatus and setup used for the experimental campaigns.

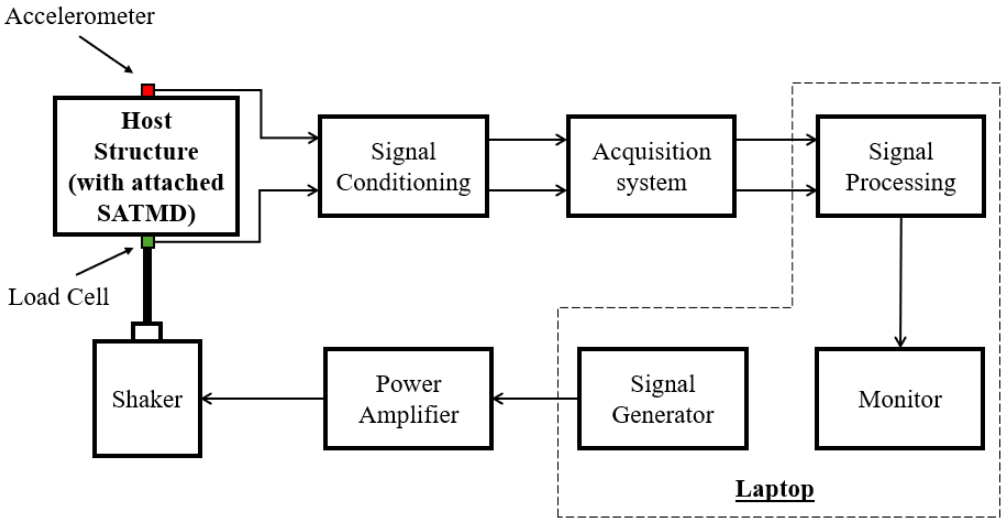


Figure 3.1. Experimental Setup.

All conducted experimental campaigns for the current thesis used the concept and the experimental setup, as described in Figure 3.1. The excited structure is either the SATMD device itself or host structure with the SATMD device firmly attached to it. The various structures are excited with an LDS electromechanical shaker (models V406 or V201, depicted in Figure 3.2a, and b, respectively). The actuation signals are either white noise signal with frequency bandwidth up to 2048 Hz, or tonal (and multi-tonal) signals, harmonically exciting the structure. All signals are generated on LabVIEW, converted to analog, amplified (LDS PA500L power amplifier used), and finally driven to the shaker to continuously excite the structure. A load cell (PCB 208C03) is intervened between the shaker stinger and the tested structure. One or more accelerometers (PCB M352C66) were used to measure the accelerations normal to the plane of tested structure, placed at various locations. The time signals of the applied force from the actuator as well as the accelerations were simultaneously conditioned by a PCB 442C04 signal conditioner, before directed to a NI USB-6366 data acquisition board. Sampling rate was set at 5000S/s and the time signal density was ~0.1msec providing excellent resolution at the frequency range of interest. When tonal excitation is applied, the time signals are directly saved and converted to frequency domain via Fast Fourier Transform (FFT) later by the author. When white noise excitation is

applied, the measured time signal of the applied force and the generated acceleration are transformed to frequency domain via (FFT) and used for the extraction of the measured Frequency Response Functions (FRFs) in a NI VI, illustrated on the laptop monitor (Figure 3.4). 20 consecutive FRFs with white noise excitation are averaged (Figure 3.4) to produce less noisy frequency response results.



(a) *(b)*

Figure 3.2. Shakers used for the laboratory tests. (a) LDS V406; (b) LDS V201.



Figure 3.3. Complete experimental setup for a down-scaled airframe model.

A complete example of the experiment configuration on a host structure with an attached SATMD device is depicted in Figure 3.3. A down-scaled airframe prototype is suspended with elastic belts and is excited by an LDS electromechanical shaker, mounted at the middle of the horizontal tail. Accelerations normal to the plane of the tested structure were measured at three different locations; 1. at the fuselage tip 2. at the fuselage center, and 3. at the wing tip. The piezoelectric SATMD antivibration device is attached below the airframe fuselage tip. The FRF of the fuselage tip for one configuration of the attached SATMD is depicted in Figure 3.4.

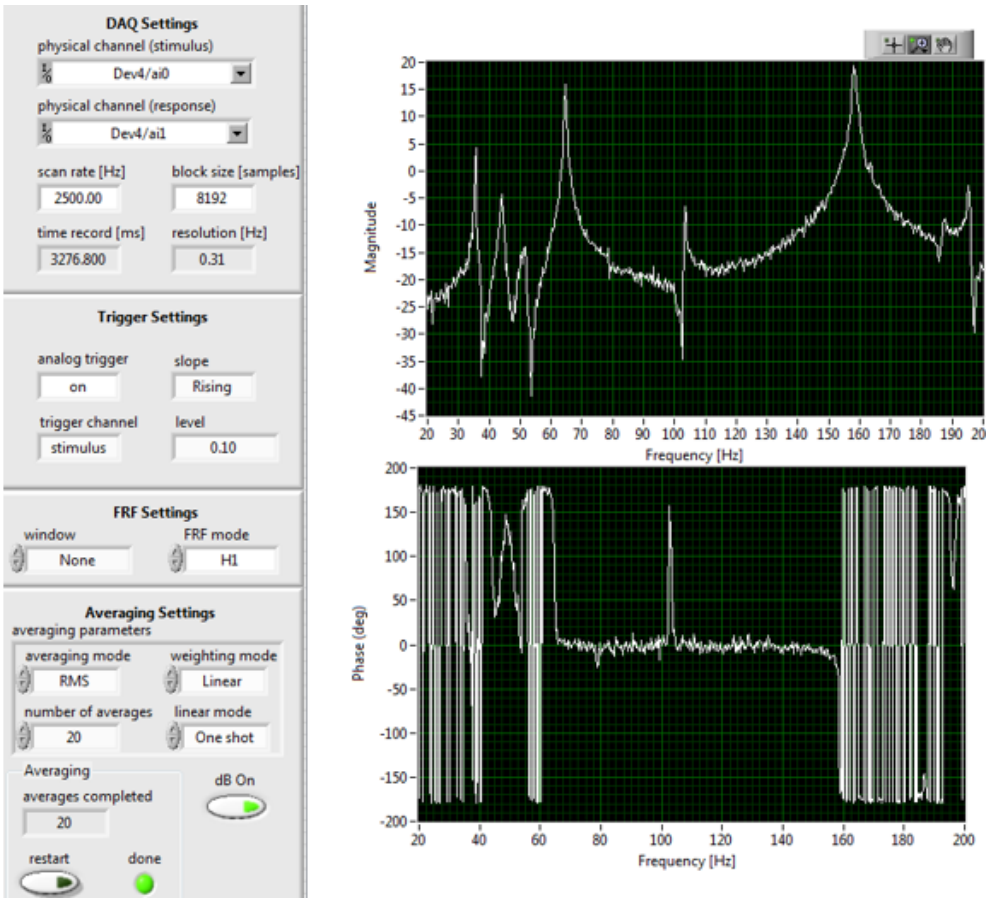


Figure 3.4. Constructed FRF example based on experimental measurements.

Chapter 4: Modeling, Specification and Characterization of the Piezoelectric SATMD

This Chapter addresses the concept and development of the proposed electromechanical antivibration device. For the computational model, the single-layer piezoelectric constitutive equations are presented and manipulated such that the equivalent properties of multilayer piezoelectric devices are formed. These equivalent properties are necessary for the electromechanical equilibrium of the sole SATMD and the prediction of sole device behavior. The selection of the piezoelectric transducer is crucial, as it highly affects the performance of the antivibration device, in terms of electromechanical coupling and need for auxiliary mass. Based on the piezoelectric device selection, the SATMD device assembly is carefully selected, considering the application of the device to the existing structure and the addition of the auxiliary mass, which should move with minimal losses. An experimental campaign is designed and executed for the characterization of the device equivalent properties. Finally, the effects of the shunt circuit resistance and inductance to the auxiliary mass are demonstrated and discussed.

4.1 Sole SATMD Computational Model

The piezoelectric transducer used for the antivibration application is crucial, since it highly affects the electromechanical coupling and general performance of the antivibration device. To select a piezoelectric transducer with the appropriate features, its properties and electromechanical equilibrium must be first studied and understood.

4.1.1 Constitutive Equations in Piezoelectric Layers

The constitutive equations of a homogeneous piezoelectric layer correlate the mechanical stress and strain, to the electric displacement and field, at each point of the piezoelectric material. The piezoelectric material is assumed to remain in its linear range, such that the Hooke's law for elastic materials is valid. Moreover, linear piezoelectricity is considered, according to which the electric field also remains in its linear range [137]. Among the four different combinations between the stress, strain, electric displacement, and electric field tensors, two forms are most commonly used [138].The first form is:

$$S_i = s_{ij}^E \sigma_j + d_{ik} E_k \tag{4.1a}$$

$$D_l = d_{lj} \sigma_j + \varepsilon_{lk}^\sigma E_k \tag{4.1b}$$

where s_{ij} is the elastic compliance tensor, d_{ik} or d_{lj} is the tensor of the piezoelectric strain coefficients, ε_{lk} is the electric permittivity tensor of the material, S_i are the engineering strains, σ_j are the mechanical stresses, D_l are the electric displacements, and E_k are the electric fields. The stress and

strain tensors are expressed with the extended vectorial notation (Voigt notation), therefore $i, j = 1,...,6$ and $k, l = 1,...,3$. Moreover, the piezoelectric strain tensor in piezoelectric materials is written in matrix form as:

$$d = \begin{bmatrix} 0 & 0 & 0 & 0 & d_{15} & 0 \\ 0 & 0 & 0 & d_{24} & 0 & 0 \\ d_{31} & d_{32} & d_{33} & 0 & 0 & 0 \end{bmatrix} \tag{4.2}$$

where the lines correspond to the three directions of the electric field, and the columns to the engineering strains.

Equation (4.1a) describes the relationship between the engineering strain and the applied stress and electric field on the piezoelectric layer. Except for the $s_{ij}^{E}\sigma_j$ term representing the elastic strains generated by the applied stress on the piezoelectric material (Hooke's law), an additional strain component $d_{ik}E_k$ emerges which represents the induced strains due to the converse piezoelectric effect. On the other hand, Equation (4.1b) describes the relationship between the electric displacement (also known as electric flux) at a point of a piezoelectric layer, to the applied stress and electric field. The component $\varepsilon_{lk}^{\sigma}E_k$ represents the electric charge per unit area developed at the presence of an applied electric field E_k, due to the electric permittivity of the material, as occurs in a capacitor. The additional component $d_{lj}\sigma_j$ represents the electric charge generated in the piezoelectric material due to the direct piezoelectric effect.

Furthermore, a set of equations which relate the stress and electric displacement to the strain and electric field in the piezoelectric material are needed for the formulation of many piezoelectric multilayer and structural models, reaching the second form of the constitutive equations:

$$\sigma_i = C_{ij}^{E}S_j - e_{ik}E_k \tag{4.3a}$$

$$D_l = e_{lj}S_j + \varepsilon_{lk}^{S}E_k \tag{4.3b}$$

where:

$$e_{ik} = C_{ij}^{E}d_{jk} \tag{4.4a}$$

$$\varepsilon_{lk}^{S} = \varepsilon_{lk}^{\sigma} - d_{li}e_{ik} \tag{4.4b}$$

and C_{ij}^{E} is the elastic stiffness tensor and e_{ik} or e_{lj} is the tensor of the piezoelectric stress coefficients. Superscripts E, σ, S are used in all equations to indicate constant electric field, stress, and strain conditions, respectively, reflecting the fact that the values of elastic and electric coefficients in piezoelectric materials may vary depending on the applied electric and mechanical conditions. Regarding the directions in thin piezoelectric layers, the most common practice is depicted in Figure 4.1. The polarization axis "3" is perpendicular to the surface of the film, which is defined on axes "1"

and “2”. The shear planes are indicated by the subscripts “4”, “5”, “6”, and are perpendicular to the directions “1”, “2”, and “3”, respectively.

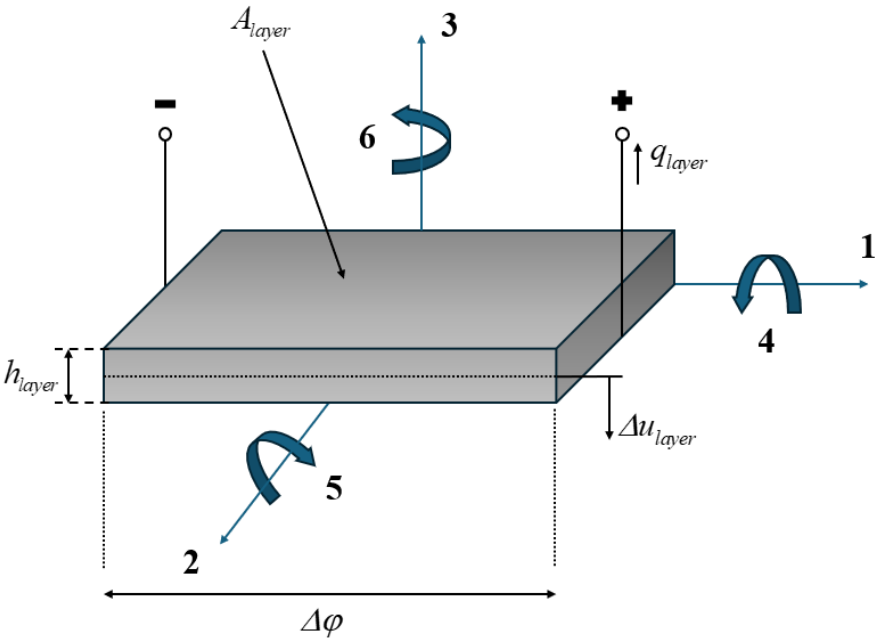


Figure 4.1. Piezoelectric layer.

4.1.2 Multilayer Piezoelectric Devices Equivalent Properties

Single piezoelectric layers feature rather small piezoelectric coefficients and are unable to provide the mechanical stiffness needed for the auxiliary mass oscillation in the studied antivibration mechanism. For these reasons, our Structural Mechanics and Smart Materials (SMSM) group turned its interest to the multilayer piezoelectric materials, which are known for their higher piezoelectric coefficients [139] and provide sufficient stiffness for the auxiliary mass oscillation. Multilayer piezoelectric materials, also known as piezoelectric stack configurations, entail a large number of stacked thin piezoelectric layers, separated by electrodes (Figure 4.2a). The piezoelectric layers are mechanically connected in series, and electrically connected in parallel. Each piezoelectric layer is polarized along the direction 3 (Figure 4.1), which coincides with the longitudinal direction of the piezoelectric stack (Figure 4.2b). The positive or negative poling direction determines whether a positive electrical voltage induces compression or expansion of the piezoelectric material, and vice versa. Taking into consideration the alternating connection of the electrodes (positive electrode followed by negative electrode), adjacent layers of the stack must have opposite poling direction (red arrows in Figure 4.2a), such that all layers move in the same direction and the phenomena are magnified [140]. This stack configuration yields high total deformation or force with low voltage input (converse piezoelectric phenomenon), or high charge output with low deformation (direct piezoelectric phenomenon). To model the electromechanical equilibrium of multilayer piezoelectric materials, equivalent stack properties (Figure 4.2b) are preferred

for their simplicity and small computational cost. Therefore, this subsection studies the equivalent piezoelectric multilayer material electromechanical properties.

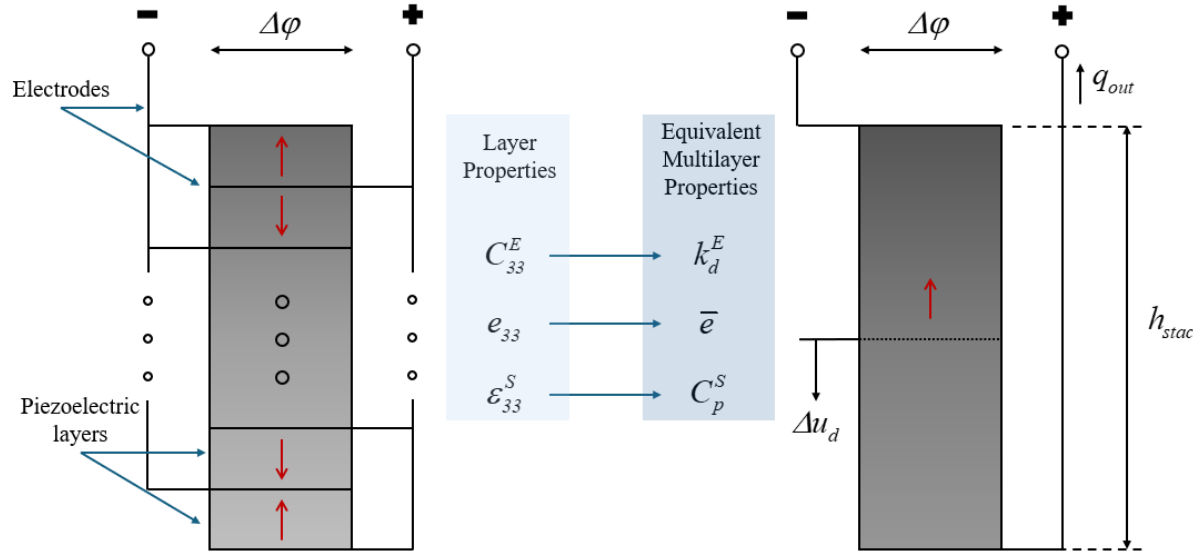


Figure 4.2. Multilayer piezoelectric material and equivalent stack model.

When a piezoelectric layer is used in its thickness mode, both stress and electric field exist along the direction "3", as shown in Figure 4.1. Then Equations (4.3a) can be expressed as [141]:

$$\sigma_3 = C_{33}^E S_3 - e_{33} E_3 \tag{4.5}$$

Multiplying with the surface area of the piezoelectric layer A_{layer} and considering:

$$S_3 = \frac{\Delta u_{layer}}{h_{layer}} \tag{4.6a}$$

$$E_3 = -\frac{\Delta\varphi}{h_{layer}} \tag{4.6b}$$

$$A_{layer}\sigma_3 = f_p \tag{4.6c}$$

where Δu_{layer} is the layer displacement in direction 3, h_{layer} is the piezoelectric layer thickness, $\Delta\varphi$ is potential difference that is created due to the electric field, f_p is the force that the piezoelectric layer induces in direction 3 (Figure 4.1), Equation (4.5) is transformed to:

$$h_{layer} f_p = C_{33}^E A_{layer} \Delta u_{layer} + A_{layer} e_{33} \Delta\varphi \tag{4.7}$$

Considering a multilayer piezoelectric stack with N_{layers} number of layers mechanically connected in series, the multilayer device thickness h_{stack} and displacement in direction 3 Δu_d can be defined as [141]:

$$h_{stack} = N_{layers} h_{layer} \tag{4.8a}$$

$$\Delta u_d = N_{layers} \Delta u_{layer} \tag{4.8b}$$

Using Equations (4.8a, b), Equation (4.7) is transformed to:

$$f_p = k_p^E \Delta u_d + \bar{e} \Delta \varphi \tag{4.9}$$

where:

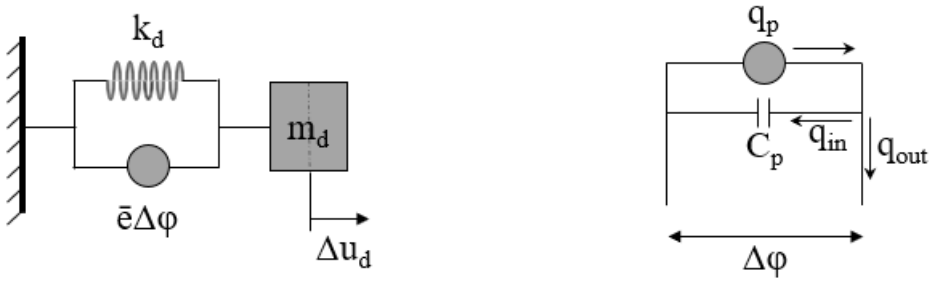
$$k_p^E = \frac{C_{33}^E A_{layer}}{h_{stack}} \tag{4.10a}$$

$$\bar{e} = \frac{A_{layer} e_{33}}{h_{layer}} \tag{4.10b}$$

k_p^E is the equivalent mechanical stiffness of the multilayer piezoelectric material under zero electric field, or in short circuited condition of the piezoelectric device terminals. It corresponds to the pure mechanical stiffness of the device; therefore, it will be used as:

$$k_d = k_p^E \tag{4.11}$$

$\bar{e}$ stands for the equivalent piezoelectric stress coefficient of the multilayer piezoelectric material, is measured in N/V and quantifies the equivalent force output of the device per voltage input, indicating the level of the piezoelectric coupling. Equation (4.9) describes that when an external mechanical load is applied, the elastic energy of the piezoelectric stack is divided both in an elastic term and an electric term (Figure 4.3a). Moreover, when a potential difference is applied in clamped boundary conditions ($\Delta u_d = 0$), the piezoelectric force manifests its highest value, whereas in free-free ($f_p = 0$) conditions exhibits its maximum displacement.



(a) *(b)*

Figure 4.3. Piezoelectric device equilibrium. (a) Mechanical components; (b) Electrical components.

Furthermore, in its thickness mode, the Equation (4.3b) is expressed as:

$$D_3 = e_{33} S_3 + \varepsilon_{33}^S E_3 \tag{4.12}$$

Considering the Equations (4.6a, b) and

$$D_3 = \frac{q_{layer}}{A_{layer}} \tag{4.13}$$

where q_{layer} is the charge that creates the electric displacement of the closed circuit in a piezoelectric layer, Equation (4.12) is transposed to:

$$\frac{q_{layer}}{A_{layer}} = e_{33} \frac{\Delta u_{layer}}{h_{layer}} - \varepsilon_{33}^S \frac{\Delta \varphi}{h_{layer}} \tag{4.14}$$

A multilayer piezoelectric material with N_{layers} electrically connected in series creates a total charge q_{out} in the closed circuit, equal to [141]:

$$q_{out} = N_{layers} q_{layer} \tag{4.15}$$

Multiplying Equation (4.14) with the N_{layers}, this equation can be expressed as:

$$q_{out} = \overline{e} \Delta u_d - C_p^S \Delta \varphi \tag{4.16}$$

where:

$$C_p^S = \frac{\varepsilon_{33,tot}^S A_{layer}}{h_{stack}} \tag{4.17a}$$

$$\varepsilon_{33,tot}^S = N_{layers}^2 \varepsilon_{33}^S \tag{4.17b}$$

$\varepsilon_{33,tot}^S$ is the total electric permittivity of the piezoelectric multilayer (as also seen in [142]), and C_p^S is the inherent electric capacitance of the piezoelectric device, under constant strain (clamped) conditions. Stack piezoelectric devices are prestressed, due to brittleness and small tensile strength, thus the piezoelectric stack oscillation are assumed to maintain clamped conditions, and the electric capacitance will be used as:

$$C_p = C_p^S \tag{4.18}$$

Equation (4.16) can be rewritten as:

$$q_p = q_{in} + q_{out} \tag{4.19}$$

where:

$$q_p = \bar{e}\,\Delta u_d \tag{4.20a}$$

$$q_{in} = C_p \Delta\varphi \tag{4.20b}$$

indicating that the charge q_p created by the relative movement of multilayer piezoelectric material is divided into the one that charges the inherent piezoelectric capacitor, and the one that flows as current in the closed circuit (Figure 4.3). Open circuit condition ($q_{out} = 0$) leads only to the charge of the capacitor, whereas short circuit condition ($\Delta\varphi = 0$) circulates the created charge only through the circuit.

4.1.3 Sole Conventional TMD

To develop the sole SATMD computational model, the conventional sole TMD model is first examined. The dynamic equilibrium of a conventional TMD mass m_d mounted on a clamped spring-damper element (Figure 4.4) is:

$$m_d \ddot{u}_d + c_d \dot{u}_d + k_d u_d = f \tag{4.21}$$

where $u_d, \dot{u}_d, \ddot{u}_d$ represent the displacement, velocity, and acceleration responses under the excitation force f that acts on the mass, in time domain.

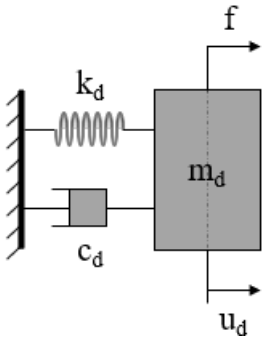
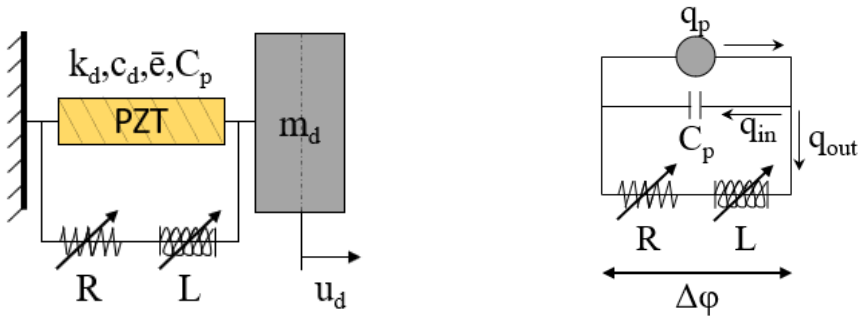


Figure 4.4. Conventional sole TMD structure.

4.1.4 Sole Piezoelectric SATMD

In the piezoelectric SATMD, the connecting spring-damper element of the conventional TMD is substituted with a suitable piezoelectric transducer (Figure 4.5a). A linear lumped model is considered for the proposed piezoelectric SATMD, which exhibits an auxiliary mass m_d, stiffness k_d and damping c_d, and can be further connected to an external electric circuit. Importing Equation (4.9) to Equation (4.21), yields:

$$m_d \ddot{u}_d + c_d \dot{u}_d + k_d u_d + \bar{e}\,\Delta\varphi = f \tag{4.22}$$



(a) *(b)*

Figure 4.5. Sole SATMD structure. (a) Schematic illustration; (b) Shunt circuit.

4.1.4.1 Open Circuit

As already mentioned, electric charge q_p is created in the piezoelectric device, which is stored in its electrical capacitance C_p, when it is not shunted by an external circuit. Hence, an additional equation of motion is introduced, which describes the equilibrium of electric charge in the piezoelectric transducer (Figure 4.5)

$$q_p = \bar{e}u_d = C_p \Delta\varphi = q_{in} \tag{4.23}$$

Combining Equations (4.22) and (4.23), the equation of motion of the mass for the open circuit SATMD can be presented as:

$$m_d\ddot{u}_d + c_d\dot{u}_d + (k_d + \frac{\bar{e}^2}{C_p})u_d = f \tag{4.24}$$

Comparing this equation to the one of the purely mechanical TMD (Equation 4.21), it is easily understood that the internal energy of the system is now stored as strain energy in the springs, but also as electrical energy in the piezoelectric element, resulting in a stiffness variation of the system by the $\bar{e}^2 / C_p$ term. This implies that the substitution of the connecting spring-damper element with a piezoelectric material is itself capable of altering the system elastic characteristics, depending on the piezoelectric coupling coefficient $\bar{e}^2 / C_p$.

4.1.4.2 Shunt Circuit

4.1.4.2.1 Equations of Motion

Incorporating a shunt circuit at the terminals of the piezoelectric device, comprising variable resistance and inductance (RL), the electric charge is divided into the capacitance of the piezoelectric element and one that circulates through the shunt circuit in form of electric current (Equation 4.19). Moreover, for the potential difference applies:

$$\Delta\varphi = \frac{q_{in}}{C_p} = R\dot{q}_{out} + L\ddot{q}_{out} \tag{4.25}$$

Considering:

$$k_p = k_d + \frac{\bar{e}^2}{C_p} \tag{4.26}$$

and combining Equations (4.19), (4.25) and (4.26), the equations of motion are transformed to:

$$\begin{bmatrix} m_d & 0 \\ 0 & L \end{bmatrix} \begin{Bmatrix} \ddot{u}_d \\ \ddot{q}_{out} \end{Bmatrix} + \begin{bmatrix} c_d & 0 \\ 0 & R \end{bmatrix} \begin{Bmatrix} \dot{u}_d \\ \dot{q}_{out} \end{Bmatrix} + \begin{bmatrix} k_p & -\frac{\bar{e}}{C_p} \\ -\frac{\bar{e}}{C_p} & \frac{1}{C_p} \end{bmatrix} \begin{Bmatrix} u_d \\ q_{out} \end{Bmatrix} = \begin{Bmatrix} f \\ 0 \end{Bmatrix} \tag{4.27}$$

4.1.4.2.2 Transfer Functions

Transposing Equation (4.27) to frequency domain and ignoring the damping factors for simplicity, the transfer function of the auxiliary mass DOF, per force input to the auxiliary mass can be obtained:

$$H_{11} = \frac{U_d}{F} = \frac{-C_p(C_p L\omega^2 - 1)}{Lm_d C_p{}^2\omega^4 - (Lk_p C_p{}^2 - m_d C_p)\omega^2 + k_p C_p - \bar{e}^2} \tag{4.28}$$

The second order that is observed in the characteristic equation for $L > 0$ predicts that two pairs of conjugate poles are created, one for each inertia feature of the SATMD, namely the auxiliary mass and inductance. The variable inductance is also expected to highly affect the poles. In addition, a zero is observed in Equation (4.28):

$$z_{11} = \frac{1}{\sqrt{LC_p}} \tag{4.29}$$

It is observed that the created antiresonance on the mass coincides with the shunt circuit eigenfrequency. Furthermore, the transfer function of the shunt circuit charge per force input to the auxiliary mass is calculated as:

$$H_{21} = \frac{Q_2}{F} = \frac{C_p \bar{e}}{Lm_d C_p{}^2 \omega^4 - (Lk_p C_p{}^2 - m_d C_p)\omega^2 + k_p C_p - \bar{e}^2} \tag{4.30}$$

where no zero is observed, therefore no antiresonance is expected in the frequency response of the charge.

4.2 Piezoelectric Device Desirable Features and Selection

The piezoelectric device in the SATMD configuration is crucial for the antivibration device performance, as it affects both the mechanical coupling between the auxiliary mass and the structure, and the electromechanical coupling between the shunt circuit and the structure.

4.2.1 Desirable Features and Characteristics for the Piezoelectric Transducer

First, the piezoelectric device should provide the mechanical stiffness needed for the auxiliary mass oscillation, to effectively replace the spring-damper element of the conventional TMD. As a result, the piezoelectric device is required to exhibit considerable stiffness in the direction the auxiliary mass movement, durability, and immutability. It is also important that the auxiliary mass of the studied antivibration device is kept in relatively small values, since the added weight is undesirable in the host applications. Additional weight in lightweight means of transportation, and especially aircrafts, would increase the fuel consumption and lead to higher CO_2 emissions, which is impermissible. Therefore, considering the auxiliary mass eigenfrequency:

$$\omega_n = \sqrt{\frac{k_d}{m_d}} \tag{4.31}$$

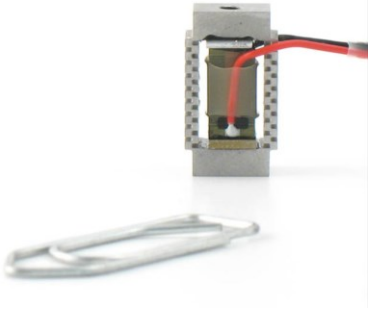
the piezoelectric device equivalent stiffness should be held at relatively low values, such that relatively small auxiliary mass can perform in low frequency bandwidths, where the structural vibrations are more perceptible.

Considering the piezoelectric device electric properties, the equivalent capacitance is required to have minimal values. First, small capacitance yields high piezoelectric coupling through the stiffness variation term $\bar{e}^2 / C_p$ and the coupling terms $\bar{e} / C_p$, as seen in the stiffness matrix components. In addition, small capacitor values in the direct piezoelectric phenomenon (Equation 4.16) will lead to lower charge storage q_{in}, and higher charge flow in the shunt circuit (q_{out}). This will lead to higher electric energy in the shunt circuit and its better manipulation by the variable resistance and inductance values.

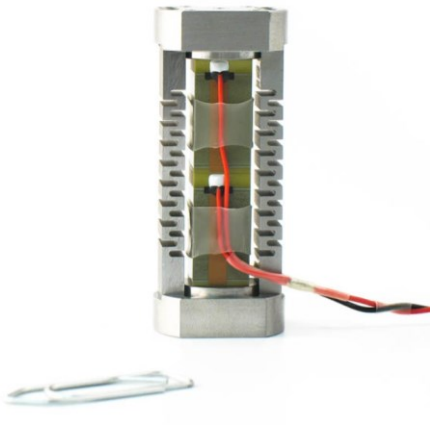
Finally, considering the electromechanical properties, the piezoelectric device should exhibit high equivalent piezoelectric coefficient, such that a significant part of the kinetic energy can be transformed into electrical energy and consequently directed in the shunting circuit.

4.2.2 Piezoelectric Device Configurations and Selection

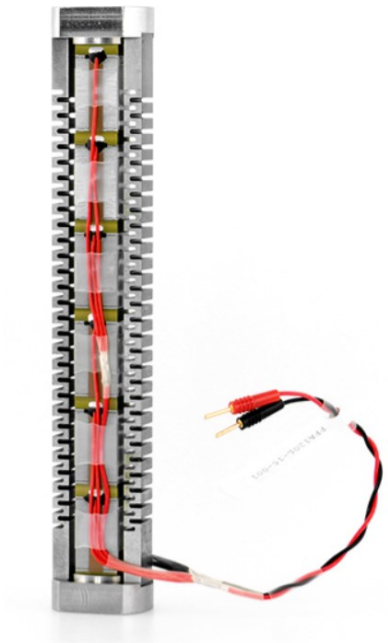
Considering the desirable features of the piezoelectric device, as mentioned in the previous subsection, the SMSM group investigated the market for piezoelectric stacks. Such configurations are constitutive from PZT material, thus exhibit very high piezoelectric coefficient, maintaining relatively low equivalent capacitance, and can support the movement of the auxiliary mass; however, the conventional parallel pre-stressed piezoelectric stacks exhibit very high stiffness for the studied antivibration application. As an example, the PPA120L (Figure 4.6a) piezoelectric device [143], produced by CEDRAT TECHNOLOGIES [144] consists of 6 smaller stacks mechanically connected in series, exhibits a high equivalent piezoelectric coefficient, and features 36 MN/m equivalent stiffness. As a result, if this device was used for the SATMD configuration, the auxiliary mass needed for tuning the mechanical eigenfrequency of the device to 50Hz, would be approximately 365kg (Equation 4.31). Similar piezoelectric devices with less interior stacks and same surface layer area exhibit even higher stiffness. On the other hand, piezoelectric stacks with plies of smaller dimensions have less stiffness, however, also exhibit lower equivalent piezoelectric coefficients, which is unwanted.



(a) PPA10M



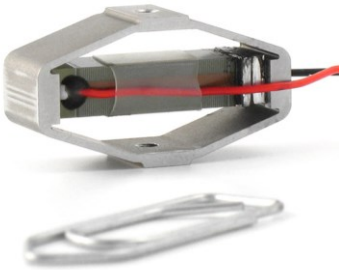
(b) PPA40L



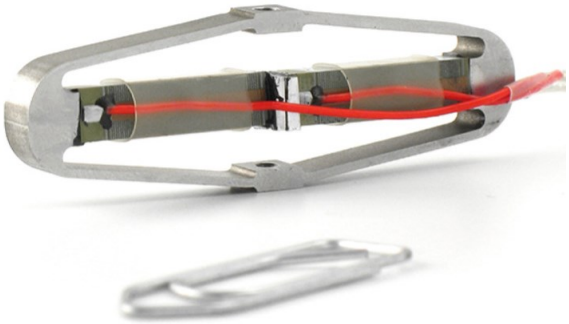
(c). PPA120L

Figure 4.6. Examples of prestressed piezoelectric devices, produced by CEDRAT TECHNOLOGIES.

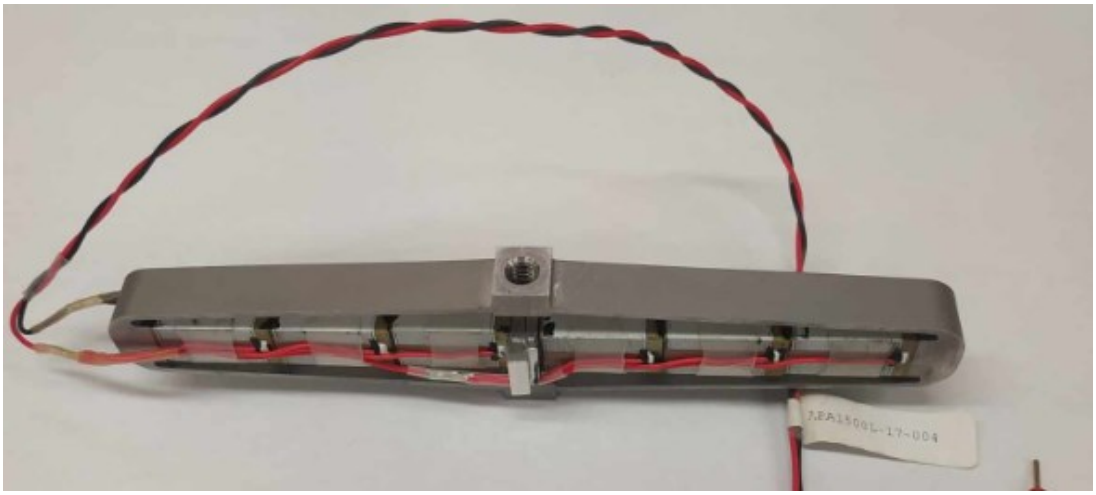
For these reasons, our interest turned to other configurations which entail piezoelectric stacks, and also include mechanical amplification mechanisms. Great examples of such devices are the amplified piezoelectric actuators (APA), patented and produced by CEDRAT TECHNOLOGIES [145], where an external elliptical shell made of stainless steel magnifies, along the short axis, the deformation occurring along the piezoelectric stack axis. As a result, the piezoelectric device works along the short axis, where the stroke is greatly amplified, and the mechanical stiffness is highly reduced. Furthermore, the elliptical frame also provides the user with mechanical interfaces for the integration to the targeted host structures. Finally, we selected the APA1500L device (Figure 4.7c), which includes 6 piezoelectric stacks, and features a much smaller mechanical stiffness along the working direction (67 kN/m). Therefore, the auxiliary mass needed for tuning the mechanical eigenfrequency of the device to 50Hz, would be approximately 0.68kg (Equation 4.31), that is three orders of magnitude less than the example studied for the parallel pre-stressed device.



(a) APA40SM



(b) APA200M



(c) APA1500L

Figure 4.7. Examples of amplified piezoelectric devices, produced by CEDRAT TECHNOLOGIES. (c) is the one that is used for studied SATMD.

4.3 SATMD Host Structure Integration and Components

Other than the piezoelectric device, the components that constitute the SATMD and their assembly is presented in this subsection. The structural integration of the SATMD is also addressed.

4.3.1 Host Structure Integration and Uniaxial Movement

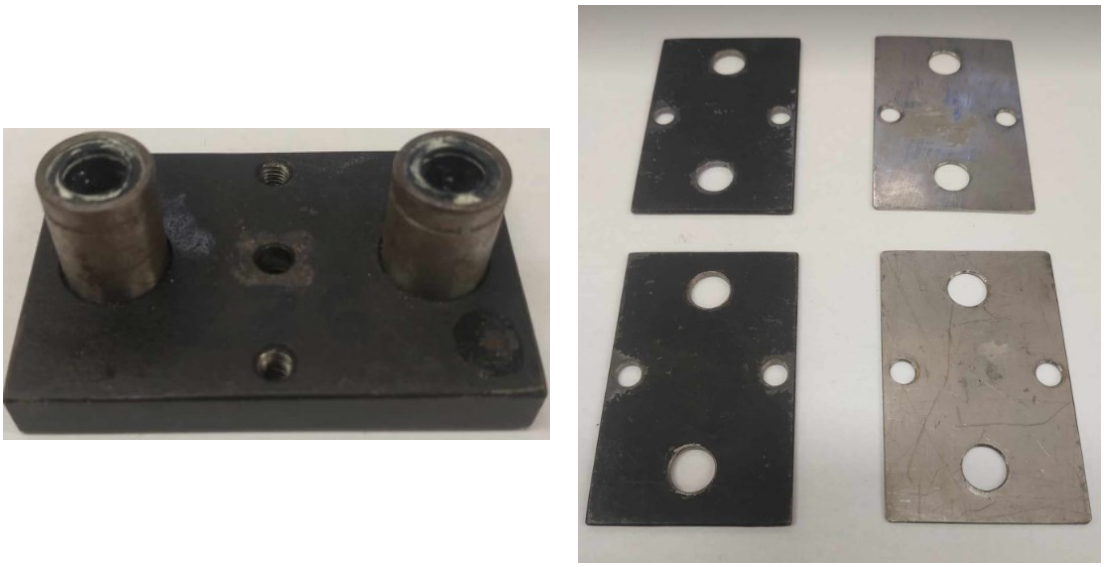
The piezoelectric device will act as a spring-damper element for the auxiliary mass movement. Therefore, it should be firmly attached to the surface of the structure of interest, such that it strictly follows its movement and agrees with the model assumption. Furthermore, the auxiliary mass should be forced to move only along the working direction of the piezoelectric device, such that no out-of-axis oscillations are existent, and that the structural integrity of the piezoelectric device is guaranteed. Considering these aspects, the SMSM lab designed and manufactured the aluminum base with vertical guides, seen in Figure 4.8. This base features four through holes near its four corners, and a through hole at its center. The corner holes allow for four bolts to firmly connect the base to the host structure, while the center hole allows for a small bolt to firmly connect the piezoelectric device to the base. On the other hand, the vertical guides of the base enforce the axial movement of the auxiliary mass, if an auxiliary mass with the linear bearings is utilized. Finally, it should be stressed that, in the final integration of the SATMD to the host structure, the connecting elements inherent mechanical characteristics are expected to affect the antivibration device equivalent mechanical stiffness and damping.



Figure 4.8. Aluminum base with vertical guides.

4.3.2 Auxiliary Mass and SATMD Assembly

The auxiliary mass is composed of a main component with two linear bearings to minimize friction (Figure 4.9a) and multiple additional components of 20g and 40g (Figure 4.9b, c), to allow for free adjustment of the total auxiliary mass, for the mechanical tuning of the SATMD. The main component has a through hole in its center, such that a small bolt firmly attaches it to the piezoelectric devices free end, and two through holes with internal thread, such that the additional masses are firmly connected to the main component using two bolts. Finally, the additional components have two through holes aligned with the vertical guides, and two more through holes for the connection to the main mass. The assembly of the anti-vibration setup is illustrated in Figure 4.10.



(a) *(b)*

Figure 4.9. Auxiliary mass used for the SATMD. (a) Main auxiliary mass component with two linear bearings; (b) Additional auxiliary mass components.

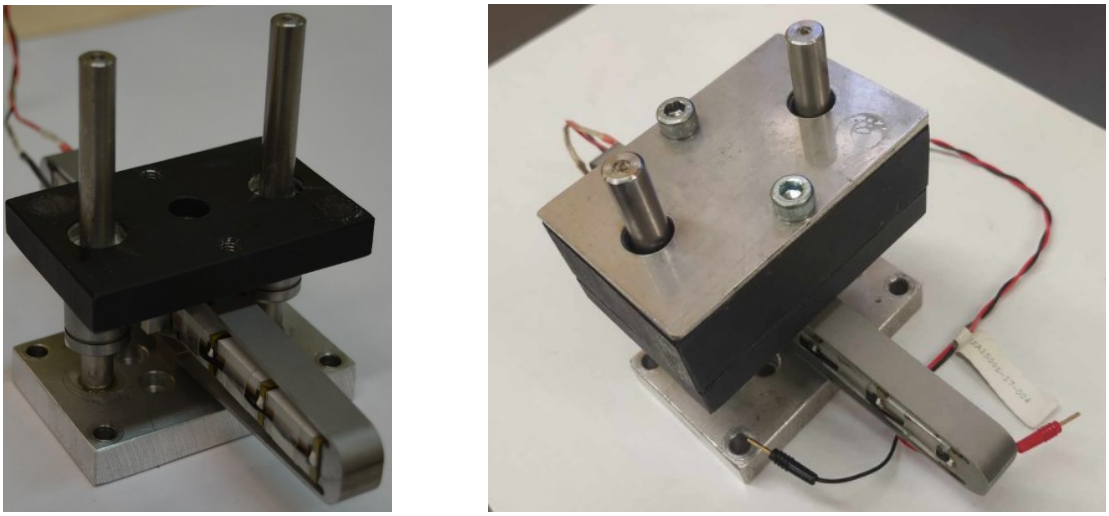
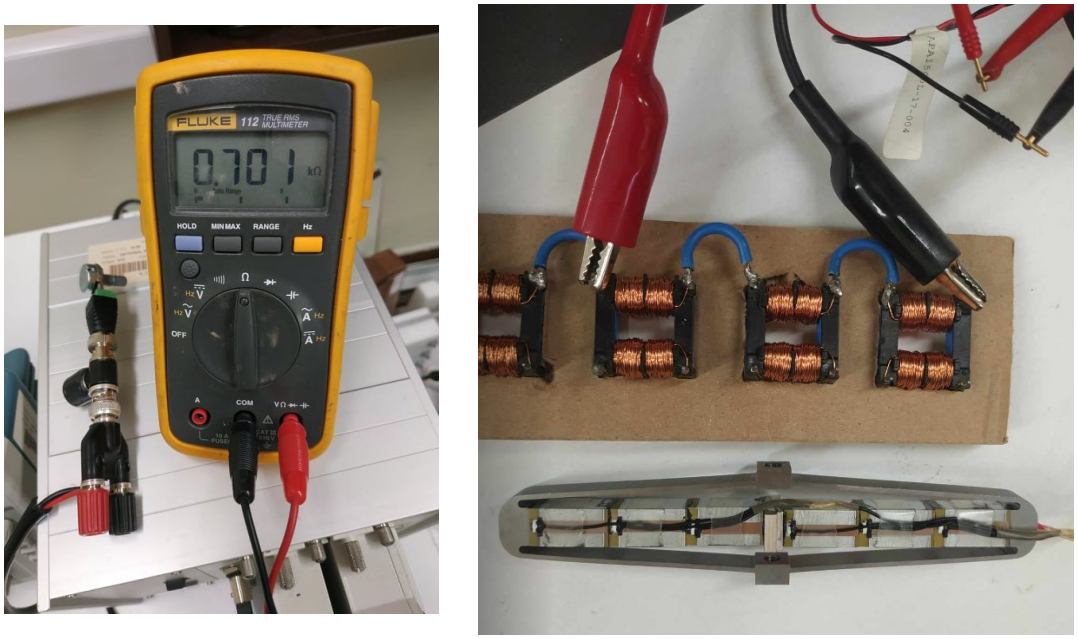


Figure 4.10. Assembly of the SATMD.

4.3.3 Shunt circuit

The terminals of the piezoelectric device are connected to the resistive-inductive (RL) shunt circuit. The alteration of the electric circuit combined impedance is expected to greatly affect the mechanical behavior of the antivibration device, due to the high electromechanical coupling introduced by the specialty piezoelectric device. The resistive impedance is controlled by an easily tunable potentiometer (Figure 4.11a), whereas variable inductive loads are introduced by reconfiguring various sets of coils (Figure 4.11b), each having a predefined inductance. It is pointed out that the coils are not ideal, meaning that they do not introduce pure inductance to the circuit, but they also add a small amount of resistance. To mitigate this imperfection, the resistance of each coil combination was measured using a RLC meter, before included in the analytical model of the shunted piezoelectric SATMD.



(a) *(b)*

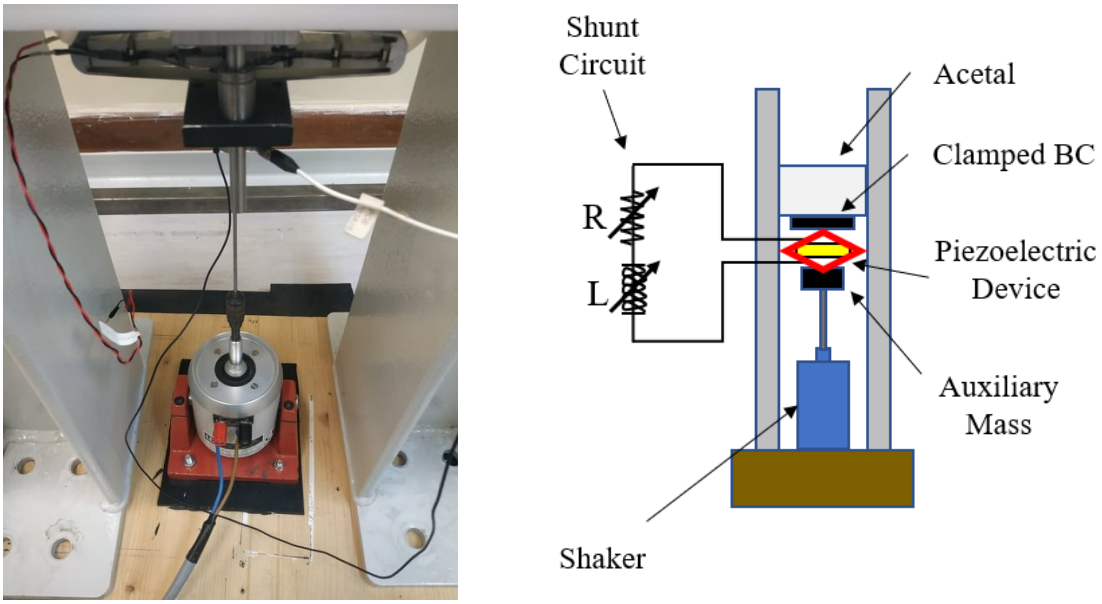
Figure 4.11. Shunt circuit elements. (a) Potentiometer; (b) Coils.

4.4 Experimental Setup for SATMD Characterization

An extensive experimental campaign was carried out, firstly to characterize the equivalent mechanical and electromechanical properties of the SATMD, and secondly to demonstrate and comprehend the shunt circuit impedance effects. Although the selected specialty piezoelectric device APA1500L entails a number of pre-stressed stacks in a mechanical frame and the device functions in the transverse direction to the stacks, the Equations (4.9) and (4.19) are valid, because the stacks are connected mechanically in series and electrically in parallel. Therefore, the Equations of equilibrium (4.27) and respective transfer function (4.28) and (4.30) will be used for comparison to experimental measurements, and the equivalent electromechanical properties $k_d, \overline{e}, C_p$ are sought for the SATMD characterization.

The APA1500L technical data sheet (Appendix A) provides the values for several parameters of the piezoelectric device, in terms of quasistatic performance, dynamic performance, control and driving, and dimensions. This device was also tested by the SMSM group and the author for its characterization and extraction of the useful equivalent parameters. For this reason, an experimental campaign was designed and carried out for the sole SATMD. To achieve clamped boundary condition on the one end of the piezoelectric device, the aluminum base is mounted on an acetal block, which is firmly attached to two vertical bars, as seen in (Figure 4.12a). A small auxiliary mass (main mass component) is excited with white noise via a clamped electromechanical shaker. The Experimental Apparatus used for the vibration testing is described in Chapter 3, and the shaker used was the V201 model. The force input

and auxiliary mass acceleration are measured, in order to obtain the auxiliary mass Frequency Response Functions (FRFs). The piezoelectric device terminals can be directly connected (Short Circuit), unconnected (Open Circuit), or shunted (RL shunt circuit), such that various SATMD configurations can be monitored.



(a) *(b)*

Figure 4.12. Sole SATMD characterization setup. (a) Experimental Setup; (b) Schematic illustration.

The inherent piezoelectric device equivalent capacitance C_p is given as 26 μF, however measured by the lab multimeter at 27 μF. The mechanical (k_d, c_d) and electromechanical ($\bar{e}$) equivalent parameters of this device were extracted by comparison of the experimental results to Equation (4.27). It is stressed, that dielectric and piezoelectric losses of piezoelectric transducers may not always be negligible [146], hence, in this work the mechanical losses of the device and the transducer are represented by the equivalent c_d damping term. First, to calculate the equivalent k_d, c_d parameters in this configuration, the Short Circuit SATMD was excited (piezoelectric device terminals are short circuited). Its frequency response is illustrated with the black dots in Figure 4.13. One eigenfrequency is observed at 86 Hz, which corresponds to the Passive TMD pole. For the computational model (Equation 4.27) in this clamped configuration, the piezoelectric device mass is added to the auxiliary mass. The Short Circuit model entails a minimal resistance of 2 Ohm and zero inductive impedance. The equivalent mechanical parameters, such that the computational Short Circuit curve (black line in Figure 4.13) coincides with the experimental curve, are observed in Table 4.1. Subsequently, the Open Circuit SATMD was excited (piezoelectric device terminals are left open), and its frequency response is illustrated with the blue dots in Figure 4.13. The new eigenfrequency is shifted to 91 Hz. The higher frequency is explained by the

fact that the internal energy of the system is now stored not only as strain energy in the device stiffness, but also as electrical energy in the piezoelectric element. The SATMD device stiffening in Open Circuit conditions is owed to the $\bar{e}^2 / C_p$ term (Equation 4.24). The piezoelectric device equivalent piezoelectric coefficient $\bar{e}$, such that the computational curve (blue line in Figure 4.13) demonstrates great agreement with the experimental curve, is shown in Table 4.1.

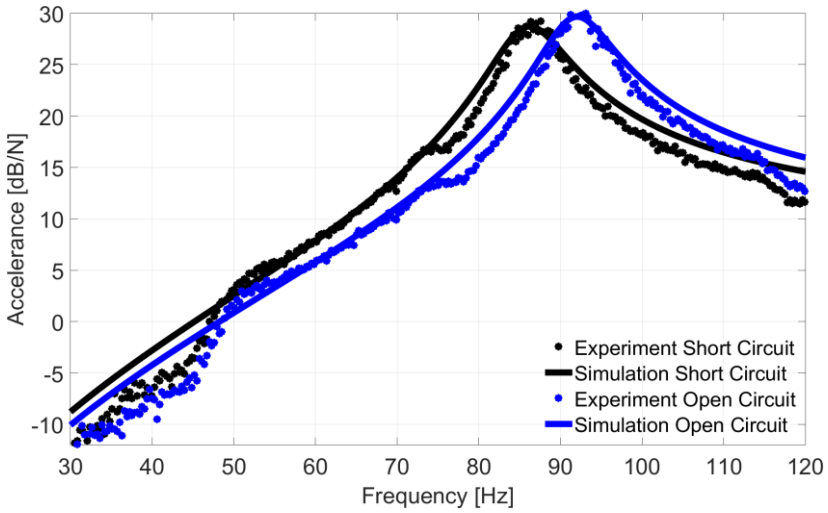


Figure 4.13. Frequency response (acceleration) of mass in the sole SATMD configuration in short (black color) and open circuit (blue color). Analytical results are presented with continuous curves and experimental measurements with full circles.

Table 4.1. SATMD model parameters.

Auxiliary mass	Equivalent total damping	Equivalent lumped stiffness	Equivalent Capacitance	Equivalent Piezoelectric Coefficient
m_d [kg]	c_d [Ns/m]	k_d [kN/m]	C_p [μF]	$\bar{e}$ [N/V]
0.38	45	111	27	0.65

4.5 Shunt Circuit Impedance Effects

Various shunt circuit impedances are experimentally studied to visualize their effect to the SATMD mass and to evaluate the validity of the developed model.

4.5.1 Resistance Effect

The effect of a purely resistive shunting circuit is investigated first. Figure 4.14a, b illustrate the experimental and simulation results, respectively, for various resistance values, demonstrating excellent

agreement and validating the developed model (Equation 4.27). As expected, there is considerable effect of the resistive impedance on the FRF of the system, mostly as added damping, as the frequency response acceleration of the structure varies between the two extreme situations: open circuit (infinite resistance) and short circuit. Starting the interpretation from the short circuit (minimal resistance) configuration, the charge generated in the piezoelectric stack is almost entirely transferred to the shunt system, leaving the piezoelectric capacitor uncharged; thus, there is minimal dissipation and damping. At the same time the strain energy in the piezoelectric device reaches its highest value that minimizes its phenomenal stiffness, as manifested by the lower values in the corresponding frequency peaks. As the shunt resistance increases, some of the electrical energy flowing through the shunt circuit is dissipated into heat, and some charge is stored at the capacitor, which leads to reduced elastic energy in the piezoelectric device. The first effect adds damping to the system, while the second one increases the phenomenal stiffness of the device. At certain levels of resistance, the energy dissipation is maximized. For higher resistance, a low pass filter is created in the shunt circuit, which reduces the flow of energy and dissipation through the resistor. The maximum strain energy in the piezoelectric device is also reduced, leading to phenomenal stiffening, which dominates the system response, resulting in higher amplitudes and frequencies, as the infinite resistance (open circuit situation) is reached. Similar resistant-dependent behavior is expected in the host structure where the SATMD will be mounted.

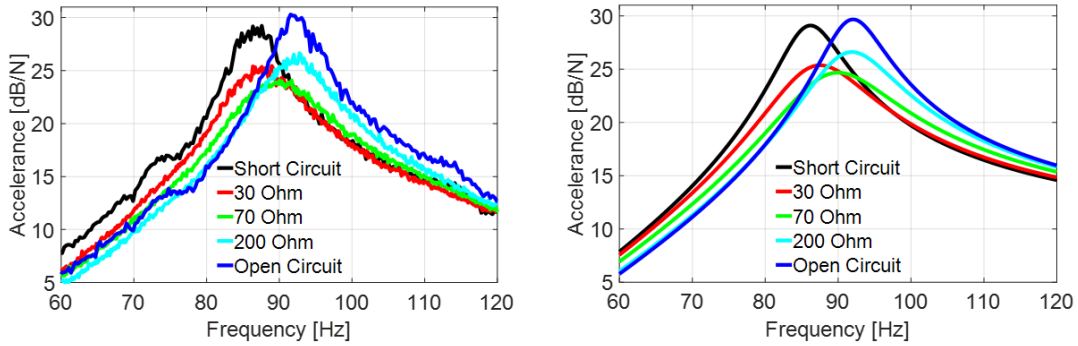


Figure 4.14. Resistance effect in the frequency response (acceleration) of mass of the sole SATMD under various resistive impedances. (a) Experimental results; (b) Simulation results.

4.5.2 Inductance Effect

The scope of this section is to thoroughly study the effect of the undamped electric pole (R=0) introduced by pure inductance. This investigation contributes to the complete understanding of the enhancement of electromechanical coupling and the second pair of poles that is introduced (Equation 4.28). However, ideal coils with zero resistance are non-existent, thus the experimental study with similar inductance values, and resistance, is presented in the next subsection.

The effect of inductive impedance increase under zero resistance and small mechanical damping (c_d = 5 Ns/m) is illustrated in Figure 4.15a, b, where the amplitude of the auxiliary mass acceleration, and the electric charge of the shunt circuit (q_{out}) are presented in the frequency domain. These surface plots can be intuitively understood as the frequency response functions of each DOF that correspond to various inductance values. The frequency peaks in each plot are indicated by the red and yellow colors, whereas the blue areas imply lower magnitudes.

As predicted by the SATMD characteristic equation (Equation 4.28), the inductance adds a second pair of poles into the system, which is manifested as a second modal peak, both in the mechanical (Figure 4.15a) and the electrical (Figure 4.15b) DOFs' response. As seen in both figures for very low impedance values, the higher modal frequency is separated from the structural modal frequency at 86 Hz, yet the electromechanical coupling is not negligible (dark red area at 86 Hz of the electrical DOF Figure 4.15b), which further explains the resistance effect to the structural DOF response, seen in the previous subsection. As inductance rises in both Figures the second, higher mode descends to lower frequency band, while the lower mode also shifts to lower frequencies. In the structural DOF response (Figure 4.15a), this second mode rapidly increases its amplitude (dark red and thicker area), as it approaches the lower mode, whereas the lower mode decreases its amplitude (lighter red and less thick area). On the other hand, in the electrical DOF response (Figure 4.15b), the opposite effect is evident. For higher inductance values, the lower-band mode slowly moves to even lower frequency vicinities, whereas the higher-band mode reaches the Open Circuit frequency (91 Hz). Regarding the mode amplitudes in higher inductive impedance, the initially high amplitude modes have given their place to the initially low amplitude modes, in both structural and electrical responses. Furthermore, an inductance-dependent moving antiresonance is observed in the structural frequency response (dark blue curve in Figure 4.15a), whereas no antiresonance is evident in the electrical frequency response (Figure 4.15b), as predicted by Equations (4.28) and (4.30), respectively. These observations lead to several high importance conclusions, which are expected to also apply for the host structure where the SATMD will be attached:

- Very high coupling and interaction is achieved between the mechanical and the electric circuit dynamics.
- As inductance increases, both electromechanical modes descend to lower frequency bandwidths.
- As inductance increases, the initially purely structural mode (auxiliary mass resonance at 86 Hz) is progressively acquiring a higher electrical component in its mode shape, until it is transformed into a purely electrical mode.
- Conversely, the initially purely electrical mode (shunt circuit resonance at very high frequency) is progressively acquiring a higher structural component in its mode shape, until it is transformed into a purely structural mode.

- Specific impedance values (in this case near 100 mH) produce increased electromechanical coupling near the initial structural eigenfrequency, manifested by dark red colors for this inductance in both electromechanical modes in both Figures, resulting in large conversion of kinetic to electrical energy and vice versa, during the system vibration. This could open the way for high energy dissipation if resistance is added.

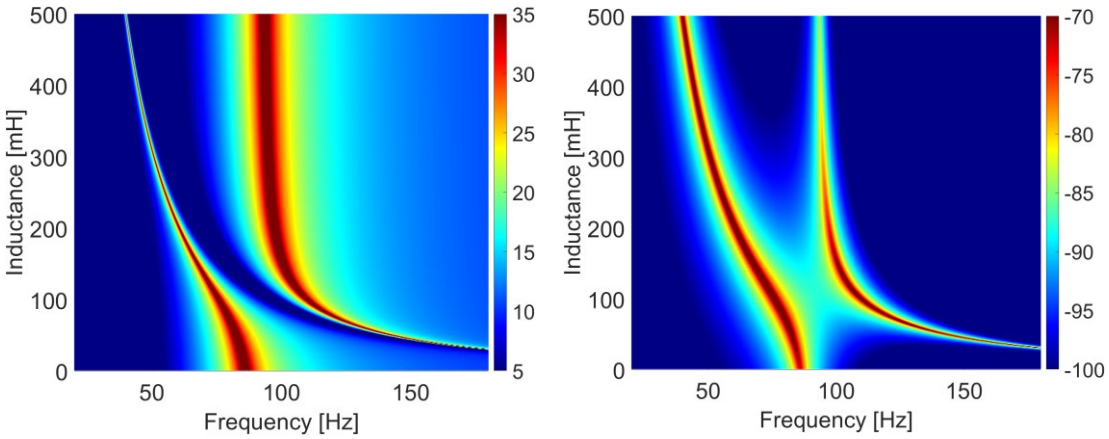


Figure 4.15. Inductance effect in the frequency response of the sole SATMD. (a) Acceleration of mass; (b) Charge in the shunt circuit.

4.5.3 Combined Impedance Effect

The effect of the combined inductance and resistance impedance on the measured and computational dynamic response of the auxiliary mass is demonstrated for specific coil combinations in Figure 4.16a, b, respectively. Great agreement is observed between experimental and simulation results, validating the developed model (Equation 4.27) and yielding results as expected from the purely inductive impedance (previous subsection). A mostly satisfying and promising observation is that, in the studied combined impedance shunt circuits, two electromechanical modes are clearly depicted in the structural response of the SATMD, which previously demonstrated only one structural mode (attributed to the auxiliary mass oscillation in the Short Circuit configuration). This verifies the strong electromechanical coupling. For 110 mH and 11.8 Ohm (blue curve in Figure 4.16), the initially structural mode has descended from 86 Hz to 70 Hz, while the higher electromechanical mode is evident at 110 Hz. Moreover, in this configuration the amplitude of both peaks has been decreased, due to the coils' inherent resistance presence, which dissipates some of the converted electrical energy to heat. In addition, the studied impedance combination (110 mH and 11.8 Ohm) has created a damped antiresonance near 90 Hz. The other studied impedance (400 mH and 8.2 Ohm, illustrated in red color in Figure 4.16) has shifted the initially structural mode to very lower frequency band (near 40 Hz), along with the antiresonance (near 50Hz). The initial electrical mode is evident near the Open Circuit vicinity.

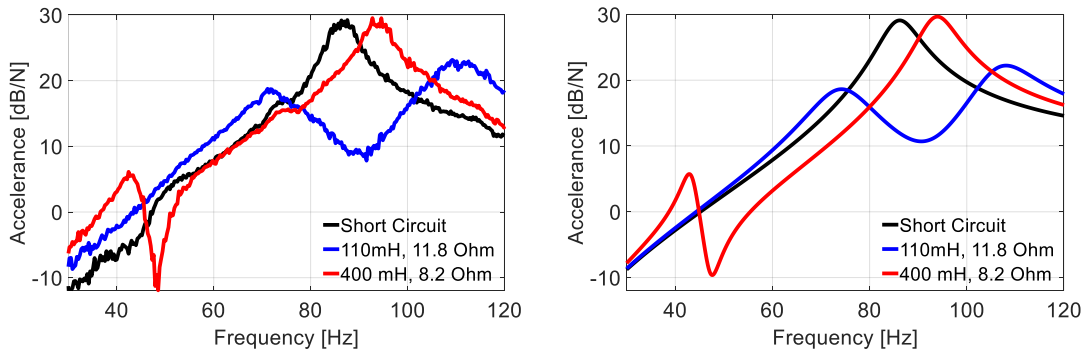


Figure 4.16. Combined resistance-inductance effect in the frequency response (acceleration) of mass of the sole SATMD under various impedances. (a) Experimental results; (b) Simulation results.

4.6 Concluding Remarks

In this Chapter, the SATMD antivibration device was developed and tested. The single-layer piezoelectric constitutive equations are presented and manipulated such that the equivalent mechanical, electrical, and electromechanical properties of multilayer piezoelectric devices are formed. For the piezoelectric SATMD modeling, these equivalent properties are used in a linear lumped model. The equations of equilibrium reveal the development of two pairs of electromechanically coupled poles.

The most important desirable characteristics of the selected piezoelectric device are relatively low equivalent stiffness and high piezoelectric coefficient. To this end, the APA1500L piezoelectric device was selected, which satisfies both requirements. Except for the piezoelectric device, the rest of the SATMD mechanical components were designed and manufactured. The selected technique for the SATMD integration to the host structure ensures rigidity and minimal interaction. The auxiliary mass can be freely selected for the mechanical SATMD tuning and is allowed to oscillate with minimal losses with the use of guides and linear bearings. The shunt circuit connected to the piezoelectric device terminals can be equipped with a potentiometer for variable resistance and various coil configurations for inductance.

To characterize piezoelectric SATMD and demonstrate its behavior, an experimental campaign was carried out. The equivalent mechanical properties were extracted by comparison of the experimental Short Circuit configuration to the predicted results. The capacitance was measured by a multimeter, and the piezoelectric coefficient was found by comparison of the Open Circuit experiment to the respective simulation. It stressed that the electrical and electromechanical properties remain unchanged in any SATMD configuration, however the mechanical properties may experience small changes, depending on the SATMD mounting to the host structures.

The effects of the shunt circuit impedance were compared to computational results, demonstrating great agreement. Purely resistive impedance adds damping to the SATMD structural mode, dissipating the

converted electrical energy to dissipated heat. Inductive impedance loads highly amplifies the SATMD electromechanical coupling and shifts both electromechanical modes to lower frequency vicinities. These effects are expected to appear in a similar manner to the host structures, where the SATMD will be applied. More importantly, these shunt circuit changes can be seamlessly applied during the host structure operational times. As a result, the SATMD device can be semi-actively tuned to maintain beneficial or even optimal antivibration performance, in the case of potential alterations in the host structure dynamic characteristics or excitation frequency. This retuning capability is responsible for title of this device: the Semi-Active Tuned Mass Damper.

Chapter 5: Modeling and Performance of SATMD on a Lumped Mass Host Structure

The SATMD vibration reduction performance is first evaluated on a simplified structure. This structure exhibits only one DOF, such that it allows the in-depth investigation of the complex electromechanical system effects and tuning mechanisms. The equations of equilibrium for the SATMD – lumped mass structure system are formulated, and the respective transfer functions are calculated and analyzed. The computational results are compared to the experimental measurements of the SATMD on a designed lumped mass structure experimental setup. The passive TMD performance of the antivibration device is demonstrated, before diving into the shunt circuit impedance effects to the host structure. The structure lumped mass and auxiliary mass have comparable values, such that the SATMD effects are magnified.

5.1 SATMD – Lumped Mass Structure System Model

The conventional TMD on a lumped mass structure is first examined. Then, the electromechanical equilibrium is developed for the shunted piezoelectric SATMD with equivalent properties.

5.1.1 Conventional TMD

Considering a simplified lumped mass structure with only one DOF, where a conventional purely mechanical TMD is attached, as illustrated in Figure 5.1.

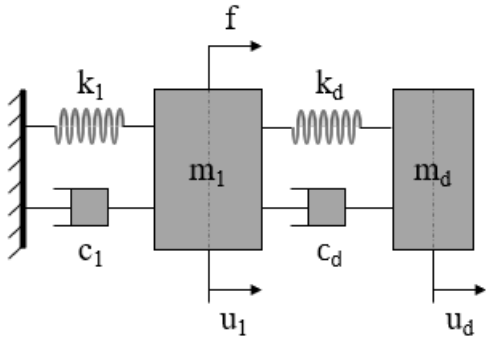


Figure 5.1. Conventional TMD on lumped mass structure.

The dynamic equilibrium equations of the system have the form:

$$\begin{bmatrix} m_1 & 0 \\ 0 & m_d \end{bmatrix}\begin{Bmatrix} \ddot{u}_1 \\ \ddot{u}_d \end{Bmatrix}+\begin{bmatrix} c_1+c_d & -c_d \\ -c_d & c_d \end{bmatrix}\begin{Bmatrix} \dot{u}_1 \\ \dot{u}_d \end{Bmatrix}+\begin{bmatrix} k_1+k_d & -k_d \\ -k_d & k_d \end{bmatrix}\begin{Bmatrix} u_1 \\ u_d \end{Bmatrix}=\begin{Bmatrix} f \\ 0 \end{Bmatrix} \tag{5.1}$$

where $u,\dot{u},\ddot{u}$ represent the displacement, velocity, and acceleration responses under the excitation force f that acts on the main structure, in time domain. Subscript *1* indicates the structural system of interest, whereas subscript *d* represents the TMD.

5.1.2 Piezoelectric SATMD

First, the electromechanical equilibrium is achieved for the piezoelectric SATMD on lumped mass structure. Then, the system transfer functions are calculated, such that the dynamic behavior of each component of the system is predicted.

5.1.2.1 Equations of motion

In the piezoelectric SATMD configuration, the connecting spring-damper element of the conventional TMD is replaced by a shunted piezoelectric device, as shown in Figure 5.2a.

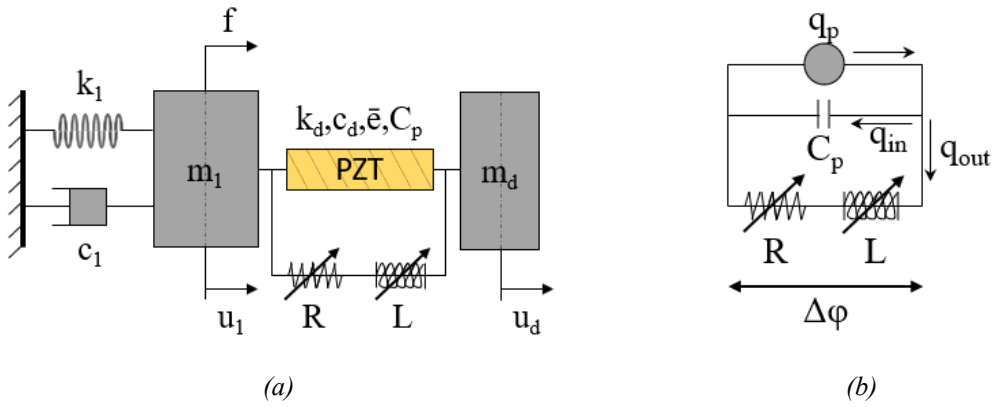


Figure 5.2. SATMD on lumped mass structure. (a) Schematic illustration; (b) Shunt circuit.

In this configuration, Equation (4.9) is transformed and the internal force f_p is related to its deformation and the applied electric potential difference $\Delta\varphi$ at its edges as:

$$\begin{Bmatrix} f_p \\ -f_p \end{Bmatrix}=\begin{bmatrix} k_d & -k_d \\ -k_d & k_d \end{bmatrix}\begin{Bmatrix} u_1 \\ u_d \end{Bmatrix}+\begin{Bmatrix} -\bar{e} \\ \bar{e} \end{Bmatrix}\Delta\varphi \tag{5.2}$$

Importing Equation (5.2) to Equation (5.1), the equations of motion of the combined electromechanical system can be expressed as:

$$\begin{bmatrix} m_1 & 0 \\ 0 & m_d \end{bmatrix}\begin{Bmatrix} \ddot{u}_1 \\ \ddot{u}_d \end{Bmatrix}+\begin{bmatrix} c_1+c_d & -c_d \\ -c_d & c_d \end{bmatrix}\begin{Bmatrix} \dot{u}_1 \\ \dot{u}_d \end{Bmatrix}+\begin{bmatrix} k_1+k_d & -k_d \\ -k_d & k_d \end{bmatrix}\begin{Bmatrix} u_1 \\ u_d \end{Bmatrix}+\begin{bmatrix} -\bar{e} \\ \bar{e} \end{bmatrix}\Delta\varphi=\begin{Bmatrix} f \\ 0 \end{Bmatrix} \tag{5.3}$$

Furthermore, an electric charge q_p is generated by the relative movement of the host structure and the auxiliary mass, due to the direct piezoelectric effect. When a shunt circuit is connected to the piezoelectric transducer terminals, employing variable resistive and inductive impedance, Equation 4.19 is transformed to:

$$q_p=\bar{e}(u_d-u_1)=q_{in}+q_{out} \tag{5.4}$$

(as shown in Figure 5.2b) and regarding the potential difference, Equation (4.25) is transformed to:

$$\Delta\varphi=\frac{q_{in}}{C_p}=R\dot{q}_{out}+L\ddot{q}_{out} \tag{5.5}$$

Combining the last two Equations, the final expression of the charge equilibrium in the shunt circuit becomes:

$$\bar{e}(u_1-u_d)+C_pL\ddot{q}_{out}+C_pR\dot{q}_{out}+q_{out}=0 \tag{5.6}$$

Expressing the potential difference in terms of inductance and resistance (Equation 5.5), and combining Equations (5.3) and (5.6), the dynamic equations of the SATMD – lumped mass system can be presented as:

$$\begin{bmatrix} m_1 & 0 & \bar{e}L \\ 0 & m_d & -\bar{e}L \\ 0 & 0 & L \end{bmatrix}\begin{Bmatrix} \ddot{u}_1 \\ \ddot{u}_d \\ \ddot{q}_{out} \end{Bmatrix}+\begin{bmatrix} c_1+c_d & -c_d & \bar{e}R \\ -c_d & c_d & -\bar{e}R \\ 0 & 0 & R \end{bmatrix}\begin{Bmatrix} \dot{u}_1 \\ \dot{u}_d \\ \dot{q}_{out} \end{Bmatrix}+\begin{bmatrix} k_1+k_d & -k_d & 0 \\ -k_d & k_d & 0 \\ \frac{\bar{e}}{C_p} & -\frac{\bar{e}}{C_p} & \frac{1}{C_p} \end{bmatrix}\begin{Bmatrix} u_1 \\ u_d \\ q_{out} \end{Bmatrix}=\begin{Bmatrix} f \\ 0 \\ 0 \end{Bmatrix} \tag{5.7}$$

where q_{out} provides the third, electrical DOF, necessary to fully describe the electromechanically coupled system. On the other hand, from Equations (5.4) and (5.5), expressing the potential difference as:

$$\Delta\varphi=\frac{\bar{e}(u_d-u_1)-q_{out}}{C_p} \tag{5.8}$$

and combining Equations (5.3) and (5.6), the dynamic equations of the SATMD – lumped mass system can be presented as:

$$\begin{bmatrix} m_1 & 0 & 0 \\ 0 & m_d & 0 \\ 0 & 0 & L \end{bmatrix}\begin{Bmatrix} \ddot{u}_1 \\ \ddot{u}_d \\ \ddot{q}_{out} \end{Bmatrix}+\begin{bmatrix} c_1+c_d & -c_d & 0 \\ -c_d & c_d & 0 \\ 0 & 0 & R \end{bmatrix}\begin{Bmatrix} \dot{u}_1 \\ \dot{u}_d \\ \dot{q}_{out} \end{Bmatrix}+\begin{bmatrix} k_1+k_d+\frac{\bar{e}^2}{C_p} & -k_d-\frac{\bar{e}^2}{C_p} & \frac{\bar{e}}{C_p} \\ -k_d-\frac{\bar{e}^2}{C_p} & k_d+\frac{\bar{e}^2}{C_p} & -\frac{\bar{e}}{C_p} \\ \frac{\bar{e}}{C_p} & -\frac{\bar{e}}{C_p} & \frac{1}{C_p} \end{bmatrix}\begin{Bmatrix} u_1 \\ u_d \\ q_{out} \end{Bmatrix}=\begin{Bmatrix} f \\ 0 \\ 0 \end{Bmatrix} \tag{5.9}$$

Both Equations (5.7) and (5.9) describe the same phenomenon and yield the same results. The structure of the latter Equation (5.9) is preferred and will be used in more complex systems, due to its symmetric matrices and the presence of the $\bar{e}^2 / C_p$ term, which implies the stiffness variation of the device due to the piezoelectric material. Moreover, considering the state space variables:

$$z_1 = u_1, z_2 = u_d, z_3 = q_{out}, z_4 = \dot{u}_1, z_5 = \dot{u}_d, z_6 = \dot{q}_{out} \tag{5.10}$$

and remembering Equation (4.26), Equation (5.9) can be transformed to state space as:

$$\{\dot{z}\} = [A_L]\{z\} + [B_L] f \tag{5.11}$$

where:

$$\{\dot{z}\} = \begin{Bmatrix} \dot{z}_1 \\ \dot{z}_2 \\ \dot{z}_3 \\ \dot{z}_4 \\ \dot{z}_5 \\ \dot{z}_6 \end{Bmatrix}, \{z\} = \begin{Bmatrix} z_1 \\ z_2 \\ z_3 \\ z_4 \\ z_5 \\ z_6 \end{Bmatrix}, [B_L] = \begin{bmatrix} 0 \\ 0 \\ 0 \\ 1/m_1 \\ 0 \\ 0 \end{bmatrix} \tag{5.12}$$

and

$$[A_L] = \begin{bmatrix} 0 & 0 & 0 & 1 & 0 & 0 \\ 0 & 0 & 0 & 0 & 1 & 0 \\ 0 & 0 & 0 & 0 & 0 & 1 \\ -\dfrac{k_1 + k_p}{m_1} & \dfrac{k_p}{m_1} & -\dfrac{\bar{e}}{m_1 C_p} & -\dfrac{c_1 + c_d}{m_1} & \dfrac{c_d}{m_1} & 0 \\ \dfrac{k_p}{m_d} & -\dfrac{k_p}{m_d} & \dfrac{\bar{e}}{m_d C_p} & \dfrac{c_d}{m_d} & -\dfrac{c_d}{m_d} & 0 \\ -\dfrac{\bar{e}}{L C_p} & \dfrac{\bar{e}}{L C_p} & -\dfrac{1}{L C_p} & 0 & 0 & -\dfrac{R}{C_p} \end{bmatrix} \tag{5.13}$$

In the special case of only resistive shunt impedance $(L = 0)$, the state space system is reduced to:

$$\{\dot{z}\} = [A_R]\{z\} + [B_R] f \tag{5.14}$$

where:

$$\{\dot{z}\} = \begin{Bmatrix} \dot{z}_1 \\ \dot{z}_2 \\ \dot{z}_3 \\ \dot{z}_4 \\ \dot{z}_5 \end{Bmatrix}, \{z\} = \begin{Bmatrix} z_1 \\ z_2 \\ z_3 \\ z_4 \\ z_5 \end{Bmatrix}, [B_R] = \begin{bmatrix} 0 \\ 0 \\ 0 \\ 1/m_1 \\ 0 \end{bmatrix} \tag{5.15}$$

and

$$[A_R]=\begin{bmatrix} 0 & 0 & 0 & 1 & 0 \\ 0 & 0 & 0 & 0 & 1 \\ -\frac{\bar{e}}{RC_p} & \frac{\bar{e}}{RC_p} & -\frac{1}{RC_p} & 0 & 0 \\ -\frac{k_1+k_p}{m_1} & \frac{k_p}{m_1} & -\frac{\bar{e}}{m_1 C_p} & \frac{c_1+c_d}{m_1} & \frac{c_d}{m_1} \\ \frac{k_p}{m_d} & -\frac{k_p}{m_d} & \frac{\bar{e}}{m_d C_p} & \frac{c_d}{m_d} & -\frac{c_d}{m_d} \end{bmatrix} \tag{5.16}$$

5.1.2.2 Transfer Functions

Transposing Equation (5.9) to frequency domain and ignoring the damping factors for simplicity, the transfer function of the host structure DOF, per force input to the host structure can be obtained:

$$H_{11}=\frac{U_1}{F}=\frac{Lm_d C_p{}^2\omega^4-(Lk_p C_p{}^2+m_d C_p)\omega^2+k_p C_p-\bar{e}^2}{-[C_p{}^2 Lm_1 m_d\omega^6-(C_p m_1 m_d+C_p{}^2 Lk_1 m_d+C_p{}^2 Lk_p m_1+C_p{}^2 Lk_p m_d)\omega^4\ldots} \tag{5.17}$$
$$\overline{-(\bar{e}^2 m_1+\bar{e}^2 m_d-C_p k_1 m_d-C_p k_p m_1-C_p k_p m_d-C_p{}^2 Lk_1 k_p)\omega^2+\bar{e}^2 k_1-C_p k_1 k_p]}$$

The characteristic equation of this configuration exhibits 3rd order variables for inductive shunt impedance $(L>0)$, predicting three pairs of conjugate poles. One of them is attributed to the 1-DOF host structure, while the other two are attributed to the two inertia features of the SATMD, namely the auxiliary mass and inductance. The variable inductance is expected to highly affect the poles. In addition, comparing Equation (4.28) to Equation (5.17), it can be observed that the poles of the first coincide with the zeros of the latter. This major observation signifies several highly important antivibration conclusions:

- The SATMD introduces two highly tunable inductance-dependent antiresonances to the host structure.
- The host structure antiresonance frequency vicinities can be predicted by the sole SATMD poles.
- The host structure antiresonance frequency vicinities are independent of the host structure dynamic characteristics, and as a result only the frequency response of the targeted host structure is adequate for the accurate design of the SATMD, which can achieve close-to-optimal antivibration performance.

Next, the transfer function of the auxiliary mass DOF is obtained, per force input to the host structure:

$$H_{21}=\frac{U_d}{F}=\frac{-(Lk_pC_p{}^2\omega^2-k_pC_p+\bar{e}^2)}{-[C_p{}^2Lm_lm_d\omega^6-(C_pm_lm_d+C_p{}^2Lk_lm_d+C_p{}^2Lk_pm_l+C_p{}^2Lk_pm_d)\omega^4\ldots} \tag{5.18}$$

$$\overline{-(\bar{e}^2m_l+\bar{e}^2m_d-C_pk_lm_d-C_pk_pm_l-C_pk_pm_d-C_p{}^2Lk_lk_p)\omega^2+\bar{e}^2k_l-C_pk_lk_p]}$$

One conjugate pair of zeros is created, whose natural frequency is:

$$z_{21}=\sqrt{\frac{\bar{e}^2-k_pC_p}{Lk_pC_p{}^2}} \tag{5.19}$$

Therefore, an inductance-dependent antiresonance is expected on the auxiliary mass frequency response.

Finally, the transfer function of the shunt circuit DOF, per force input to the host structure is:

$$H_{31}=\frac{Q_{out}}{F}=\frac{-(C_p\bar{e}m_d\omega^2)}{-[C_p{}^2Lm_lm_d\omega^6-(C_pm_lm_d+C_p{}^2Lk_lm_d+C_p{}^2Lk_pm_l+C_p{}^2Lk_pm_d)\omega^4\ldots} \tag{5.20}$$

$$\overline{-(\bar{e}^2m_l+\bar{e}^2m_d-C_pk_lm_d-C_pk_pm_l-C_pk_pm_d-C_p{}^2Lk_lk_p)\omega^2+\bar{e}^2k_l-C_pk_lk_p]}$$

Thus, no antiresonance is expected in the shunt circuit frequency response.

5.2 Experimental Setup of Lumped Mass Host Structure

The experimental setup is illustrated in Figure 5.3. The 1-DOF host structure consists of a solid mass firmly attached at the center of a Carbon Fiber Reinforced Polymer (CFRP) double cantilever beam, permitting only vertical movement (1-DOF).

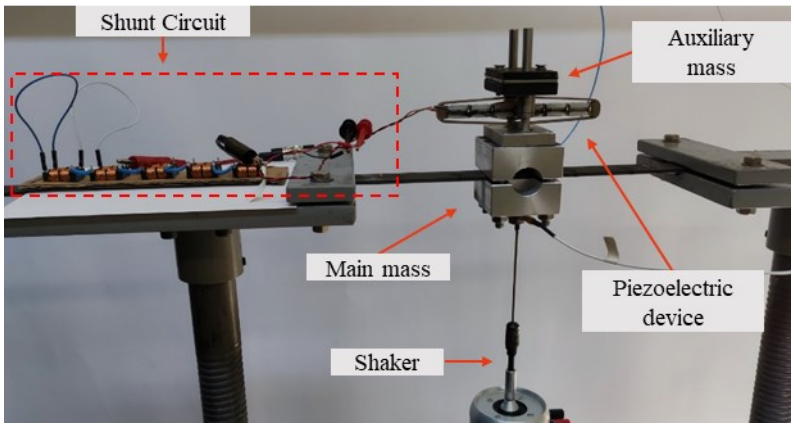


Figure 5.3. Experimental setup for the SATMD on a simplified host structure.

The Experimental Apparatus used for the vibration testing is described in Chapter 3. The force excitation is induced directly through the main mass via the V201 model shaker, which applies a white

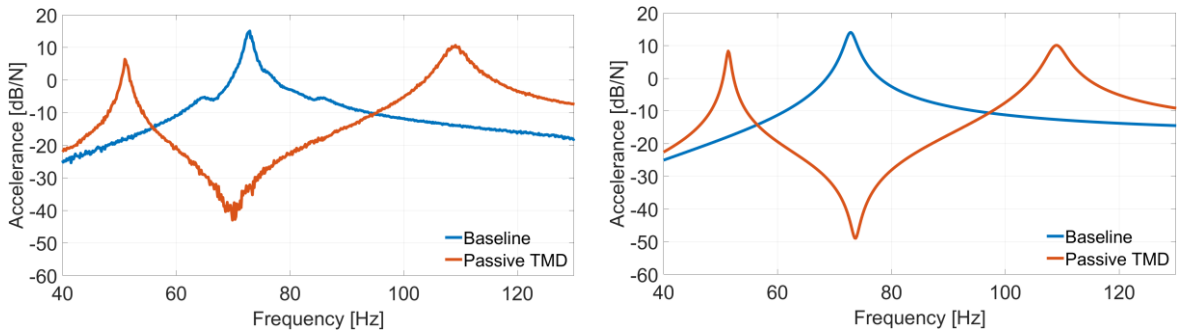
noise excitation to the structure, in order to obtain its acceleration Frequency Response Functions (FRFs), using an accelerometer. For the electromechanically shunted SATMD, the APA1500L piezoelectric device is attached between the main and the absorber mass, whose terminals are shunted to a circuit with electrical impedance. Resistive and inductive impedance is controlled by the same means, as mentioned in Section 4.3.3. The rest of the used setup is as described in the Experimental Apparatus (Section 3).

5.3 Baseline Performance with Passive TMD

A sufficient computational representation of the dynamic system was accomplished, considering the host structure as a lumped mass m_1 with 1-DOF, mounted on a spring damper element (k_1, c_1) Figure 5.2a. Knowing the lumped mass m_1 , the host structure lumped stiffness k_1 and damping c_1 were calibrated by comparison to experimental results (blue color in Figure 5.4) and are shown in Table 5.1.

Table 5.1. Model parameters and characteristics.

Lumped Mass		**Equivalent total Damping**		**Equivalent mechanical Stiffness**	
m_1[kg]	m_d[kg]	c_1[Ns/m]	c_d[Ns/m]	k_1[kN/m]	k_d[kN/m]
0.85	0.518	10	4	178	111



(a) *(b)*

Figure 5.4. Frequency response of the host structure (main mass) without (Baseline) and with the passive TMD. (a) Experimental results; (b) Simulation results.

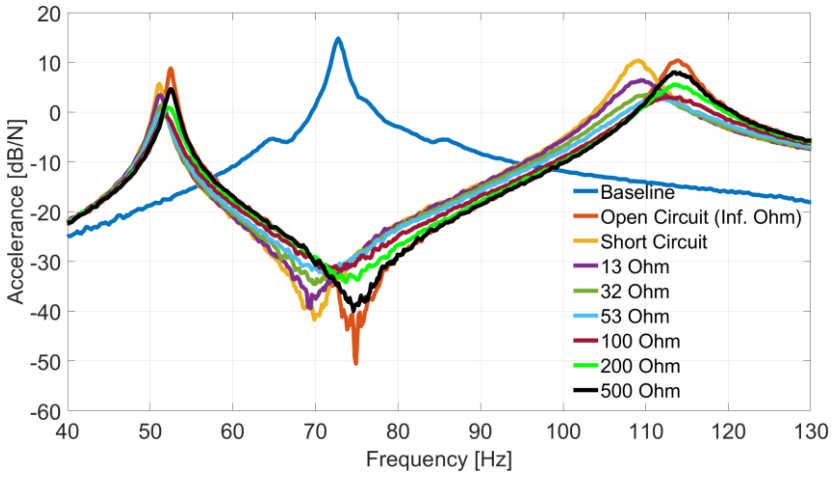
A strong resonance is observed at approximately 73Hz, which is the eigenfrequency of this 1-DOF baseline structure. For the piezoelectric SATMD, knowing the device equivalent lumped stiffness k_d from the sole SATMD experimental campaign (Section 4.4), the absorber mass m_d was selected in order to eliminate the baseline resonance under the short circuit (Passive TMD) condition by Equation (4.31). The modelled SATMD lumped equivalent damping c_d in this configuration is calibrated by comparison of the main mass frequency response in short circuit conditions (Figure 5.4). The

attachment of the mechanical TMD highly attenuates the amplitude of vibration in the band vicinity of the baseline eigenfrequency, proving the great vibration suppression capabilities of the passive damper for a single mode (Equation 5.1). However, the TMD also introduces two new frequency peaks, away from the baseline resonance, corresponding to: structural Mode I for the lowest eigenfrequency (approximately 53Hz) and structural Mode II for the higher one (approximately 110Hz). The shunt resistance and inductance of the SATMD will be used to attenuate the amplitude of these two new frequency peaks to achieve broadband vibration control.

5.4 Resistance Effect

The effect of a purely resistive shunting circuit is investigated first. Figure 5.5a and b illustrate the experimental and simulation (Equation 5.9) results, respectively, for resistance values that extend between 3 Ohm and 500 Ohm. Excellent agreement is observed. As expected, there is considerable effect of the resistive impedance on the FRF of the system, mostly as added damping, as the frequency response acceleration of the structure varies between the two extreme situations: open circuit (infinite resistance) and short circuit (close-to-zero resistance).

(a)



(b)

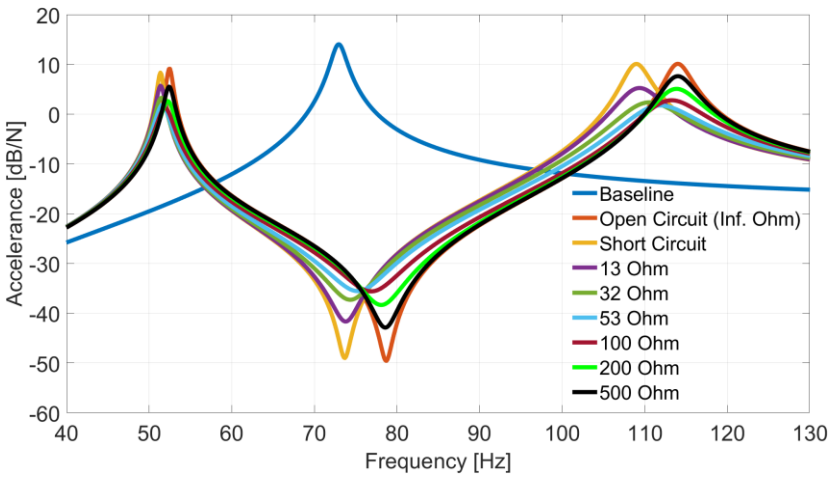


Figure 5.5. Resistance effect on host structure: (a) Experimental results; (b) Simulation results.

Similarly to the sole SATMD configuration (Subsection 4.5.1), the short circuit charge generated in the piezoelectric stack is almost entirely transferred to the shunt system, leaving the piezoelectric capacitor uncharged; thus, there is no dissipation and damping. At the same time the strain energy in the piezoelectric device reaches its highest value that minimizes its phenomenal stiffness, as manifested by the lower values in the corresponding frequency peaks (yellow color curves in Figure 5.5). As the shunt resistance increases, some of the electrical energy flowing through the shunt circuit is dissipated into heat, and some charge is stored at the capacitor, which leads to reduced elastic energy in the piezoelectric device. The first effect adds damping to the system manifested in the two structural Modes and the antiresonance, while the second effect increases the phenomenal stiffness of the device, progressively shifting the respective curves to higher frequency vicinity. At certain and different levels of resistance for each structural Mode, the energy dissipation is maximized, and the Modes exhibit their highest damping. For higher resistance, a low pass filter is created in the shunt circuit, which reduces the flow of energy and dissipation through the resistor. The maximum strain energy in the piezoelectric device is also reduced, leading to phenomenal stiffening, which dominates the system response, resulting in higher amplitudes and frequencies, as the infinite resistance (open circuit situation visualized in the orange curves of Figure 5.5) is reached.

As experimentally and analytically illustrated, comparing the passive TMD (short circuit) response with the resistive cases of the SATMD, the highest vibration suppression in the vicinity of structural Mode I is captured for 100 Ohm (dark red curve), whereas the attenuation of structural Mode II occurs for 53 Ohm (light blue curve). The values of these modal peak amplitude reductions are depicted in dB in the summary Table 5.2. The level of the most effective vibration control resistance is different for each mode, however a resistive impedance area with multi-modal suppression capabilities is existent. In order to attain further insight regarding the optimal resistance for each mode, the poles of state space system A_R matrix (Equations 5.14-5.16) are plotted in the complex plane. (Figure 5.6), for increasing values of resistance. For each structural mode, only the positive conjugate poles p_1 and p_2 are illustrated, in blue and green color, respectively. The variation of the pole position follows the observed trends in Figure 5.6, where symbol "o" represents the poles at the starting short circuit position ($R \rightarrow 0$), while "x" the poles in the final position ($R \rightarrow \infty$). As the resistance increases, the real part of each pole and respective modal damping increases up to a maximum value, and then it gradually decreases again. The maximum damping of each structural Mode I and II, occurs at 98 and 52 Ohm, respectively. On the other hand, the imaginary part of the poles increases monotonically with resistance, indicating the increase in the modal frequency due to stiffening of the piezoelectric stack. The real pole p_3, denoted with red, represents the inverse of the time constant of the electric circuit and is equal to the cut-off frequency of the circuit. As resistive impedance increases, the cut-off frequency of the electric circuit

decreases. When it reaches the modal frequency of structural Mode II, the respective modal damping reaches its maximum value, i.e.

$$\left|Re(p_2)\right| = max, \;\; if \;\; p_3 = Im(p_2) \tag{5.21}$$

This point corresponds to R=52 Ohm, and the respective pole locations in Figure 5.6 are shown with symbol "*" in the root loci. Similarly, when resistance value reaches 98 Ohm, the respective cut-off frequency of the electric circuit reaches the modal frequency of Mode I, and the respective modal damping is maximized, as illustrated with symbol "+". For resistance between the previous values, simultaneous vibration suppression is obtained for both modes.

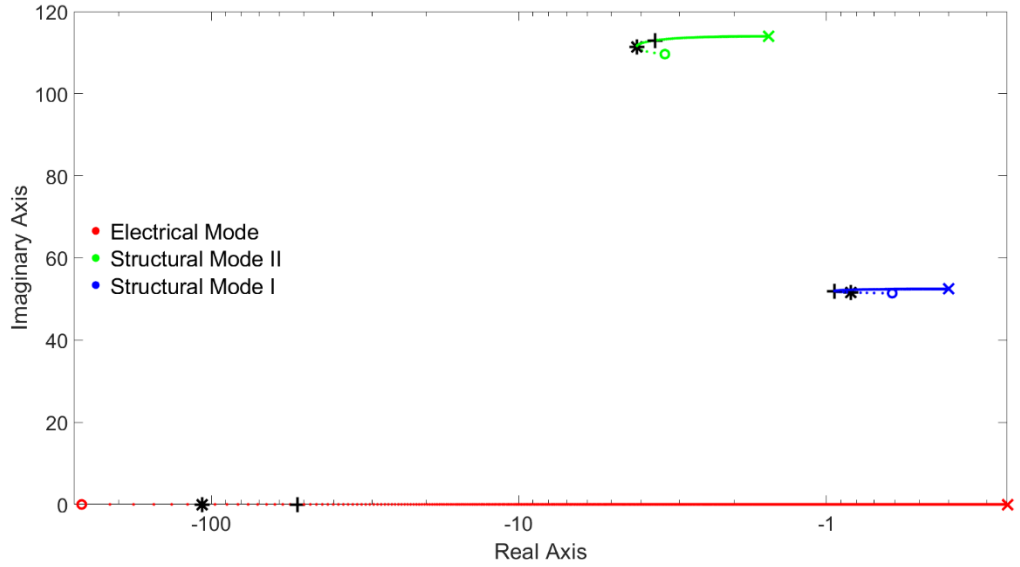
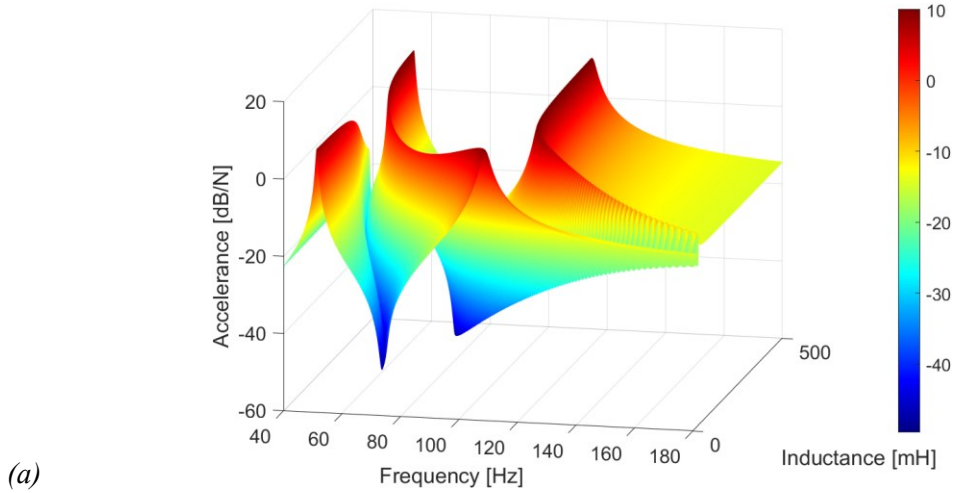


Figure 5.6. Root Loci for increasing resistance. Symbols "+" and "" indicate the pole locations of maximum modal damping for structural mode I and II, respectively.*

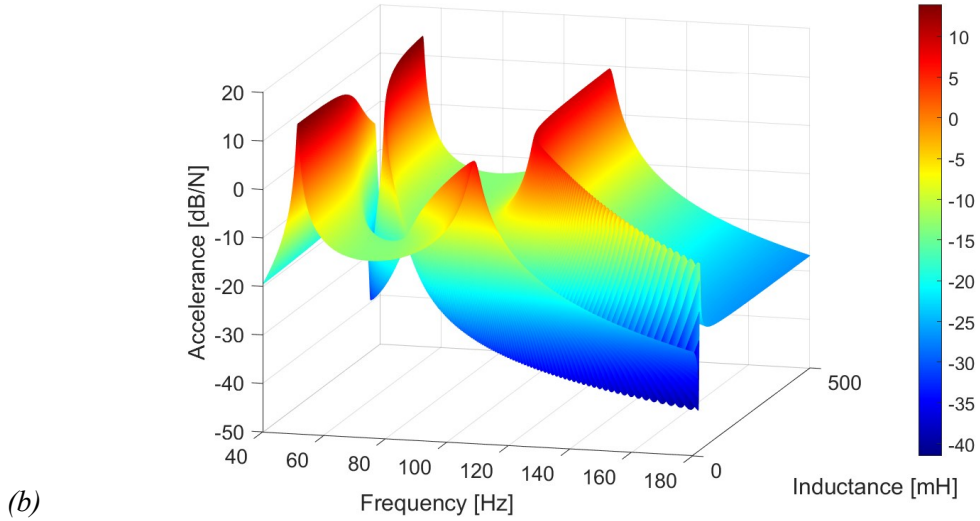
5.5 Inductance Effect

The effect of inductive impedance increase under negligible resistance (R=1 Ohm) is illustrated in Figure 5.7, where the amplitude of the main and auxiliary mass accelerations, and the electric charge q_{out} are presented in the frequency domain. The 3D plots can be intuitively understood as the frequency response functions of each DOF that correspond to various impedance values. As seen in the characteristic equation of Equation (5.17), the inductive impedance adds a third complex conjugate pair of poles into the system, corresponding to a mostly electrical mode, which are manifested as a third modal peak in Figure 5.7, and has a great effect on the dynamics of the electromechanical TMD. As seen in Figure 5.7 for very low impedance values, the electric modal frequency is separated from the structural modal frequencies, hence there is relatively small coupling and interaction between the mechanical and the electric circuit dynamics. As inductance rises, the third, electrical mode descends to lower frequency band, and as it approaches the higher mechanical mode (Figure 5.7c), its amplitude

is increasing rapidly, as shown for the cases of 35 mH and 50 mH in Figure 5.7d. The respective modal peak appears in the response of the auxiliary and main mass (Figure 5.7a, b), demonstrating that the electrical pole progressively acquires higher mechanical component in its eigenvector. The latter indicate progressively increasing strong electromechanical coupling in the whole system, and large conversion of kinetic to electrical energy. As the inductive impedance approaches 100mH, the two frequencies approach each other, and acquire very high amplitude. Further inductance increase leads to the separation of the two peaks, the structural peak vastly raises its amplitude, whereas the electrical peak reduces it. These denote that the electrical pole has passed through the second mode and has progressively decoupled from it. As the inductance increases further, the electrical mode tends to reach the first structural mode. Similarly to the previous case, as the inductance increases from 100mH to 300mH, the electrical and first structural modes become highly coupled, while further inductance increase, leads to opposite amplitude movement in the 3D plots, indicating the new electrical pole pass-through and subsequent decoupling.



(a)



(b)

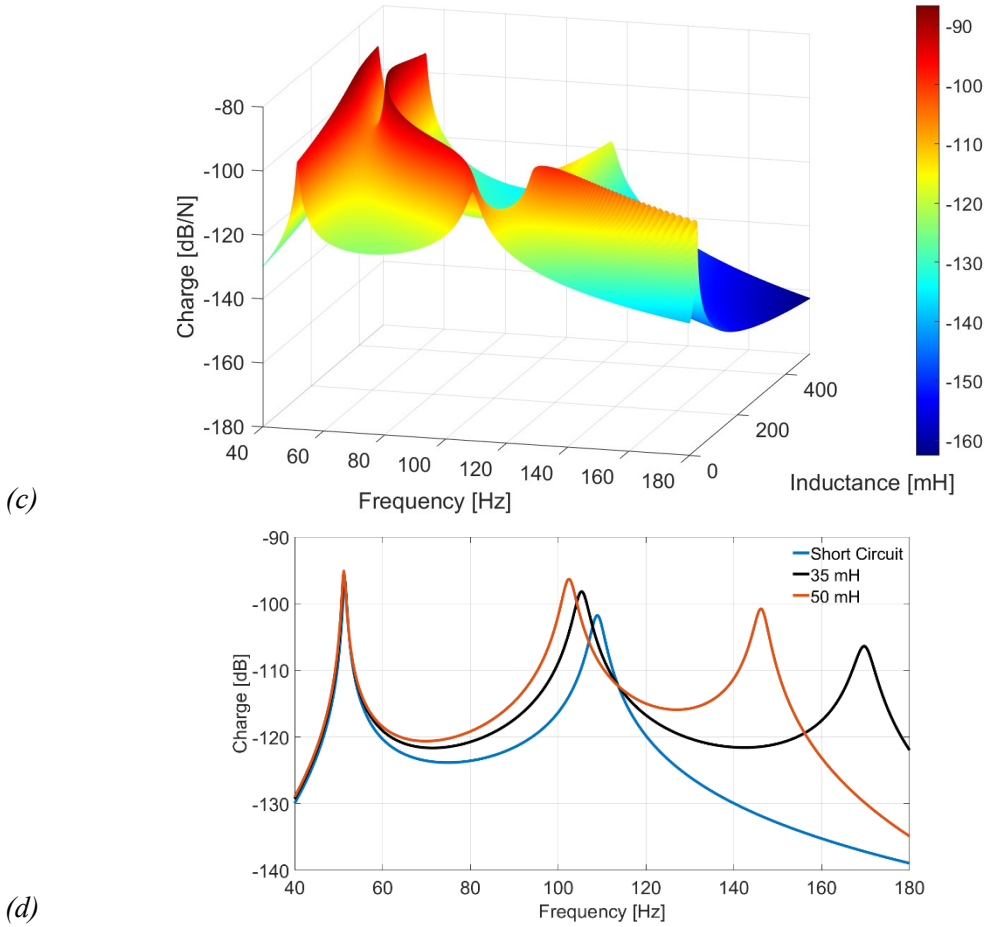


Figure 5.7. Inductance effect on frequency response functions. (a) Main mass acceleration; (b) Auxiliary mass acceleration; (c) Shunt circuit charge; (d) Shunt circuit charge cases: short circuit, 35mH and 50mH.

It is important to stress out the high coupling between the electrical and mechanical modes for specific inductance ranges. The high electromechanical coupling has two important mechanisms for controlling the main-mass vibration. First, it effectively introduces a second resonant oscillator in the system, also introducing a second anti-resonance in the structural mass, which is highly tunable via inductance. Most importantly, the inductance increases the electromechanical coupling, resulting in large conversion of kinetic to electrical energy and vice versa, during the system vibration. The latter opens the way for high energy dissipation, as outlined in the next subsection.

Observing the acceleration response of the main mass from the view presented in Figure 5.8, the system modes shifting with increasing inductance becomes more clear. This figure also depicts, in the black dashed curves, the sole SATMD poles and their frequency shifting (Equation 4.28), for the studied mass (m_d =0.518 kg) and for increasing inductance values. As shown in Figure 5.8, for all inductance values, the two poles of the sole SATMD coincide with the two induced anti-resonances to the host structure. This highlights the independence of the inductance tuning of the SATMD from the host structure and validates the observation that the poles of the Equation (4.28) coincide with the zeros of Equation (5.17). As a result, the inductance needed to tune the antivibration device to specific frequencies depends only

on the SATMD characteristics, meaning that the host structure dynamic characteristics are not needed for tuning. Furthermore, Figure 5.8 demonstrates that the SATMD poles maintain distinct frequency values and can simultaneously suppress vibrations at two distinct tonal frequencies, below and above the modal frequency of the short-circuited SATMD.

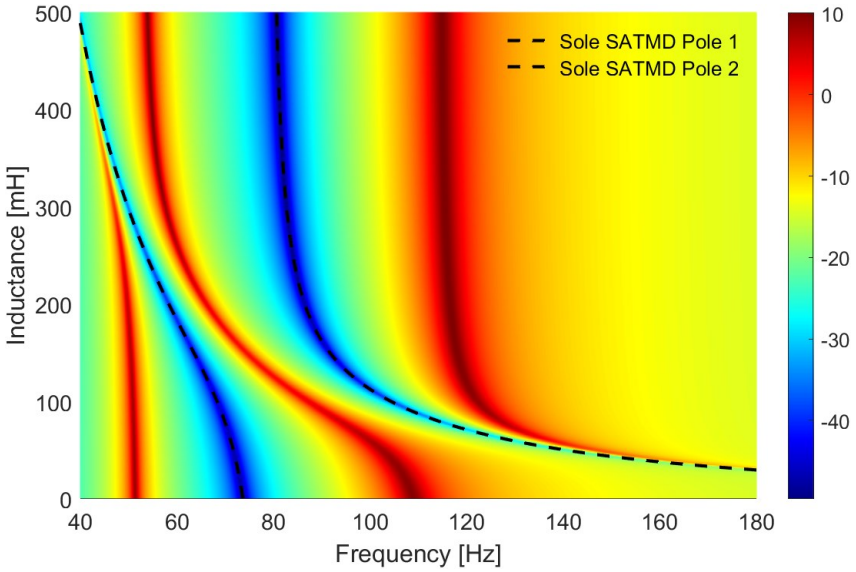


Figure 5.8. Inductance effect on frequency response of the main structure (colored results) and the sole SATMD eigenfrequencies with the same auxiliary mass (black dashed curves).

Moreover, it is obvious that the two mechanical modes are coupled with the electrical one, and vice versa, for all the inductance values. However, inductance variation may cause an initially mechanical mode to obtain the higher electrical component in its eigenvector, than the initially electrical mode. Therefore, the electrical mode at each inductance increment in the system can be defined as the one whose electrical component of its eigenvector is the highest between the three modes. In this study, the inductance values where the electrical component of an initially mechanical mode become the highest in the system, are defined as bifurcation points. For better illustration of the bifurcations that occur under varying inductance values and negligible resistance (R=1 Ohm), the electrical components of the eigenvectors, and the pole movement, as derived by the A_L system matrix of the state space (Equations 5.11 – 5.13), are shown in Figure 5.9a, b, respectively. In Figure 5.9a, the electrical component of each eigenvector (Φ_{el1}, Φ_{el2}, Φ_{el3}) alters as inductance increases, illustrated by the three different curves: solid curve, dashed-dotted curve, dashed curve, respectively. For very small inductance values, Φ_{el1}, Φ_{el2}, Φ_{el3} correspond to electrical mode, structural Mode II and structural Mode I, respectively, however inductance increase leads to the diversification of the electrical components, and thus bifurcations, since for each inductance increment, the highest electrical component always corresponds to the electrical mode. The electrical component of the electrical mode is denoted with red color, the electrical component of structural mode II with green, and the electrical component of structural mode I with blue. In Figure 5.9b, for the first and second structural mode, and the electrical mode, only the positive conjugate poles are illustrated (in red, blue, and green color, respectively). Symbol “o” represents the

poles at the starting short circuit position (L→0), symbol "x" the poles in the final position (L=590 mH), and the directions of the arrows indicate the pole movement under a steady inductance increment. The system roots move on 3 separate Loci (1, 2, and 3), however the structural and electrical poles bifurcate with inductance increase. For low, progressively increasing inductance values, the electrical mode is moving on Locus 1, the higher structural mode on Locus 2, and the lower structural mode on Locus 3.

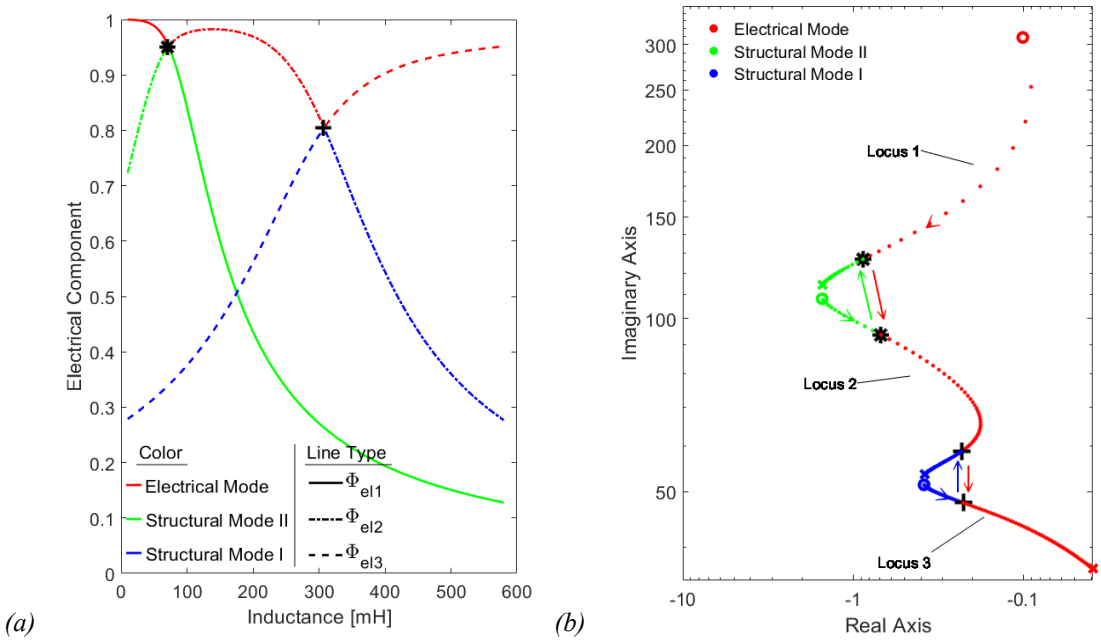


Figure 5.9. The two bifurcation points (symbols "" and "+") with inductance increase and R=1 Ohm. (a) Electrical components of the eigenvectors; (b) Root Loci.*

The first bifurcation occurs for L=70 mH, denoted with symbol "*" in both Figure 5.9a, b. At this point, the electrical components Φ_{el1} and Φ_{el2} are equal, whereas for higher inductive impedance Φ_{el2} attains the highest value between the electrical components, and thus corresponds to the electrical mode. For L=70 mH the electrical pole and the structural pole II have moved to the "*" position of Locus 1 and Locus 2, respectively. The root of the structural mode I for L=70 mH is not marked with "*" for visualization reasons, since this pole has hardly altered its root. For higher inductance values a pole jump is associated with this bifurcation, and the electrical pole has moved to Locus 2, whereas the structural mode II has moved to the green roots of Locus 1. Similarly, as inductance continues to rise, the second bifurcation point, shown with the symbol "+", occurs for L=305 mH. For this inductance value Φ_{el2} and Φ_{el3} are equal, whereas for higher inductance Φ_{el3} attains the highest value and corresponds to the electrical mode. In Figure 5.9b, the electrical pole and the structural pole I have moved to the "+" positions of Loci 2 and 3, respectively, whereas for higher inductance a second pole jump is observed, and the electrical pole continues in Locus 3, while the structural pole in the blue roots of Locus 2. Again, the "+" symbol is not shown for the mode that does not participate in the bifurcation (structural mode II), for visualization reasons. Even higher inductance values move the electrical pole to lower frequency band (lower values of the imaginary axis), whereas the poles of structural modes I

and II approach their open circuit positions, since only a very small amount of electric current is able to flow through the shunt circuit. In summary, the inductance variation leads to the movement of the electrical mode on the red roots, whereas structural mode I and II move on the blue and green roots, respectively.

The electrical component of the eigenvectors and the pole movement of the electromechanical system for increasing inductance values is also presented for the case of considerable resistive impedance (R=20 Ohm) in Figure 5.10a, b. The increase of resistance slightly affects the system eigenvectors, and the bifurcations occur under the similar circumstances as in the case of negligible resistance. However, all electrical roots, and the majority of the structural roots in Figure 5.10b, exhibit much higher values of their real part, compared to the case of R=1 Ohm, indicating greater energy conversion and dissipation, and also a highly damped electrical mode.

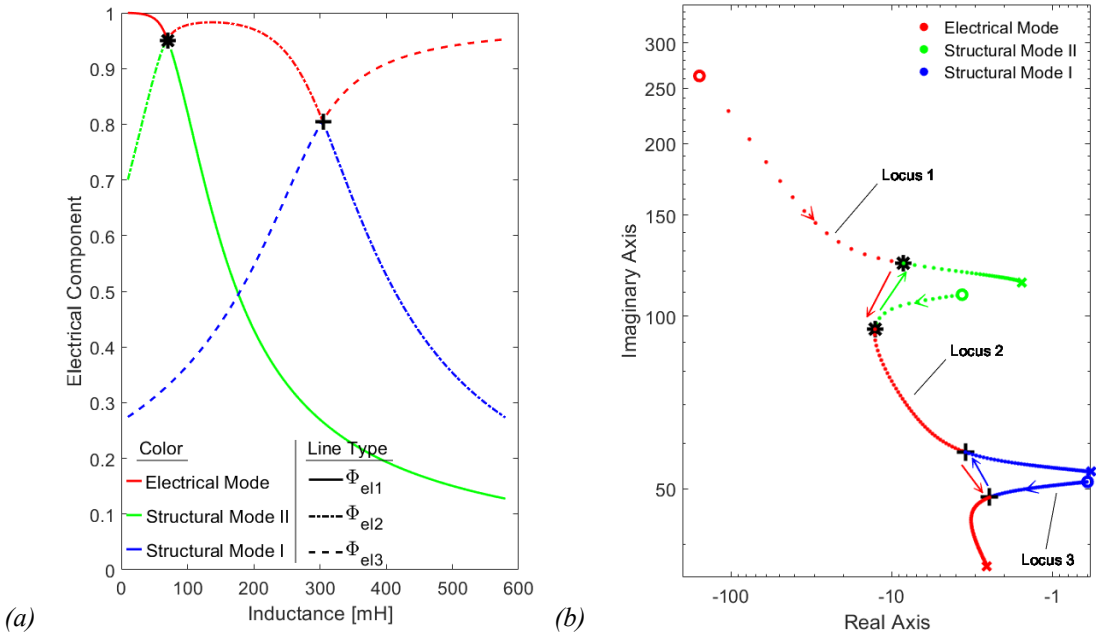


Figure 5.10. The two bifurcation points (symbols "" and "+") with inductance increase and R=20 Ohm. (a) Electrical components of the eigenvectors; (b) Root Loci.*

5.6 Combined Impedance Effect

To demonstrate the combined inductance and resistance effect of the SATMD, an inductance value is first selected, that yields very high electromechanical coupling, and the frequency response of the main mass is subsequently studied, for various resistance values. Towards this direction, Figure 5.11a illustrates the frequency response of the shunt circuit current for minimal resistance (1 Ohm) and various inductance values, suggesting that 100 mH creates high electromechanical coupling to all mechanical modes. Additionally, Figure 5.11b depicts the frequency response of the main mass acceleration for the selected 100 mH, and for various resistance values. Figure 5.11a indicates that for 100 mH, the electrical eigenfrequency lies around 90 Hz, indicated by the dark red color on the plot. However, for this

inductance value all Modes become highly coupled, having considerably high electrical components, therefore the addition of resistance is expected to induce sufficient damping, due to energy dissipation into heat. As demonstrated in Figure 5.11b, the addition of resistance achieves reduction in all structural Modes of the host structure. The Mode at 90 Hz is indeed more heavily affected, and progressively vanishes with higher resistance values. The other two Modes are reduced until a certain resistance value, succeeded by the phenomenal stiffening effect, which progressively increases the amplitude of the vibrations. It is therefore concluded that resistance has higher effect in the Modes with higher electrical component in their eigenvectors. Furthermore, for the selected inductance of 100 mH and approximately 25 Ohm, Figure 5.11b demonstrates that the Mode at 90 Hz has vanished, while the other two Modes are significantly dampened, and very high broadband control is expected.

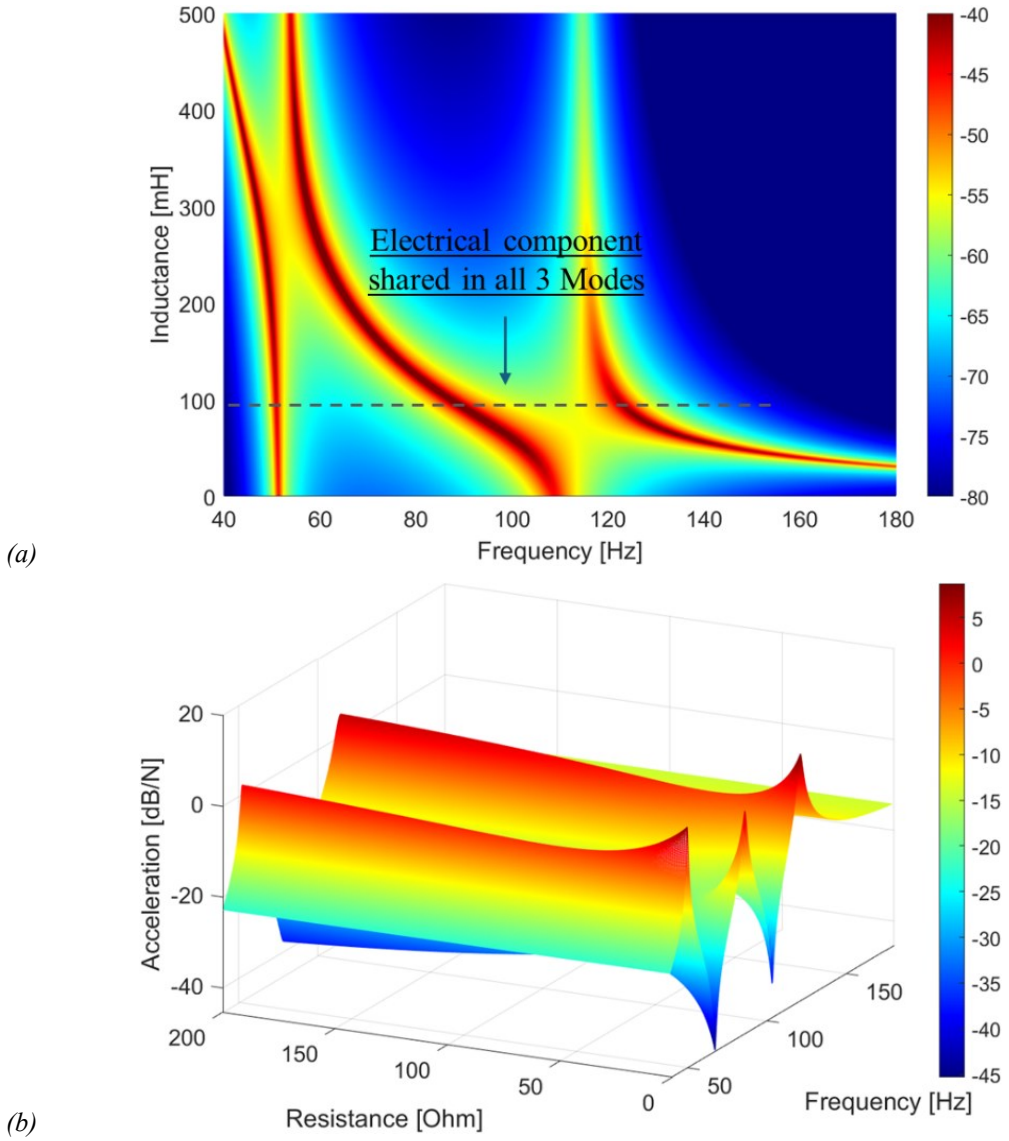


Figure 5.11. Combined resistance-inductance effect: (a) Frequency response of the shunt circuit current for minimal resistance and various inductance values; (b) Frequency response of the main mass acceleration for 100 mH, and for various resistance values.

The investigation of the combined inductance and resistance effect on the measured and simulation dynamic response of the electromechanical TMD is demonstrated in Figure 5.12a, b, respectively. A most excellent agreement between the experimental and simulation results is depicted, with minor differences near the first structural resonance for relatively high inductance values, which are most likely attributed to possible imperfections in the connections of multiple coils in series, and as a result in the increased uncertainty in the inductance and resistance levels.

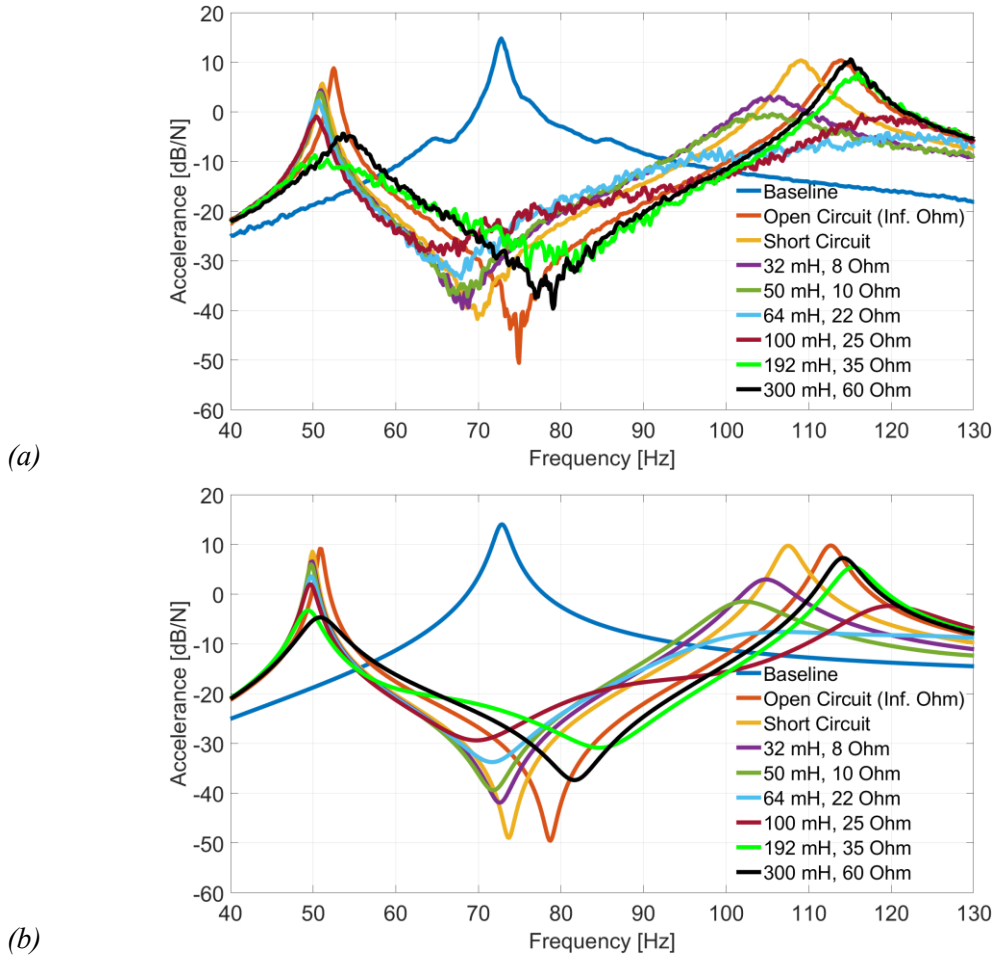


Figure 5.12. Combined resistance-inductance effect on structure: (a) Experimental results; (b) Simulation results.

As explained earlier, the addition of resistance in the shunt circuit was expected to allow the dissipation of the high electrical energy which is available due to the high electromechanical coupling observed in the system, when the electrical pole moved near the structural modes. This is indeed demonstrated in Figure 5.12. Comparing the amplitude of the short circuit TMD with the investigated cases of resistive-inductive SATMD in the simulation and the experiment, the practical elimination of the second structural mode for a combined inductance L=64 mH and resistance R=22 Ohm is observed (denoted by the light blue curves), due to very strong electromechanical coupling. Similarly, the first structural mode is vastly suppressed for L=192 mH and R=35 Ohm (indicated by the light green curves). Furthermore, the third modal peak attributed to the coupled electrical mode has practically disappeared

in the obtained experimental and theoretical frequency response results, together with the associated new antiresonance, due to high damping, because of the energy dissipation that takes place in the electric circuit. It is clearly depicted by the modal peak amplitude reductions summarized in Table 5.2, that much greater vibration reduction can be achieved using an R-L circuit, compared to the purely resistive results, both for each structural mode, and for multi-modal control. For the multi-modal control in Table 5.2 (Simultaneous on Both Modes), the depicted dB reduction is the least simultaneous vibration reduction achieved by the reported impedance values. In summary, the previous results have demonstrated the great potential of the electromechanical TMD to provide semi-active multi-modal vibration control capabilities of a given structure, through proper combination of the R, L values.

Table 5.2. Ultimate experimentally obtained reductions in modal peaks.

	Impedance	**R [Ohm]**	**L [mH]**	**Modal peak Reduction [dB]**
Structural Mode I	Resistive	100	-	9
	Combined	35	192	16
Structural Mode II	Resistive	53	-	7
	Combined	22	64	15
Simultaneous on Both Modes	Resistive	53	-	7
	Combined	25	100	10

5.7 Concluding Remarks

In this Chapter, the performance of the piezoelectric SATMD was evaluated experimentally and numerically on a simplified lumped mass structure. The equations of the SATMD – host structure system were formulated, and the transfer functions showed that the introduced antiresonances on the host structure coincide with the sole SATMD eigenfrequencies. The following main conclusions are summarized based on the obtained analytical and experimental results: Resistive impedance increases the damping capabilities of the coupled electromechanical system, due to the dissipation of electrical energy in the shunt resistance, leading up to 7dB simultaneous acceleration reduction of the structural modes. Inductive impedance introduces a new, highly tunable, oscillator in the system, which enhances the coupling and conversion of kinetic to electrical energy, especially near the bifurcation points. Appropriate inductance tuning results in the practical elimination of each structural mode, and can also lead to multimodal vibration control, achieving 10dB reduction. The SATMD was found able to compensate for the purely mechanical TMD disadvantages, providing broadband vibration suppression and control to the host structure, and offering great retuning capabilities. The experimental measurements validated the developed models.

Chapter 6: Modeling and Performance of SATMD on Large and Flexible Structures

This Chapter addresses the performance of the proposed piezoelectric SATMD on large and flexible structures, such as airframes of lightweight means of transportation. These structures exhibit lightly damped structural modes in relatively low frequency bandwidths, functioning under high amplitude vibrations during their operating time. A reduced-ordered modal space structural dynamics model is formulated, coupled with the SATMD device, and the RL shunt electric circuit. The SATMD performance is demonstrated experimentally and numerically on a scaled-down airframe prototype structure under broadband white noise excitation, as well as multi-tonal harmonic excitation. The shunt circuit impedance is studied to enhance the passive TMD control capabilities and provide vibration reduction in multiple frequency ranges. Subsequently, the SATMD is evaluated on a field application on a BO-105 S helicopter during real-flight conditions.

6.1 SATMD – Large and Flexible Structure System Model

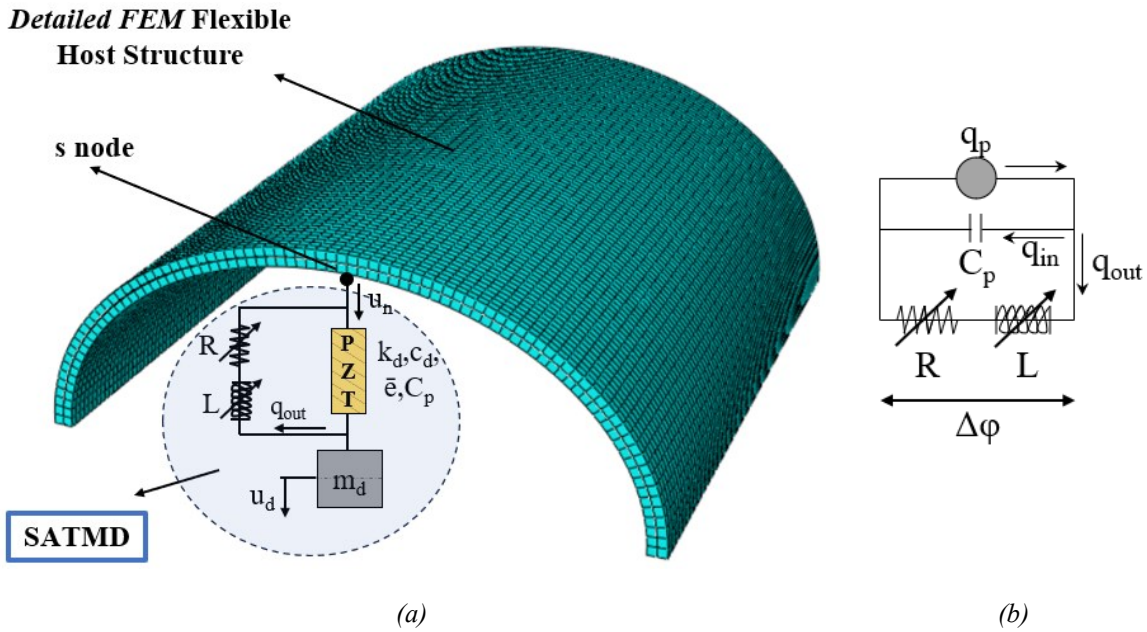
Multiple DOF structures in mechanical systems are usually conveniently modelled using the finite element method. When such structures are excited with varying dynamic loads, the system matrices are frequently transformed to modal space and investigated inside specific frequencies, achieving great reduction in the model size. The SATMD – multiple DOF structure system is formulated in the sections below, integrating the piezoelectric SATMD device equilibrium into the modal space model of the host structure.

6.1.1 Detailed Finite Element Model

In the realm of structural analysis, flexible and large structures are typically modelled as equivalent discretized linear structure systems which include a great number of degrees of freedom (DOFs) and intricate system matrices. In the current work, the finite element method is used to synthesize the standard dynamic system of equations in the time domain,

$$M_{kl}\ddot{u}_l + C_{kl}\dot{u}_l + K_{kl}u_l = F_k \tag{6.1}$$

where: u is the vector of the N structural displacements, $k,l = 1,...,N$, M,C,K represent the structural mass, damping, and stiffness matrices, respectively, and $\boldsymbol{F}$ represents the applied external loads.



(a) *(b)*

Figure 6.1. Shunted piezoelectric SATMD attached to a multi-DOF host structure. (a) FEM discretized host structure; (b) Shunt circuit.

To model the integrated structure-SATMD behavior, the proposed lumped piezoelectric device is assumed to be attached to the s node of a detailed FEM host structure, where u_n is the nodal displacement of the structure in the direction parallel to the device operating direction (Figure 6.1a). In this case, the SATMD equilibrium is transposed from the two bottom equations of Equation (5.9), to:

$$\begin{aligned} &m_d\ddot{u}_d - c_d\dot{u}_n + c_d\dot{u}_d - k_d u_n + k_d u_d + \bar{e}\Delta\varphi = 0 \\ &\bar{e}(u_n - u_d) + C_p L\ddot{q}_{out} + C_p R\dot{q}_{out} + q_{out} = 0 \end{aligned} \tag{6.2}$$

The SATMD attachment also alters the equilibrium of the host structure. The new dynamic equations are obtained:

$$M_{kl}\ddot{u}_l + C_{kl}\dot{u}_l + K_{kl}u_l + \delta_{kn}c_d(\dot{u}_n - \dot{u}_d) + \delta_{kn}k_d(u_n - u_d) - \delta_{kn}\bar{e}\Delta\varphi = F_k \tag{6.3}$$

where δ_{kn} is the Kronecker delta.

6.1.2 Reduced Order Modal Space Model

The antivibration device performance in large and flexible host structures will be tested in a small subset of X vibration modes within a specific frequency range. Due to the large size of Equation (6.1), a reduced order model (ROM) is developed using a truncated set of properly selected modes of the undamped dynamic system of equations that projects the physical structural displacements to the modal space as:

$$u_l = \Phi_{li}Q_i^H \tag{6.4}$$

where $\boldsymbol{\Phi}_I$ are the undamped eigenvectors of the host structure provided by Equation (6.1), $\boldsymbol{Q}^H$ is the vector of modal participation factors without the presence of the SATMD, and $i = 1,...,X$ is the mode number. We assume that the dynamic characteristics of the SATMD are too small to alter the mode shapes of the host structure, thus Equation (6.3) is transposed to the modal space:

$$\Phi_{jk}M_{kl}\Phi_{li}\ddot{Q}_i + \Phi_{jk}C_{kl}\Phi_{li}\dot{Q}_i + \Phi_{jk}K_{kl}\Phi_{li}Q_i + \Phi_{jk}\delta_{kn}c_d(\Phi_{ni}\dot{Q}_i - \dot{u}_d) + \Phi_{jk}\delta_{kn}k_d(\Phi_{ni}Q_i - u_d) - \Phi_{jk}\delta_{kn}\overline{e}\Delta\varphi = \Phi_{jk}F_k \tag{6.5}$$

where $\boldsymbol{Q}$ is the vector of the modal participation factors of the host structure with the attached SATMD. Furthermore, remembering Equation (5.4), the charge equilibrium now can be expressed as (Figure 6.1b):

$$q_p = q_1 + q_{out} = \overline{e}(u_d - u_n) = \overline{e}(u_d - \Phi_{ni}Q_i) \tag{6.6}$$

and, remembering Equation (5.8), the potential difference can be expressed as:

$$\Delta\varphi = \frac{q_{in}}{C_p} = \frac{q_p - q_{out}}{C_p} = \frac{\overline{e}(u_d - \Phi_{ni}Q_i) - q_{out}}{C_p} \tag{6.7}$$

Considering the orthogonality of the mode shapes, using the simplifying terms

$$\begin{aligned} \Phi_{jk}\delta_{kn} &= \Phi_{jn} \\ \Phi_{jk}F_k &= P_j \end{aligned} \tag{6.8}$$

and expressing the potential difference as in Equation (6.7), the final expressions of the coupled electromechanical system are obtained:

$$\begin{aligned} &\overline{M}_{ii}\ddot{Q}_i + \overline{C}_{ii}\dot{Q}_i + \overline{K}_{ii}Q_i + c_d\Phi_{jn}\Phi_{ni}\dot{Q}_i - c_d\Phi_{jn}\dot{u}_d + k_d\Phi_{jn}\Phi_{ni}Q_i + \frac{\overline{e}^2}{C_p}\Phi_{ni}Q_i - k_d\Phi_{jn}u_d - \frac{\overline{e}^2}{C_p}u_d + \frac{\overline{e}}{C_p}\Phi_{jn}q_{out} = P_j \\ &m_d\ddot{u}_d + c_d\dot{u}_d + k_du_d + \frac{\overline{e}^2}{C_p}u_d - c_d\Phi_{ni}\dot{Q}_i - k_d\Phi_{ni}Q_i - \frac{\overline{e}^2}{C_p}\Phi_{ni}Q_i - \frac{\overline{e}}{C_p}q_{out} = 0 \\ &\overline{e}(\Phi_{ni}Q_i - u_d) + C_pL\ddot{q}_{out} + C_pR\dot{q}_{out} + q_{out} = 0 \end{aligned} \tag{6.9}$$

where $\overline{\boldsymbol{M}}, \overline{\boldsymbol{K}}$ are the modal mass and stiffness diagonal matrices respectively, and $\boldsymbol{P}$ is the modal force. The modal damping matrix $\overline{\boldsymbol{C}}$ is assumed to be diagonal, and in this work, it is synthesized from measured modal damping values of the baseline structure. Considering the equivalent piezoelectric stiffness (Equation 4.26), the Equations (6.9) are expressed in matrix form as:

$$\begin{bmatrix} \bar{\boldsymbol{M}} & \boldsymbol{0} & \boldsymbol{0} \\ \boldsymbol{0} & m_d & 0 \\ \boldsymbol{0} & 0 & L \end{bmatrix} \begin{Bmatrix} \ddot{\boldsymbol{Q}} \\ \ddot{u}_d \\ \ddot{q}_{out} \end{Bmatrix} + \begin{bmatrix} \bar{\boldsymbol{C}} + c_d \boldsymbol{\Phi_n}^T \boldsymbol{\Phi_n} & -c_d \boldsymbol{\Phi_n}^T & \boldsymbol{0} \\ -c_d \boldsymbol{\Phi_n} & c_d & 0 \\ \boldsymbol{0} & 0 & R \end{bmatrix} \begin{Bmatrix} \dot{\boldsymbol{Q}} \\ \dot{u}_d \\ \dot{q}_{out} \end{Bmatrix} + \begin{bmatrix} \bar{\boldsymbol{K}} + k_p \boldsymbol{\Phi_n}^T \boldsymbol{\Phi_n} & -k_p \boldsymbol{\Phi_n}^T & \frac{\bar{e}}{C_p} \boldsymbol{\Phi_n}^T \\ -k_p \boldsymbol{\Phi_n} & k_p & -\frac{\bar{e}}{C_p} \\ \frac{\bar{e}}{C_p} \boldsymbol{\Phi_n} & -\frac{\bar{e}}{C_p} & \frac{1}{C_p} \end{bmatrix} \begin{Bmatrix} \boldsymbol{Q} \\ u_d \\ q_{out} \end{Bmatrix} = \begin{Bmatrix} \boldsymbol{P} \\ 0 \\ 0 \end{Bmatrix} \quad (6.10)$$

where $\boldsymbol{\Phi_n}$ is a line-vector, where each element is the amplitude of the respective mode shape of the n DOF. Equation (6.10) computes the modal displacements of the host structure in modal space and the antivibration device DOFs (auxiliary mass displacement and shunt charge) in physical space. To predict the structural performance, the host structure modal displacements return to the physical space through the Equation (6.4). Equations (6.10) and (6.4) will be used, in time or in frequency domain, for the comparison of the developed model to the experimental measurements of the down-scaled airframe prototype.

6.2 Scaled-Down Airframe Prototype Structure

The piezoelectric SATMD vibration control capabilities are experimentally and numerically demonstrated on a lab-scale airframe structure. This Section covers the experimental setup and development of the finite element (FE) model, before evaluating the antivibration device performance on broadband multi-modal excitation and multi-tonal excitation.

6.2.1 Experimental Setup

A simplified structural dynamics model of a small regional aircraft was designed and manufactured to accommodate lab-dimensions, while maintaining similarity in dynamic characteristics [147] (Figure 6.2a). The protype was fabricated having a total mass of approximately 112kg and consists of the following components: (i) a 3m steel tubular beam representing the aircraft fuselage; (ii) two aluminum plate-strips for the wings and the horizontal tail stabilizer, respectively; and (iii) three plastic connectors for the mounting of the wings, the horizontal tail and the proposed antivibration device, respectively. The dimensions, the materials and the properties of the airframe prototype are shown in Table 6.1 and were used as input in the numerical simulation. To achieve realistic flight conditions (free-free boundary conditions), the structure is suspended with elastic belts from the modal points of the fuselage first bending modal frequency (L/4 and 3L/4). The simplified aircraft prototype was excited via an electromechanical shaker (Experimental Apparatus in Chapter 3), mounted at the middle of the horizontal tail. Accelerations normal to the plane of the tested structure were measured at three different locations; 1. at the fuselage tip 2. at the fuselage center, and 3. at the wing tip. The Experimental Apparatus used for the vibration testing is described in Chapter 3, and the shaker used was the V406

model. The FRFs of the measured acceleration versus the applied force were extracted, for each of the three locations. The measured FRFs of the fuselage tip acceleration versus the applied force are illustrated in Figure 6.3 in the range of the frequency domain up to 180Hz. The multi-modal vibration suppression capabilities of the proposed electromechanical damper are investigated for the three high amplitude modal peaks in the frequency range of 30Hz-70Hz, namely Mode I (36Hz), Mode II (47Hz) and Mode III (64Hz).

Table 6.1. Dimensions, materials and properties of the prototype and numerical simulation.

Components	Dimensions (mm)		Materials	Properties	
Fuselage	Length	3000	Steel	Density	8000 kg/m^3
	Outer Diameter	100		Young's Modulus	180 GPa
	Thickness	5		Poisson Ratio	0.3
Wings	Length	3200	Aluminum	Density	2700 kg/m^3
	Width	200		Young's Modulus	90 GPa
	Thickness	15		Poisson Ratio	0.33
Tail	Length	1000	Aluminum	Density	2700 kg/m^3
	Width	200		Young's Modulus	90 GPa
	Thickness	15		Poisson Ratio	0.33

(a)



(b)

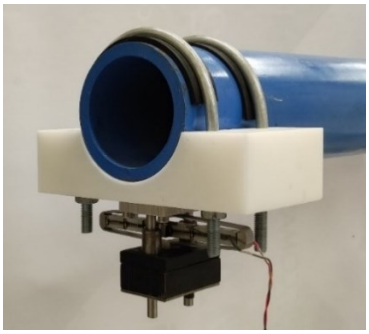


Figure 6.2. Experimental Setup. (a) Down-scaled airframe model; (b) Piezoelectric device attached under fuselage tip in vertical direction.

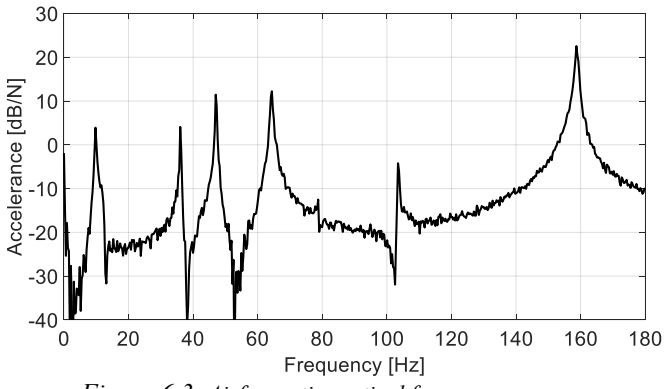


Figure 6.3. Airframe tip vertical frequency response.

6.2.2 Host Structure Finite Element and ROM Model

For the simulation, a converged detailed finite element model was developed in Abaqus software using 4-node reduced integration shell elements for both the tubular steel beam and the aluminum wings and tail (1406 nodes in total). The undamped normalized mode shapes of the three targeted modes are presented in Figure 6.4a-c, while the color interpretation is shown in Figure 6.4d, indicating that all three modes appear to be combined fuselage-wing-tail bending modes. The undamped eigenvectors of the host structure, the modal masses and modal stiffnesses, were extracted from the modal analysis executed in Abaqus. The measured modal damping values of the baseline structure were included in the modal damping matrix of the reduced system Equation (6.10). The modal characteristics of the structure are shown in Table 6.2. Results of the mode superposition analysis are compared to experimental measurements for the fuselage tip, center, and wing in Figure 6.5. Great agreement is observed in all three cases between 30Hz and 70Hz validating the developed model, and proving the usefulness of the mode superposition method, since a decoupled 3x3 problem is solved instead of the full model.

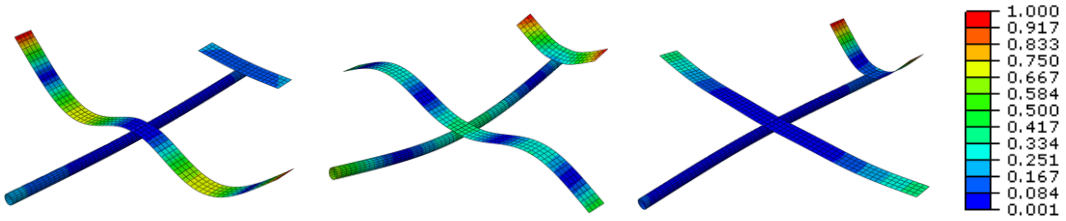
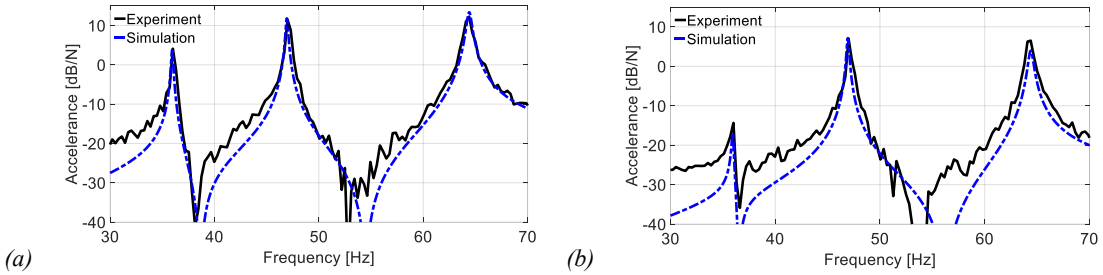


Figure 6.4. Undamped mode shapes of structural eigenfrequencies. (a) 36Hz; (b) 47Hz; (c) 64Hz; (d)Normalized amplitude of mode shapes.

Table 6.2. Modal characteristics of studied modal frequencies.

	Frequency [Hz]	Mass[kg]	Damping [Ns/m]	Stiffness [kN/m]
1	35.9	3.1	3.7	156.9
2	47.0	12.4	18.0	1076.0
3	64.4	0.6	1.9	100.5



(c)

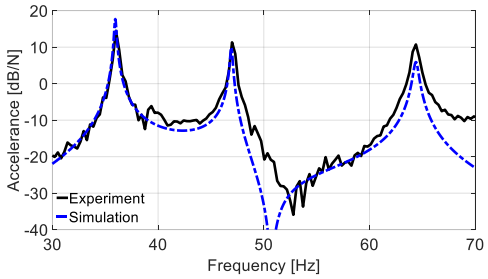


Figure 6.5. Experimental frequency response compared to mode superposition analysis. (a) Fuselage tip;(b) Fuselage center; (c) Wing tip.

6.2.3 Broadband Multi-Modal Excitation

Aircrafts function under broadband aerodynamic loads, which could be simulated by vertical forces to the rear tail. Therefore, this section addresses the piezoelectric SATMD performance under broadband white noise excitation and aiming at simultaneously reducing the structural vibrations in multiple structural modes.

6.2.3.1 Baseline Performance with Passive TMD

The developed antivibration device with the APA1500L piezoelectric transducer is used for vibration control. The antivibration device is firmly attached to a plastic connector, which is in turn attached to the fuselage tip (Figure 6.2b). As a result, the SATMD stiffness k_d is expected to exhibit a small change in comparison to the sole SATMD configuration. The amplitude of the normalized baseline structure mode shapes at the fuselage tip Φ_n , as calculated in the FE model and used in Equation (6.10) are presented in Table 6.3. Except for the attached mass, and the transducer mass which in the numerical analysis was considered to be equally distributed to the nodal displacement at the structural end and the displacement of the auxiliary mass, the rest of the lumped model parameters were aptly calibrated from correlations between experimental and simulation results (Figure 6.6), as explained below. An auxiliary mass m_d of 1.14kg tuned the short circuit TMD to Mode II (Figure 6.6a), thus the equivalent mechanical stiffness k_d is calculated from the tuning frequency (Equation 4.31) and used in the numerical analysis (Figure 6.6b). The lumped mechanical damping c_d was determined by comparing the model frequency response of the passive short circuit TMD to the respective experimental results. The SATMD auxiliary mass, and equivalent damping and stiffness are shown in Table 6.4. In Figure 6.6, the frequency response of the host structure without the attachment of the SATMD is expressed by the black curve and denoted as “Baseline”. The “Short Circuit” curve represents the passive TMD effect of the proposed damper, which highly reduces the amplitude of acceleration in the vicinity of Mode II,

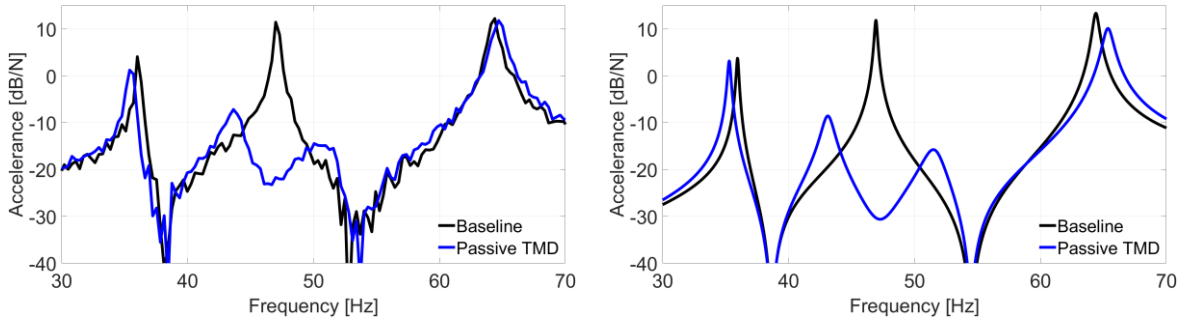
however, two new frequency peaks of much smaller amplitude are introduced at approximately 44Hz and 51Hz.

Table 6.3. Amplitude of mode shapes at fuselage tip and tail.

	Mode I	Mode II	Mode III
Tip	0.198	0.628	-0.113

Table 6.4. Piezoelectric device characteristics.

Auxiliary mass [kg]	1.14
Equivalent total Damping c_d [Ns/m]	15
Equivalent mechanical Stiffness k_d [kN/m]	100



(a) *(b)*

Figure 6.6. Frequency response (acceleration) of the fuselage tip without (Baseline) and with the passive TMD. (a) Experimental results; (b) Simulation results.

6.2.3.2 Resistance Effect

The purely resistive shunt impedance effect is first investigated. Figure 6.7a, b illustrate the experimental and simulation results of the fuselage tip accelerance in the frequency range near the passively targeted Mode II, where the effect of various resistance values is more evident. Except for the baseline and short circuit TMD presented in the previous subsection, the rest of the curves represent the effect of the SATMD when various pure resistive impedances used. Excellent agreement is observed between the experimental and simulation results, depicted in Figure 6.7a, b, respectively. As expected, there is considerable effect of the resistive impedance on the FRF of the system, mostly as added damping, as the frequency response varies between the two extreme situations: short circuit (zero resistance) and open circuit (infinite resistance). As resistance increases, the resistance effect on the passively targeted Mode II is similar to the one presented for the lumped mass structure (Section 5.4). Therefore, as resistance increases, some of the electrical energy flowing through the shunt circuit is

dissipated into heat, adding damping to the system, and some electrical energy is stored in the capacitor, increasing the phenomenal stiffness. These effects apply for Modes I and III as well, whose amplitude and frequency are also affected by the attached damper. At specific, yet different, levels of resistance, the energy dissipation is maximized for all 4 structural eigenfrequencies. For higher resistance in each case, a low pass filter is created in the shunt circuit, which reduces the flow of energy and dissipation through the resistor. The maximum strain energy in the piezoelectric device is also reduced, leading to phenomenal stiffening, which dominates the system response, resulting in higher amplitudes and frequencies for all structural modes, as the infinite resistance (open circuit condition) is reached.

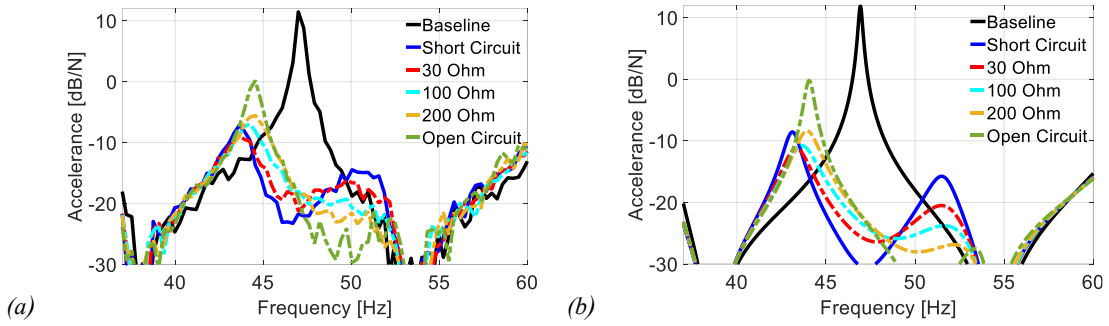
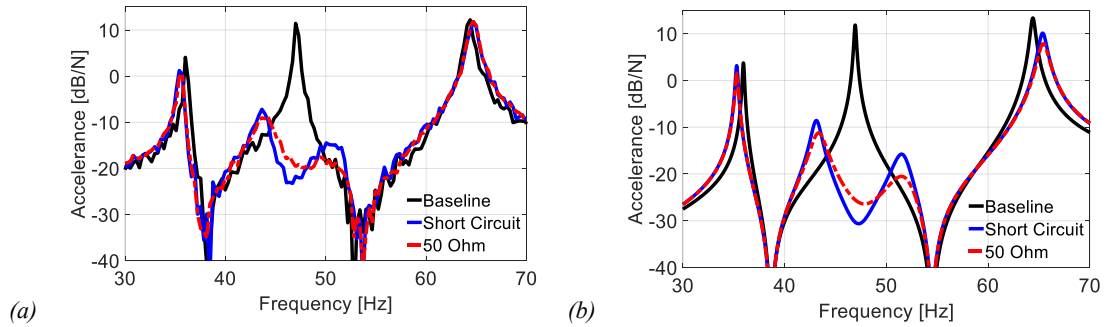


Figure 6.7: Resistance effect on fuselage tip. (a) Experimental results; (b) Simulation Results.

The effectiveness of the SATMD with a 50 Ohm shunt resistance on the accelerance at various airframe locations (fuselage tip and center, and the wing tip) is illustrated in Figure 6.8a-f over the whole bandwidth of interest. The resistive SATMD overperforms the short circuit system, as it reduces the amplitude of accelerance near the target vicinity of Mode II, and results to modest attenuation in the acceleration responses in Modes I and III. Very good correlation is observed between predicted and measured results in all locations, with minor discrepancies near the vicinity of Mode III. The analytical model seems to overestimate the vibration suppression; however, this inconsistency is considered acceptable, as the whole airframe model dynamics are approximated using only three structural modes.



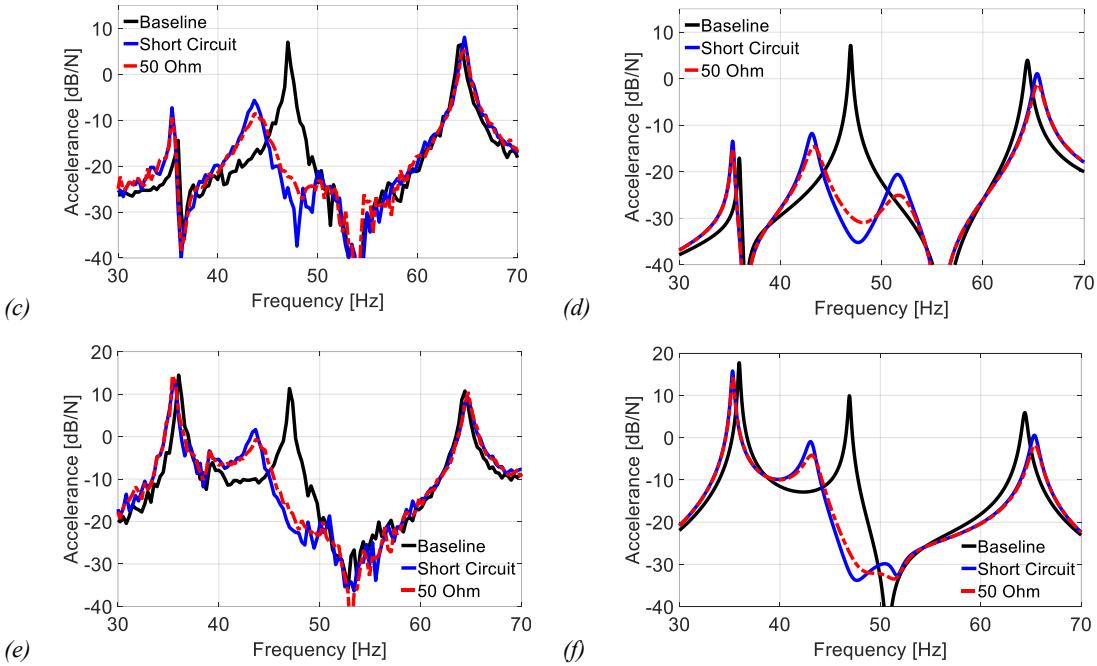


Figure 6.8: Predicted and measured accelerance at various location of the airframe structure. (a)-(b) Fuselage tip; (c)-(d) Fuselage center; (e)-(f) Wing tip.

6.2.3.3 Inductance Effect

The scope of this section is to thoroughly study the effect of the undamped electric pole (R=0) introduced by pure inductance. This investigation contributes to the complete understanding of the enhancement of electromechanical coupling and the exploitation of the anti-resonance introduced by the electrical resonator. However, it is impossible to find ideal coils with zero resistance, thus the experimental study with similar inductance values, and resistance, is presented in the next subsection.

As seen in Eq. (6.10), the inductance adds a new complex conjugate pair of roots into the system, which corresponds to an additional dominant electrical mode. Depending on the strength of electromechanical coupling, the electrical mode is not purely electrical and may contain strong mechanical components from mechanical DOFs of the host structure and the auxiliary mass, and vice versa, as also seen in the case of the lumped mass structure (Section 5.5). The effect of inductive impedance on the FRFs of the electric charge, auxiliary mass and the airframe tip acceleration is illustrated in Figure 6.9a-c. These surface plots can be intuitively understood as the frequency response of each DOF that corresponds to various impedance values. The frequency peaks in each plot are indicated by the red and yellow colors, whereas the blue areas imply lower amplitude of vibrations. The electrical mode is manifested as a new frequency peak not only in the charge FRF, but also in the structure and auxiliary mass FRFs.

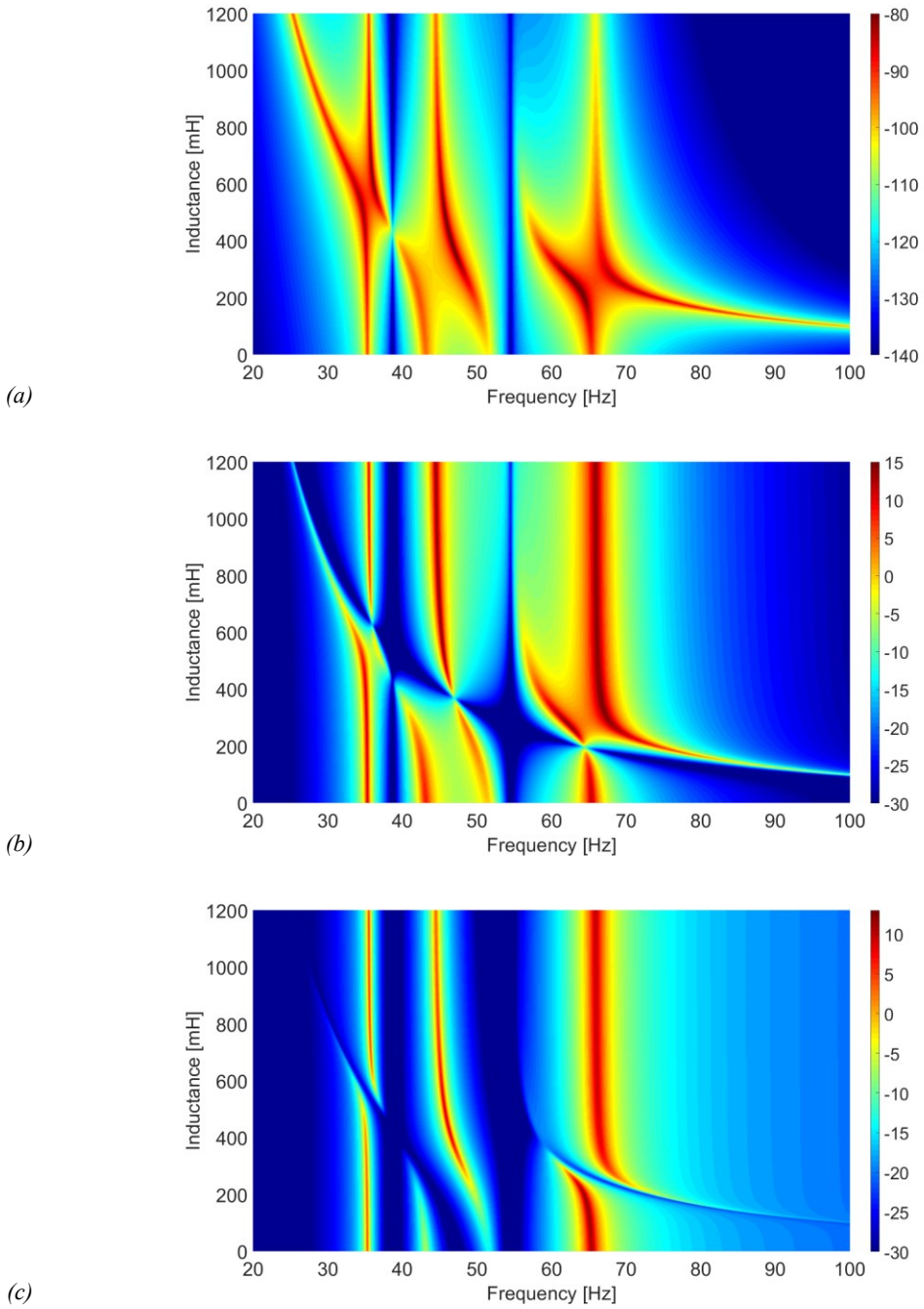


Figure 6.9: Inductance effect on the frequency response functions of key state variables. (a) Shunt circuit charge; (b) Auxiliary mass acceleration; (c) Fuselage tip acceleration.

In the electric charge FRF (Figure 6.9a), the electrical mode descends to lower frequency band as inductance rises, and as it approaches each structural mode, its amplitude is increasing rapidly, as seen in the areas of dark red color. Moreover, when the electrical resonance approaches Modes III and I, at approximately 200mH and 550mH, respectively, two close frequency peaks are observed, which indicate high coupling and large conversion of kinetic to electrical energy. For inductance higher than 600mH, the electrical resonance occupies smaller frequency values than Mode I, and becomes progressively decoupled from all structural modes, as illustrated by the brighter red and yellow areas.

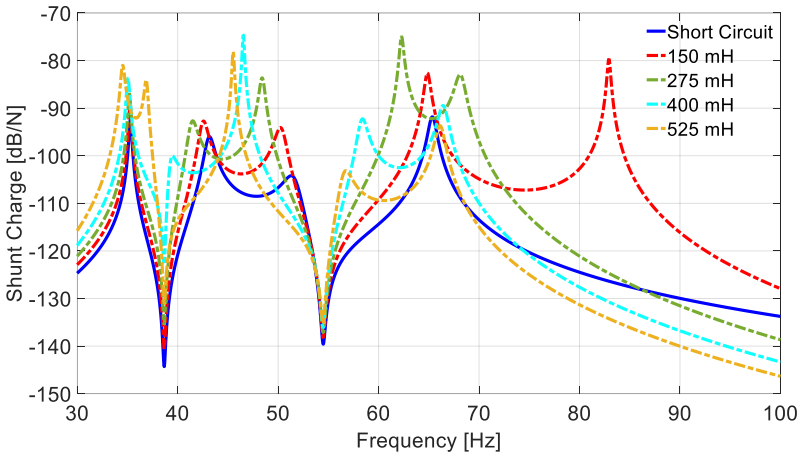
High coupling between the auxiliary mass and the shunt circuit is demonstrated (Figure 6.9b) by the resemblance with the charge plot (Figure 6.9a). One important distinction is the fact that when the electrical resonance surpasses a structural mode, its amplitude increases for larger inductance values, whereas the electrical amplitude of this structural mode decreases, due to progressive decoupling. Another major distinction is the presence of a moving anti-resonance that accompanies the electrical pole in the auxiliary mass plot (Figure 6.9b) and does not interact with the existing structural anti-resonances. This anti-resonance absorbs kinetic energy from the auxiliary mass but has no effect on the host structure.

The airframe tip response vs. the inductance (Figure 6.9c) exhibits apparent differences with the aforementioned figures. Two distinct anti-resonances are observed, which correspond to the structural oscillator (auxiliary mass) and the electrical oscillator (shunt circuit charge), respectively. These two anti-resonances coexist for all inductance values, and, if the SATMD electromechanical characteristics where appropriately designed, could highly suppress two distinct structural modes. The electrical mode affects the structural Modes I and III only when it approaches them, whereas the electrical anti-resonance affects the mechanical anti-resonance of the short circuit TMD at 47Hz, shifting it to lower frequencies. To better quantify the inductance effect to the studied DOFs, the frequency responses are further analysed and illustrated in Figure 6.10 for 150mH, 275mH, 400mH and 525mH.

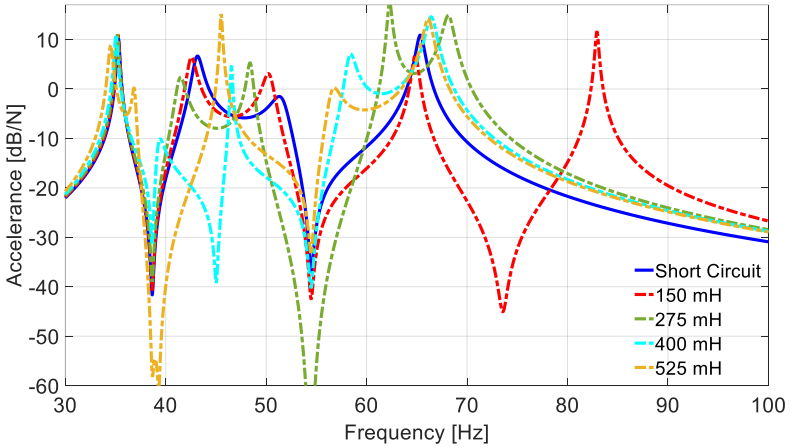
L=150mH: The electrical resonance is observed at approximately 83Hz, as manifested in all three plots of Figure 6.10. A respective anti-resonance is evident in the FRFs of the auxiliary mass and the structure, in different frequencies. Modes I and III are not extensively affected, however an initial detuning of the auxiliary mass anti-resonance is observed.

L=275mH: The electrical resonance has moved to approximately 62Hz (Figure 6.10a), shifting Mode III to slightly higher frequency. The anti-resonance is tuned to Mode III in the airframe tip (Figure 6.10), whereas in the auxiliary mass the anti-resonance exhibits the same frequency with the existing structural anti-resonance at 55Hz, demonstrating extremely low amplitude (Figure 6.10b). Mode I is slightly affected, while the passive TMD tuning deteriorates, and Mode II attains higher amplitude in the structure.

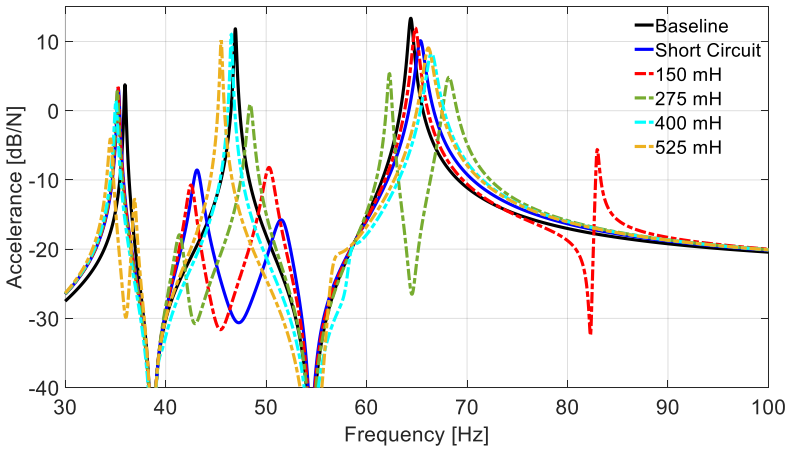
L=400mH: The electrical peak has moved to 45Hz (Figure 6.10a), shifting the lower amplitude peaks due to the passive TMD away from their initial frequency values. The auxiliary mass anti-resonance is close to its respective resonance (Figure 6.10), not letting the latter to exhibit high amplitude, however the airframe tip anti-resonance due to the electrical resonance has moved to the existing structural anti-resonance at approximately 39Hz. Thus, Mode II in Figure 6.10c exhibits very high amplitude, and no new anti-resonance can be observed at the passively targeted Mode with inductance. Finally, Mode I is again slightly affected.



(a)



(b)



(c)

Figure 6.10: Inductance effect on frequency response functions for 150mH, 275mH, 400mH, 525mH. (a) Shunt circuit charge; (b) Auxiliary mass acceleration; (c) Fuselage tip acceleration.

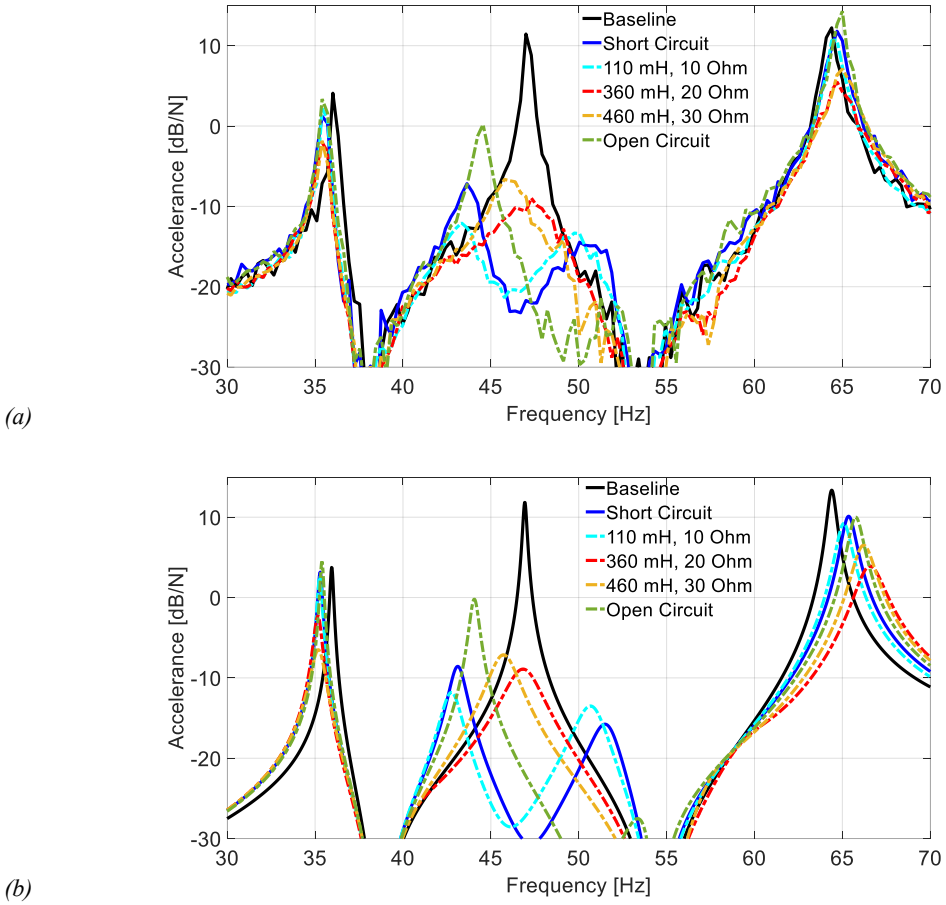
L=525mH: The electrical resonance has moved to approximately 36Hz (Figure 6.10a), shifting Mode I to slightly lower frequency. The anti-resonance is tuned to Mode I in the airframe tip (Figure 6.10c), whereas in the auxiliary mass the anti-resonance frequency is very close to the existing structural anti-resonance at 39Hz (Figure 6.10b). Still high coupling is observed between the electrical mode and

structural Mode II, manifested by the high amplitude of 45Hz in all Figure 6.10, whereas Mode III is progressively decoupled from the shunt circuit.

Similarly to the case of the lumped mass structure (Section 5.5), two important mechanisms seem to highly affect the host structure. First, the inductance effectively introduces a second resonant oscillator in the system, associated with a second anti-resonance in the studied structure, which is highly tunable. Secondly, the inductance increases the electromechanical coupling when the electrical mode approaches the structural ones, resulting to high conversion of kinetic to electrical energy and vice-versa, during the system vibration. The latter is very important for the broadband vibration control studied in this Section and opens the way for high energy dissipation in a resistive-inductive shunt circuit, as outlined in the next subsection.

6.2.3.4 Combined Impedance Effect

The combined effect of inductance and resistance is illustrated by the experimental and simulation results of the fuselage tip accelerance in the whole bandwidth of interest in Figure 6.11a, b, respectively.



(a)

(b)

Figure 6.11: Inductance effect on fuselage tip. (a) Experimental results; (b) Simulation Results.

The inherent resistance of the inductance coils was measured and included in the simulations. Excellent agreement between the experimental and simulation results is depicted, with the only difference being the less damped simulated frequency peaks in the simulation results, which is most likely attributed to possible imperfections in the connections of multiple coils in series, and as a result in the increased uncertainty in the inductance and resistance levels. As depicted by the cyan curve, a relatively low inductance of 110mH with 10 Ohm resistance achieves better vibration attenuation near the passively targeted Mode II. For higher inductance and associated resistance, the modal peak attributed to the coupled electrical mode has practically disappeared in both experimental and predicted frequency response results due to high damping and the energy dissipation that takes place in the electric circuit, as seen in the red and yellow curves. The combined 360mH and 20 Ohm impedance exhibits high simultaneous multi-modal vibration suppression results, because the inductance of 360mH is near the created anti-resonance of Mode III (Figure 6.9c), while the electrical mode is also highly coupled with Modes I and II (Figure 6.9a), thus providing increased electric energy to be dissipated by the resistance for these two Modes. The higher inductance of the 460 mH and 30 Ohm impedance combination has shifted the electrical resonance to lower frequency vicinity (Figure 6.9a), improving the attenuation in the vicinity of Mode I, and having the opposite result in Mode III. Most importantly, it is observed that for higher inductance and associated resistance, all studied structural modes are simultaneously highly attenuated, leading to efficient multi-modal vibration control. It is furthermore demonstrated that alterations of shunt impedance can retune the vibration reduction capabilities of the SATMD in the frequency vicinity of interest and accommodate potential in-flight changes in structural and loading parameters.

The effect of a combined 360mH and 20 Ohm impedance on the fuselage center and the wing tip is illustrated in Figure 6.12a-d. Again, almost excellent agreement between theoretical results and experiments is demonstrated in all measured sites in Figure 6.12. Similarly with the fuselage tip, considerable simultaneous vibration attenuation is observed over the whole studied frequency bandwidth of the fuselage center and the wing tip (Figure 6.12a-d). The multi-modal experimental dB reductions of the considered impedance, compared to the baseline structure, in all measured points are shown in Table 6.5. Translating the dB reduction of the fuselage tip to magnitude reduction, the acceleration of Mode II is decreased by one order of magnitude, while the amplitude of acceleration of the other two Modes is at least halved.

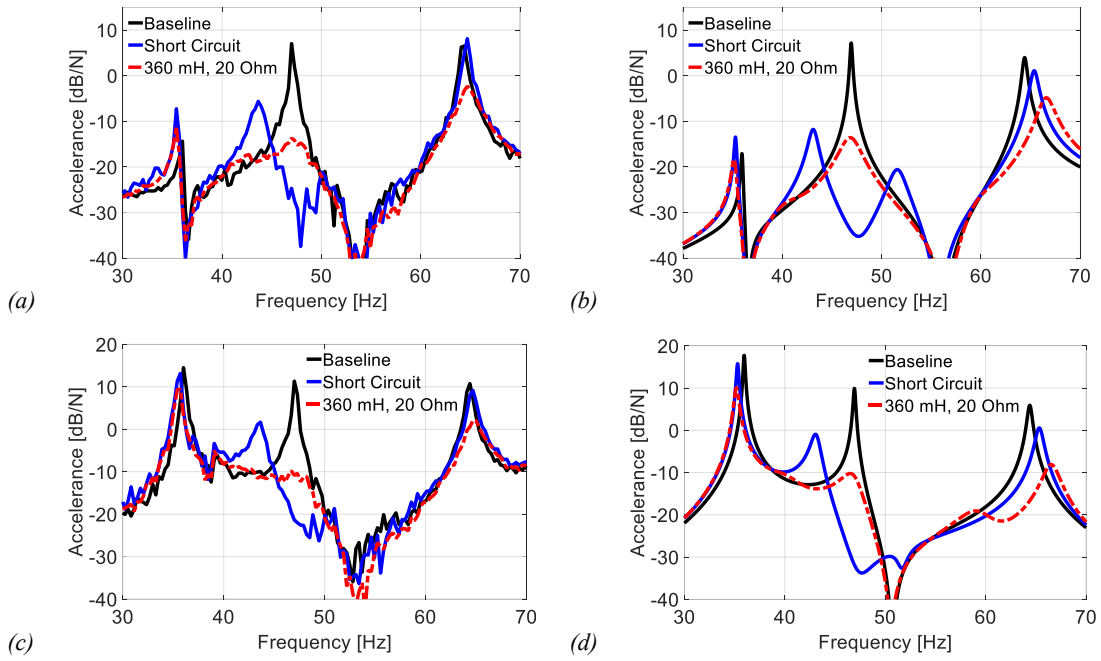


Figure 6.12: Inductance effect on the accelerance; left column experimental, right column simulation results. (a)-(b) Fuselage center; (c)-(d) Wing tip.

Table 6.5: Experimental accelerance reduction at various airframe locations compared to baseline in the vicinity of each Mode.

Location	Accelerance (dB)		
	Mode I	Mode II	Mode III
Fuselage tip	6.0	20.3	6.7
Fuselage center	-3.1	20.7	8.8
Wing tip	5.1	21.1	8.7

Finally, to demonstrate the effectiveness of the proposed SATMD and the ability to derive the response of the numerical system of Eq. (6.10) in time domain, numerical time integration was considered with the Newmark implicit method, as described in [148] (Appendix B). Dirac excitation was considered, and the results in Figure 6.13a, b and c illustrate the response of the tip of the airframe in the baseline, the Short Circuit and combined 360mH and 20 Ohm impedance system, respectively. It is shown that the system with the SATMD (Figure 6.13c) achieves a certain amplitude of acceleration twice faster than the passive TMD system (Figure 6.13b), and four times faster than the baseline system, thus proving the high performance of the SATMD (Figure 6.13a). In summary, the previous results have demonstrated the great potential of the proposed electromechanical SATMD to provide multi-modal vibration control capabilities to the whole body of a large flexible structure, through proper combination of the R, L values.

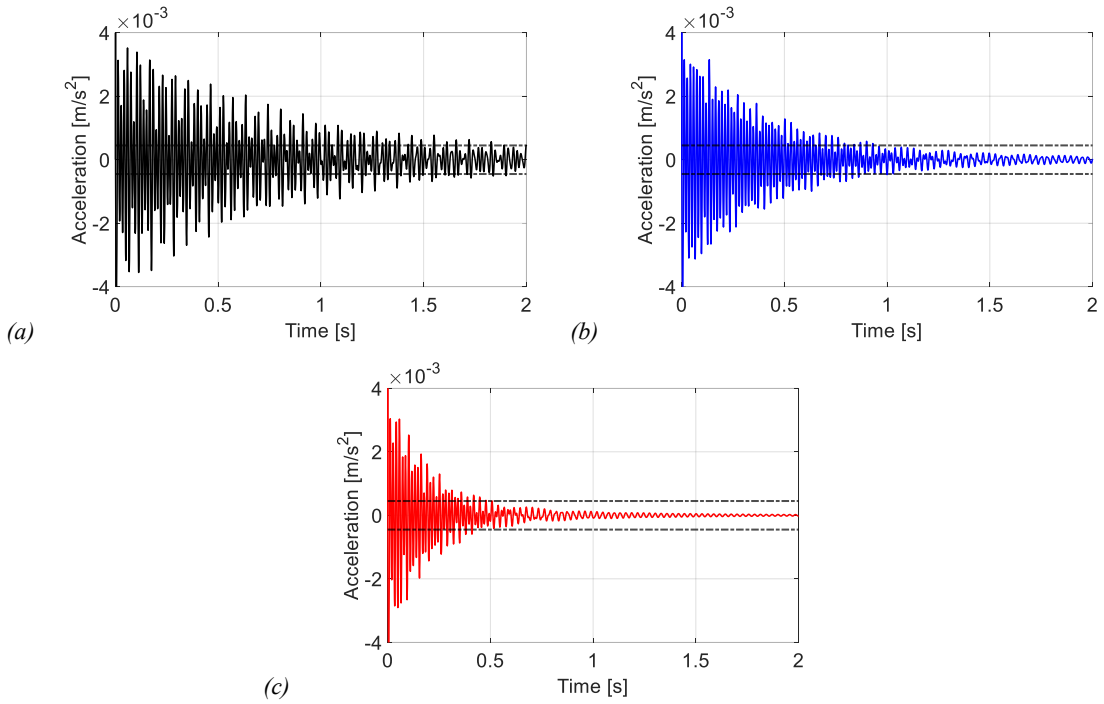


Figure 6.13: Acceleration response of the fuselage tip to Dirac Excitation. (a) Baseline system, (b) Short Circuit system; (c) SATMD system.

6.2.4 Multi-Tonal Excitation

Forced multi-tonal vibrations are a common problem in flexible structures such as lightweight means of transportation, where engines and rotors function under constant or frequency-varying harmonic excitations. Some undesirable effects of tonal excitations are human discomfort and material wear due to fatigue. The piezoelectric SATMD is studied in this Section for its ability to suppress tonal excitations in distinct frequency ranges.

6.2.4.1 Baseline Performance with Passive TMD

Here, the experimental setup is the same as the one used in Section 6.2.1. The finite element model used to simulate the structural dynamics is the same as the one used in Section 6.2.2, however in this case, the truncated mode superposition model, encompasses all structural modes in the frequency range of 20Hz to 180Hz. The modal damping values of the baseline structure were extracted from measured FRF results. The modal characteristics of the structure are shown in Table 6.6.

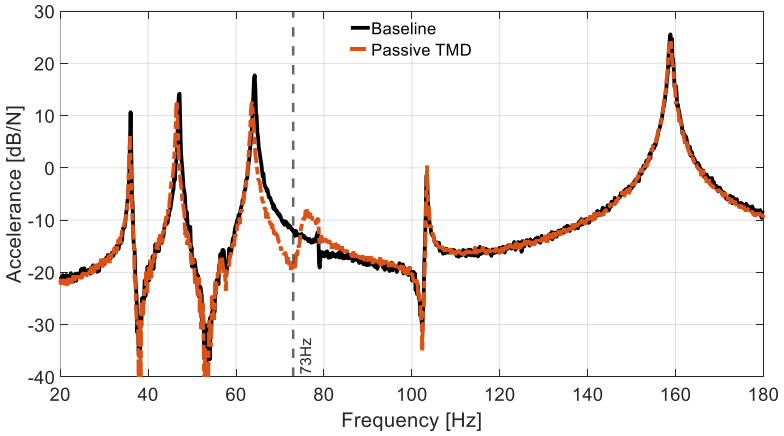
The developed antivibration device with the APA1500L piezoelectric transducer is used in this study as well, mounted on a plastic connector, which is in turn attached to the fuselage tip. As a result, the antivibration device equivalent stiffness remains intact in comparison to Section 6.2.3.1, whereas the equivalent damping term slightly changes (Table 6.7). The focus is on the suppression of tonal vibrations with harmonic frequencies, as the capability of the SATMD to suppress broadband vibrations

has already been investigated. For this reason, the auxiliary mass was selected as seen in Table 6.7, such that the short-circuited device (Passive TMD behavior with eliminated piezoelectric coupling) introduces an anti-resonance at 73Hz, not coinciding with the host structure eigenfrequencies. The measured and predicted from Equation (6.10) FRFs of the structure with the attached short-circuited SATMD are compared in Figure 6.14, demonstrating great agreement. As expected, a single antiresonance is introduced at the short-circuited modal frequency of the SATMD.

Table 6.6. Modal Characteristics of the studied modal frequencies.

Mode	**Frequency [Hz]**	**Mass[kg]**	**Damping [Ns/m]**	**Stiffness [kN/m]**
1	35.9	3.1	3.7	156.9
2	47.0	12.4	18.0	1076.0
3	64.4	0.6	1.9	100.5
4	78.9	4.0	2.0	976.5
5	103.2	2.4	3.0	1010.4
6	158.8	17.1	45.0	17019.2

(a)



(b)

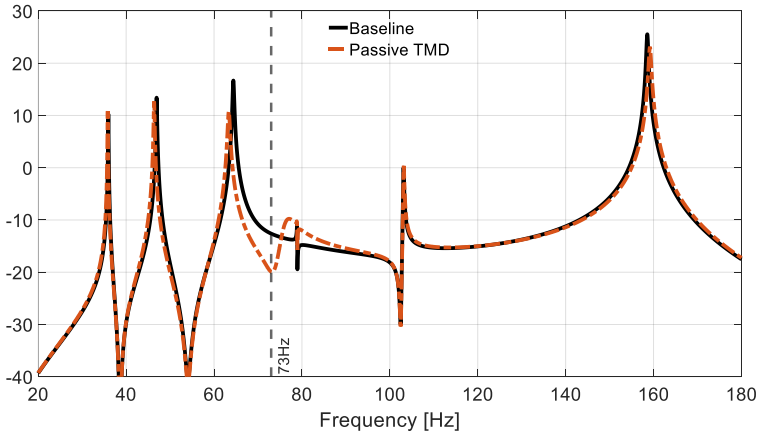


Figure 6.14. Frequency response (acceleration) of the fuselage tip without (Baseline) and with the passive TMD. (a) Experimental results; (b) Simulation results.

Table 6.7. SATMD Specifications.

Auxiliary mass m_d [kg]	0.46
Equivalent total Damping c_d [Ns/m]	7
Equivalent mechanical Stiffness k_d [kN/m]	100

6.2.4.2 Inductance Effect

As explained in Section 4.5.2, the SATMD introduces two inductance-dependent electromechanically coupled modes and modal frequencies. The inductance effect of the 0.46kg SATMD on the host structure is illustrated in Figure 6.15, which depicts the predicted frequency response by Equation (6.10) of the airframe tip, that corresponds to various inductance values for the case of negligible resistance. The frequency peaks are indicated by the red and yellow colors, whereas the blue areas imply lower amplitude of vibrations.

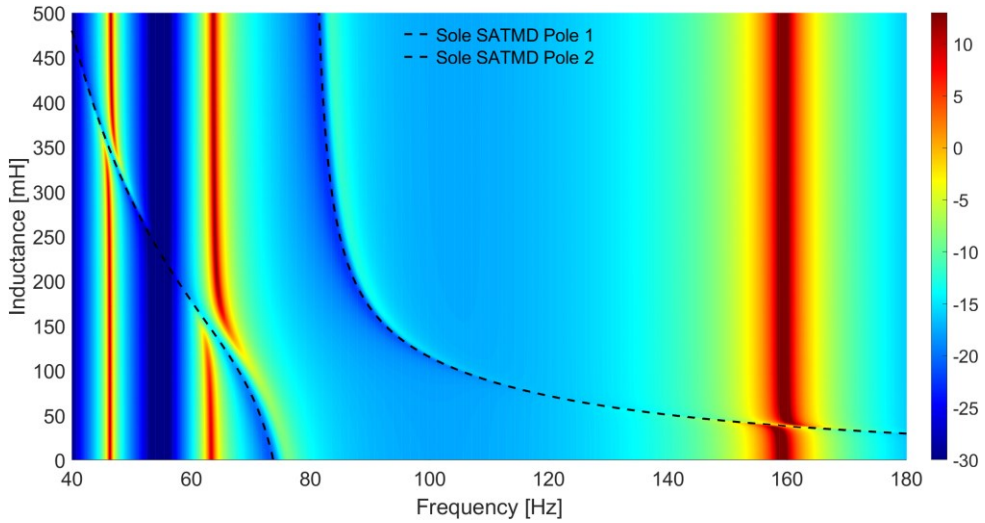
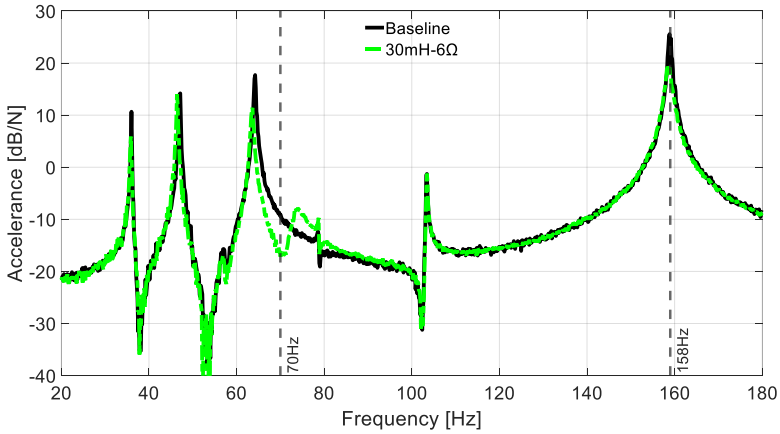


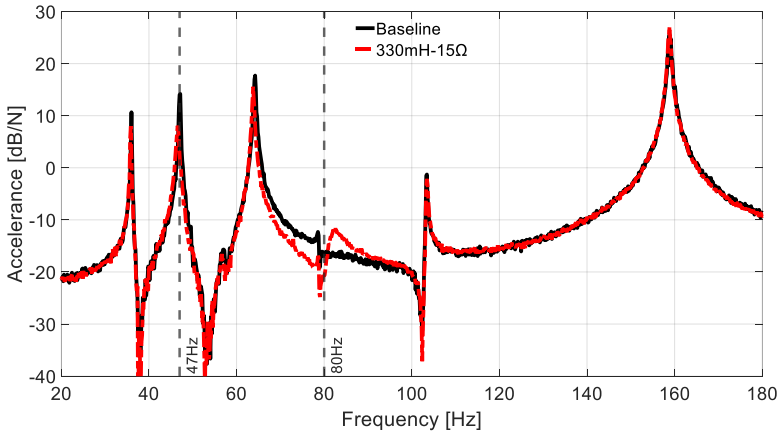
Figure 6.15. Inductance effect on frequency response of the fuselage tip (colored results) and the sole SATMD eigenfrequencies with the same auxiliary mass (black dashed curves).

For zero inductance in Figure 6.15, the auxiliary mass mode is evident in the host structure response as an anti-resonance, depicted in the blue color area at 73Hz, as also shown in Figure 6.14. As the inductance increases, the second electromechanical mode appears as a second anti-resonance in the 20-180Hz range and crosses the 158Hz structural mode at L=35mH, highly reducing its amplitude. For higher inductance values, the electromechanical anti-resonance frequency reduces rapidly and finally stabilizes near 80Hz. At the same time, the mechanical anti-resonance is shifting to lower frequency vicinities, progressively approaching and crossing the 64Hz structural mode at approximately 130mH, and finally crosses the 47Hz structural mode at approximately 330mH. Figure 6.15 also depicts, in the black dashed curves, the sole SATMD poles and their frequency shifting, for increasing inductance

values (Equation 4.28), exhibiting the studied auxiliary mass and equivalent stiffness. As shown in Figure 6.15, for all inductance values, the two poles of the sole SATMD coincide with the two induced anti-resonances to the host structure. This advances the already proved independence of the inductance tuning of the SATMD from the host lumped mass structure, to any multi-DOF structure. As a result, the inductance needed to tune the antivibration device to specific frequencies depends only on the SATMD characteristics, meaning that the host structure dynamic characteristics are not needed for tuning. The frequency manipulation of the two introduced anti-resonances with simple inductance alterations yields the semi-active capabilities of the SATMD and demonstrates its adaptability to potential frequency fluctuations. Furthermore, Figure 6.15 demonstrates that the SATMD poles maintain distinct frequency values and can simultaneously suppress vibrations at two distinct tonal frequencies, below and above the modal frequency of the short-circuited SATMD. This SATMD attribute could also prove beneficial to tonal frequencies with high amplitude harmonics, as in the case of the helicopter.



(a)



(b)

Figure 6.16. Experimental inductance effect on the frequency response functions of the fuselage tip acceleration, with the Passive TMD tuned to 73Hz; (a) 30 mH - 6 Ohm; (b) 330mH - 15 Ohm.

The computational results are duplicated in experiments, involving assemblies of 10mH coils attached to the SATMD device, to yield various inductance values. For the shake of brevity, only the measured frequency responses of the airframe tip with a low and high inductance attached to the SATMD are

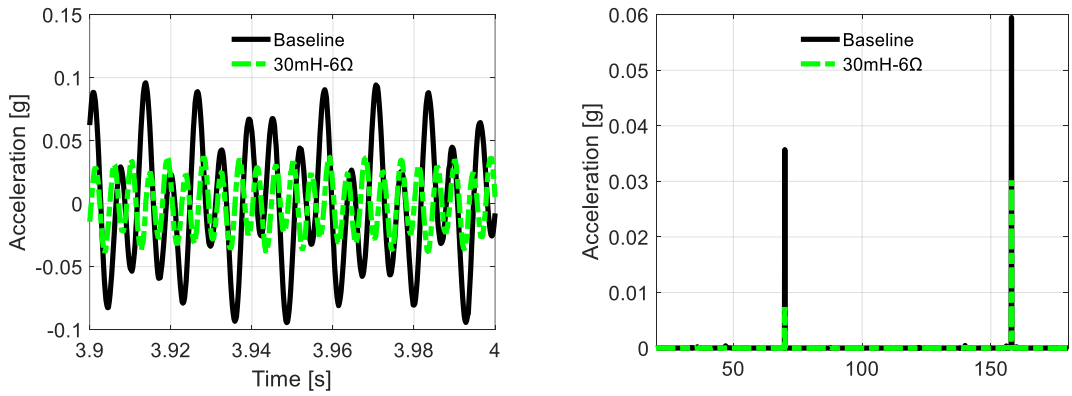
illustrated in Figure 6.16. The measured resistance of coil assemblies is also shown for the shake of completeness. For 30mH (green curve in Figure 6.16a), the first anti-resonance is shifted to slightly lower frequency bandwidth (70Hz), compared to the Passive TMD (73Hz), whereas the second electromechanical anti-resonance is in the vicinity of the 158Hz structural mode, lowering its amplitude. For 330mH (red curve in Figure 6.16b), the lower anti-resonance is shifted close to the 47Hz structural mode, highly reducing its amplitude, whereas the higher anti-resonance has approached its saturation value near 80Hz.

6.2.4.3 Simultaneous Suppression of Tonal Excitations

The simultaneous reduction of vibrations by two tonal excitations is studied numerically and experimentally for two different cases. In both cases, one tonal frequency is placed away from the modal frequencies and the second lies in the vicinity of one modal frequency. In the numerical simulations, Equation (6.10) is solved in time domain using the Newmark implicit numerical time integration method (Appendix), and the solution is transformed to the frequency domain via Fast Fourier Transformation (FFT). A similar experimental campaign was conducted for comparison and verification. Subsequently, a single tonal excitation is experimentally induced at a frequency with a very high amplitude first harmonic.

6.2.4.3.1 Tonal excitations at 70Hz and 158Hz

In this case the first tonal frequency is placed between modal frequencies 4 and 5 (Table 6.6), and the second tonal excitation is placed near the 6th modal frequency. Following the predicted antiresonance frequency in Figure 6.15, we apply the SATMD with the auxiliary mass as in Table 6.7, and a shunt circuit of 30mH and 6Ω. Figure 6.17 illustrate measured and simulated time and frequency responses of the resultant structure-SATMD system. Both simulated and experimental results show great simultaneous vibration reduction in each tonal frequency. Apparently, the inductance of the SATMD has provided the simultaneous reduction of the 2nd tonal frequency near the high modal frequency. Moreover, very good agreement between predicted and experimental results is illustrated in Figure 6.17.



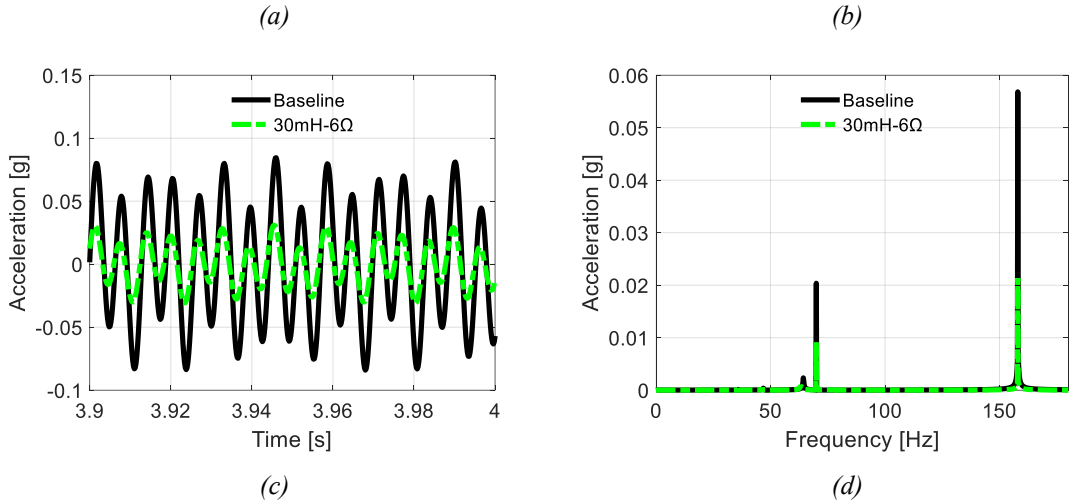
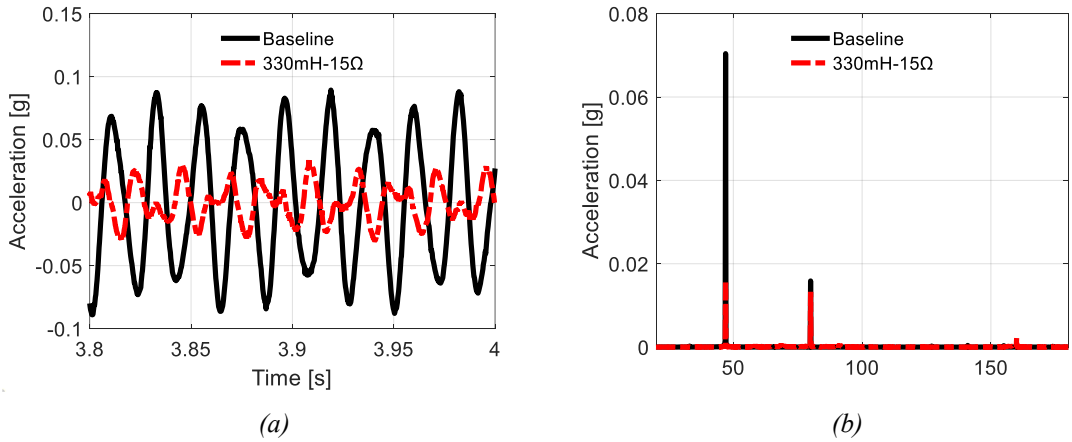
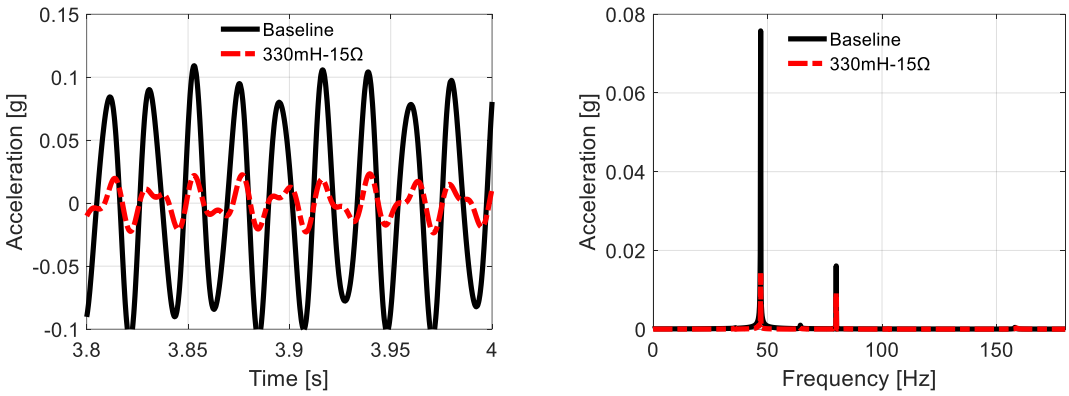


Figure 6.17. Predicted and measured tip acceleration under tonal excitations at 70Hz and 158Hz without and with the SATMD; (a), (b) Time- and frequency-domain measurements; (c), (d) Time- and frequency-domain simulation results.

6.2.4.3.2 Tonal excitations at 47Hz and 80Hz

As a second case study, the first tonal frequency is placed near the 2nd resonant frequency, and the second tonal frequency remains between the modal frequencies 4 and 5 of the model airframe (Table 6.6). The SATMD is again applied with the same auxiliary mass (0.46kg), and a shunt circuit of 330mH and 15Ω (red curve in Figure 6.16b). Similarly, to the previous case, simulated and experimental results are illustrated in the time and frequency domain in Figure 6.18. The 47Hz tonal excitation near the 2nd mode is highly attenuated (over 70%) by the shifting of the mechanical anti-resonance to lower frequency vicinity. Very good agreement between simulation and experimental results is again depicted in Figure 6.18. A remarkable conclusion of this case study is that the SATMD can achieve the suppression of the 47Hz tonal excitation using a much smaller auxiliary mass compared to a conventional TMD of the same stiffness, since the auxiliary mass needed to tune the same passive SATMD at 47Hz is 1.14kg, that is, almost 2.5 times of the 460g auxiliary mass of the SATMD.





(c) *(d)*

Figure 6.18. Predicted and measured tip acceleration under tonal excitations at 70Hz and 158Hz without and with the SATMD; (a), (b) Time- and frequency-domain measurements; (c), (d) Time- and frequency-domain simulation results.

Finally, it is important to stress that the experiments validate the predicted semi-active capabilities of the SATMD. Using the same auxiliary mass and only changing the shunt inductance, which could be realized with coils in series and a switch, the introduced anti-resonances can suppress tonal vibrations in a very broad frequency spectrum, both below and above the modal frequency of the short-circuited SATMD.

6.2.4.4 Single Tonal Excitation and High Amplitude Harmonic

To study the cases where harmonics of the fundamental tonal excitation frequency are excited, and the performance of the SATMD in such conditions, the 158Hz structural mode was decided to be excited as the 1st harmonic vibration. For this reason, a single tonal excitation is induced at 79Hz. To accomplish tuning of the device anti-resonances close to 79Hz and 158Hz simultaneously, an auxiliary mass of 350g was chosen, to initially tune the passive damper to 84Hz (purple curve in Figure 6.19), and 30mH inductance is applied, along to its intrinsic resistance (light blue curve in Figure 6.19). As seen in the frequency response of the structure, the selected mass and inductance achieve tuning of the SATMD to both 79Hz and 158Hz. To demonstrate the effectiveness of this configuration, a single tonal excitation at 79Hz is induced. Figure 6.20a illustrates the time domain experimental measurements without (black curve) and with the SATMD (light blue curve), while Figure 6.20b depicts their FFT transformations to the frequency domain. A single excitation at 79Hz yields two tonal vibrations, at 79Hz and at its 1st harmonic at 158Hz, as seen in the black curve of the FFT of Figure 6.20b. As shown in both Figure 6.20, both the tonal frequency and its 1st harmonic are satisfactorily reduced, demonstrating the SATMD capabilities in such vibrating conditions.

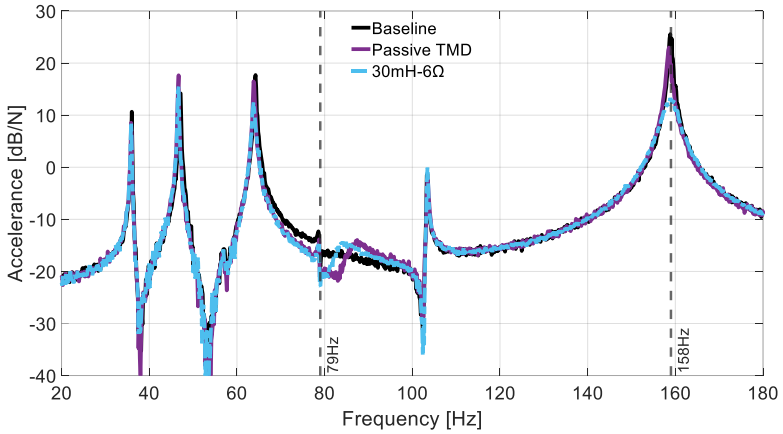
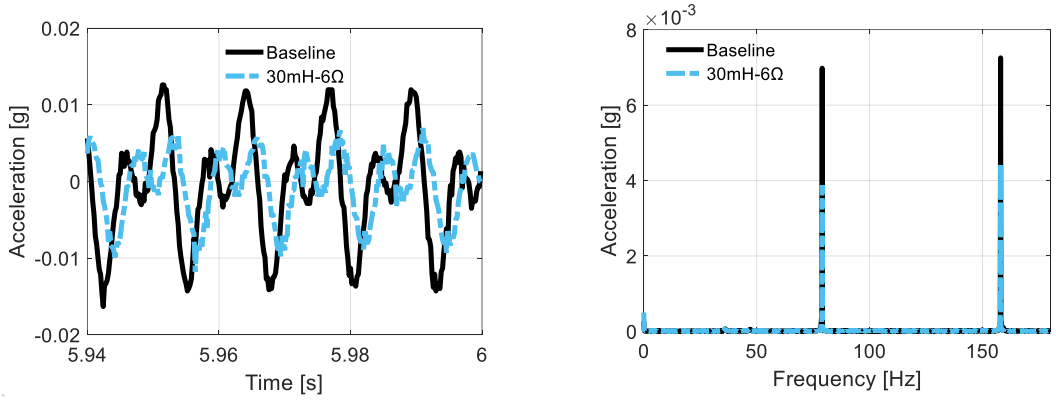


Figure 6.19. Experimental inductance effect on the frequency response functions of the fuselage tip acceleration, with the Passive TMD tuned to 84Hz; 30 mH - 6 Ohm.



(a) *(b)*

Figure 6.20. Measured tip acceleration under tonal excitations at 79Hz and 158Hz without and with the SATMD; (a), (b) Time domain measurements; (b) Frequency domain results.

6.3 Field Application on a BO-105 S Helicopter Structure

The demonstrated performance of the two anti-resonances can provide beneficial results to structures which function under multiple tonal vibrations, such as helicopters. In most helicopter configurations, the predominant vibratory loads originate from the main rotor speed and its harmonics. More specifically, for a rotor of N_b blades, the highest vibrations are manifested in $i * N_b / rev$ frequencies, where $i = 1, 2, \ldots$ [149]. The impact of higher harmonics is often less important, since high frequency vibrations are less perceptible by pilots and passengers, unless they excite a high amplitude structural mode. Despite advancements in design technologies aimed at mitigating vibrations, the incorporation of devices for vibration attenuation continues to be a prevailing norm within the rotorcraft industry. Such techniques include modifications of blade dynamics [150], [151], rotor isolation [152], [153], and fuselage vibration suppression [154]. More information on the passive, active, and semi-active anti-vibration methods on helicopters can be found [155].



(a) *(b)*

Figure 6.21. BO 105 S Helicopter used for the experimental campaign; (a) Front view; (b) Rear view and SATMD position.

For a field application, the SATMD device was tested on a BO105 S [156] helicopter to evaluate the device performance on a real large flexible structure. Although rotorcrafts are designed to avoid resonance with engine frequencies, most helicopters still function under heavy oscillations compared to airplanes [157]. In the framework of the TRANVIC Project [158], two approximately 20-minutes flights, without and with the SATMD, respectively, took place at the general airport of Pachi, in Megara, Greece. Figure 6.21 illustrates the BO 105 S helicopter, where the experiments were conducted. Major limitations for the position of the SATMD application were the minimal interference with the existing structure, and the limited space in the cabin area. To this end, the SATMD was decided to be firmly attached in vertical direction at the luggage area and specifically at the position seen in Figure 6.21b, to mitigate the vertical vibrations of the helicopter airframe. The accelerometer was attached at the same position, to evaluate the vibratory behavior of the airframe during flight conditions without and with the SATMD. A high speed DAQ board was used to perform the testing campaign operating on NI LabVIEW platform, using 5120Hz sampling rate, with frame size 30000 samples for the generated FFTs.

The Project's focus was on the forward cruise speed movement. Without the SATMD, typical results of the accelerometer in cruise speed conditions are illustrated in Figure 6.22 up to 100Hz. Measured vibrations are integer multiples of 7Hz (main rotor rotation speed), and the highest amplitude accelerations are observed at 28Hz (4/rev), 56Hz (8/rev) and 84Hz (12/rev).

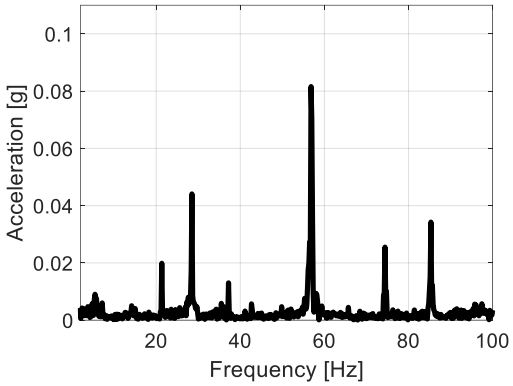


Figure 6.22. FFT vertical acceleration of BO 105 S during cruise speed conditions without the SATMD.

Considering the simultaneous distant frequency vibration control capabilities of the SATMD, the tonal vibrations at 56Hz and 84Hz were decided to be suppressed. Selecting an auxiliary mass of 0.7kg, the Passive TMD anti-resonance is tuned at 60Hz. Adding 150mH to the shunt circuit, the SATMD poles are tuned to 55Hz and 86Hz (Equation 4.28), both of which are close to the targeted tonal vibrations. With the SATMD firmly attached to the surface of the luggage area, the effect of the Passive TMD and 150mH SATMD in cruise speed conditions are depicted in Figure 6.23a and b, respectively. It is observed that the Passive TMD has minimal effect to the tonal vibrations, and only noticeable vibration reduction is achieved in the tonal vibration of 56Hz, since the passive device is not accurately tuned. Great vibration reduction is illustrated with the 150mH SATMD in Figure 6.23b, where the inductance shifts the mechanical resonator to 55Hz, and simultaneously tunes the electromechanical resonator to 86Hz. As a result, the SATMD has achieved approximately 60% reduction (or 8dB) in the amplitudes of the helicopter vibrations at 56Hz and 84Hz, leading to beneficial vibration attenuation.

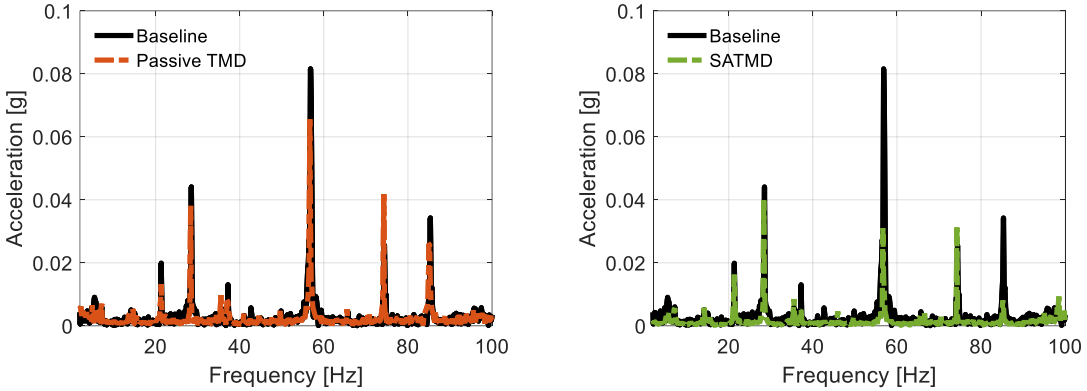


Figure 6.23. FFT vertical acceleration of BO 105 S during cruise speed condition. (a) Passive TMD with 0.7kg auxiliary mass; (b) SATMD with 0.7kg auxiliary mass and 150 mH inductance.

6.4 Concluding Remarks

This Chapter demonstrated the performance of the studied antivibration device on large and flexible structures, such as aircrafts and helicopters. For the computational model, a reduced-ordered modal space structural dynamics model is formulated, coupled with the SATMD device, and the RL shunt electric circuit. A scaled-down airframe prototype was fabricated to act as the laboratory large and flexible structure for the antivibration device testing. As the lightweight means of transportation are expected to function under unsteady broadband aerodynamic conditions and / or tonal excitations due to engines and rotors, both white noise and multi-tonal loads were applied to the lab-scale airframe structure. In broadband excitation conditions, the studied SATMD achieved, both experimentally and numerically, multi-modal vibration control and damping in three major structural modes. In multi-tonal vibrations, the SATMD can highly suppress excessive vibrations in two distinct frequency vicinities, thanks to the two introduced tunable resonant oscillators, namely the auxiliary mass and the shunt circuit eigenfrequency. The experimental measurements validated the developed model in all studied cases. Furthermore, it was shown that the two introduced antiresonances are independent of the host structure dynamic characteristics, and as a result the appropriate SATMD auxiliary mass and inductance can be decided based only on the structure frequency response. This special and versatile feature was used for the antivibration performance of the SATMD in a BO105 S helicopter, where, after discovering its critical frequencies, the auxiliary mass and shunt circuit inductance were accurately selected to suppress two excessive vibrations during real-flight conditions.

Chapter 7: SATMD Design Strategy

The design variables of the piezoelectric SATMD, namely (1) the location of its structural integration and (2) its electromechanical characteristics, are investigated and optimized in this Chapter. As a case study, the selected host structure is the down-scaled airframe prototype presented in the previous Chapter, which functions under broadband excitation. The position of the SATMD integration on the structure of interest is expected to highly affect the antivibration device performance. Given the selected piezoelectric device APA1500L, the tunable electromechanical properties of the antivibration device are the auxiliary mass and shunt impedance circuit. Nevertheless, the electromechanical characteristics of the piezoelectric device are also studied in this Chapter, since an appropriately designed custom piezoelectric transducer could yield higher vibration control results.

7.1 SATMD Position Selection

Selecting the placement of a TMD for improved vibration control results can be a challenging procedure in complex structures [61]. In the current study, the selection of the SATMD placement is decided based on the coupling terms of Equation (6.10) and the mode shapes of the targeted structural frequencies. Without loss of generality, and to further analyse the electromechanical coupling of Equation (6.10), the equations of a structure – SATMD system are formed, considering only 2 structural modes.

$$\begin{bmatrix} \bar{M}_1 & 0 & 0 & 0 \\ 0 & \bar{M}_2 & 0 & 0 \\ 0 & 0 & m_d & 0 \\ 0 & 0 & 0 & L \end{bmatrix} \begin{Bmatrix} \ddot{Q}_1 \\ \ddot{Q}_2 \\ \ddot{u}_d \\ \ddot{q}_{out} \end{Bmatrix} + \begin{bmatrix} \bar{C}_1 + c_d \Phi_{n_1}^2 & c_d \Phi_{n_1} \Phi_{n_2} & -c_d \Phi_{n_1} & 0 \\ c_d \Phi_{n_1} \Phi_{n_2} & \bar{C}_2 + c_d \Phi_{n_2}^2 & -c_d \Phi_{n_2} & 0 \\ -c_d \Phi_{n_1} & -c_d \Phi_{n_2} & c_d & 0 \\ 0 & 0 & 0 & R \end{bmatrix} \begin{Bmatrix} \dot{Q}_1 \\ \dot{Q}_2 \\ \dot{u}_d \\ \dot{q}_{out} \end{Bmatrix}$$
$$+ \begin{bmatrix} \bar{K}_1 + (k_d + \frac{\bar{e}^2}{C_p}) \Phi_{n_1}^2 & (k_d + \frac{\bar{e}^2}{C_p}) \Phi_{n_1} \Phi_{n_2} & -(k_d + \frac{\bar{e}^2}{C_p}) \Phi_{n_1} & \frac{\bar{e}}{C_p} \Phi_{n_1} \\ (k_d + \frac{\bar{e}^2}{C_p}) \Phi_{n_1} \Phi_{n_2} & \bar{K}_2 + (k_d + \frac{\bar{e}^2}{C_p}) \Phi_{n_2}^2 & -(k_d + \frac{\bar{e}^2}{C_p}) \Phi_{n_2} & \frac{\bar{e}}{C_p} \Phi_{n_2} \\ -(k_d + \frac{\bar{e}^2}{C_p}) \Phi_{n_1} & -(k_d + \frac{\bar{e}^2}{C_p}) \Phi_{n_2} & (k_d + \frac{\bar{e}^2}{C_p}) & -\frac{\bar{e}}{C_p} \\ \frac{\bar{e}}{C_p} \Phi_{n_1} & \frac{\bar{e}}{C_p} \Phi_{n_2} & -\frac{\bar{e}}{C_p} & \frac{1}{C_p} \end{bmatrix} \begin{Bmatrix} Q_1 \\ Q_2 \\ u_d \\ q_{out} \end{Bmatrix} = \begin{Bmatrix} P_1 \\ P_2 \\ 0 \\ 0 \end{Bmatrix} \quad (7.1)$$

In Equation (7.1) Φ_{n_1} , Φ_{n_2} are the amplitudes of the mode shapes of modes 1, 2, respectively, at the *n* DOF of the structural system, where the SATMD is positioned. Taking into consideration that: (i) the

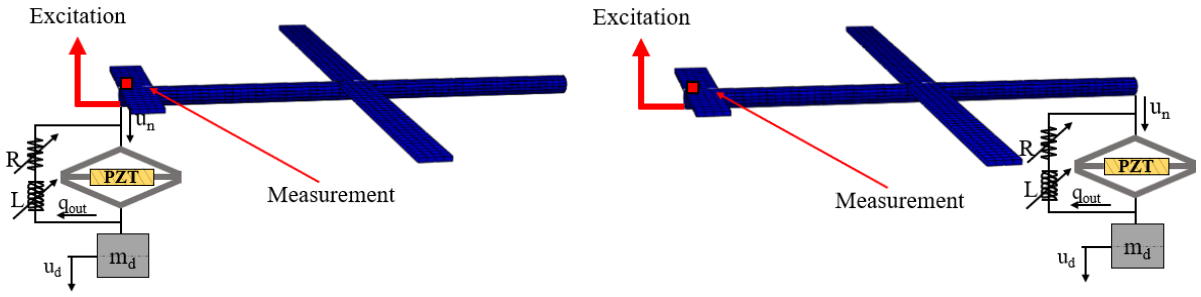
mode shape amplitudes augment the coupling terms between the structural modes and the auxiliary mass (elements (1,3) and (2,3) in damping and stiffness matrix), and between the structural modes and the shunt circuit (elements (1,4) and (2,4) in stiffness matrix), and (ii) high coupling and interaction between the structural modes and the SATMD is desirable, such that the energy conversion and the potential for vibration control is maximized, it is easily understood that the SATMD should be attached to the airframe structure at a position where all the respective modal deflections Φ_n have high values, ideally equal to 1.

To support this argument, the case studies below are presented for the scaled-down airframe model, which is also studied for the SATMD design. Examining the mode shapes of the targeted eigenfrequencies in Figure 6.4, only two positions with relatively high amplitude are observed on the fuselage for all three Modes: the fuselage tip and the fuselage tail. The amplitudes of the mode shapes at these positions in the vertical direction are presented in Table 7.1. The black curves in Figure 7.2 illustrates the frequency response of the middle point of the fuselage tail, when a broadband excitation is applied at the same point (Figure 7.1). Selecting an auxiliary mass for the SATMD to tune the structural Mode II, the tail frequency response for the passive TMD is shown in Figure 7.2a, for the device attachment at the fuselage tail (Figure 7.1a) with the red curve and at the fuselage tip (Figure 7.1b) with the blue curve. Therefore, the only alteration at the solved Equation (6.10) is the $\boldsymbol{\Phi}_n$ line-vector. The results in Figure 7.2a clearly demonstrate that the attachment of the passive TMD to the fuselage tip, which exhibits higher amplitude at Mode II than the respective amplitude of the tail, yields better vibration control results at the targeted structural Mode. Even though the excitation and measurement coincide, the SATMD position for optimal performance is not at the same position, but at the position of the maximum amplitude of the targeted mode shape. Continuing the study for the SATMD position that concerns the electromechanical coupling, and maintaining the SATMD auxiliary mass and positions as shown in Figure 7.1, the inductance to tune the structural Mode III can be found by the sole SATMD characteristic equation (4.28) as L = 276 mH. The frequency response with the selected auxiliary mass and 276 mH at the fuselage tip is shown in Figure 7.2b, where the results with the SATMD at tail (Figure 7.1a) are depicted with red color, and the results with SATMD at tip (Figure 7.1b) are depicted with blue color. It is clearly illustrated that the SATMD at the tail, which has higher mode shape amplitude at Mode III, yields better antivibration results. Although the passive TMD had better performance at the tip for Mode II (Figure 7.2a), its results are outperformed in Mode III by the SATMD at the tail, verifying that the vibration control efficiency is augmented by the amplitude of the mode shapes.

Table 7.1. Amplitude of mode shapes at fuselage tip and tail.

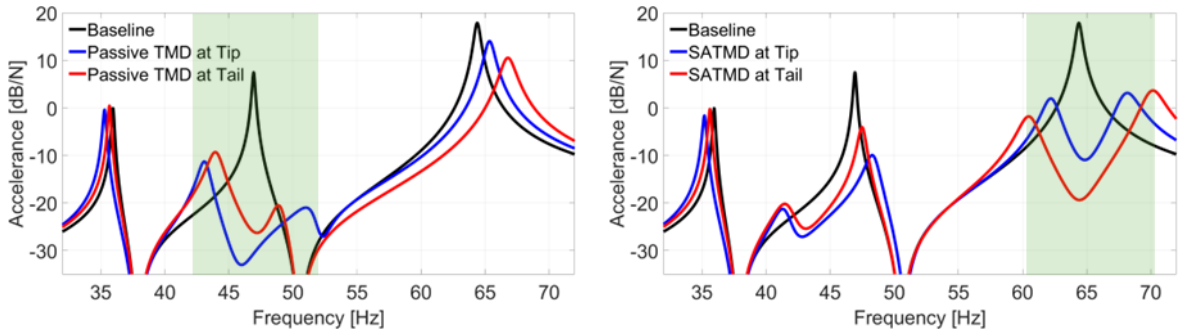
	Mode I	Mode II	Mode III
Tip	0.198	0.628	-0.113

Tail	0.127	0.380	0.192



(a) *(b)*

Figure 7.1. Scaled-down airframe model with the excitation and measurement coinciding at the middle of the airframe tail, and the SATMD attached to different positions. (a) SATMD at tail; (b) SATMD at tip.



(a) *(b)*

Figure 7.2. Numerical results of the airframe model, with the auxiliary mass selected to tune Mode II, and the SATMD positions presented in Figure 7.1. (a) Passive TMD performance; (b) SATMD performance, selecting inductance to tune Mode III.

The examined case studies indicate that the SATMD that aims at the vibration reduction of a specific structural mode should be placed at the host structure position which exhibits the highest mode shape amplitude for this mode. In the current study, the SATMD optimization aims at the simultaneous multi-modal vibration control of three structural modes of the down-scaled airframe, namely Modes I, II, and III. Setting a weight $w_i = 1$ for each one of the three targeted modes, the summed amplitudes of mode shapes for each n DOF of the fuselage of the host structure is calculated as:

$$\Phi_{n,total} = \sum_{i=1}^{3} w_i \Phi_{n_i} \tag{7.2}$$

Examining only the vertical DOFs of the fuselage, since the SATMD is placed in vertical direction on the fuselage, such that no imbalances occur, the maximum $\Phi_{n,total}$ is achieved for the fuselage tip. This

result is expected, observing the mode shapes of the host structure (Figure 6.4). Therefore, the optimal position of the SATMD for multi-modal vibration control is the fuselage tip.

7.2 SATMD Electromechanical Properties

Continuing to the selection of the electromechanical properties of the piezoelectric SATMD, these are: $m_d, R, L, C_p, \overline{e}$. Aiming at multi-modal vibration control with such a complex antivibration device, a multi-parameter optimization is needed. However, having gathered the knowledge of the shunt impedance effects to the host structure in the previous Chapters, an ad-hoc design strategy for each one of the SATMD tunable electromechanical properties is first attempted. Then the optimal parameters emerge through optimization algorithms, and their results are compared to the ad-hoc design.

7.2.1 SATMD Properties from Ad-Hoc Design

Having selected a piezoelectric device, the only tunable SATMD properties are m_d, R, L . As observed by the sole SATMD characteristic equation (4.28), the auxiliary mass and inductance define the SATMD eigenfrequencies, and as proved in Section 5.1.2, the host structure antiresonances. The resistance introduces damping to the host structure response, which is critical for the broadband vibration control. As a consequence, the $m_d - L$ effect to the host structure is first analyzed. After selecting a pair of these inertia values, the resistance is chosen next.

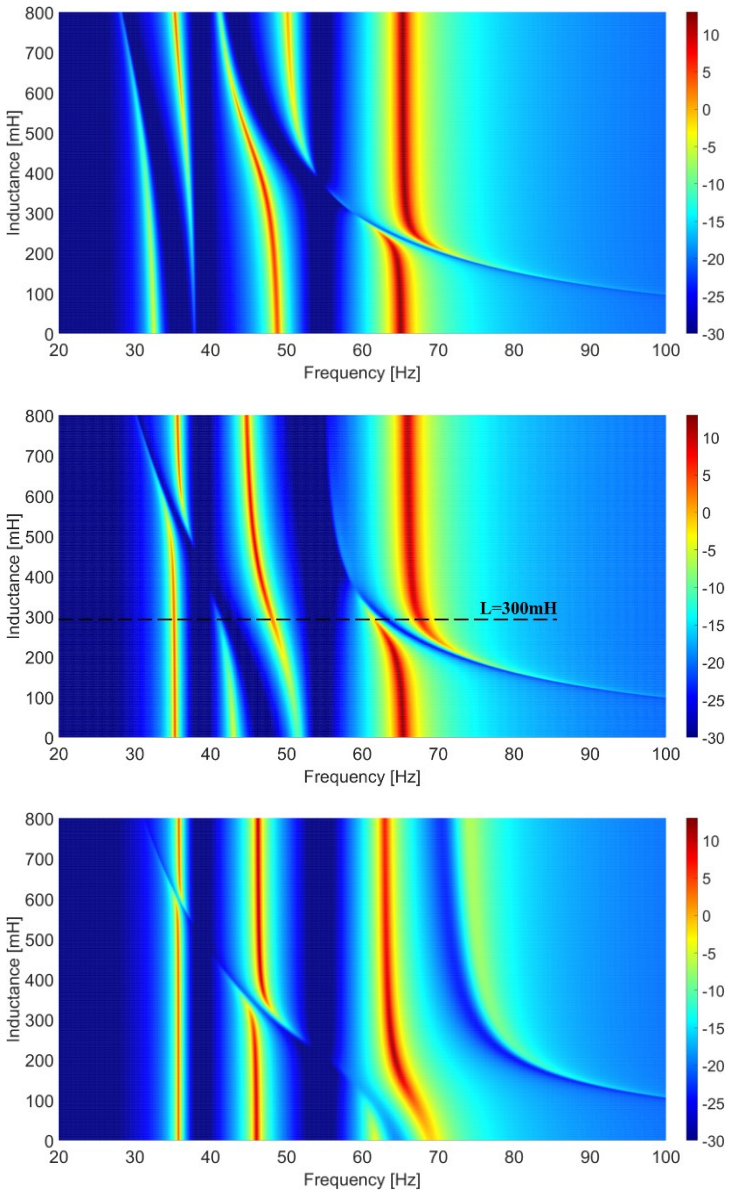
7.2.1.1 Auxiliary Mass and Inductance

Since searching the $m_d - L$ results for all auxiliary mass values is impractical, the auxiliary mass is selected to passively suppress the three targeted structural Modes (Table 7.2). For each auxiliary mass, the inductance is subsequently investigated. The frequency response of the fuselage tip for various inductance values for each of the selected auxiliary masses are presented in Figure 7.3a, b, c, respectively. In all three presented cases, both introduced antiresonances descend to lower frequency ranges as inductance increases, however the rate of shifting is different in each case. Passively tuning the SATMD to Mode I (Figure 7.3a), the antiresonance that surfs across the higher structural Mode at 65 Hz has small width compared to Figure 7.3b and c, therefore it can absorb trivial energy from this Mode. Taking also into consideration the large auxiliary mass that this Mode needs, this option is factored out. Passively tuning the SATMD to Mode III (Figure 7.3c), it is observed that only one antiresonance passes through all the targeted modes, therefore the simultaneous tuning of the SATMD to at least two structural Modes is impossible. Finally, tuning the SATMD to Mode II (Figure 7.3b), it

is easily observed that for approximately 300 mH, one antiresonance passes through Mode III, while the other is still near Mode II, absorbing high energy from it. For this reason, this is the value that is selected for inductance in the ad-hoc design, while the ad-hoc design auxiliary mass is the one passively tuning the SATMD to Mode II (1.14kg).

Table 7.2. Auxiliary masses to tune different structural Modes.

	Mode I	Mode II	Mode III
Auxiliary Mass [kg] m_d	1.93	1.14	0.60



(a)

(b)

(c)

Figure 7.3. Inductance effect on the fuselage tip, selecting different auxiliary masses for the SATMD. (a) Auxiliary mass for Mode I; (b) Auxiliary mass for Mode II; (c) Auxiliary mass for Mode III.

The frequency response of the electric current for various shunt circuit inductance values is presented in Figure 7.4 for the selected auxiliary mass. The red and dark red areas indicate the frequencies where the electrical component of the system is distributed. For 300 mH, the largest electrical components are exhibited for the frequencies between 50 Hz and 70 Hz, while smaller amounts of electric energy are also witnessed at the structural Modes. As a result, added resistance in this configuration is expected to dissipate energy from all Modes and dampen them, while more damping is expected near Modes II and III.

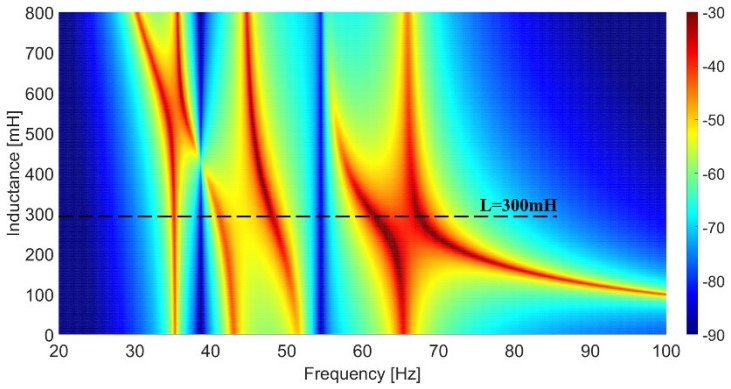


Figure 7.4. Inductance effect on the electric current when the auxiliary mass tunes the SATMD to Mode II.

7.2.1.2 Resistance

The frequency response of the airframe tip is shown in Figure 7.5 for various resistance values, having selected the designed $m_d - L$ values from the previous subsection.

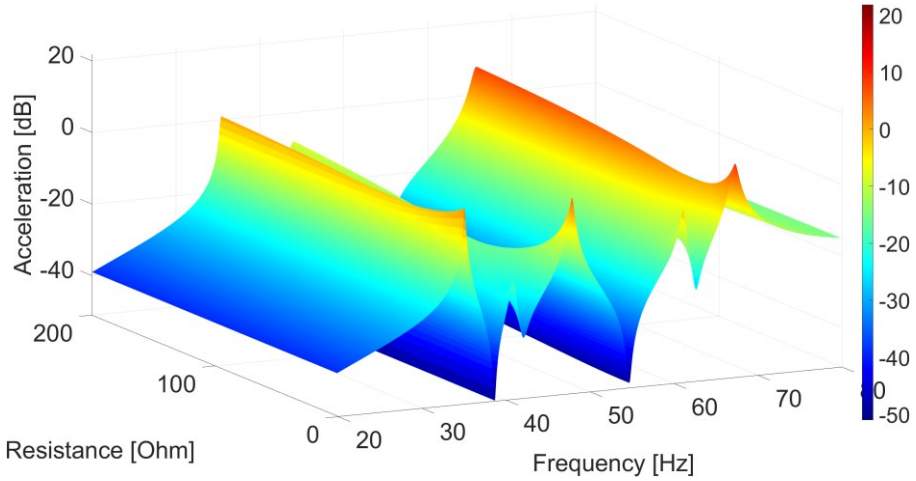


Figure 7.5. Resistance effect on the fuselage tip for auxiliary mass that tune the SATMD to Mode II, and inductance that tunes the Mode III.

For negligible resistance, the two structural antiresonances are present in Modes II and III, reducing the accelerations around the respective modes. Adding small resistance to the shunt circuit, the remaining peaks of these Modes are further reduced, while the peak in Mode I is also reduced, as seen in Figure 7.5. As expected from the current Figure 7.4, higher damping is observed near the structural Modes II

and III. Increasing further the resistance, all structural peaks are progressively increased again, due to the phenomenal stiffening, as described in Sections 5.4 and 5.6, which dominates the system response.

The summation of the fuselage tip frequency acceleration across the whole studied frequency range for a single resistance value R_i is calculated as:

$$\ddot{u}_{R_i,tip,total} = \sum_{f_i=30Hz}^{75Hz} |\ddot{u}_{R_i,tip,f_i}| \tag{7.3}$$

The ad-hoc design resistance value is selected as the one that minimizes the above equation:

$$R_{ad-hoc} = R_{\min(\ddot{u}_{R_i,tip,total})} \tag{7.4}$$

and is shown in Table 7.3. The performance of the ad-hoc design SATMD values is depicted in Figure 7.6. The passive TMD (blue curve) creates an antiresonance at Mode II, whereas the L-SATMD (red curve) brings the second antiresonance to Mode III, while the initial antiresonance has remained in the vicinity of Mode II, producing high reduction to both Modes. Adding the ad-hoc design value of resistance (green curve), Mode I is satisfactorily reduced, while further reduction is depicted in Modes II and III. Although optimization routines are expected to produce higher vibration control results, the ad-hoc design values present decent vibration control performance.

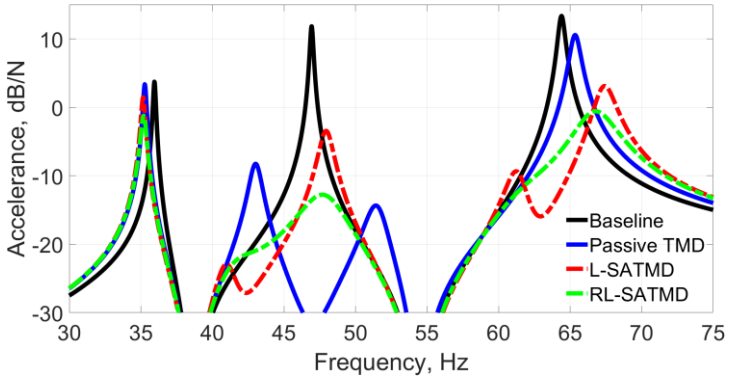


Figure 7.6. Frequency response (acceleration) of fuselage tip without the SATMD and with various designed shunt circuit configurations of the SATMD, selecting auxiliary mass to tune Mode II (the passive TMD, the L-SATMD, and RL-SATMD).

7.2.2 SATMD Properties from Optimal Design

The optimal SATMD parameters for multi-modal vibration control under broadband excitation emerge through the minimization of the below objective function:

$$\min f(SATMD_{parameters}) = \sum_{f_i=30Hz}^{75Hz} |\ddot{u}_{tip,f_i}| \tag{7.5}$$

where the $SATMD_{parameters}$ are combinations of the available electromechanical properties $m_d, R, L, C, \bar{e}$. The optimization is performed utilizing the Sequential Quadratic Programming (SQP), executed for 30 different starting points, and aiming to a global minimum provided by the MATLAB *fmincon* function. Finally, the constraint of at least 6 dB reduction in each structural Mode with the SATMD is applied in the optimization algorithms that include C and $\bar{e}$ as optimization parameters.

7.2.2.1 Auxiliary Mass as Selected in the Ad-Hoc Design

For comparison to the results with the ad-hoc design auxiliary mass, the optimization is initially performed for several combinations of the available parameters, and for m_d = 1.14 kg.

7.2.2.1.1 R-L Shunt Impedance

The SATMD performance with the selected auxiliary mass and optimal R-L parameters is depicted in Figure 7.7 with the dark yellow color, while the R-L parameters are shown in Table 7.3. The results illustrate that, for higher vibration control performance, Mode III should be highly reduced. No dB reduction constraint is used in this optimization scheme, to exploit the real optimal vibration control capabilities of the SATMD with the selected auxiliary mass. The optimal SATMD parameters are illustrated in Table 7.3, whereas the reductions in each Mode are depicted in Table 7.4. The comparable results with the ad-hoc design and optimal R-L demonstrate the success of the ad-hoc design strategy.

Table 7.3. Ad-hoc and optimal SATMD parameters, with selected auxiliary mass.

	m_d [kg]	R [Ohm]	L [mH]	C [μF]	$\bar{e}$ [N/V]
Designed SATMD	1.14	25	300	27	0.65
Unconstrained Optimal RL SATMD	1.14	21.2	258	27	0.65
Constrained Optimal RLC SATMD	1.14	47.6	476	17	0.65
Custom Optimal SATMD	1.14	46.1	320	26.6	0.99

7.2.2.1.2 R-L-C Shunt Impedance

A change in the shunt circuit capacitance could improve the vibration control performance. Such alteration can be realized in three different ways:

I. Selecting a different piezoelectric device. Selecting different number, materials or dimensions of piezoelectric layers or stacks would yield a new equivalent capacitance C_p. However, the rest of the equivalent electromechanical properties ($k_d, \bar{e}$) would also experience changes, therefore new design or optimization would be needed with the new system parameters.

II. Adding capacitors to the existing R-L circuit. The total system capacitance will be increased, since the new capacitors will be connected in parallel to the inherent piezoelectric capacitance (and the net capacitance is the sum of all individual capacitances), no matter how the connection of the new capacitors to the existing shunt circuit is achieved (parallel or series). Increasing the system capacitance is not expected to yield better electromechanical coupling and vibration mitigation results, for the reasons described in Section 4.2.1.

III. Adding negative capacitance to the system. The use of negative capacitance in various configurations enables the attenuation performance of the shunt circuit to be increased [103], [105]. De Marneffe and Preumont [104] analysed pure negative capacitors, whereas other authors focused on more complex circuits, entailing complex negative impedances, entailing significant levels of resistance [100], [106], [159]. A negative capacitor is practically realised with an operational amplifier, which needs an external power supply, and poses issues relating to the possible instabilities in the electromechanical system, because of its active nature [105].

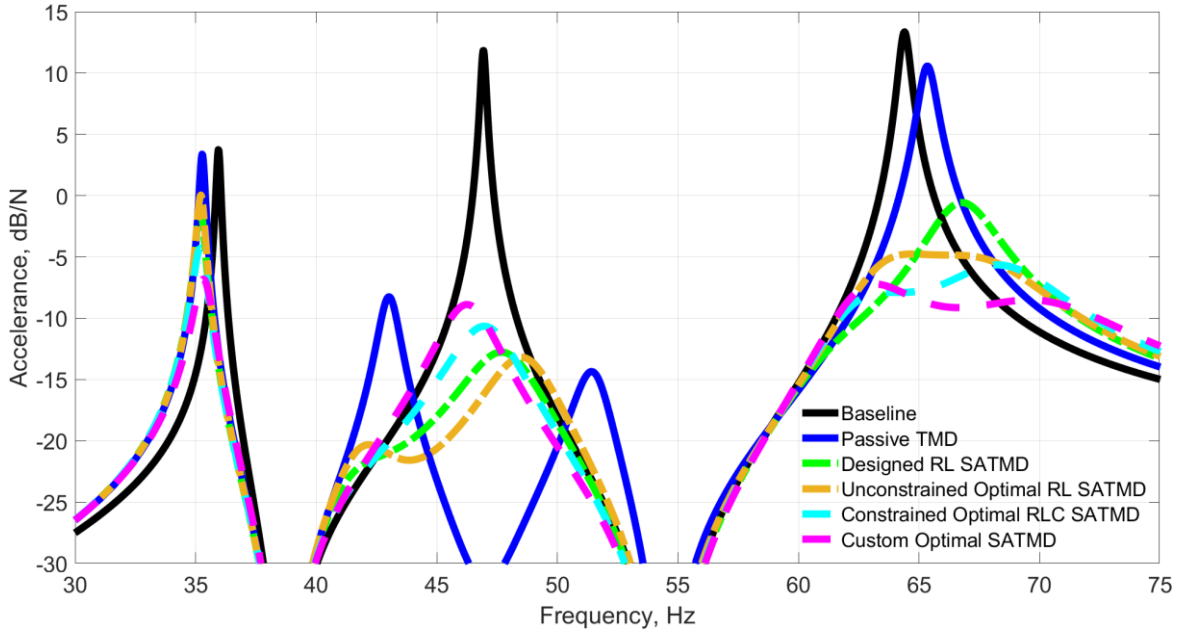


Figure 7.7. Frequency response (acceleration) of fuselage tip without the SATMD and with various shunt circuit configurations of the SATMD, selecting auxiliary mass to tune Mode II (the passive TMD, the designed RL-SATMD, and the optimal SATMDs with progressively ascending number of optimization parameters).

Taking the above into account, a computational study takes place, where the system capacitance C is considered as an optimization parameter together with the R-L values and for the selected auxiliary mass (Equation 7.5), without concerns of how the equivalent capacitance change is achieved, using the

selected piezoelectric device. The optimal R-L-C values are depicted in Table 7.3, and the system capacitance C is reduced, as expected. The effect to the fuselage tip with these optimal circuit values is illustrated in Figure 7.7 with the 6dB reduction in each Mode constraint and with cyan color, showing greater vibration reduction performance for structural Modes I and III, compared to the optimal R-L performance. Mode II exhibits higher acceleration, but still its reduction levels are still very high compared to the baseline value (Table 7.4).

Table 7.4. Reductions achieved in each structural Mode with various SATMD parameters, with selected auxiliary mass.

	Mode I		**Mode II**		**Mode III**	
	dB	**Mag %**	**dB**	**Mag %**	**dB**	**Mag %**
Designed SATMD	5.0	44%	24.3	94%	13.9	80%
Unconstrained Optimal RL SATMD	3.7	35%	25	95%	18.2	88%
Constrained Optimal RLC SATMD	8.0	60%	22.3	92%	19.0	89%
Custom Optimal SATMD	10.5	70%	20.7	91%	20.4	90%

7.2.2.1.3 Custom Piezoelectric Transducer with R-L-C Shunt Impedance

The last parameter of the SATMD is the equivalent piezoelectric coefficient $\bar{e}$. Such a change can be implemented only by using a different piezoelectric device, entailing different number, materials or dimensions of piezoelectric layers or stacks. To have a new equivalent piezoelectric coefficient, together with a new equivalent capacitor C_p, which will emerge by an optimization algorithm, would require the production of a new custom piezoelectric transducer. Including the shunt circuit R-L parameters to the optimization algorithm (Equation 7.5), and using the selected auxiliary mass, the optimal design parameters are shown in Table 7.5. Since higher electromechanical coupling is expected with higher $\bar{e}$ (as pointed out in Section 4.2.1), an upper limit $\bar{e} = 1$ was set in the optimization. The optimal results entail the highest possible electromechanical coupling, as expected, since higher coupling creates higher electrical energy from the transformed kinetic energy, which can be then manipulated in the shunt circuit. The effect of these parameters to the fuselage tip frequency response is demonstrated in Figure 7.7 with the magenta curve. Compared to the previous optimization results, greater vibration mitigation is achieved in structural Modes I and III (as also seen in Table 7.6), while losing small antivibration performance on Mode II. Furthermore, similar acceleration amplitudes are achieved for all three structural Modes, achieving great simultaneous multi-modal vibration control.

As these optimal values produce remarkable vibration control results, further investigation is made by observing the frequency response of the fuselage tip acceleration and the shunt circuit current. These responses are illustrated in Figure 7.8 for various values of inductance, the optimal $\bar{e}, C$ parameters found for the custom piezoelectric device (Table 7.5) and for negligible R. Figure 7.8a shows that for the optimal inductance value (L = 320 mH), one antiresonance crosses through the higher Mode III, leaving a relatively high frequency peak at approximately 65 Hz, while the other antiresonance is neat the lower Mode I. At the same time, as seen in Figure 7.8b, the electrical component of the shunt circuit is distributed between all Modes, but mostly between Modes II and III. Therefore, the optimal resistance value in the algorithm highly reduces the remaining peaks in Modes II and III, simultaneously dampening also the structural Mode I.

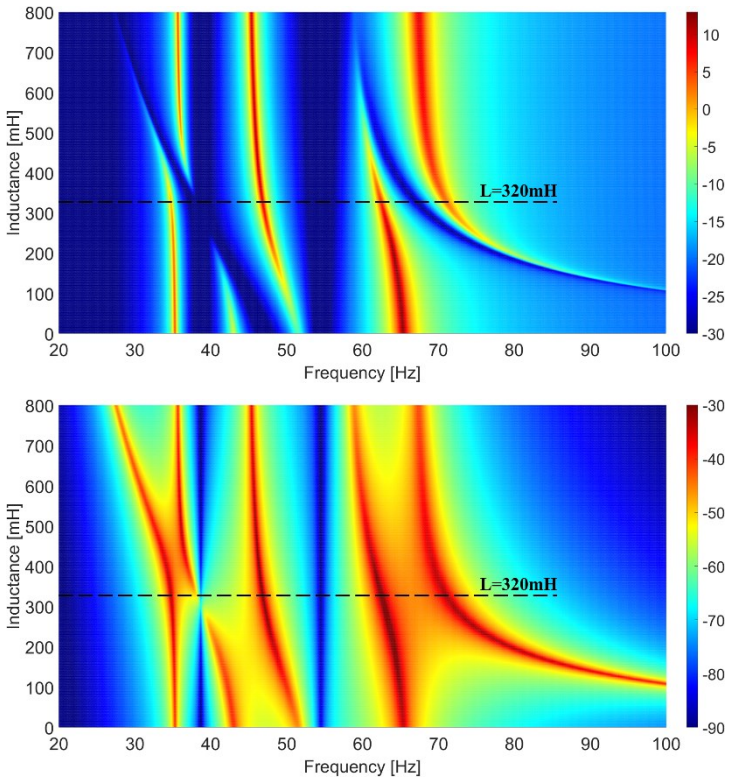


Figure 7.8. Inductance effect on the frequency responses of the SATMD with auxiliary mass that tunes Mode II and optimal C and ē. (a) Acceleration of tip; (b) Shunt circuit current.

The total results in Figure 7.7 indicate that optimal SATMD parameters produce higher multi-modal vibration mitigation performance, compared to the ad-hoc design values. Finally, it is important to stress that very high vibration reduction is accomplished, selecting an auxiliary mass with approximately 1% mass ratio compared to the host structure.

7.2.2.2 Auxiliary mass as an Optimization Parameter

In this Section, the SATMD auxiliary mass is included in the studied parameters (Equation 7.5) for optimal vibration reduction performance. Similarly to the previous section, the optimization algorithm

is applied for several combinations of the studied parameters, each one including the auxiliary mass. The auxiliary mass is investigated between the one that tunes the higher frequency Mode (lowest limit) and the lower frequency Mode (upper limit). Higher auxiliary mass is expected to greatly affect the host structure Modes and alter the structure frequency response. This investigation reveals the total vibration control capacity of the antivibration device on the studied host structure, under broadband excitation. The optimal parameters found for each studied combination is shown in Table 7.5, while their effects to the fuselage tip is illustrated in Figure 7.9.

Table 7.5. Optimal SATMD parameters, including the auxiliary mass.

	m_d [kg]	R [Ohm]	L [mH]	C [μF]	$\bar{e}$ [N/V]
Constrained Optimal m_dRL SATMD	1.48	14.8	245	27	0.65
Constrained Optimal m_dRLC SATMD	1.51	20.25	323	21.1	0.65
Custom Optimal SATMD	1.58	21.46	281	26.8	0.99

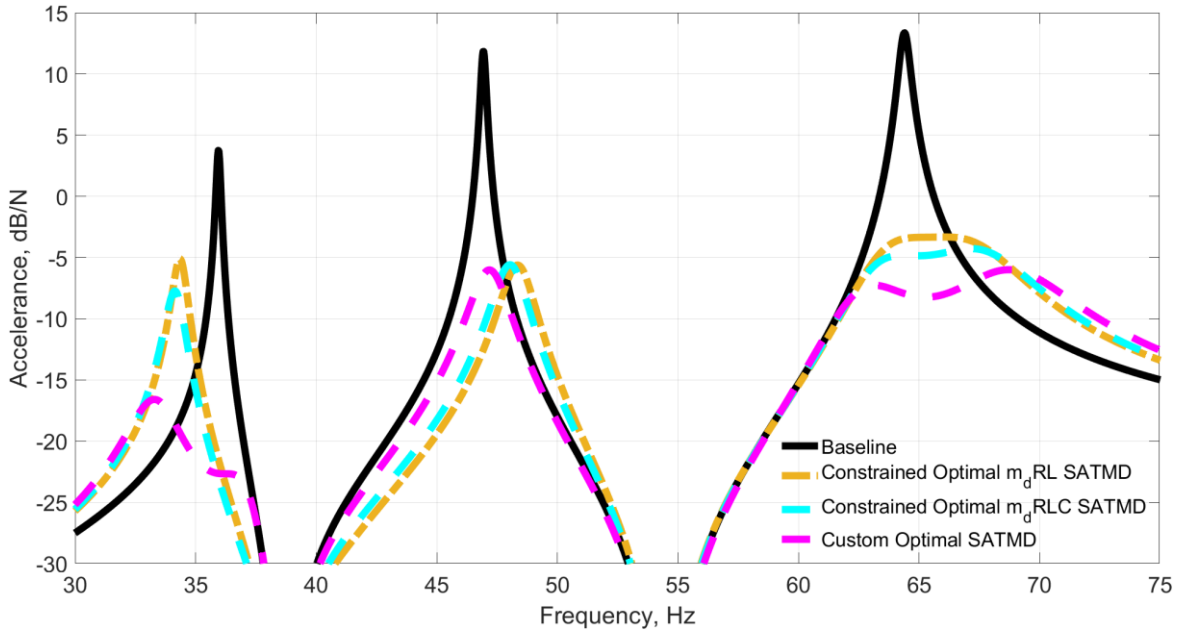


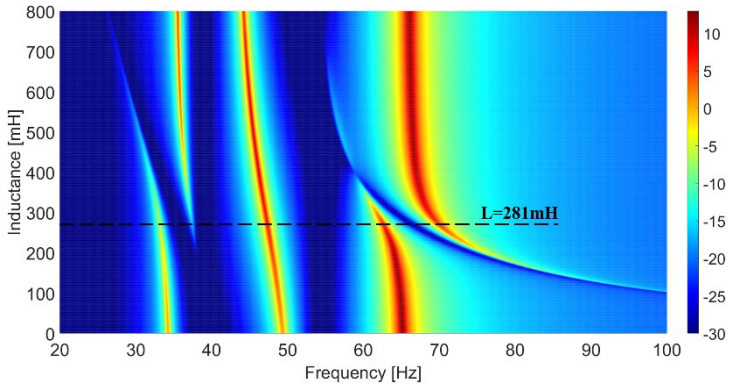
Figure 7.9. Frequency response (acceleration) of fuselage tip without the SATMD and with optimal shunt circuit configurations of the SATMD, including the auxiliary mass in the optimization (the optimal SATMDs with progressively ascending number of optimization parameters).

Table 7.6. Reductions achieved in each structural Mode with various SATMD parameters.

	Mode I		Mode II		Mode III	
	dB	**Mag %**	**dB**	**Mag %**	**dB**	**Mag %**
Constrained Optimal m_dRL SATMD	8.9	64%	17.4	87%	16.6	85%
Constrained Optimal m_dRLC SATMD	11.4	73%	17.4	87%	17.6	87%
Custom Optimal SATMD	20.3	90%	17.8	89%	19.3	89%

Very high multi-modal vibration control is achieved with the custom SATMD, which for various inductance values, the optimized values $m_d, \bar{e}, C$, and negligible resistance, have the effect on the fuselage tip and the current that is illustrated in Figure 7.10. Figure 7.10a shows that for the optimal inductance value (L = 281 mH), the two antiresonances cross through Modes I and III, while Figure 7.10b, demonstrates that the electrical component of the shunt circuit is distributed between all Modes, but mostly between Modes II and III. Therefore, the optimal resistance value in the algorithm highly reduces the remaining peaks in Modes II and III, simultaneously dampening also the structural Mode I.

(a)



(b)

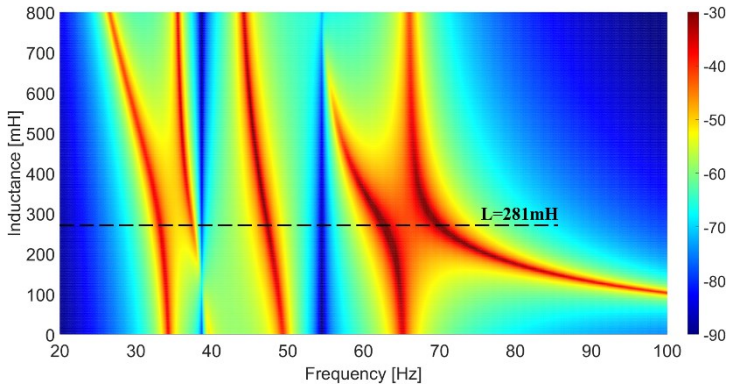


Figure 7.10. Inductance effect on the frequency responses of the SATMD with optimal auxiliary mass, C and ē. (a) Acceleration of tip; (b) Shunt circuit current.

The total results show that including more parameters in the optimization yields better multi-modal control performance. In addition, running the optimization algorithm with more parameters allows for higher flexibility for SATMD multi-modal tuning, with ever higher auxiliary mass, which can absorb more kinetic energy from the existing structure. A very impressive result is that optimizing all the electromechanical parameters of the SATMD, simultaneous 90% acceleration reduction is achieved in all studied structural modes. Furthermore, all optimization schemes conclude to an auxiliary mass that does not accurately tune a structural Mode (Table 7.2) and are rather conveniently placed between the Modes I and II. Inductance highly interacts with the auxiliary mass antiresonance, while resistance absorbs more energy near the shunt circuit eigenfrequency, therefore mass tuning and multi-parameter optimization is needed. The custom SATMD produces higher vibration control to Modes I and III (Table 7.6). The total optimization results for the down-scaled airframe prototype indicate that similar studies will yield enhanced results to other large and flexible structures.

7.3 Concluding Remarks

This Chapter investigated the ad-hoc and optimally designed parameters of the SATMD for multi-modal vibration control of the down-scaled airframe prototype, introduced in Section 6.2. Selecting an auxiliary mass that tunes the antivibration device to a host structural Mode, the design strategy and optimization of the shunt circuit R-L parameters yielded similar results. Maintaining the same auxiliary mass, optimization of the system capacitance and piezoelectric coupling coefficient produced better antivibration efficiency. Including the auxiliary mass in the optimization scheme, simultaneous 90% acceleration reduction is achieved in all studied structural modes, and it was concluded that the auxiliary mass is not necessarily tuned to a host structure Mode. The multi-parameter optimization produced the highest broadband vibration mitigation results, indicating that similar optimization studies are expected to produce enhanced performance to other large and flexible structures.

Chapter 8: Development and Testing of Adaptive Control Concept for the SATMD

Changes in the structural dynamic characteristics of airframe structures (such as mass diminution in aircraft due to fuel consumption) lead to frequency-varying applied loads during operation. This detunes the anti-vibration devices, greatly reducing their effect. The piezoelectric SATMD capability to alter its frequency and damping tuning has been showcased in the previous Chapters, by applying alterations to the R-L shunt circuit, validating its semi-active control efficiency. In this Chapter, an adaptive control concept is developed and tested, such that the antivibration device can be self-tuned and retuned, to achieve high vibration control efficiency. The required inductance and resistance changes are calculated based on host structure acceleration measurements. The developed adaptive algorithm is put into test in two case studies of changes in the dynamic characteristics on the scaled-down airframe protype, studied numerically.

8.1 Adaptive Control Concept

Any semi-active control methodology that aims at adaptive vibration control under dynamic loading conditions includes two basic components [67]:

A. The identification of the host system structural changes.
B. The tuning of the antivibration device tunable parameters to cope with the structural changes.

The adaptive control concept of the studied antivibration device relies on the already investigated mechanisms with which the shunt resistance and inductance interact with the existing host structure. The inductance introduces a second resonant oscillator, besides the auxiliary mass, therefore a second pole to the sole SATMD system (Equation 4.28). The inductance variation shifts the imaginary term of both poles, making them highly frequency tunable. Together, the one or the other pole can cover the whole frequency bandwidth. As seen in Equation (5.17), the sole SATMD eigenfrequencies coincide with the host structure antiresonances and are completely independent of the host structure dynamic characteristics.

On the other hand, the shunt resistance dissipates the electric energy that has been transformed from the structure kinetic energy, therefore introducing damping to the system. As seen in Section 5.6, higher energy can be dissipated at the structural Modes near the shunt circuit eigenfrequency, which depends on both the SATMD and the host structure dynamics (characteristic equation of Equation 5.17). For a given inductance value (and associated shunt circuit eigenfrequency), optimal resistance for broadband control might differ from the optimal resistance for each structural Mode. Higher resistance values result

to the stiffening of the host structure, as seen in Sections 5.4 and 5.6. For these reasons, a total vibrations indicator should be used the appropriate resistance tuning over a wide time range, such the acceleration RMS.

These shunt circuit effects to the host structure favor the following adaptive control strategy. Details about each adaptive control component is given in the subsections below.

A. System Identification. The host structure dynamic characteristics are considered unknown, and the system identification relies only on the frequency response of the structure. One accelerometer is attached to the host structure position, which coincides with the structural integration placement of the antivibration device. The measured time signal is stored and transformed to frequency domain every predetermined time periods (control periods).
B. Parameters Tuning.
    a. Inductance: The highest acceleration peak in the frequency domain is located, from now on defined as critical frequency f_{crit}, and the appropriate inductance is applied to create an anti-resonance at that peak. This inductance remains unchanged until the new f_{crit} input from the next control period.
    b. Resistance: Consecutives RMS values of acceleration are compared. Starting from negligible resistance, if the new RMS value is smaller than the previous one, then the applied damping is beneficial, and more resistance can be added. On the other hand, when the RMS value starts increasing, this means that the limit of beneficial damping has been reached, and the phenomenal stiffening dominates, or the f_{crit} is not accurately found by the frequency response estimation. Both conditions deteriorate the vibration control results, thus the resistance should be decreased.

All in all, the adaptive control is based on the versatile tuning of the SATMD shunt circuit impedance, which can be realized by a variable potentiometer for resistance tuning and a simple switching circuit with coils in series for inductance tuning. It is important to stress that, for the realization of the adaptive piezoelectric SATMD, a controller is needed for the calculations and the changes (potentiometer, switching coils) in the shunt circuit. A small power supply is needed for the controller actions. This power could be provided by the piezoelectric SATMD itself, as seen in the preliminary study energy harvesting study [160], making this device an autonomous SATMD. Although the energy harvesting capabilities seem to be very promising and appealing, this topic escapes the thesis objectives, and therefore could be addressed in a future study. Following the developed strategy, changes in the shunt electrical components can deliver real-time adaptive vibration control, while the mechanical system of the SATMD (auxiliary mass and piezoelectric device stiffness-damping) remains intact.

8.1.1 System Identification

The measured structural acceleration (time series) is used to estimate the frequency response of the host structure and provide the f_{crit} for the inductance value. Several methods can be used for such a transformation, such as the Discrete Fourier Transformation (DFT) and its variation for faster calculations (FFT), the Power Spectral Density (PSD), Autoregressive (AR) or Autoregressive Moving Average (ARMA) models, etc. Since the examined host structures are expected to experience changes that will alter their frequency response during their operational time and therefore adaptive control needed, multiple frequency estimations are obtained over time. In this study, two methods are used: the Welch method, which is a non-parametric technique for estimating the PSD of a signal [161], and the Recursive AR (RAR) model [162], where the AR model parameters are recursively updated over time using new observations. The performance of each method is evaluated based on the achieved vibration control using a purely inductive shunt circuit impedance. The method that estimates the f_{crit} more accurately will produce an inductance that better targets the highest acceleration peak and therefore will yield higher vibration reduction results.

8.1.2 Parameters Tuning

The tunable shunt circuit parameters are the inductance and the resistance.

8.1.2.1 Inductance

As explained earlier, the inductance is selected based on the f_{crit}^{k} that emerges from the frequency response of the k control period and is used to create an antiresonance at this frequency. Based on the SATMD characteristic equation (4.28), the new inductance L^{k+1} needed to create an antiresonance at f_{crit}^{k} is calculated as:

$$L^{k+1} = \frac{C_p(k_p - m_d(2\pi f_{crit}^{k})^2) - \bar{e}^2}{(2\pi f_{crit}^{k})^2 C_p{}^2 (k_p - m_d(2\pi f_{crit}^{k})^2)} \tag{8.1}$$

This inductance remains unchanged until the new f_{crit} input from the new control period.

8.1.2.2 Resistance

As already discussed, if the current acceleration RMS value a_{RMS}^{k} is smaller than the previous one a_{RMS}^{k-1}, then the new resistance R^{k+1} should be higher than the current R^{k}, whereas if the a_{RMS}^{k} is greater than the a_{RMS}^{k-1}, the R^{k+1} should be lower than the R^{k}. This can be summed up in the following equation for the resistance:

$$R^{k+1} = R^k + G_R(a_{RMS}^k - a_{RMS}^{k-1}) \tag{8.2}$$

where the G_R is the resistance gain that multiplies the RMS acceleration difference, such that the updated resistance values fluctuate between reasonable limits, based on RMS magnitude.

8.1.3 Adaptive Control Algorithm

The applied adaptive control algorithm is shown in the flowchart of Figure 8.1. Broadband excitation is applied to the SATMD – host structure system. The host structure acceleration is measured for each time increment at the position which coincides with the SATMD placement (a_t). Multiple a_t measurements are stored and used to estimate the frequency response (FR) and the critical frequency f_{crit}^k of the structure at that point, as well as the RMS value of the structural acceleration a_{RMS}^k, for every k time period. Based on these values, the updated values of inductance L^{k+1} and resistance R^{k+1} are calculated and used as input, which alter the host structure response. These values remain unchanged until the new inputs of f_{crit} and a_{RMS} from the next control period.

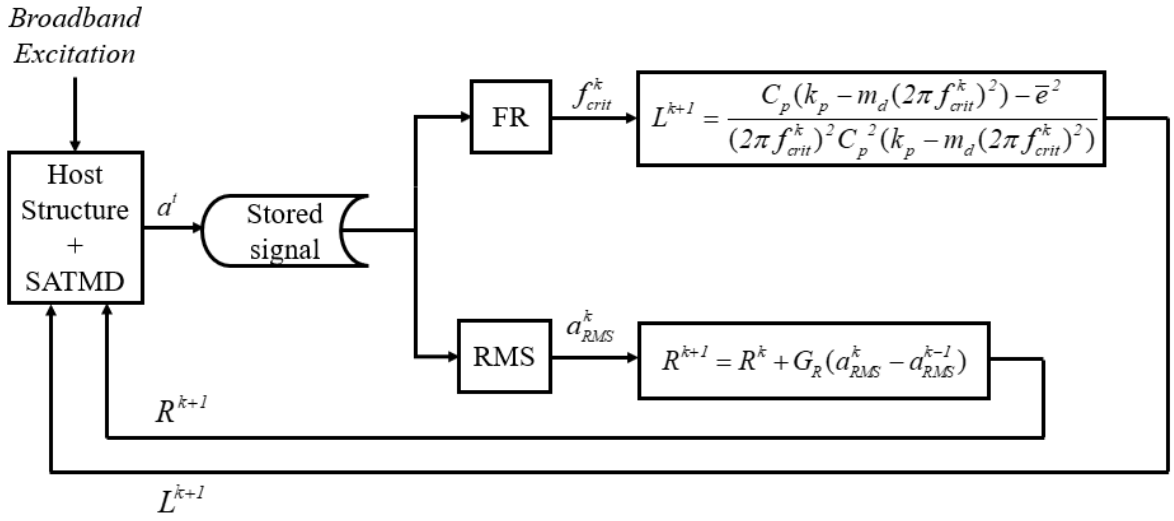


Figure 8.1. Adaptive algorithm for the SATMD.

8.2 Case Studies in Scaled-Down Airframe Prototype Structure

The developed algorithm is numerically tested on the scaled-down airframe prototype, presented in Section 6.2, which is assumed to function under white noise excitation in the 10 Hz to 100 Hz frequency range, applied at the tail center. The piezoelectric SATMD is attached to the fuselage tip and features an auxiliary mass of 1.14 kg, passively tuning the structural Mode II. Two case studies are considered, where the dynamic characteristics of the host structure change gradually, and abruptly, respectively,

simulating typical conditions experienced by various types of aircrafts. A gradual mass diminution takes place in all operating aircrafts due to the fuel consumption. In aerospace engineering, an aircraft's fuel fraction, is the weight of the fuel or propellant divided by the gross take-off weight of the craft. Most contemporary civil aircrafts exhibit a fuel fraction close to, or even higher than 40%, therefore they may experience very high mass reduction during one flight. In addition, an abrupt and large mass diminution occurs when firefighting aircrafts release great amounts of water or retardant to combat wildfires. For example, the Canadair CL-415 have a capacity of 6137 kg for waterbombing, with an empty weight of 13608 kg.

8.2.1 Case Studies' Details

This section addresses the time constants of the control algorithm, the details of the structural frequency response estimation, and the applied resistance gain for the case studies.

8.2.1.1 Time Increment and Control Period

Considering the applied excitation, Equation (6.10) is solved in time domain, using the Newmark implicit integration for the calculations, and only the three truncated modal structural Modes I, II, and III for the host structure solution. Given the excitation frequency range and to ensure that the Newmark results are accurate, the selected time increment is:

$$\Delta t = \frac{1}{10 f_{\max exc}} \tag{8.3}$$

Therefore, the time increment of 0.001 s is used for the Newmark integration. The sampling of the accelerometer is assumed to occur with the same rate, yielding a sampling frequency f_s of 1000 Hz. Although this sampling frequency is much higher than needed according to the Nyquist-Shannon sampling theorem [163], the computational cost of the solved models remains minimal, due to the small order of the truncated model. To maintain satisfactory supervision and control of the system, the control algorithm (Figure 8.1) is implemented every 0.1s, or every 100 samples (Control Period: $\Delta T = 0.1s$), therefore this is also the frequency of the updated shunt circuit parameters.

8.2.1.2 Welch Method

The Welch method is a technique for estimating the Power Spectral Density (PSD) of a signal [161]. Better PSD estimates yield more accurate f_{crit}^{k} estimations, therefore the induced inductance provides higher vibration suppression. The Welch method is a modification of the periodogram method, which

estimates the PSD by computing the squared magnitude of the Fourier Transform of the signal. Since, the periodogram method may suffer from high variance, the Welch method divides the signal into overlapping segments, computes the periodogram for each segment, and averages them to obtain a smoother and more reliable estimate of the PSD. This averaging process helps reduce variance and provides better frequency resolution.

In this study, the signal length used for the Welch method is 5000 samples (therefore every 5 s), and the signal is divided into segments of 512 samples (Hamming window length), using 256 samples overlap from segment to segment. To maintain high quality adaptive control and calculate the updated shunt circuit parameters every $\Delta T = 0.1s$, a 4.9 s overlap exists between the successive PSD estimates.

8.2.1.3 Recursive AR Model

As described in [164], a RAR model of order n, is of the form:

$$y[k] + \sum_{i=1}^{n} a_i[k]\, y[k-1] = e[k], \quad e[k] \sim i.i.dN\left(0, \sigma_e^2[k]\right) \tag{8.4}$$

with $y[k]$ $(k = 1, 2, ..., t)$ designating the measured acceleration, $e[k]$ the corresponding zero-mean innovations (one-step-ahead prediction error) sequence that should be serially uncorrelated and characterized by generally time-dependent variance $\sigma_e^2[k]$. n designates the AR model order and $a_i[k]$ the time-dependent AR parameters. RAR model estimation is, at each time instant t, achieved via the Recursive Least Squares (RLS) algorithm obtained from the following estimation criterion [165]:

$$\hat{\theta}[t] := \arg_{\theta^k} \min \sum_{k=1}^{t} \lambda^{t-k} e^2\left[k, \theta^{k-1}\right] \tag{8.5}$$

with $\hat{\theta}[t]$ designating the estimated AR parameter vector at the current time instant t and $\lambda \in (0, 1]$ a forgetting factor used to assign more importance to more recent innovations signal values, its selection essentially implying trade-off between tracking ability of the non-stationary signal characteristics and model estimation accuracy. The RLS algorithm is customarily initialized via $\hat{\theta}[0] = \boldsymbol{0}$ and initial parameter covariance matrix $\boldsymbol{P}[0] = a\boldsymbol{I}$ with a designating a large positive value and $\boldsymbol{I}$ the unity matrix. The estimated frequency response of the model emerges from the parameters $\hat{\theta}[t]$ of the model, therefore the developed model is required to have minimal deviation from the actual signal, such that the f_{crit}^{k} is accurately calculated and the induced inductance provides beneficial antivibration effects.

In this study, the appropriate RAR model order and forgetting factor are decided based on the Baysian information (BIC) [166] and the residual sum of squares over the series sum of squares (RSS/SSS)

[162] criteria. The first criterion penalizes models with higher number of parameters, thus favoring simpler models that still provide a good fit to the data, while the second one directly assesses the goodness of fit of the model to the data. Very low values for both criteria are wanted for a satisfactory model order.

5000 acceleration samples are obtained from the accelerometer under the white noise excitation, with the SATMD attached to the fuselage tip, operating with the auxiliary mass that passively tunes the structural Mode II, and the optimal R-L values found for this auxiliary mass (Section 7.2.2.1.1). The signal is presented in Figure 8.2. The examined forgetting factors vary from 0.995 to 0.999 and produce very similar results. The BIC and RSS/SSS values for forgetting factor 0.999 and model order 1 to 40 are illustrated in Figure 8.3. Both criteria illustrate very low values for model orders larger than 10. Model order $n = 30$ is selected, as further order increase produces very small improvements.

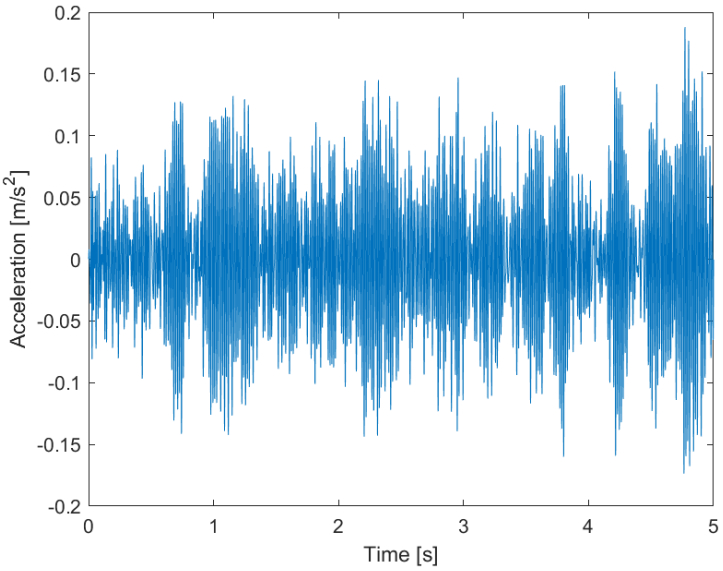
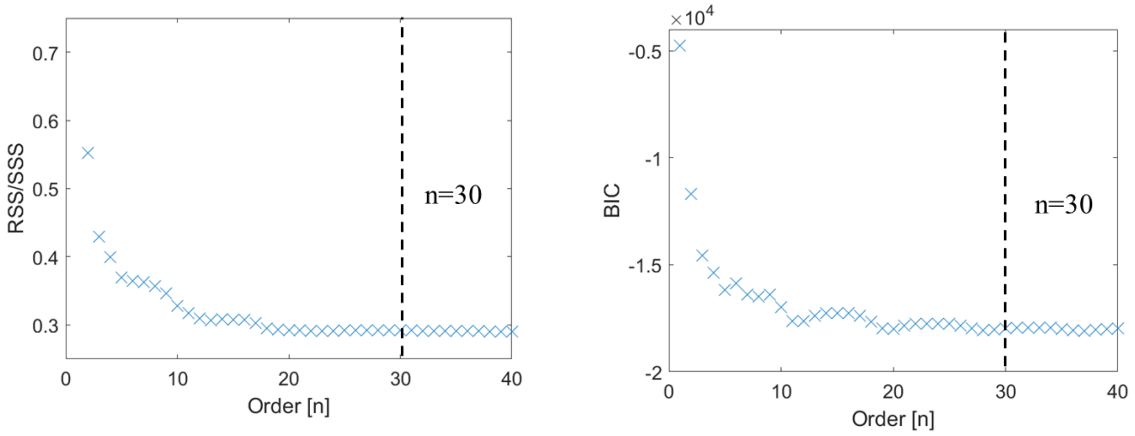


Figure 8.2. Numerical acceleration results of the fuselage tip of the airframe model, under white noise excitation, with the SATMD at the fuselage tip, operating with the auxiliary mass that passively tunes the structural Mode II, and the optimal R-L values found for this auxiliary mass.



(a) *(b)*

Figure 8.3. Results on the RAR order based on model selection criteria. (a) RSS/SSS; (b) BIC.

8.2.1.4 Resistance Gain

The resistance gain G_R multiplies the difference between consecutive RMS values, to increase or decrease the updated resistance. An ad hoc rule is established here for the resistance gain:

$$R_{diff.} = G_R \left(a_{RMS}^{k} - a_{RMS}^{k-1} \right) \tag{8.6}$$

where $R_{diff.}$ is an indicative resistance value that should be added or subtracted in every resistance update. In this study, the time frame selected to measure the RMS acceleration is 5 s (5000 samples). Considering that the control algorithm (Figure 8.1) is implemented every 0.1s, a 4.9 s overlap exists between the successive RMS values. Furthermore, as seen in Chapter 7, the resistance values that provide beneficial multi-modal damping with the used SATMD device are between 21.2 Ohm and 41.6 Ohm (Table 7.3 and 7.5). Taking into account the short time periods that the updated shunt circuit values are applied, and the beneficial value range of resistance, a small amount of $R_{diff.} = 0.04$ Ohm is considered as sufficient for each update. As examples for the RMS values, the RMS of the measured acceleration in Figure 8.2 is 0.0568 m/s^{2,} , and 0.0566 m/s^2 when excluding the last 100 samples. According to Equation (8.6), a resistance gain of $G_R = 200$ is needed to alter the updated resistance per 0.04 Ohm, therefore this resistance gain is considered for the case studies below.

8.2.2 Gradual mass change

To test the developed control algorithm, a gradual change in the dynamic characteristics of the lab-scale airframe is investigated, due to a gradual mass diminution (Figure 8.4a). A linear reduction of the total airframe mass takes place for 20 seconds, leading to 33% loss. The airframe mass remains unchanged before and after this incident (Figure 8.4a). The frequency response estimations of the Welch method and the RAR model for each control time period k yield the highest peak f_{crit}^{k} at the frequencies seen in Figure 8.4b. Initially, the control algorithm is applied only with inductance (and the short circuit resistance of 2 Ohm), to select which of the two methods produces better vibration control results. Subsequently, the control algorithm is run again with the resistance control, and the selected method for applied inductance.

Starting the interpretation from the Welch method (green curve), frequency peaks with very small frequency fluctuations are found in the whole studied time spectrum. For the first 20 seconds where the structure remains unchanged, the f_{crit}^{k} are found near the highest amplitude Mode III at 65 Hz, indicating good PSD estimation with the Welch method. In the time frame 20 seconds to 40 seconds where the gradual mass diminution takes place, the Welch method produces frequency peaks of progressively

higher frequency. Such effect is indeed expected in the frequency response of the structure, since reducing the structural mass, while maintaining the same structural stiffness, leads to higher frequency Modes. In the last 20 seconds, the Welch method produces relatively constant f_{crit}^{k} values near the final frequency of the reduced mass, again indicating great PSD estimation.

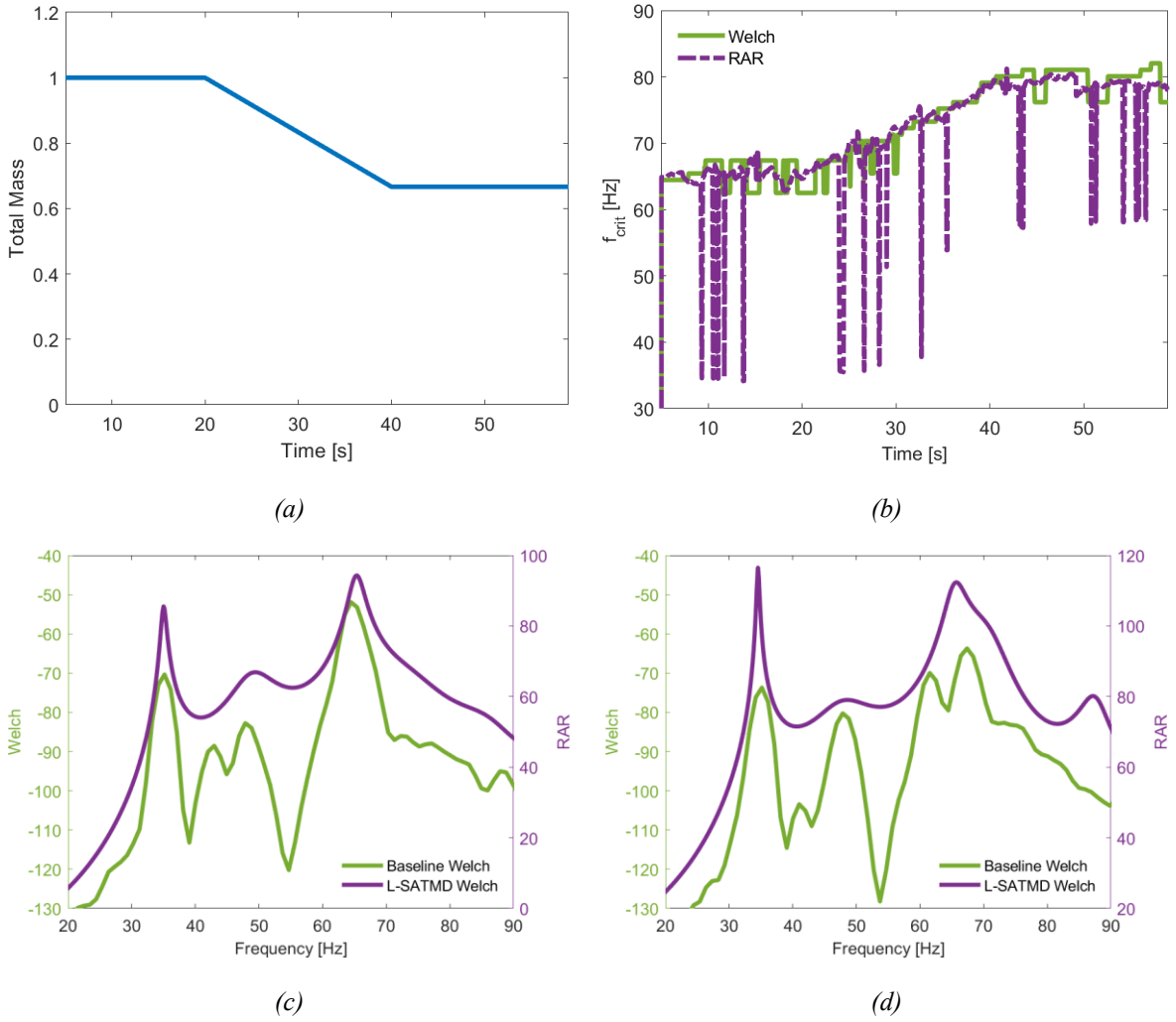


Figure 8.4. Frequency response estimations with gradual mass change. (a) Mass change in time; (b) Critical frequencies found with Welch and RAR model; (c) Welch and RAR frequency response estimation at 7.2s; (d) Welch and RAR frequency response estimation at 10.5s.

Continuing with the RAR model results (purple curves), the frequency peaks are again relatively constant, following the Welch method trajectory and indicating good frequency response estimations, however some high frequency fluctuations are occasionally exhibited. These fluctuations occur when the RAR frequency response estimate that the highest Mode III has sustained such great reductions, due to the applied inductance, that lower Modes I and II emerge with higher amplitude. To visualize this variation, the estimated frequency responses with the two methods are illustrated at 7.2 s and 10.5 s, in Figure 8.4c, d, respectively. In each figure, the estimated responses are plotted for the L-SATMD, with colors that refer to each method. In Figure 8.4b, both estimated responses of the L-SATMD create a

f_{crit}^{k} near the structural Mode III (65 Hz), which is considerable reduced, due to the appropriately applied inductance. This result is illustrated for the 7.2 s in Figure 8.4c, where both methods' highest amplitudes coincide at approximately 65 Hz. On the hand, at the frequency response of Figure 8.4d, the RAR model yields a f_{crit}^{k} at structural Mode I (36 Hz), due to the high reduction of the continuously applied inductance for Mode III. As a result, clear discrepancy is observed at 10.5 s in Figure 8.4d between the two estimated f_{crit}^{k}. Similar differences between the two methods' frequency response estimations lead to the other f_{crit}^{k} fluctuations found with the RAR model.

The found f_{crit}^{k} for each control time period k produce the inductance values (Equation 8.1) depicted in Figure 8.5b. Similarly to each method's f_{crit}^{k}, the calculated inductances exhibit small fluctuations with the Welch method (green curve), whereas the RAR model produces relatively steady inductance values with some big fluctuations (purple curve). The RMS accelerations with the two methods' applied inductances are illustrated in Figure 8.5c for the whole studied time spectrum, with their respective colors. They produce similar results, however the RAR model leads to higher vibration control (lower RMS values) during the mass alteration, proving its superior tracking ability of the non-stationary signal characteristics and model estimation accuracy, compared to the non-parametric Welch method. This results to a greater vibration control on the whole studied time period, as seen in Figure 8.5c and Table 8.1. Therefore, the RAR model is selected as the frequency estimator, and the RL-SATMD is studied with this model.

The calculated resistance variation in time based on the calculated acceleration RMS values (Equation 8.2) is shown in Figure 8.5a. The acceleration RMS variation due to the RL-SATMD, with based on the f_{crit}^{k} RAR model estimations and inductance tuning (Figure 8.5c), is illustrated with cyan color in Figure 8.5c. Starting from low resistance values, the applied inductance due to the found f_{crit}^{k} leads to considerable RMS reduction. As a result, the resistance (Equation 8.2) calculates progressively higher resistance values, leading to beneficial energy dissipation in heat, and therefore to better vibration control and lower RMS values (Figure 8.5c). From 10 s to 20 s, the resistance fluctuates between 14 Ohm and 18 Ohm (Figure 8.5a), and together with the applied inductance, produces very high vibration control, as seen in the acceleration RMS values. At 20 s, when the mass begins to alter, higher RMS values are calculated, associated with the imperfect inductance tuning and the higher amplitude accelerations. As a result, the resistance is progressively reduced (Figure 8.5a). Still, the applied control produces very high vibration suppression, as seen in Figure 8.5c. At 40 s, when the mass alteration seizes, the resistance starts fluctuating around the final resistance value of the alteration period, still achieving high vibration control. For stable structure mass, the resistance is calibrated based on (Equation 8.2), and the yielded RMS results remain very low, compared to the baseline values.

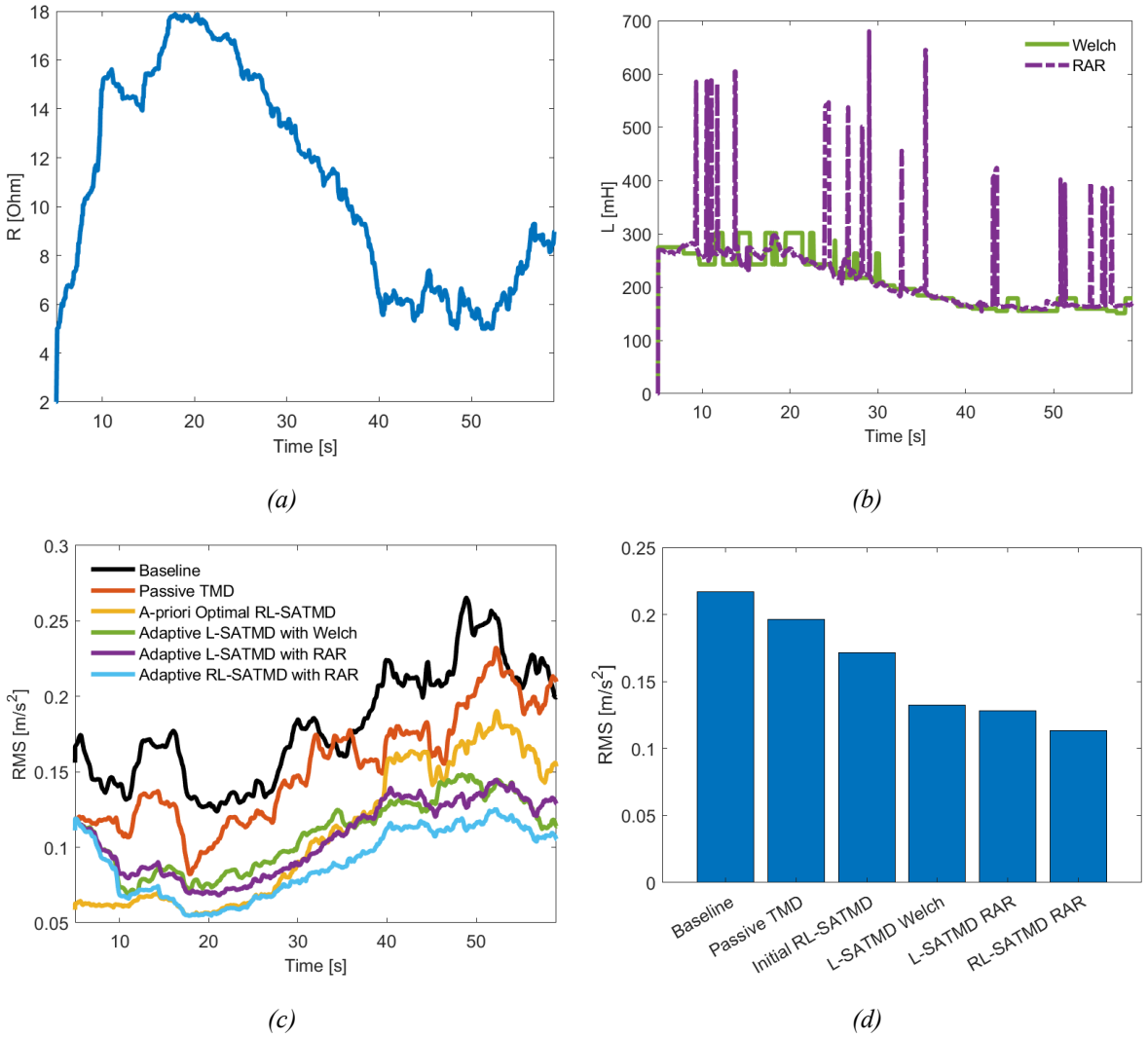


Figure 8.5. Results of the adaptive control algorithm gradual mass change case study. (a) Resistance; (b) Inductance; (c) RMS values; (d) values after 20 s.

Table 8.1. RMS acceleration values in the gradual mass change case study.

	Baseline	Passive TMD	Initial RL-SATMD	L-SATMD Welch	L-SATMD RAR	RL-SATMD RAR
Total RMS [m/s^2]	0.185	0.159	0.131	0.112	0.109	0.0943
RMS after 20 s [m/s^2]	0.217	0.196	0.172	0.132	0.127	0.112

Figure 8.5c depicts the RMS acceleration values for various SATMD configurations on the host structure. The Baseline curve (black line) refers to the acceleration when no SATMD device is attached, whereas the A-priori optimal RL-SATMD (yellow curve) refers to the RL values found for optimal multi-modal vibration control in Table 7.3. The rest of the curves refer to self-explanatory SATMD conditions. The Passive TMD configuration achieves considerable vibration control compared to the Baseline response for the first 20 s, when the auxiliary mass is accurately tuned to Mode II. As the

structure mass changes, its efficiency is reduced, and higher RMS accelerations are observed due to the structural antiresonance detuning. The RMS acceleration with the A-priori Optimal RL-SATMD configuration yields very high vibration control in the first 20 s. However, similarly to the Passive TMD, the device is detuned for changing dynamic characteristics, producing higher acceleration values. The L-SATMD configurations produce very good vibration control in the whole studied time spectrum, proving the great estimation of the f_{crit}^{k} with the examined methods, and the efficiency of the applied algorithm. The acceleration RMS with the RL-SATMD configuration starts from the same point with the L-SATMD, but progressively achieves higher vibration control, due to the damping that appropriate resistance values create. The RL-SATMD configuration achieves very high adaptive vibration mitigation results proving the semi-active capabilities of the device and the effectiveness of the developed adaptive algorithm. The total RMS acceleration values and the RMS acceleration values after 20 s for all studied configurations is depicted in Table 8.1. Finally, the acceleration signal of these configurations is illustrated in Figure 8.6.

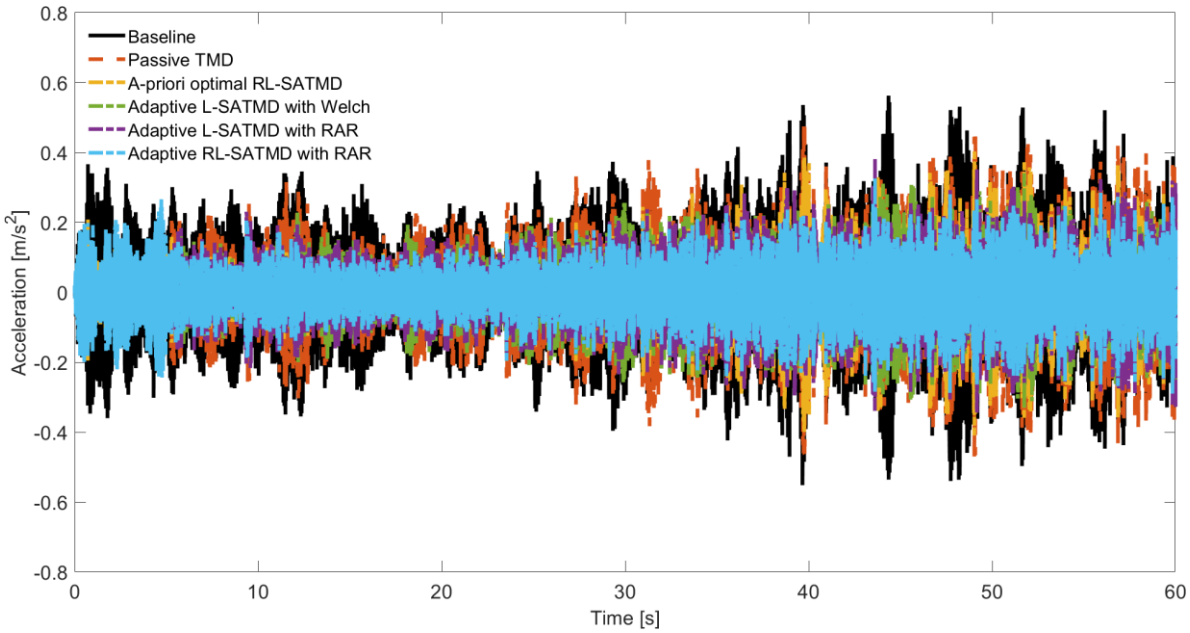


Figure 8.6. Acceleration results of the gradual mass change case study in time.

8.2.3 Abrupt mass change

In this subsection, an abrupt change in the dynamic characteristics of the host structure is considered, leading to a sudden 23% loss of the structural mass at 15 s (Figure 8.7a). The frequency response estimations of the Welch method and the RAR model for each control time period k yield the highest peak f_{crit}^{k} at the frequencies seen in Figure 8.7b. Similarly to the previous case study, the control algorithm is applied only with inductance, to select which of the two methods produces better vibration control results. As seen in the f_{crit}^{k} that each method estimates, the RAR model identifies first the

structural change, as the purple curve (RAR model) steps from 65 Hz to 75 Hz approximately 1 s before the green curve (Welch method). Thus, the RAR model is used in the RL-SATMD configuration. The f_{crit}^{k} change creates a change in the applied inductance, as seen in Figure 8.8b. The resistance level remains relatively stable before 15 s, and then quickly drops to lower values to compensate for the inductance mistuning, due to the sudden mass diminution. The RMS acceleration values are illustrated for all the studied configurations in Figure 8.8c. The L-SATMD configuration with the RAR frequency estimation (purple curve) achieves better vibration control than the similar configuration with the Welch estimation (green curve). The RL-SATMD proves superior in terms of vibration suppression, producing the lowest acceleration RMS values, and proving the adaptive algorithm efficiency in abrupt changes of the system structural dynamics. The total RMS acceleration values and the RMS acceleration values after 15 s for all studied configurations is depicted in Table 8.2. Finally, the acceleration signal of these configurations is illustrated in Figure 8.9.

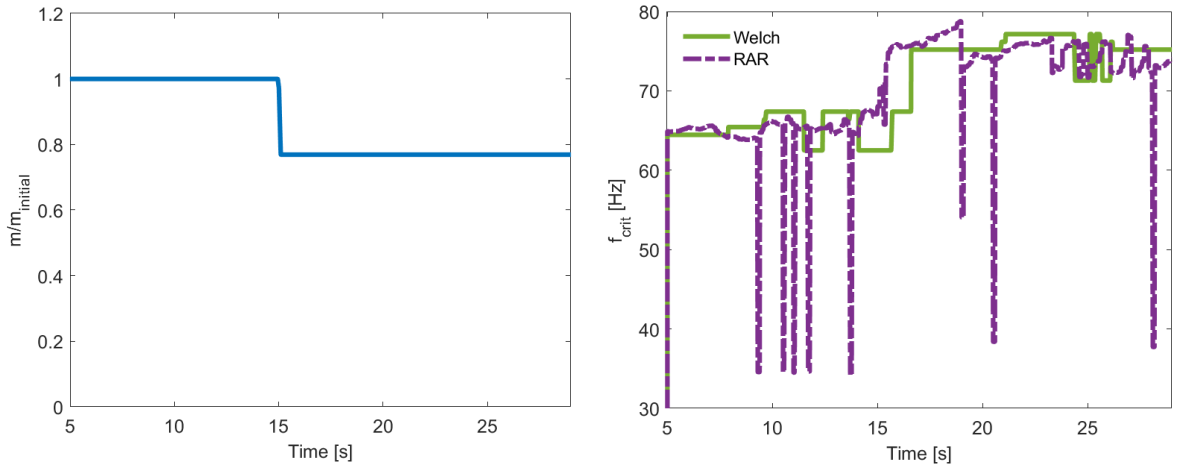
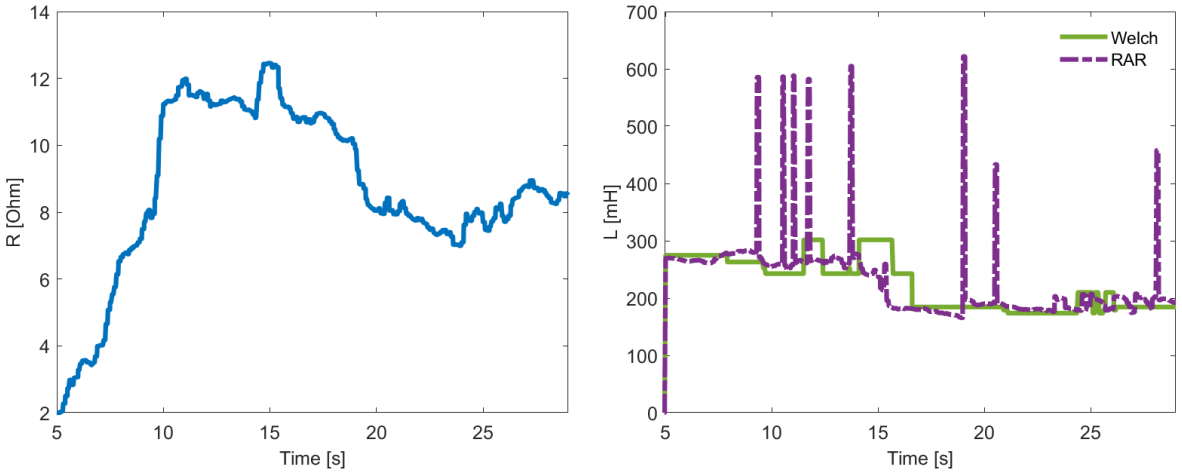


Figure 8.7. Frequency response estimations with abrupt mass change. (a) Mass change in time; (b) Critical frequencies found with Welch and RAR model.



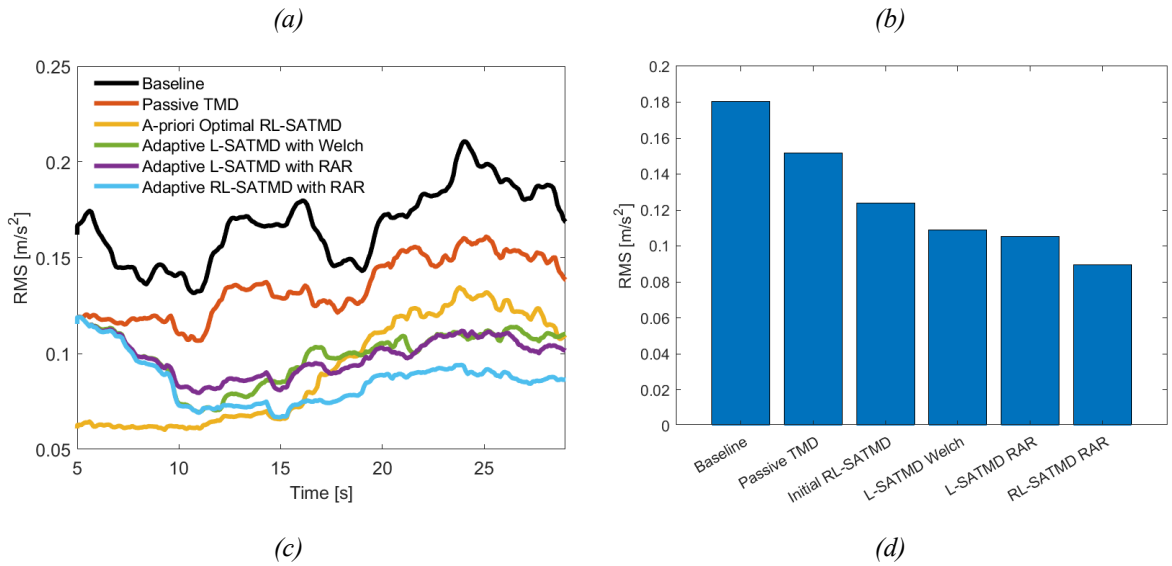


Figure 8.8. Results of the adaptive control algorithm in the abrupt mass change case study. (a) Resistance; (b) Inductance; (c) RMS values; (d) values after 20 s.

Table 8.2. RMS acceleration values in the abrupt mass change case study.

	Baseline	Passive TMD	Initial RL-SATMD	L-SATMD Welch	L-SATMD RAR	RL-SATMD RAR
Total RMS [m/s²]	0.170	0.1367	0.0983	0.102	0.101	0.089
RMS after mass change [m/s²]	0.180	0.152	0.124	0.109	0.105	0.089

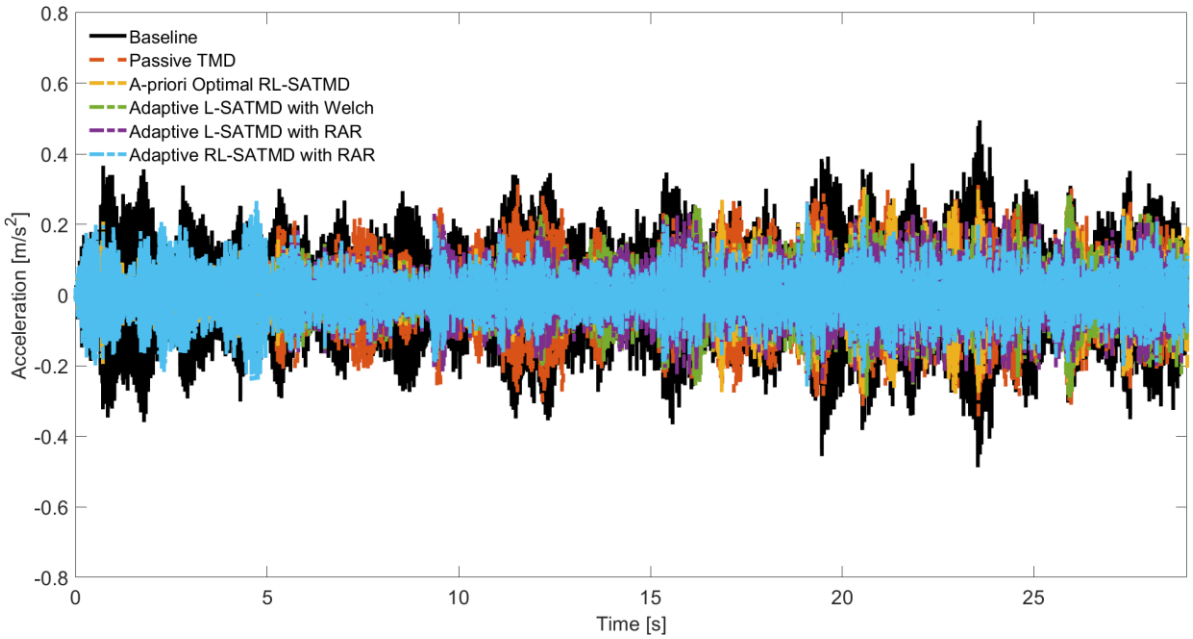


Figure 8.9. Acceleration results of the abrupt mass change case study in time.

8.3 Concluding Remarks

This Chapter addressed the adaptive vibration control capabilities of the proposed semi-active antivibration device. The adaptive control concept and algorithm was developed based on the effects that each of the tunable parameters (resistance and inductance) introduces to the host structure behavior. The Welch method and a RAR model were used to estimate the frequency response of the structure based on the measured acceleration, yielding the highest frequency peak f_{crit}^{k} at each control time period k. The inductance to suppress each f_{crit}^{k} is independent of the host structure dynamics and yields from the frequency estimations, whereas the resistance is calculated based on the acceleration response of the structure. The developed adaptive algorithm was put into test on the scaled-down airframe model, which was assumed to undergo both gradual and abrupt mass alterations. The antivibration device achieved very high adaptive vibration control, proving the semi-active capabilities of the device and the effectiveness of the adaptive algorithm.

Chapter 9: Conclusions and Suggestions

In the final chapter of this dissertation, the main conclusions and achievements of the work are summarized, before identifying interesting research topics for future investigations.

9.1 General Conclusions

This dissertation addressed the development, evaluation, and application of a novel semi-active shunted piezoelectric Tuned Mass Damper (SATMD). A great deal of the existing challenges and literature gaps for the stacked piezoelectric TMDs were covered in this work. Starting from the SATMD concept and the high vibration attenuation potential of such a device, this research work covered all the steps from sole device evaluation, interaction with single and multiple DOF structures and optimization, and finally reached the successful adaptive control of an altering dynamics flexible structure, under broadband frequency loading. The most important conclusions of the conducted research are highlighted below.

- ✓ The SATMD antivibration device was developed, tested, and modeled, revealing two pairs of electromechanically coupled poles. The APA1500L piezoelectric transducer was selected for low effective stiffness and high piezoelectric coupling. The effects of the shunt circuit impedance were compared to computational results, demonstrating great agreement.
- ✓ The performance of the piezoelectric SATMD was evaluated experimentally and numerically on a simplified lumped mass structure. The equations of the SATMD – host structure system were formulated, and the transfer functions showed that the introduced antiresonances on the host structure coincide with the sole SATMD eigenfrequencies. Resistive impedance increases the damping capabilities of the coupled electromechanical system. Inductive impedance introduces a new, highly tunable, oscillator in the system, which enhances the coupling and conversion of kinetic to electrical energy, especially near the bifurcation points. The SATMD was found able to compensate for the purely mechanical TMD disadvantages, providing broadband vibration suppression and control to the host structure, and offering great retuning capabilities. The experimental measurements validated the developed models.
- ✓ The performance of the studied antivibration device was then studied on large and flexible structures. For the computational model, a reduced-ordered modal space structural dynamics model is formulated, coupled with the SATMD device, and the RL shunt electric circuit. A scaled-down airframe prototype was fabricated to act as the laboratory flexible structure for the antivibration device testing. In broadband excitation conditions, the studied SATMD achieved, both experimentally and numerically, multi-modal vibration control and damping in three major structural modes. In multi-tonal vibrations, the SATMD can highly suppress excessive vibrations in two distinct frequency vicinities, thanks to the two introduced tunable resonant

oscillators, namely the auxiliary mass and the shunt circuit eigenfrequency. Furthermore, it was shown that the two introduced antiresonances are independent of the host structure dynamic characteristics, and as a result the appropriate SATMD auxiliary mass and inductance can be decided based only on the structure frequency response. This special and versatile feature was used for the antivibration performance of the SATMD in a BO105 S helicopter, where, after discovering its critical frequencies, the auxiliary mass and shunt circuit inductance were accurately selected to suppress two distant frequency vibrations during real-flight conditions.

- ✓ The ad-hoc and optimally designed parameters of the SATMD for multi-modal vibration control of the down-scaled airframe prototype were investigated. Selecting an auxiliary mass that tunes the antivibration device to a host structural Mode, the ad-hoc design strategy and optimization of the shunt circuit R-L parameters yielded similar results. Maintaining the same auxiliary mass, optimization of the system capacitance and piezoelectric coupling coefficient produced better antivibration efficiency. Including the auxiliary mass in the optimization scheme, simultaneous 90% acceleration reduction is achieved in all studied structural modes, and it was concluded that the auxiliary mass is not necessarily tuned to a host structure Mode.
- ✓ An adaptive control concept and algorithm was developed based on the effects that each of the tunable parameters (resistance and inductance) introduces to the host structure behavior. The Welch method and a RAR model were used to estimate the frequency response of the structure based on the measured acceleration, yielding the highest frequency peak at each control time period. The inductance to suppress each critical frequency is independent of the host structure dynamics, whereas the resistance is calculated based on the acceleration response of the structure. The developed adaptive algorithm was put into test on the scaled-down airframe model, which was assumed to undergo both gradual and abrupt mass alterations. The antivibration device achieved real-time adaptive vibration control, proving the semi-active capabilities of the device and the effectiveness of the adaptive algorithm.

Finally, revisiting all the special attributes of the developed antivibration device, the benefits that is offers to flexible host structures are presented here.

- ➢ Great vibration attenuation, both for broadband loading conditions (since appropriate resistive-inductive impedance provides great damping), and for multiple tonal excitations (since the auxiliary mass and inductance provide two resonant absorbers).
- ➢ Petite device with low added weight, due to the specialty low-effective-stiffness piezoelectric device.
- ➢ Superior semi-active behavior and ease of frequency and damping tuning, through shunt circuit alterations.
- ➢ Ease of application and minimal structural interference.

- Low need for power supply, which is needed only for potential shunt circuit alterations, and could be provided by the piezoelectric stack itself, making the studied mechanism a very attractive autonomous antivibration-harvester device.

9.2 Suggestions for Future Research

Some issues remain open from this work, which could constitute interesting investigations for future studies, and are presented below.

- Alternative case studies could be examined for the SATMD optimization and adaptation. A "flatness" in the frequency response of the acceleration could be set as goal for the optimal SATMD, such that a more uniform vibration control is achieved. Furthermore, the variations of the unsteady aerodynamic loads could be assumed as frequency-variable applied loads to be compensated by the adaptive SATMD.
- This work considered only theoretical alterations of the shunt circuit capacitance for the shake of SATMD optimization. Negative capacitance or other shunt circuit configurations could highly enhance the behavior of the SATMD.
- Energy harvesting of piezoelectric devices has been deeply investigated, both for shunted piezoelectric patches [167], and for piezoelectric configurations similar to the one used in this study [168]. The simultaneous energy harvesting and vibration control has also been addressed in various reports, however it is not covered in the current study. Incorporating energy harvesting to the developed SATMD device could supply the device itself for autonomous semi-active performance, or other devices in the same circuitry.
- A very interesting topic could also be the development of an SATMD device, entailing two or more piezoelectric stack devices with a single auxiliary mass, connected mechanically and electrically in series or in parallel, and the investigation of this new device dynamics. Furthermore, the integration of a number SATMD devices in the same host structure could yield impressive results, since it could create the double number in anti-resonances. The interaction between the newly introduced anti-resonances and anti-vibration devices' poles could be of great scientific interest.
- Finally, the experimental implementation of the proposed adaptive algorithm for the SATMD attached to a host structure could also constitute a very interesting topic.

Appendix A: APA1500L Technical Data Sheet

www.cedrat-technologies.com | actuator@cedrat-tec.com

CEDRAT TECHNOLOGIES
Innovation in Mechatronics

APA1500L

AMPLIFIED PIEZO ACTUATOR APA®

KEY FEATURES

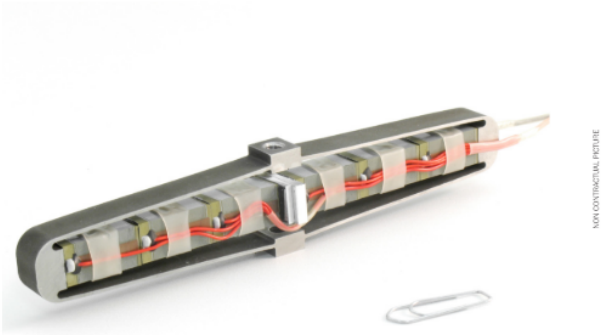
- Low voltage piezo ceramic
- Optimal preload for high dynamics
- Mechanical Amplification
- Compact Size
- High Resolution

RELATED PRODUCTS

- CTEC benchtop controllers
- CTEC OEM controllers

AVAILABLE OPTIONS

- SG sensor
- Vacuum compatibility
- Ultra High Vacuum
- Non magnetic shell



NON CONTRACTUAL PICTURE

PARAMETER	VALUE	UNIT
› Quasistatic performances		
Nominal Stroke	1 500	µm
Min stroke	1 300	µm
Resolution(1)	83	nm
Blocked force	99	N
Stiffness	0.067	N/µm
› Dynamic performances		
Resonance frequency (free-free)(2)	720	Hz
Resonance frequency (blocked-free)(3)	140	Hz
Force limit(4)	72	N
› Control & driving		
Voltage range	-20 ... 150	V
Capacitance(5)	26	µF
› Dimensions & interfaces		
Height	30	mm
Length	141	mm
Width incl wires	20	mm
Mass	140	g
› Standard mechanical interfaces	See ICD	
› Electrical interface	See ICD	

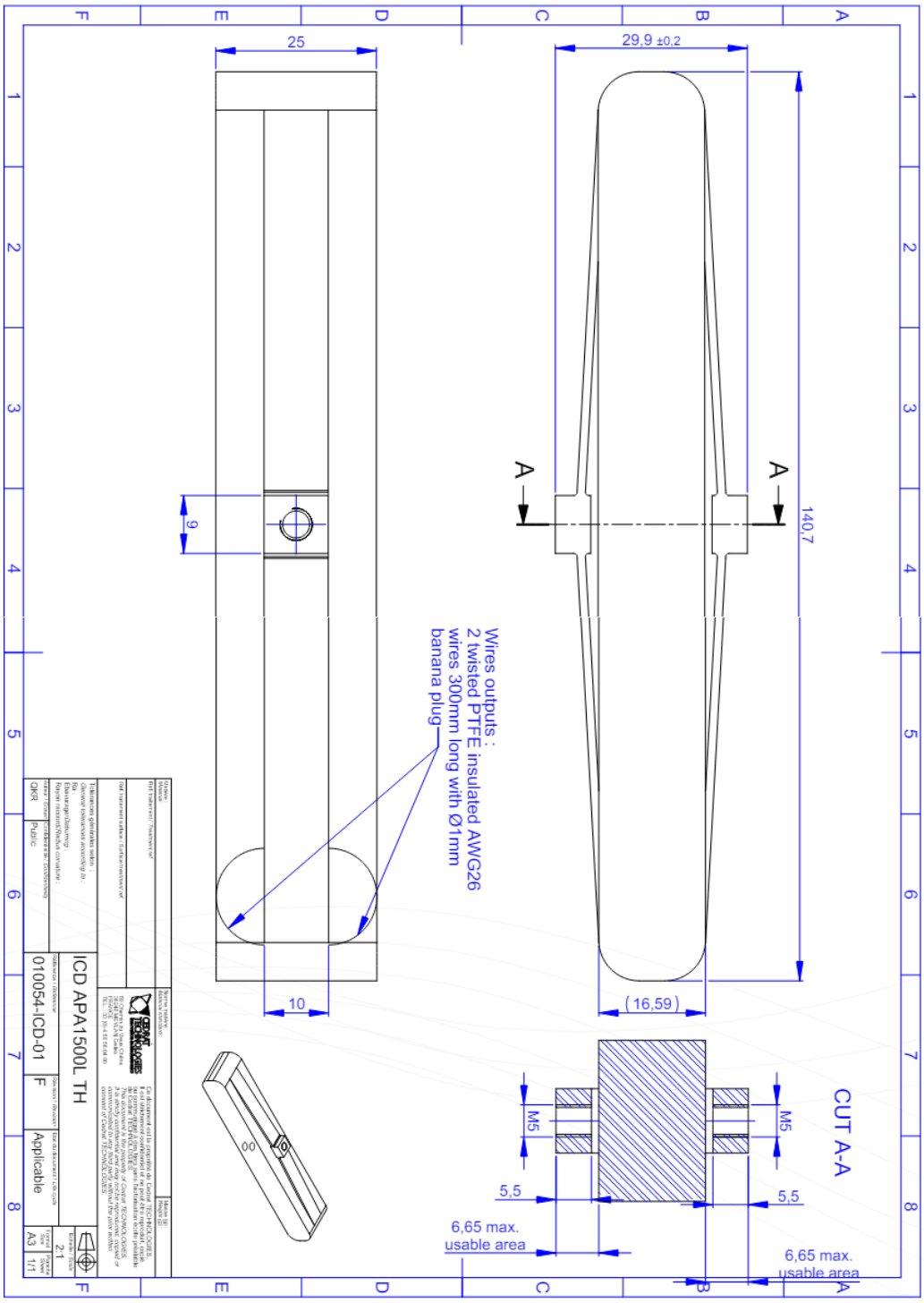
ANNOTATIONS

(1) Quasistatic excitation. With standard LA75 range amplifier. SNR=85 dB computed as RMS output signal /RMS output Noise floot at [0;200 Hz]
(2) Free-free: The actuator mounts are free
(3) Blocked-free: The actuator is fixed to a mechanical support assumed infinitely stiff
(4) Maximum pulling or pushing external force, valid up to 90% of the blocked-free resonance frequency of the actuator
(5) Capacitance +/- 20%, at 1 V RMS, low frequency, without load

Copyright © CEDRAT TECHNOLOGIES | 01/2024

CEDRAT TECHNOLOGIES • 59 Chemin du Vieux Chêne • Inovallée • 38246 MEYLAN Cedex France • Tel. : +33 (0)4 56 58 04 00

www.cedrat-technologies.com | actuator@cedrat-tec.com



Copyright © CEDRAT TECHNOLOGIES | 01/2024

Appendix B: Newmark Implicit Numerical Time Integration Method

Initial calculations:

1. Form stiffness $\boldsymbol{K}$, mass $\boldsymbol{M}$, and damping $\boldsymbol{C}$ matrices.
2. Initialize displacements ${}^{0}\boldsymbol{U}$, velocities ${}^{0}\dot{\boldsymbol{U}}$ and accelerations ${}^{0}\ddot{\boldsymbol{U}}$.
3. Select time step Δt and parameters α and δ and calculate the integration constants:
4. $$\delta \geq 0.5; \qquad \alpha \geq 0.25(0.5+\delta)^2;$$
$$\alpha_0 = \frac{1}{\alpha \Delta t^2}; \qquad \alpha_1 = \frac{\delta}{\alpha \Delta t}; \qquad \alpha_2 = \frac{1}{\alpha \Delta t}; \qquad \alpha_3 = \frac{1}{2\alpha} - 1;$$
$$\alpha_4 = \frac{\delta}{\alpha} - 1; \qquad \alpha_5 = \frac{\Delta t}{2}\left(\frac{\delta}{\alpha} - 2\right); \qquad \alpha_6 = \Delta t(1-\delta); \qquad \alpha_7 = \delta \Delta t$$
5. Form effective stiffness matrix $\hat{\boldsymbol{K}}$: $\hat{\boldsymbol{K}} = \boldsymbol{K} + a_0\boldsymbol{M} + a_1\boldsymbol{C}$.
6. Triangularize $\hat{\boldsymbol{K}}$: $\hat{\boldsymbol{K}} = \boldsymbol{L}\boldsymbol{D}\boldsymbol{L}^T$.

For each time step:

1. Calculate effective loads at time $t + \Delta t$:
   ${}^{t+\Delta t}\hat{\boldsymbol{R}} = {}^{t+\Delta t}\boldsymbol{R} + \boldsymbol{M}(a_0{}^{t}\boldsymbol{U} + a_2{}^{t}\dot{\boldsymbol{U}} + a_3{}^{t}\ddot{\boldsymbol{U}}) + \boldsymbol{C}(a_1{}^{t}\boldsymbol{U} + a_4{}^{t}\dot{\boldsymbol{U}} + a_5{}^{t}\ddot{\boldsymbol{U}})$
2. Solve for displacements at time $t + \Delta t$:
   $\boldsymbol{L}\boldsymbol{D}\boldsymbol{L}^T{}^{t+\Delta t}\boldsymbol{U} = {}^{t+\Delta t}\hat{\boldsymbol{R}}$
3. Calculate accelerations and velocities at time $t + \Delta t$:
   ${}^{t+\Delta t}\ddot{\boldsymbol{U}} = a_0({}^{t+\Delta t}\boldsymbol{U} - {}^{t}\boldsymbol{U}) - a_2{}^{t}\dot{\boldsymbol{U}} - a_3{}^{t}\ddot{\boldsymbol{U}}$
   ${}^{t+\Delta t}\dot{\boldsymbol{U}} = {}^{t}\dot{\boldsymbol{U}} + a_6{}^{t}\ddot{\boldsymbol{U}} + a_7{}^{t+\Delta t}\ddot{\boldsymbol{U}}$

References

[1] S. S. Rao and M. Sunar, "Piezoelectricity and its use in disturbance sensing and control of flexible structures: A survey," *Appl. Mech. Rev.*, vol. 47, no. 4, pp. 113–123, 1994, doi: 10.1115/1.3111074.

[2] M. Saber, "Semi-passive vibration control using shunted piezoelectric materials," 2008.

[3] Z. D. Xu, Y. X. Liao, T. Ge, and C. Xu, "Experimental and Theoretical Study of Viscoelastic Dampers with Different Matrix Rubbers," *J. Eng. Mech.*, vol. 142, no. 8, 2016, doi: 10.1061/(asce)em.1943-7889.0001101.

[4] M. C. Constantinou and M. D. Symans, "Experimental study of seismic response," *Struct. Des. Tall Build.*, vol. 2, no. January, pp. 93–132, 1993.

[5] M. Gutierrez Soto and H. Adeli, "Tuned Mass Dampers," *Arch. Comput. Methods Eng.*, vol. 20, no. 4, pp. 419–431, 2013, doi: 10.1007/s11831-013-9091-7.

[6] "Mechanical Vibrations. Fourth Edition. J. P. Den Hartog. McGraw-Hill, New York, 1956. 67s. 6d.," *J. R. Aeronaut. Soc.*, vol. 61, no. 554, pp. 139–139, Feb. 1957, doi: 10.1017/S0368393100131049.

[7] S. F. Ali, "Semi-active Control of Earthquake Induced Vibrations in Structures using MR Dampers: Algorithm Development, Experimental Verification and Benchmark Applications," no. July, p. 473, 2008, [Online]. Available: http://engweb.swan.ac.uk/~alisk/publication_fol/MyPapers/Ali_thesis.pdf.

[8] G. Caruso, "A critical analysis of electric shunt circuits employed in piezoelectric passive vibration damping," *Smart Mater. Struct.*, vol. 10, no. 5, pp. 1059–1068, 2001, doi: 10.1088/0964-1726/10/5/322.

[9] S. Behrens, A. J. Fleming, and S. O. Reza Moheimani, "Electromagnetic shunt damping," *IEEE/ASME Int. Conf. Adv. Intell. Mechatronics, AIM*, vol. 2, no. May 2020, pp. 1145–1150, 2003, doi: 10.1109/AIM.2003.1225504.

[10] F. Ranglin, Z. Weicun, and F. Dongshuai, "Comparative study of active engine mount control methods," *Proc. 2017 9th Int. Conf. Model. Identif. Control. ICMIC 2017*, vol. 2018-March, no. Icmic, pp. 600–605, 2018, doi: 10.1109/ICMIC.2017.8321526.

[11] Y. Li, X. Wang, R. Huang, and Z. Qiu, "Active vibration and noise control of vibro-acoustic system by using PID controller," *J. Sound Vib.*, vol. 348, pp. 57–70, 2015, doi: 10.1016/j.jsv.2015.03.017.

[12] I. Nishimura, T. Kobori, M. Sakamoto, N. Koshika, K. Sasaki, and S. Ohrui, "Active tuned mass damper," *Smart Mater. Struct.*, vol. 1, no. 4, pp. 306–311, 1992, doi: 10.1088/0964-1726/1/4/005.

[13] H. R. Owji, A. H. N. Shirazi, and H. H. Sarvestani, "A comparison between a new semi-active tuned mass damper and an active tuned mass damper," *Procedia Eng.*, vol. 14, pp. 2779–2787,

2011, doi: 10.1016/j.proeng.2011.07.350.

[14] E. F. Crawley and J. De Luis, “Use of piezoelectric actuators as elements of intelligent structures,” *AIAA J.*, vol. 25, no. 10, pp. 1373–1385, 1987, doi: 10.2514/3.9792.

[15] L. Gaudiller and J. Der Hagopian, “Active control of flexible structures using a minimum number of components,” *J. Sound Vib.*, vol. 193, no. 3, pp. 713–741, 1996, doi: 10.1006/jsvi.1996.0310.

[16] S. Devasia, T. Meressi, B. Paden, and E. Bayo, “Piezoelectric Actuator Design for Vibration Suppression: Placement and sizing,” *J. Guid. Control. Dyn.*, vol. 16, no. 5, pp. 859–864, 1993, doi: 10.2514/3.21093.

[17] D. J. Inman, “Active modal control for smart structures,” *Philos. Trans. R. Soc. A Math. Phys. Eng. Sci.*, vol. 359, no. 1778, pp. 205–219, 2001, doi: 10.1098/rsta.2000.0721.

[18] X. Li, Y. Chen, R. Zhu, and G. Huang, “An active meta-layer for optimal flexural wave absorption and cloaking,” *Mech. Syst. Signal Process.*, vol. 149, p. 107324, 2021, doi: 10.1016/j.ymssp.2020.107324.

[19] G. M. Chatziathanasiou, N. A. Chrysochoidis, and D. A. Saravanos, “Dynamic analysis of an active isolation mount using feedforward and feedback control schemes,” in *Proceedings of the International Conference on Structural Dynamic , EURODYN*, 2020, vol. 2, pp. 4189–4199, [Online]. Available: https://www.scopus.com/inward/record.uri?eid=2-s2.0-85098691815&partnerID=40&md5=b017c621e7a3ed35cca2f26cfaa2db87.

[20] N. Olgac and B. T. Holm-Hansen, “A Novel active vibration absorption technique: Delayed resonator,” *Journal of Sound and Vibration*, vol. 176, no. 1. pp. 93–104, 1994, doi: 10.1006/jsvi.1994.1360.

[21] J. C. Doyle, K. Glover, P. P. Khargonekar, and B. A. Francis, “State-Space Solutions to Standard H2and H∞, Control Problems,” *IEEE Trans. Automat. Contr.*, vol. 34, no. 8, pp. 831–847, 1989, doi: 10.1109/9.29425.

[22] L. Zuo and S. A. Nayfeh, “The two-degree-of-freedom tuned-mass damper for suppression of single-mode vibration under random and harmonic excitation,” *J. Vib. Acoust.*, vol. 128, no. 1, pp. 56–65, 2006, doi: 10.1115/1.2128639.

[23] B. Seba, N. Nedeljkovic, J. Paschedag, and B. Lohmann, “H∞ Feedback control and Fx-LMS feedforward control for car engine vibration attenuation,” *Appl. Acoust.*, vol. 66, no. 3, pp. 277–296, 2005, doi: 10.1016/j.apacoust.2004.07.015.

[24] D. Mylonas, A. Erspamer, C. Yiakopoulos, and I. Antoniadis, “An extrapolation-based virtual sensing technique of improving the control performance of the FxLMS algorithm in a maritime environment,” *Appl. Acoust.*, vol. 193, p. 108756, 2022, doi: 10.1016/j.apacoust.2022.108756.

[25] T. Roy and D. Chakraborty, “GA-LQR based optimal vibration control of smart frp composite structures with bonded PZT patches,” *J. Reinf. Plast. Compos.*, vol. 28, no. 11, pp. 1383–1404, 2009, doi: 10.1177/0731684408089506.

[26] T. Butz and O. Von Stryk, “Modelling and simulation of electro- and magnetorheological fluid dampers,” *ZAMM Zeitschrift fur Angew. Math. und Mech.*, vol. 82, no. 1, pp. 3–20, 2002, doi: 10.1002/1521-4001(200201)82:1<3::AID-ZAMM3>3.0.CO;2-O.

[27] M. J. Brennan, “Some recent developments in adaptive tuned vibration absorbers/neutralisers,” *Shock Vib.*, vol. 13, no. 4–5, pp. 531–543, 2006, doi: 10.1155/2006/563934.

[28] A. J. Fleming and S. O. R. Moheimani, “Adaptive piezoelectric shunt damping,” *Smart Mater. Struct.*, vol. 12, no. 1, pp. 36–48, 2003, doi: 10.1088/0964-1726/12/1/305.

[29] M. De Volder, K. Yoshida, S. Yokota, and D. Reynaerts, “The use of liquid crystals as electrorheological fluids in microsystems: Model and measurements,” *J. Micromechanics Microengineering*, vol. 16, no. 3, pp. 612–619, 2006, doi: 10.1088/0960-1317/16/3/017.

[30] S. J. Dyke, B. F. Spencer, M. K. Sain, and J. D. Carlson, “Modeling and control of magnetorheological dampers for seismic response reduction,” *Smart Mater. Struct.*, vol. 5, no. 5, pp. 565–575, 1996, doi: 10.1088/0964-1726/5/5/006.

[31] Y. Liu, H. Matsuhisa, and H. Utsuno, “Semi-active vibration isolation system with variable stiffness and damping control,” *J. Sound Vib.*, vol. 313, no. 1–2, pp. 16–28, 2008, doi: 10.1016/j.jsv.2007.11.045.

[32] F. Weber, “Semi-active vibration absorber based on real-time controlled MR damper,” *Mech. Syst. Signal Process.*, vol. 46, no. 2, pp. 272–288, 2014, doi: 10.1016/j.ymssp.2014.01.017.

[33] H. Davorin, B. Pinhas, and R. Michael, “Semi-Active versus Passive or Active Tuned Mass Dampers for Structural Control,” *J. Eng. Mech.*, vol. 109, no. 3, pp. 691–705, Jun. 1983, doi: 10.1061/(ASCE)0733-9399(1983)109:3(691).

[34] J. A. B. Gripp and D. A. Rade, “Vibration and noise control using shunted piezoelectric transducers: A review,” *Mech. Syst. Signal Process.*, vol. 112, pp. 359–383, 2018, doi: 10.1016/j.ymssp.2018.04.041.

[35] F. H. (DE), “DEVICE FOR DAMPING VIBRATIONS OF BODIES.,” no. 0989958. 1911, [Online]. Available: https://www.freepatentsonline.com/0989958.html.

[36] S. Elias and V. Matsagar, “Research developments in vibration control of structures using passive tuned mass dampers,” *Annu. Rev. Control*, vol. 44, pp. 129–156, 2017, doi: 10.1016/j.arcontrol.2017.09.015.

[37] S. Krenk, “Frequency analysis of the tuned mass damper,” *J. Appl. Mech. Trans. ASME*, vol. 72, no. 6, pp. 936–942, 2005, doi: 10.1115/1.2062867.

[38] D. Richiedei, I. Tamellin, and A. Trevisani, “Beyond the Tuned Mass Damper: a Comparative Study of Passive Approaches to Vibration Absorption Through Antiresonance Assignment,” *Arch. Comput. Methods Eng.*, no. 0123456789, 2021, doi: 10.1007/s11831-021-09583-w.

[39] J. Høgsberg, B. Lossouarn, and J. F. Deü, “Tuning of vibration absorbers by an effective modal coupling factor,” *Int. J. Mech. Sci.*, vol. 268, no. September 2023, p. 109009, 2024, doi: 10.1016/j.ijmecsci.2024.109009.

[40] S. Elias, V. Matsagar, and T. K. Datta, “Distributed Tuned Mass Dampers for Multi-Mode Control of Benchmark Building under Seismic Excitations,” *J. Earthq. Eng.*, vol. 23, no. 7, pp. 1137–1172, Aug. 2019, doi: 10.1080/13632469.2017.1351407.

[41] A. Y. Tuan and G. Q. Shang, “Vibration control in a 101-storey building using a tuned mass damper,” *J. Appl. Sci. Eng.*, vol. 17, no. 2, pp. 141–156, 2014, doi: 10.6180/jase.2014.17.2.05.

[42] N. Debnath, S. K. Deb, and A. Dutta, “Multi-modal vibration control of truss bridges with tuned mass dampers under general loading,” *JVC/Journal Vib. Control*, vol. 22, no. 20, pp. 4121–4140, 2016, doi: 10.1177/1077546315571172.

[43] J. F. Wang, C. C. Lin, and B. L. Chen, “Vibration suppression for high-speed railway bridges using tuned mass dampers,” *Int. J. Solids Struct.*, vol. 40, no. 2, pp. 465–491, 2003, doi: 10.1016/S0020-7683(02)00589-9.

[44] A. Pipinato, “Extending the fatigue life of steel truss bridges with tuned mass damper systems,” *Adv. Civ. Eng.*, vol. 2019, 2019, doi: 10.1155/2019/5409013.

[45] V.-N. Dinh and B. Basu, “Passive control of floating offshore wind turbine nacelle and spar vibrations by multiple tuned mass dampers,” *Struct. Control Heal. Monit.*, vol. 22, no. 1, pp. 152–176, Jan. 2015, doi: https://doi.org/10.1002/stc.1666.

[46] H. Zuo, K. Bi, and H. Hao, “Using multiple tuned mass dampers to control offshore wind turbine vibrations under multiple hazards,” *Eng. Struct.*, vol. 141, pp. 303–315, 2017, doi: 10.1016/j.engstruct.2017.03.006.

[47] T. Pais and D. Boote, “Developments of Tuned Mass Damper for yacht structures,” *Ocean Eng.*, vol. 141, no. May 2016, pp. 249–264, 2017, doi: 10.1016/j.oceaneng.2017.06.046.

[48] P. Tatiana, B. Dario, and V. Gianmarco, “Vibration analysis for the comfort assessment of a superyacht under hydrodynamic loads due to mechanical propulsion,” *Ocean Eng.*, vol. 155, no. February, pp. 310–323, 2018, doi: 10.1016/j.oceaneng.2018.02.058.

[49] Y. M. Huang and C. R. Fuller, “Vibration and noise control of the fuselage via dynamic absorbers,” *J. Vib. Acoust. Trans. ASME*, vol. 120, no. 2, pp. 496–502, 1998, doi: 10.1115/1.2893857.

[50] Y. M. Huang and C. C. Chen, “Optimal design of dynamic absorbers on vibration and noise control of the fuselage,” *Comput. Struct.*, vol. 76, no. 6, pp. 691–702, 2000, doi: 10.1016/S0045-7949(99)00190-X.

[51] S. Cinquemani, F. Braghin, and F. Resta, “Semi active tunable mass damper for helicopters,” *Act. Passiv. Smart Struct. Integr. Syst. 2017*, vol. 10164, p. 1016431, 2017, doi: 10.1117/12.2259987.

[52] S. Chesné, G. Inquieté, P. Cranga, F. Legrand, and B. Petitjean, “Innovative Hybrid Mass Damper for Dual-Loop Controller,” *Mech. Syst. Signal Process.*, vol. 115, pp. 514–523, 2019, doi: 10.1016/j.ymssp.2018.06.023.

[53] T. Igusa and K. Xu, “Vibration control using multiple tuned mass dampers,” *Journal of Sound*

and Vibration, vol. 175, no. 4. pp. 491–503, 1994, doi: 10.1006/jsvi.1994.1341.

[54] A. Kareem and S. Kline, "Performance of multiple mass dampers under random loading," *Int. J. Rock Mech. Min. Sci. Geomech. Abstr.*, vol. 32, no. 6, p. A289, 1995, doi: 10.1016/0148-9062(95)99300-m.

[55] L. Zuo and S. A. Nayfeh, "Minimax optimization of multi-degree-of-freedom tuned-mass dampers," *J. Sound Vib.*, vol. 272, no. 3–5, pp. 893–908, 2004, doi: 10.1016/S0022-460X(03)00500-5.

[56] N. Su, Z. Chen, Y. Xia, and J. Bian, "Hybrid analytical H-norm optimization approach for dynamic vibration absorbers," *Int. J. Mech. Sci.*, vol. 264, no. September 2023, p. 108796, 2024, doi: 10.1016/j.ijmecsci.2023.108796.

[57] G. C. Marano, S. Sgobba, R. Greco, and M. Mezzina, "Robust optimum design of tuned mass dampers devices in random vibrations mitigation," *J. Sound Vib.*, vol. 313, no. 3–5, pp. 472–492, 2008, doi: 10.1016/j.jsv.2007.12.020.

[58] M. Zilletti, S. J. Elliott, and E. Rustighi, "Optimisation of dynamic vibration absorbers to minimise kinetic energy and maximise internal power dissipation," *J. Sound Vib.*, vol. 331, no. 18, pp. 4093–4100, 2012, doi: 10.1016/j.jsv.2012.04.023.

[59] A. E. Mustafa, A. Javed, and K. Ali, "Optimization of linear multiple-tuned mass damper to control nonlinear vibrations of high-speed railway PRC bridges," *Structures*, vol. 63, no. April 2023, p. 106319, 2024, doi: 10.1016/j.istruc.2024.106319.

[60] O. Lavan, "Multi-objective optimal design of tuned mass dampers," *Struct. Control Heal. Monit.*, vol. 24, no. 11, pp. 1–16, 2017, doi: 10.1002/stc.2008.

[61] Y. Arfiadi and M. N. S. Hadi, "Optimum Placement and Properties of Tuned Mass Dampers Using Hybrid Genetic Algorithms," *Int. J. Optim. Civ. Eng.*, vol. 1, no. September, pp. 167–187, 2011.

[62] A. J. Felber, "Development of a hybrid bridge evaluation system," no. December, pp. 1–277, 1994.

[63] W. H. Chen *et al.*, "Theoretical and experimental modal analysis of the Guangzhou New TV Tower," *Eng. Struct.*, vol. 33, no. 12, pp. 3628–3646, 2011, doi: 10.1016/j.engstruct.2011.07.028.

[64] A. Aloisio, D. Pasca, R. Tomasi, and M. Fragiacomo, "Dynamic identification and model updating of an eight-storey CLT building," *Eng. Struct.*, vol. 213, no. March, p. 110593, 2020, doi: 10.1016/j.engstruct.2020.110593.

[65] R. E. Kalman, "A new approach to linear filtering and prediction problems," *J. Fluids Eng. Trans. ASME*, vol. 82, no. 1, pp. 35–45, 1960, doi: 10.1115/1.3662552.

[66] A. J. Roffel and S. Narasimhan, "Extended Kalman filter for modal identification of structures equipped with a pendulum tuned mass damper," *J. Sound Vib.*, vol. 333, no. 23, pp. 6038–6056, 2014, doi: 10.1016/j.jsv.2014.06.030.

[67] S. Schleiter and O. Altay, “Identification and semi-active control of structures with abrupt stiffness degradations,” *Mech. Syst. Signal Process.*, vol. 163, no. June 2021, p. 108131, 2022, doi: 10.1016/j.ymssp.2021.108131.

[68] G. L. Lin, C. C. Lin, B. C. Chen, and T. T. Soong, “Vibration control performance of tuned mass dampers with resettable variable stiffness,” *Eng. Struct.*, vol. 83, pp. 187–197, 2015, doi: 10.1016/j.engstruct.2014.10.041.

[69] Z. Wang, H. Gao, H. Wang, and Z. Chen, “Development of stiffness-adjustable tuned mass dampers for frequency retuning,” *Adv. Struct. Eng.*, vol. 22, no. 2, pp. 473–485, 2019, doi: 10.1177/1369433218791356.

[70] A. Gideon P. Stein and O. A. D. Ferencz, “Ulllted States Patent,” vol. 2, no. 12, pp. 2–9, 2012.

[71] L. Wang, W. Shi, X. Li, Q. Zhang, and Y. Zhou, “An adaptive-passive retuning device for a pendulum tuned mass damper considering mass uncertainty and optimum frequency,” *Struct. Control Heal. Monit.*, vol. 26, no. 7, pp. 1–21, 2019, doi: 10.1002/stc.2377.

[72] “Structural Design Tall Build - 2018 - Wang - Study on self-adjustable variable pendulum tuned mass damper.pdf.” .

[73] D. Rizos, G. Feltrin, and M. Motavalli, “Structural identification of a prototype pre-stressable leaf-spring based adaptive tuned mass damper: Nonlinear characterization and classification,” *Mechanical Systems and Signal Processing*, vol. 25, no. 1. pp. 205–221, 2011, doi: 10.1016/j.ymssp.2010.07.001.

[74] T. Pinkaew and Y. Fujino, “Effectiveness of semi-active tuned mass dampers under harmonic excitation,” *Eng. Struct.*, vol. 23, no. 7, pp. 850–856, 2001, doi: 10.1016/S0141-0296(00)00091-2.

[75] W. Shi, L. Wang, Z. Lu, and H. Wang, “Experimental and numerical study on adaptive-passive variable mass tuned mass damper,” *J. Sound Vib.*, vol. 452, pp. 97–111, 2019, doi: 10.1016/j.jsv.2019.04.008.

[76] M. Maślanka, “Optimised semi-active tuned mass damper with acceleration and relative motion feedbacks,” *Mech. Syst. Signal Process.*, vol. 130, pp. 707–731, 2019, doi: 10.1016/j.ymssp.2019.05.025.

[77] K. A. Williams, G. T. Chiu, and R. J. Bernhard, “ARTICLE IN PRESS Dynamic modelling of a shape memory alloy adaptive tuned vibration absorber,” vol. 280, pp. 211–234, 2005, doi: 10.1016/j.jsv.2003.12.040.

[78] S. Manzoni, A. Argentino, F. Lucà, M. Berardengo, and M. Vanali, “SMA-based adaptive tuned mass dampers: Analysis and comparison,” *Mech. Syst. Signal Process.*, vol. 186, no. November 2022, p. 109883, 2023, doi: 10.1016/j.ymssp.2022.109883.

[79] R. L. Forward, “Electronic damping of vibrations in optical structures,” *Appl. Opt.*, vol. 18, no. 5, p. 690, 1979, doi: 10.1364/ao.18.000690.

[80] N. W. Hagood and A. von Flotow, “Damping of structural vibrations with piezoelectric materials

and passive electrical networks," *J. Sound Vib.*, vol. 146, no. 2, pp. 243–268, 1991, doi: https://doi.org/10.1016/0022-460X(91)90762-9.

[81] C. L. Davis and G. A. Lesieutre, "A modal strain energy approach to the prediction of resistively shunted piezoceramic damping," *J. Sound Vib.*, vol. 184, no. 1, pp. 129–139, 1995, doi: 10.1006/jsvi.1995.0308.

[82] D. A. Saravanos, "Damped vibration of composite plates with passive piezoelectric-resistor elements," *J. Sound Vib.*, vol. 221, no. 5, pp. 867–885, 1999, doi: 10.1006/jsvi.1998.2037.

[83] T. S. Plagianakos and D. A. Saravanos, "Hybrid multidamped composite plates with viscoelastic composite plies and shunted piezoelectric layers," *J. Intell. Mater. Syst. Struct.*, vol. 14, no. 1, pp. 57–66, 2003, doi: 10.1177/1045389X03014001006.

[84] D. I. Chortis, N. A. Chrysochoidis, D. S. Varelis, and D. A. Saravanos, "A damping mechanics model and a beam finite element for the free-vibration of laminated composite strips under in-plane loading," *J. Sound Vib.*, vol. 330, no. 23, pp. 5660–5677, 2011, doi: 10.1016/j.jsv.2011.06.025.

[85] J. Høgsberg and S. Krenk, "Balanced calibration of resonant shunt circuits for piezoelectric vibration control," *J. Intell. Mater. Syst. Struct.*, vol. 23, no. 17, pp. 1937–1948, 2012, doi: 10.1177/1045389X12455727.

[86] J. D. Richardt, B. Lossouarn, J. Høgsberg, and J. F. Deü, "Calibration of multiple shunted piezoelectric transducers with correction for residual modes and shunt interactions," *JVC/Journal Vib. Control*, no. 444070, 2024, doi: 10.1177/10775463241241838.

[87] N. W. Hagood and E. F. Crawley, "Experimental investigation of passive enhancement of damping for space structures," *J. Guid. Control. Dyn.*, vol. 14, no. 6, pp. 1100–1109, 1991, doi: 10.2514/3.20763.

[88] S. Wu, "Multiple PZT transducers implemented with multiple-mode piezoelectric shunting for passive vibration damping," vol. 3672, no. March, pp. 112–122, 1999.

[89] J. Dosch, G. Lesieutre, G. Koopmann, and C. Davis, "Inertial piezoceramic actuators for smart structures," vol. 2447, pp. 14–25.

[90] W. Zhou, Muhammad, W. Chen, Z. Chen, and C. W. Lim, "Actively controllable flexural wave band gaps in beam-type acoustic metamaterials with shunted piezoelectric patches," *Eur. J. Mech. - A/Solids*, vol. 77, p. 103807, 2019, doi: https://doi.org/10.1016/j.euromechsol.2019.103807.

[91] K. K. Bera, S. Biswas, and A. Banerjee, "Optimized piezo-shunted metadamping towards the high-stiff high-damped metamaterial," *J. Intell. Mater. Syst. Struct.*, vol. 35, no. 7, pp. 705–717, 2024, doi: 10.1177/1045389X241229104.

[92] C. Xu, Y. Yang, C. H. Wang, and L. Zhao, "Simultaneous low-frequency vibration suppression and energy harvesting using a metastructure with alternately combined nonlinear local resonators," *Mech. Syst. Signal Process.*, vol. 211, no. December 2023, p. 111241, 2024, doi:

10.1016/j.ymssp.2024.111241.

[93] A. Dwivedi, A. Banerjee, S. Adhikari, and B. Bhattacharya, “Optimal electromechanical bandgaps in piezo-embedded mechanical metamaterials,” *Int. J. Mech. Mater. Des.*, vol. 17, no. 2, pp. 419–439, 2021, doi: 10.1007/s10999-021-09534-0.

[94] J. J. Hollkamp, “Multimodal Passive Vibration Suppression with Piezoelectric Materials and Resonant Shunts,” *J. Intell. Mater. Syst. Struct.*, vol. 5, no. 1, pp. 49–57, 1994, doi: 10.1177/1045389X9400500106.

[95] S. Wu, “Method for multiple-mode shunt damping of structural vibration using a single PZT transducer,” in *Smart Structures and Materials 1998: Passive Damping and Isolation*, 1998, vol. 3327, pp. 159–168, doi: 10.1117/12.310680.

[96] S. Behrens and S. O. R. Moheimani, “Current flowing multiple-mode piezoelectric shunt dampener,” in *Smart Structures and Materials 2002: Damping and Isolation*, 2002, vol. 4697, pp. 217–226, doi: 10.1117/12.472658.

[97] A. J. Fleming, S. Behrens, and S. O. R. Moheimani, “Synthetic impedance for implementation of piezoelectric shunt-damping circuits,” *Electron. Lett.*, vol. 36, no. 18, pp. 1525–1526, 2000, doi: 10.1049/el:20001083.

[98] A. J. Fleming, S. Behrens, and S. O. Reza Moheimani, “Optimization and implementation of multimode piezoelectric shunt damping systems,” *IEEE/ASME Trans. Mechatronics*, vol. 7, no. 1, pp. 87–94, 2002, doi: 10.1109/3516.990891.

[99] O. Alfahmi and A. Erturk, “Programmable hardening and softening cubic inductive shunts for piezoelectric structures: Harmonic balance analysis and experiments,” *J. Sound Vib.*, vol. 571, no. February 2023, p. 118029, 2024, doi: 10.1016/j.jsv.2023.118029.

[100] C. H. Park and A. Baz, “Vibration control of beams with negative capacitive shunting of interdigital electrode piezoceramics,” *JVC/Journal of Vibration and Control*, vol. 11, no. 3. pp. 331–346, 2005, doi: 10.1177/107754605040949.

[101] M. Neubauer, R. Oleskiewicz, K. Popp, and T. Krzyzynski, “Optimization of damping and absorbing performance of shunted piezo elements utilizing negative capacitance,” *J. Sound Vib.*, vol. 298, no. 1–2, pp. 84–107, 2006, doi: 10.1016/j.jsv.2006.04.043.

[102] M. Neubauer and J. Wallaschek, “Vibration damping with piezoceramics shunted to negative capacitance networks,” in *2009 IEEE/ASME International Conference on Advanced Intelligent Mechatronics*, 2009, pp. 1100–1105, doi: 10.1109/AIM.2009.5229733.

[103] M. Berardengo, S. Manzoni, O. Thomas, and M. Vanali, “Piezoelectric resonant shunt enhancement by negative capacitances: Optimisation, performance and resonance cancellation,” *J. Intell. Mater. Syst. Struct.*, vol. 29, no. 12, pp. 2581–2606, 2018, doi: 10.1177/1045389X18770874.

[104] B. De Marneffe and A. Preumont, “Vibration damping with negative capacitance shunts: Theory and experiment,” *Smart Mater. Struct.*, vol. 17, no. 3, 2008, doi: 10.1088/0964-

1726/17/3/035015.

[105] M. Berardengo, O. Thomas, C. Giraud-Audine, and S. Manzoni, “Improved resistive shunt by means of negative capacitance: New circuit, performances and multi-mode control,” *Smart Mater. Struct.*, vol. 25, no. 7, 2016, doi: 10.1088/0964-1726/25/7/075033.

[106] S. Manzoni, S. Moschini, M. Redaelli, and M. Vanali, “Vibration attenuation by means of piezoelectric transducer shunted to synthetic negative capacitance,” *J. Sound Vib.*, vol. 331, no. 21, pp. 4644–4657, 2012, doi: 10.1016/j.jsv.2012.05.014.

[107] C. Richard, D. Guyomar, D. Audigier, and G. Ching, “Semi-passive damping using continuous switching of a piezoelectric device,” in *Smart Structures and Materials 1999: Passive Damping and Isolation*, 1999, vol. 3672, pp. 104–111, doi: 10.1117/12.349773.

[108] W. W. Clark, “Vibration control with state-switched piezoelectric materials,” *J. Intell. Mater. Syst. Struct.*, vol. 11, no. 4, pp. 263–271, 2000, doi: 10.1106/18CE-77K4-DYMG-RKBB.

[109] C. Richard, D. Guyomar, D. Audigier, and H. Bassaler, “<title>Enhanced semi-passive damping using continuous switching of a piezoelectric device on an inductor</title>,” *Smart Struct. Mater. 2000 Damping Isol.*, vol. 3989, pp. 288–299, 2000, doi: 10.1117/12.384569.

[110] J. Ducarne, O. Thomas, and J. F. Deü, “Structural vibration reduction by switch shunting of piezoelectric elements: Modeling and optimization,” *J. Intell. Mater. Syst. Struct.*, vol. 21, no. 8, pp. 797–816, 2010, doi: 10.1177/1045389X10367835.

[111] Y. Wu *et al.*, “Bidirectional energy-controlled piezoelectric shunt damping technology and its vibration attenuation performance,” *International Journal of Mechanical System Dynamics*. 2024, doi: 10.1002/msd2.12101.

[112] S. O. R. Moheimani, “A survey of recent innovations in vibration damping and control using shunted piezoelectric transducers,” *IEEE Trans. Control Syst. Technol.*, vol. 11, no. 4, pp. 482–494, 2003, doi: 10.1109/TCST.2003.813371.

[113] S. Wu, “Piezoeleciric shunts with a parallel R-L circuit for structural damping and vibration control Shu-yau Wu McDonnell Douglas Aerospace Company 5301 Bolsa Avenue, Huntington Beach, CA 92647,” *Spie*, vol. 2720, no. Lc, 1996.

[114] P. Gardonio and D. Casagrande, “Shunted piezoelectric patch vibration absorber on two-dimensional thin structures: Tuning considerations,” *J. Sound Vib.*, vol. 395, pp. 26–47, 2017, doi: 10.1016/j.jsv.2017.02.019.

[115] J. Kim, Y. H. Ryu, and S. B. Choi, “New shunting parameter tuning method for piezoelectric damping based on measured electrical impedance,” *Smart Mater. Struct.*, vol. 9, no. 6, pp. 868–877, 2000, doi: 10.1088/0964-1726/9/6/318.

[116] J. Kim and J.-K. Lee, “Broadband transmission noise reduction of smart panels featuring piezoelectric shunt circuits and sound-absorbing material,” *J. Acoust. Soc. Am.*, vol. 112, no. 3, pp. 990–998, 2002, doi: 10.1121/1.1497367.

[117] J. Kim and J. Y. Choi, “Performance test for transmitted noise reduction of smart panels using

piezoelectric shunt damping," *Smart Mater. Struct.*, vol. 14, no. 4, pp. 587–593, 2005, doi: 10.1088/0964-1726/14/4/017.

[118] P. Gardonio, G. Konda Rodrigues, L. Dal Bo, and E. Turco, "Extremum seeking online tuning of a piezoelectric vibration absorber based on the maximisation of the shunt electric power absorption," *Mech. Syst. Signal Process.*, vol. 176, no. November 2021, p. 109171, 2022, doi: 10.1016/j.ymssp.2022.109171.

[119] D. E. Casagrande, P. Gardonio, and G. Konda Rodrigues, "Tonal vibration control with a self-tuning absorber employing the extremum seeking algorithm," *Mech. Syst. Signal Process.*, vol. 211, no. December 2023, p. 111254, 2024, doi: 10.1016/j.ymssp.2024.111254.

[120] J. J. Hollkamp and T. F. Starchville, "A Self-Tuning Piezoelectric Vibration Absorber," *J. Intell. Mater. Syst. Struct.*, vol. 5, no. 4, pp. 559–566, 1994, doi: 10.1177/1045389X9400500412.

[121] D. Niederberger, A. Fleming, S. O. R. Moheimani, and M. Morari, "Adaptive multi-mode resonant piezoelectric shunt damping," *Smart Mater. Struct.*, vol. 13, no. 5, pp. 1025–1035, 2004, doi: 10.1088/0964-1726/13/5/007.

[122] P. Gardonio, M. Zientek, and L. Dal Bo, "Panel with self-tuning shunted piezoelectric patches for broadband flexural vibration control," *Mech. Syst. Signal Process.*, vol. 134, p. 106299, 2019, doi: 10.1016/j.ymssp.2019.106299.

[123] G. Konda Rodrigues, P. Gardonio, L. Dal Bo, and E. Turco, "Piezoelectric patch vibration control unit connected to a self-tuning RL-shunt set to maximise electric power absorption," *J. Sound Vib.*, vol. 536, no. June, p. 117154, 2022, doi: 10.1016/j.jsv.2022.117154.

[124] J. Paixão, E. Foltête, E. Sadoulet-Reboul, G. Chevallier, and S. Cogan, "Self-adaptive piezoelectric vibration absorber with semi-passive tunable resonant shunts," *J. Sound Vib.*, vol. 583, no. March, p. 118424, 2024, doi: 10.1016/j.jsv.2024.118424.

[125] M. Lallart, L. Yan, Y. C. Wu, and D. Guyomar, "Electromechanical semi-passive nonlinear tuned mass damper for efficient vibration damping," *J. Sound Vib.*, vol. 332, no. 22, pp. 5696–5709, 2013, doi: 10.1016/j.jsv.2013.06.006.

[126] O. Heuss, R. Salloum, D. Mayer, and T. Melz, "Tuning of a vibration absorber with shunted piezoelectric transducers," *Arch. Appl. Mech.*, vol. 86, no. 10, pp. 1715–1732, 2016, doi: 10.1007/s00419-014-0972-5.

[127] K. Yamada and T. Asami, "Passive vibration suppression using 2-degree-of-freedom vibration absorber consisting of a beam and piezoelectric elements," *J. Sound Vib.*, vol. 532, no. April, p. 116997, 2022, doi: 10.1016/j.jsv.2022.116997.

[128] S. Manzoni, M. Berardengo, F. Boccuto, and M. Vanali, "Piezoelectric-shunt-based approach for multi-mode adaptive tuned mass dampers," *Mech. Syst. Signal Process.*, vol. 200, no. July, p. 110537, 2023, doi: 10.1016/j.ymssp.2023.110537.

[129] M. Rezaei, R. Talebitooti, W. H. Liao, and M. I. Friswell, "Integrating PZT layer with tuned mass damper for simultaneous vibration suppression and energy harvesting considering exciter

dynamics: An analytical and experimental study," *J. Sound Vib.*, vol. 546, no. October 2022, p. 117413, 2023, doi: 10.1016/j.jsv.2022.117413.

[130] C. L. Davisa, G. A. Lesieutrea, and J. Doschb, "I ' I ',", vol. 3045, pp. 51–59.

[131] C. L. Davis and G. A. Lesieutre, "Actively tuned solid-state vibration absorber using capacitive shunting of piezoelectric stiffness," *J. Sound Vib.*, vol. 232, no. 3, pp. 601–617, 2000, doi: 10.1006/jsvi.1999.2755.

[132] S. F. Ali and S. Adhikari, "Energy harvesting dynamic vibration absorbers," *J. Appl. Mech. Trans. ASME*, vol. 80, no. 4, pp. 1–9, 2013, doi: 10.1115/1.4007967.

[133] J. Høgsberg, "Vibration control by piezoelectric proof-mass absorber with resistive-inductive shunt," *Mech. Adv. Mater. Struct.*, vol. 6494, 2019, doi: 10.1080/15376494.2018.1551587.

[134] G. Zhao, N. Alujević, B. Depraetere, and P. Sas, "Dynamic analysis and 2 optimisation of a piezo-based tuned vibration absorber," *J. Intell. Mater. Syst. Struct.*, vol. 26, no. 15, pp. 1995–2010, 2015, doi: 10.1177/1045389X14546652.

[135] Y. A. Lai, J. Y. Kim, C. S. W. Yang, and L. L. Chung, "A low-cost and efficient d33-mode piezoelectric tuned mass damper with simultaneously optimized electrical and mechanical tuning," *J. Intell. Mater. Syst. Struct.*, vol. 32, no. 6, pp. 678–696, 2021, doi: 10.1177/1045389X20966056.

[136] W. Sheng and H. Xiang, "A piezoelectric tuned mass damper for simultaneous vibration control and energy harvesting," *Smart Mater. Struct.*, vol. 33, no. 1, 2024, doi: 10.1088/1361-665X/ad1317.

[137] W. G. Cady, *Piezoelectricity: An Introduction to the Theory and Applications of Electromechanical Phenomena in Crystals*, no. v. 1. Dover Publications, 1964.

[138] H. F. Tiersten, *Linear Piezoelectric Plate Vibrations: Elements of the Linear Theory of Piezoelectricity and the Vibrations of Piezoelectric Plates*. University Microfilms, 1969.

[139] T. B. Xu *et al.*, "Energy harvesting using a PZT ceramic multilayer stack," *Smart Mater. Struct.*, vol. 22, no. 6, 2013, doi: 10.1088/0964-1726/22/6/065015.

[140] R. L. Goldberg, M. J. Jurgens, D. M. Mills, C. S. Henriquez, D. Vaughan, and S. W. Smith, "Modeling of piezoelectric multilayer ceramics using finite element analysis," *IEEE Trans. Ultrason. Ferroelectr. Freq. Control*, vol. 44, no. 6, pp. 1204–1214, 1997, doi: 10.1109/58.656622.

[141] Y. Zhang, T. F. Lu, and S. Al-Sarawi, "Formulation of a simple distributed-parameter model of multilayer piezoelectric actuators," *J. Intell. Mater. Syst. Struct.*, vol. 27, no. 11, pp. 1485–1491, 2016, doi: 10.1177/1045389X15595294.

[142] F. Qian, T. B. Xu, and L. Zuo, "Material equivalence, modeling and experimental validation of a piezoelectric boot energy harvester," *Smart Mater. Struct.*, vol. 28, no. 7, pp. 0–27, 2019, doi: 10.1088/1361-665X/ab1eb7.

[143] P. P. Actuator, "PPA120L PPA120L," vol. 33, no. 3, pp. 58–59.

[144] Cedrat Technologies version 5.1, “Cedrat Technologies catalogue,” 2019, [Online]. Available: Available on request from Cedrat Technologies.

[145] F. Claeyssen, “(12) United States Patent,” vol. 2, no. 12, 2005.

[146] A. M. González, Á. García, C. Benavente-Peces, and L. Pardo, “Revisiting the characterization of the losses in piezoelectric materials from impedance spectroscopy at resonance,” *Materials (Basel).*, vol. 9, no. 2, 2016, doi: 10.3390/ma9020072.

[147] TAVAC Project: CleanSky 2 JTI , GRA 717089 : Active technologies for acoustic and vibration comfort..

[148] K. J. Bathe, *Finite Element Procedures*. 1996.

[149] Bielawa R L (2006) *Rotary Wing Structural Dynamics and Aeroelasticity*. 2nd edition. American Institute of Aeronautics and Astronautics, Inc. https://doi.org/10.2514/4.862373.

[150] I. NAGASAKA, Y. ISHIDA, T. KOYAMA, and N. FUJIMATSU, “Vibration Suppression of a Helicopter Using Pendulum Absorbers : First Elastic Mode of a Blade,” *J. Syst. Des. Dyn.*, vol. 4, no. 6, pp. 837–847, 2010, doi: 10.1299/jsdd.4.837.

[151] C. Yong, D. G. Zimcik, V. K. Wickramasinghe, and F. Nitzsche, “Development of the smart spring for active vibration control of helicopter blades,” *J. Intell. Mater. Syst. Struct.*, vol. 15, no. 1, pp. 37–47, 2004, doi: 10.1177/1045389X04039655.

[152] S. Murugan and R. Ganguli, “Aeroelastic stability enhancement and vibration suppression in a composite helicopter rotor,” *J. Aircr.*, vol. 42, no. 4, pp. 1013–1024, 2005, doi: 10.2514/1.5652.

[153] M. Jiang, X. Rui, W. Zhu, F. Yang, and Y. Zhang, “Design and control of helicopter main reducer vibration isolation platform with magnetorheological dampers,” *Int. J. Mech. Mater. Des.*, vol. 17, no. 2, pp. 345–366, 2021, doi: 10.1007/s10999-021-09529-x.

[154] G. J. Hiemenz, W. Hu, and N. M. Wereley, “Semi-active magnetorheological helicopter crew seat suspension for vibration isolation,” *J. Aircr.*, vol. 45, no. 3, pp. 945–953, 2008, doi: 10.2514/1.32736.

[155] A. Tamer, V. Muscarello, P. Masarati, and G. Quaranta, “Evaluation of vibration reduction devices for helicopter ride quality improvement,” *Aerosp. Sci. Technol.*, vol. 95, p. 105456, 2019, doi: 10.1016/j.ast.2019.105456.

[156] P. No and J. Stoppel, “SIXTH EUROPEAN ROTORCRAFT AND POWERED LIFT AIRCRAFT FORUM A COMPARISON WITH GROUND VIBRATION TESTS,” 1980.

[157] Kumar J S (2016) Helicopter Vibrations - A Perspective. *International Journal of Research in Aeronautical and Mechanical Engineering* 4(6): 50-63.

[158] T1EDK-03427, Project acronym: TRANVIC: Distributed Smart Material Arrays for Low-Frequency Broadband Active Noise and Vibration Suppression in Vehicles and Light Structures. Funded under EU and Greece, through the Operational Program

Competitiveness, Entrepreneurship and Innovation, under the call RESEARCH – CREATE – INNOVATE 2014-2020.

[159] S. Behrens, A. J. Fleming, and S. O. R. Moheimani, "A broadband controller for shunt piezoelectric damping of structural vibration," *Smart Mater. Struct.*, vol. 12, no. 1, pp. 18–28, 2003, doi: 10.1088/0964-1726/12/1/303.

[160] G. M. Chatziathanasiou, N. A. Chrysochoidis, and D. A. Saravanos, "Autonomous Semi-Active Tuned Mass Damper for Adaptive Vibration Control of Aircraft Structures," in *AIAA SCITECH 2022 Forum*, American Institute of Aeronautics and Astronautics, 2021.

[161] P. D. Welch, "The Use of Fast Fourier Transform for the Estimation of Power Spectra," *IEEE Trans. audio Electroacoust.*, vol. AU-15, no. 2, pp. 70–73, 1967, [Online]. Available: https://ieeexplore.ieee.org/document/1161901.

[162] K. Kritikakos, S. D. Fassois, and J. S. Sakellariou, "Robust early detection of hunting on railway vehicles: single-sensor based methods and critical comparisons," *Int. J. Rail Transp.*, vol. 00, no. 00, pp. 1–21, 2023, doi: 10.1080/23248378.2023.2181237.

[163] C. E. Shannon, "Communication in the Presence of Noise," *Proc. {IRE}*, vol. 37, no. 1, pp. 10–21, Jan. 1949, doi: 10.1109/jrproc.1949.232969.

[164] A. G. Poulimenos and S. D. Fassois, "Parametric time-domain methods for non-stationary random vibration modelling and analysis - A critical survey and comparison," *Mech. Syst. Signal Process.*, vol. 20, no. 4, pp. 763–816, 2006, doi: 10.1016/j.ymssp.2005.10.003.

[165] L. Ljung, *System Identification: Theory for the User*. Prentice Hall PTR, 1999.

[166] G. Schwarz, "Estimating the Dimension of a Model," *Ann. Stat.*, vol. 6, pp. 461–464, 1978, [Online]. Available: https://api.semanticscholar.org/CorpusID:123722079.

[167] G. C. Kardarakos *et al.*, "Computational and Experimental Efficiency Investigation of Nonlinear Energy Harvesting Systems Based on Monostable and Bistable Piezoelectric Beams," 2021, vol. ASME 2021, doi: 10.1115/SMASIS2021-68209.

[168] Y. Kuang, Z. J. Chew, J. Dunville, J. Sibson, and M. Zhu, "Strongly coupled piezoelectric energy harvesters: Optimised design with over 100 mW power, high durability and robustness for self-powered condition monitoring," *Energy Convers. Manag.*, vol. 237, no. December 2020, p. 114129, 2021, doi: 10.1016/j.enconman.2021.114129.

Thesis Publications

Patent

- Application for Patent in European Patent Office (EPO): “Broadband Tunable Piezoelectric Mass Damper (PIEMDAM)”, submitted on 12 October 2023, awaiting for approval.

Publications in International Refereed Journals

- Chatziathanasiou GM, Chrysochoidis NA, Saravanos DA. A semi-active shunted piezoelectric tuned mass damper for robust vibration control. Journal of Vibration and Control. 2022;28(21-22):2969-2983. doi:10.1177/10775463211026487.
- Grigorios M. Chatziathanasiou, Nikolaos A. Chrysochoidis, Christoforos S. Rekatsinas, Dimitris A. Saravanos, A semi-active shunted piezoelectric tuned-mass-damper for multi-modal vibration control of large flexible structures, Journal of Sound and Vibration, Volume 537, 2022, 117222, ISSN 0022-460X, https://doi.org/10.1016/j.jsv.2022.117222.

Accepted Papers in International Refereed Journals

- Chatziathanasiou GM, Chrysochoidis NA, Saravanos DA. Multi-Tonal Vibration Suppression in Flexible Airframe Structures via a Semi-Active Shunted Piezoelectric Tuned Mass Damper, Journal of Vibration and Control*, accepted for publication subject to revisions*.

Pending Submissions in International Refereed Journals

- Chatziathanasiou GM, Chrysochoidis NA, Saravanos DA. “Electromechanical Parameters and Placement Optimization of a Semi-Active Piezoelectric Tuned Mass Damper for Multi-Modal Vibration Control on Airframe Structures”, *in preperation.*
- Chatziathanasiou GM, Chrysochoidis NA, Saravanos DA. “Development and Testing of an Adaptive Piezoelectric Tuned Mass Damper for the Vibration Control of Flexible Structures Operating Under Altering Dynamic Characteristics”, *in preparation.*

Articles in International Conferences

- Grigoris Chatziathanasiou, Nikolaos Chrysohoidis, Georgopoulos Kostas and Dimitrios A. Saravanos. "Semi-Active Vibration Control of Aircraft Structures," AIAA 2021-1736. AIAA Scitech 2021 Forum. January 2021, doi: 10.2514/6.2021-1736.

- Chatziathanasiou, GM, Dimitriou, DK, Chrysochoidis, NA, & Saravanos, DA. "Design and Structural Integration of a Semi-Active Tuned Mass Damper for Improved Vibration Control on Airframe Structures." Proceedings of the ASME 2021 Conference on Smart Materials, Adaptive Structures and Intelligent Systems. ASME 2021 Conference on Smart Materials, Adaptive Structures and Intelligent Systems. Virtual, Online. September 14–15, 2021. V001T05A014. ASME. https://doi.org/10.1115/SMASIS2021-68211
- Grigorios M. Chatziathanasiou, Nikolaos A. Chrysochoidis and Dimitrios A. Saravanos. "Autonomous Semi-Active Tuned Mass Damper for Adaptive Vibration Control of Aircraft Structures," AIAA 2022-1342. AIAA SCITECH 2022 Forum. January 2022, doi: 10.2514/6.2022-1342.
- Grigorios M. Chatziathanasiou, Nikolaos A. Chrysochoidis and Dimitrios A. Saravanos. "VIBRATION SUPPRESSION OF LARGE FLEXIBLE STRUCTURES SUBJECTED TO TONAL EXCITATIONS VIA A SEMI-ACTIVE SHUNTED PIEZOELECTRIC TUNED MASS DAMPER", SMART 2023, 03-05 July 2023, Patras, Greece, 10th ECCOMAS Thematic Conference on Smart Structures and Materials. https://doi.org/10.7712/150123.9775.451064.
- Grigorios M. Chatziathanasiou, Nikolaos A. Chrysochoidis and Dimitrios A. Saravanos. "Adaptive Vibration Suppression with a Semi-Active Piezoelectric Tuned Mass Damper", submitted to ICAST2024: The 33rd International Conference on Adaptive Structures and Technologies, May 20-22, 2024, Atlanta, Georgia, USA.